nuclear technology

# CONTENTS — FEBRUARY 1972



Address all manuscript and editorial communications to the editorial offices, *Nuclear Technology*, Department of Nuclear Engineering, The University of Arizona, Tucson, Arizona 85721.

*Nuclear Technology* is published monthly by the American Nuclear Society, Inc., with executive and business offices at 244 East Ogden Avenue, Hinsdale, Illinois 60521, telephone 312/325-1991. Subscription rate is $30 or $110/four volumes per year. Single copy price is $13 (special issue slightly higher). It is printed in Danville, Illinois, and second class postage is paid at Hinsdale, Illinois, and at additional mailing offices. 

**ON THE COVER:**

*This month's cover is a neutron radiograph taken with a TRIGA MARK-I reactor at the Gulf Energy and Environmental Systems San Diego facility.*

## TECHNICAL PAPERS



## TECHNICAL NOTES



## DEPARTMENTS

nuclear technology

# AUTHORS — FEBRUARY 1972

## REACTORS

### THE BREEDING RATIO WITH CORRELATION TO DOUBLING TIME AND FUEL CYCLE REACTIVITY VARIATION

*C. R. Adkins*

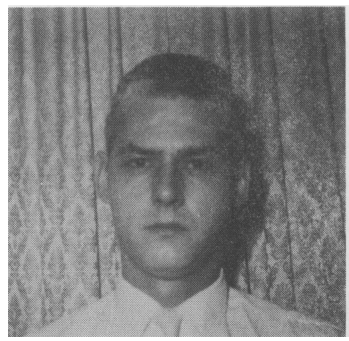

Charles Richard Adkins (PhD, nuclear engineering, Carnegie Institute of Technology, 1966) is associate professor of nuclear science and engineering, Carnegie-Mellon University, Pittsburgh, Pennsylvania. His interests are in reactor design (principally LMFBR design and optimization), reactor physics, kinetics and safety, and public acceptance of nuclear power for peaceful applications.

### MODELS FOR THE SAFE STORAGE OF FISSILE METAL

*S. J. Altschuler*
*C. L. Schuske*

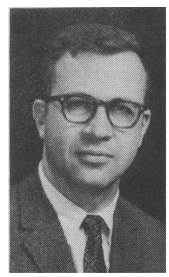

Sidney J. Altschuler (left) (BChE, The Cooper Union for the Advancement of Science and Art, 1957) is a research physicist at Dow Chemical USA's Rocky Flats Plant working on computer calculations for nuclear criticality safety purposes. C. L. Schuske (BA, Whittier College, 1943; MS, University of Southern California, 1945) is director of nuclear safety and an ANS and APS member. He is active in ANS standards committees.

## CHEMICAL PROCESSING

### THE CUSP PROCESS FOR PREPARING CONCENTRATED, CRYSTALLINE URANIA SOLS BY SOLVENT EXTRACTION

*J. P. McBride,*
*K. H. McCorkle, Jr.*
*W. L. Pattison*
*B. C. Finney*

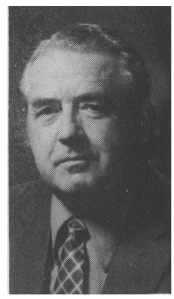

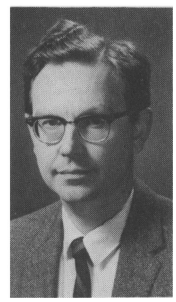

John Patrick McBride (left) (MS, physical chemistry, University of Notre Dame, 1941) joined the Metallurgical Laboratory (later, the Manhattan Project) at the University of Chicago in 1942 and became associated with Oak Ridge National Laboratory in 1944. He was a group leader in the thorium oxide slurry development program for the homogeneous reactor and was recently a group leader for sol-gel process development studies in the Chemical Technology Division. Kenneth Hall McCorkle, Jr. (PhD, chemical engineering, University of Tennessee) is engaged in nuclear fuels fabrication development for the General Atomic Division of Gulf Energy and Environmental

Systems. He was associated with the Chemical Technology Division of Oak Ridge National Laboratory from 1952 to 1971. For the past 12 years he has been engaged in research and development for oxide nuclear fuel properties and fabrication processes. William Lawrence Pattison (left) has been associated with the Chemical Development Section of the Chemical Technology Division at Oak Ridge National Laboratory since September of 1952. He has spent the past 19 years in various efforts involving the development of chemical processes for manufacture of nuclear fuel materials. He worked with the fluid fuel systems of the homogeneous reactor program at ORNL, and has been associated with the colloidal chemical systems research efforts of the laboratory in the sol-gel fuel technology program for the past 9 years. Bruce Carter Finney (BChE, University of Detroit, 1951) joined Battelle Memorial Institute, Columbus, Ohio in 1951. He became associated with Oak Ridge National Laboratory in 1957 and is presently a senior development engineer in the Chemical Technology Division.

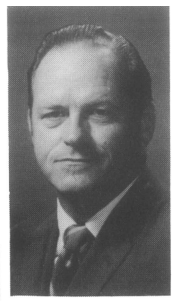

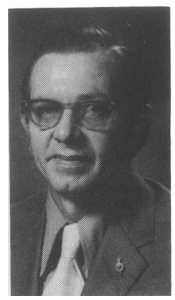

**RADIOLYSIS OF HANFORD B PLANT HDEHP EXTRACTANT**

*Wallace W. Schulz*

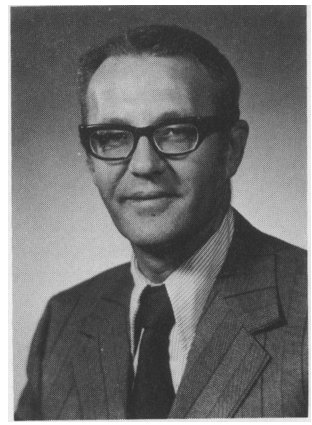

Wallace W. Schulz (BS, chemistry, University of Nevada) has over 20 years experience at Hanford in all phases of fuels reprocessing and waste management research and development activities. Now with Atlantic Richfield Hanford Company, he is currently exploring applications of macroreticular ion exchange resins to cleanup of Purex process solvent.

## FUELS

**STUDIES OF FUEL-CLAD MECHANICAL INTERACTION AND THE RESULTING INTERACTION FAILURE MECHANISM**

*E. Rolstad*
*K. D. Knudsen*

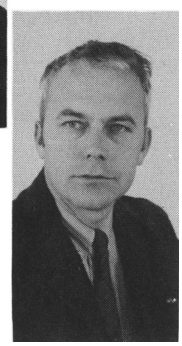

Erik Rolstad (left) (BSc, mechanical engineering, London, 1958) is in charge of the Test Fuel Data Evaluation at the OECD Halden Reactor Project. He joined the project in 1962 and was initially concerned with the thermohydraulic behavior and heat transfer limitations of the fuel assemblies in the reactor. His more recent interest is the thermal and dimensional behavior of fuel rods. In support of his work he has developed a number of computer codes which are being used in the fuel technical and thermohydraulic prediction and evaluation of the test fuel experiments at Halden. Kjell D. Knudsen (BSc, mechanical engineering, University of Manchester, United Kingdom, 1956) is head of Fuel Research Division at the OECD Halden Reactor Project, Halden, Norway. He has been with the Halden Project since 1959, serving initially as a member of the reactor operation staff in installation, maintenance, and operation. Since 1964 he has been working in the Fuel Research Division on fuel design, testing, and experiments.

### INSTRUMENTED CAPSULE FOR MEASURING FISSION-INDUCED CREEP OF OXIDE FUELS

*A. A. Solomon*
*R. H. Gebner*

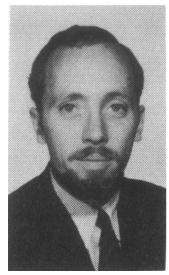

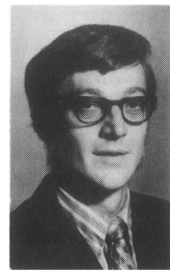

A. A. Solomon (left) (PhD, materials science, Stanford University, 1968) is employed at Argonne National Laboratory. His post-doctoral research was at Centre d'Etudes Nucléaires de Saclay, Saclay, France, 1969. Current interests include flow and fracture studies of reactor fuel and structural materials. R. H. Gebner has been associated with Argonne National Laboratory since 1964. Currently he is a member of the staff of the Reactor Analysis and Safety Division where he is involved in fuel coolant interaction studies.

## MATERIALS

### ELEVATED-TEMPERATURE DAMAGE FUNCTIONS FOR NEUTRON EMBRITTLEMENT IN PRESSURE VESSEL STEELS

*C. Z. Serpan, Jr.*
*W. N. McElroy*

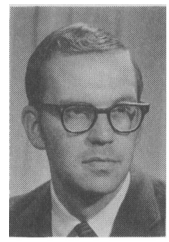

C. Z. Serpan, Jr. (left) (BS, Ohio University, 1956) is engaged in neutron dosimetry and spectrum aspects of irradiation effects studies of reactor structural materials at the Naval Research Laboratory. W. N. McElroy (PhD, Illinois Institute of Technology, 1965), at Hanford since 1967, is engaged in neutron dosimetry and fuels and materials irradiation effects studies for the LMFBR program.

## RADIOISOTOPES

### A RADIOISOTOPE-FUELED STIRLING ENGINE ARTIFICIAL HEART SYSTEM

*W. R. Martini*
*P. Riggle*
*L. T. Harmison*

L. T. Harmison (top) (PhD, nuclear engineering, University of Maryland) is the acting chief of the Medical Devices Applications Program of the National Heart and Lung Institute. He is responsible for design, development, and testing of medical devices for the diagnosis, monitoring, and treatment of cardiac and pulmonary diseases. William R. Martini (center) (PhD, chemical engineering, University of Michigan) is branch chief for Dynamic Conversion at the Donald W. Douglas Laboratories, Richland, Washington, a part of McDonnell Douglas Corporation. He has been involved in development of various energy conversion devices for 15 years and has led the development of the heart engine for 4 years. Peter Riggle (bottom) (BS, mechanical engineering, University of Washington) is project engineer in charge of analysis and testing in the Dynamic Conversion Branch. He has been involved in dynamic and thermodynamic design analysis and testing of Stirling engine artificial heart energy systems for the past 3 years. He was previously engaged in nuclear reactor heat transfer and fluid flow analysis and testing.

## SHIELDING

### BRACKETING THE PEAK PRIMARY GAMMA-RAY DOSE RATE FROM NUCLEAR DEVICES BY STEADY-STATE TRANSPORT CALCULATIONS

*H. C. Claiborne*
*W. W. Engle, Jr.*

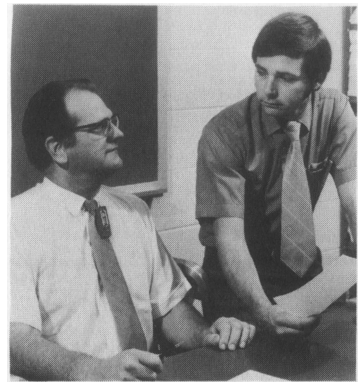

H. C. Claiborne (left) (MS, University of Tennessee) has been involved in various phases of reactor design and analysis at the Oak Ridge National Laboratory since 1953 with the past five years primarily devoted to shield design against radiation from reactors and nuclear weapons. Currently, his primary interest is in the area of radioactive waste management. W. W. Engle, Jr. (BS, University of Tennessee) is a staff member of the Neutron Physics Division of Oak Ridge National Laboratory. His present interests include the application of the discrete ordinates method to problems in the reactor and weapons radiation shielding program.

## ANALYSIS

### HEAVY ELEMENT ANALYSIS BY ISOTOPE-EXCITED X-RAY FLUORESCENCE

*J. Kuusi*
*M. Virtanen*
*P. Jauho*

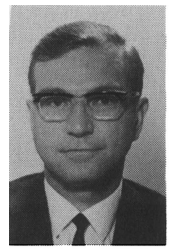

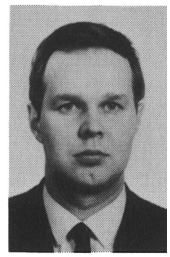

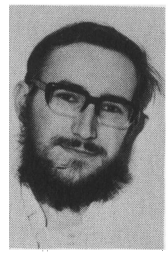

P. Jauho (top) (PhD, nuclear physics, Helsinki University, 1951) has been Director General of The State Institute of Technical Research in Finland since 1970. His main interests are in statistical and nuclear physics. J. Kuusi (center) (Doctor of Technology, radioisotope applications, Helsinki University of Technology, 1970) has been head of the Applied Radiation and Isotopes Division of The Reactor Laboratory of The State Institute of Technical Research since 1970. His main interests are in application of radiation and radioisotopes in industry, and environmental studies. M. Virtanen (bottom) (MS, analytical applications of radioisotopes, Helsinki University of Technology, 1971) is a research worker in The Reactor Laboratory of The State Institute for Technical Research. His present main interest is in tracer studies of waste water currents in lakes and sea.

## MATERIALS

### IMPURITY EFFECTS ON THE SWELLING OF IRRADIATED ALUMINUM OXIDE

*R. A. Skarupa*
*C. E. Backus*

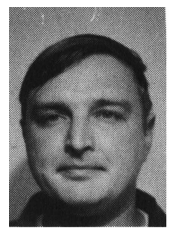

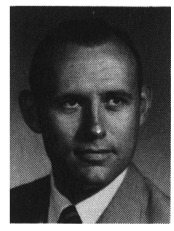

R. A. Skarupa (left) (BS, U.S. Military Academy, 1962; graduate studies in nuclear engineering at Arizona State University) is a major in the U.S. Army. He received his MS in 1971 and is presently serving in Vietnam. C. E. Backus (PhD, nuclear engineering, University of Arizona, 1965) is an associate professor of engineering at Arizona State University. During the last three years he has been a visiting staff member at the Los Alamos Scientific Laboratory working in the area of thermionic reactor development with particular emphasis on insulators in high flux fields. His interests include all direct energy converters and associated technology.

# LETTERS TO THE EDITOR

## COMMENTS ON THE REVIEW OF *NUCLEAR POWER AND THE PUBLIC*

Dear Sir:

In the review of the above-referenced book by Charles Kelber in the September 1971 issue of your magazine, I find his statement that I revealed "a common point of view that standards and regulations are imposed to establish the maximum that you can get away with" was wrong and very unfair.

Had Mr. Kelber not taken a single response directed at another point entirely out of context but rather reviewed my paper in detail, he would have read various statements such as:

> "Thus, although the government regulation for radiation doses contributed by a nuclear plant to any neighbor is 500 mrem/year, designers would attempt to keep the plant discharges below 5 mrem/yr to any neighbor averaged over plant life in order to make the contribution of the nuclear power plant insignificant (approximately 1 percent of allowable) with respect to the exposure the public normally receives." (p. 19)
>
> "Under normal operation there are traces of radioactive releases, but they are always well within release rates established by the AEC. In fact, they are kept at insignificant levels." (p. 18)
>
> "The design of nuclear power stations ensures that the total waste release—whether gaseous or liquid—is always well within the specified regulations of the AEC. In fact, as one would certainly expect, every feasible effort is made to minimize wastes which might include radioactive materials, in order to make radioactive waste discharge as small as practically feasible. Thus, the radioactive wastes of the nuclear power station are insignificant with respect to other radioactive considerations had the plant not been there at all." (pp. 9-10)
>
> "Every effort has been made to keep this release insignificant relative to natural background." (p. 8)
>
> "The systems provided for waste disposal are based on extremely conservative design criteria, and all existing regulations with respect to release are complied with by large margins." (p. 25)

How Mr. Kelber is able to make the statement he did about my attitude based on a review of the book *Nuclear Power and the Public*, containing the above quotes, is very difficult to understand. I did make the statement, "My primary responsibility as a designer is to check my design against appropriate regulations." I wouldn't retract that statement. How else would I be able to state that "all existing regulations with respect to release are complied with by large margins"?

Mr. Kelber's interpretation of my statement is unfortunate. In fact, with this review given the distribution it enjoyed by placement in your magazine, many members of the nuclear community who have always been committed to doing the job right were very disappointed.

If Mr. Kelber is simply inferring that sometimes our good intentions are misinterpreted due to our imperfect selection of words, I stand advised and will try harder in the future to make sure the proper attitudes of the nuclear industry are clear.

*A. P. Bray*

General Electric Company
175 Curtner Avenue
San Jose, California 95125

October 20, 1971

## REPLY TO COMMENTS ON THE REVIEW OF *NUCLEAR POWER AND THE PUBLIC*

Dear Sir:

Mr. Bray is understandably upset that I did not give greater emphasis to his speech, an eloquent exposition and defense of current practices in the nuclear power industry, than I did to his answer to a question about people's attitudes. But there are two considerations: Mr. Bray's well-deserved reputation and high standing in the nuclear community hardly need my endorsement in a journal addressed to that community; we know that he and his cohorts throughout the industry do a good job. Second, the central issue with respect to the public's view of our industry is often our attitude as much as it is our practice.

When Mr. Bray's questioner was taking him to task for not knowing some special data (p. 115 of *Nuclear Power and the Public*), his stated reason was: ". . .to see how the participants approach the problems that they work with as men." Mr. Bray's reply: ". . .My

primary responsibility as a designer is to check my design against appropriate regulations." is capable of two interpretations. A member of the nuclear industry would probably subconsciously add the phrase: "to verify that my designs are appropriately conservative." But it is not at all clear that a member of the general public, especially one prepared to be biased against industrial practice, would place this interpretation on the remark. He may feel that the appropriate regulations were not well taken to protect his environment. Evidently, Mr. Bray's earlier formal remarks were not enough to reassure at least one member of the public.

Mr. Bray has hit the mark in his last paragraph. However good our intentions, the public will not appreciate them until we make crystal clear in accurate terms our commitment to improving the world we all live in. We need to keep in mind that the public is rightly cynical about the beneficial effects of adherence to previously established codes and standards. They need to know that we recognize and deal with real problems that exist in the environment, problems that were very likely not even recognized when the codes and standards were established. For example, radiation exposure standards were first established to protect workers and extended from them to the general public. In retrospect, the reverse order would appear the wiser course.

Finally, I would point out that I consider the attitude toward "cost benefit" analysis a more crucial issue than the attitude toward standards. Standards are at least explicit; but if we persist in what I have termed the "every cloud has a leaden lining" approach to cost benefits, we run the very real danger of pricing ourselves out of the market. We must convince the public that not only do benefits far outweigh costs, but the costs themselves are reasonable. If this requires some revision in design, let us face the issue honestly.

*Charles N. Kelber*

Argonne National Laboratory
Argonne, Illinois 60439

November 11, 1971

# THE BREEDING RATIO WITH CORRELATION TO DOUBLING TIME AND FUEL CYCLE REACTIVITY VARIATION

REACTORS

**KEYWORDS:** *breeder reactors fast reactors, fuel cycle, reactivity, breeding ratio, variations, optimization*

C. R. ADKINS *Nuclear Science and Engineering Division*
*Carnegie-Mellon University, Pittsburgh, Pennsylvania 15213*

Received June 9, 1971
Revised September 21, 1971

*The standard definition of the breeding ratio is subject to some suspicion, since in many cases of practical interest it gives an incorrect measure of the fissile fuel doubling time and erroneous trends of the fuel cycle reactivity variation. The reasons for this behavior are given in this study, along with methods for removing the difficulties. In addition to the standard definition, the method of $\eta$ weighting due to Ott and the method of reactivity weighting due to Baker and Ross (British definition) are examined. It is shown that the $\eta$ weighting procedure is not much better than the standard definition, whereas the British definition can be used to give very good results for the doubling time and fuel cycle reactivity variation. The standard for comparison is a detailed explicit fuel cycle analysis of both the startup cycle and equilibrium cycle of an oxide fast reactor. With the methods given it is shown that the important quantities needed from a single fuel cycle analysis can be obtained just from a statics calculation, for the known composition at the beginning of the fuel cycle of interest (e.g., first fuel cycle). This result has significant importance for conceptual design studies and for optimization studies where many reactor calculations must be performed, precluding the use of an explicit fuel cycle depletion analysis. However, it is also shown that the equilibrium fuel cycle performance cannot be adequately predicted solely from start-of-life statics analysis. An approximate procedure is formulated to predict the equilibrium reactor composition, from which the equilibrium breeding gain, doubling time, and reactivity variation may be determined. The impetus for this approach is the need for an extremely rapid computational technique in optimization studies based on the equilibrium fuel cycle performance.*

## INTRODUCTION

There are currently a number of different ways of defining the breeding ratio or breeding gain of a fast reactor. Since the quantity lacks a standard definition it becomes exceedingly difficult to draw any conclusions regarding the nuclear performance or characteristics of a given system just from the quoted breeding ratio. The same reactor may be calculated by two different design groups with a significant difference occurring in the breeding performance due to different definitions.

A more important difficulty regarding definition may arise from the physical interpretation or meaningfulness of the quantity. If the breeding gain is not properly defined, there may exist no meaningful correlation between breeding gain and the reactor doubling time or fuel cycle reactivity variation. Thus, the breeding gain lacks significance as a predictor of actual reactor performance and characteristics and tends to be regarded only as a relative figure of merit which should not be taken too seriously. This is extremely unfortunate since the breeding ratio is a very familiar term among fast reactor designers and each would like to be able to better understand his reactor or be able to compare with other reactors using the breeding ratio.

There are three examples which serve to illustrate the observed discrepancies based on actual analysis using the standard definition of the breeding gain:

1. The fissile mass doubling time calculated from the breeding gain is significantly lower than that calculated using actual mass yields from fuel cycle depletion analysis.

2. From perturbation theory, it is expected that the reactivity variation over a fuel cycle is approximately proportional to the core conversion gain (cycle-time-averaged value). For a fast reactor fueled with commercial grade (PWR) plutonium, it is found from depletion analysis that the magnitude of the reactivity variation, over one fuel cycle, decreases from the startup cycle to the equilibrium cycle while the magnitude of the core conversion gain increases. This is completely the opposite from the expected trend.

3. A given reactor is analyzed for the startup fuel cycle using two different initial fuel compositions. One composition is commercial grade plutonium while the second is weapons grade plutonium. The enrichments are chosen to give the same initial mulitplication with all control removed and the same enrichment ratio for the two core zones. The magnitude of the reactivity variation, over the startup cycle, is found by depletion analysis to remain nearly the same (just slightly smaller for the weapons plutonium), but the magnitude of the core conversion gain for the weapons grade plutonium is significantly larger than that of the same reactor fueled with commercial grade plutonium.

These anomalies cause the designer to lose faith in the breeding gain as a meaningful quantity. However, instead of scrapping the quantity, it would be far better to give it a consistent, meaningful definition which may, hopefully, become a standard. This quantity should be useful for predicting the reactor doubling time at any time during the reactor life just from statics analysis (without depletion analysis), and it should predict the fuel cycle reactivity variation without explicit depletion analysis over any fuel cycle of interest. If such can be accomplished, it may not be necessary to include a detailed fuel cycle depletion analysis in conceptual design studies and reactor optimization studies, which seriously hamper an already complicated analysis where many different reactor designs must be studied. This is of particular importance in optimization studies where many reactor calculations are necessary in order to search for the path which minimizes the objective function.

There is yet another consideration which makes difficult the determination of the equilibrium breeding ratio and doubling time solely from statics analysis. A fast reactor initially fueled with commercial grade plutonium is far away from the equilibrium plutonium composition for the system. An isotopic redistribution of the plutonium occurs with the most important effect being that the valuable $^{241}Pu$ diminishes with time. This effect coupled with the buildup of fission products dictates that the plutonium enrichment must increase with time. Thus, from the startup fuel cycle to the equilibrium fuel cycle the reactor breeding gain must decrease and the doubling time increase. This effect can be included in a statics analysis only if there exists a simple but accurate way of including the fuel depletion effects (plutonium isotopic redistribution), the accumulation of fission products, and the enrichment increase in the equilibrium cycle breeding gain analysis.

It is shown that the above objectives can be met, but not merely in terms of a single start-of-life statics analysis, which magically predicts the proper reactor performance at all times during life. Using the proper definition of the breeding gain, and the reactor composition representative of a particular time in life, the correct doubling time and fuel cycle reactivity variation for that point in time can be obtained just from a statics analysis. Thus, it is easy to predict the reactor performance for the first fuel cycle, where the beginning-of-life composition is known (composition at the start of the first cycle). However, the prediction of the equilibrium cycle performance is much more difficult, requiring the specification of the equilibrium composition of the reactor which, in turn, depends on the depletion effects and the fuel management scheme chosen. In this case, one must use either a detailed depletion analysis or a less detailed approximate scheme to establish the equilibrium composition, which may then be used in a statics analysis to determine the equilibrium fuel cycle performance. It is clear that any static diffusion theory analysis of the reactor performance at any point-in-time is dependent on the knowledge of the composition at that point-in-time. Thus, the breeding gain calculation employed in this statics analysis should be the one that best describes the actual depletion analysis results about the given point-in-time, for the same reactor composition at that point-in-time. In this sense, the results of the actual depletion analysis are obtained from a statics analysis using the proper definition of breeding gain.

The question still remains, however, of how to obtain the composition at any point in time during reactor life, other than the first fuel cycle. In this study an approximate method of determining the composition is developed, with a view toward a rapid computational technique for use in optimization studies based on equilibrium cycle performance. Such studies cannot incorporate a detailed explicit depletion analysis because of the

computational difficulties encountered. However, in the numerical studies for verifying the breeding gain definition in a statics analysis, the start of equilibrium cycle composition from the explicit depletion analysis is used in a statics calculation. This is done to eliminate composition differences between the statics analysis and the explicit depletion analysis of the equilibrium fuel cycle performance, which may obscure the true differences between the two methods.

## CONCEPTUAL DEFINITIONS

The following definitions are used for the breeding gain and doubling time[1-3]:

*Standard:* breeding gain (BG)

$$= \frac{\text{surplus production rate of fuel}}{\text{destruction rate of fuel}} ,$$

where surplus production rate is production rate less destruction rate. The breeding ratio (BR) is given as BR = 1 + BG.

*British* (Baker and Ross, in Ref. 3).

The breeding gain is normalized to the total fission rate or power production,

$$\text{BG} = \frac{\text{surplus production rate of fuel}}{\text{total fission rate in reactor}} .$$

The breeding ratio may be defined in the conventional manner as

$$\text{BR} = \frac{\text{surplus production rate of fuel}}{\text{destruction rate of fuel}} ,$$

but without the simple relationship between breeding gain and breeding ratio.

Either definition of the breeding gain may take the interpretation of a point-in-time quantity by using the production, destruction, and fission rates at any given point in time. Also, either may take the interpretation of a time-averaged quantity by using the time integrated production, destruction, and fission rates over some period of time (e.g., over one fuel cycle). Doubling time ($T$) is the time necessary to double the initial fissile fuel mass of the reactor. Thus, it is a measure of the time necessary to accumulate enough fuel to start up a second similar reactor.

In general, the doubling time depends on all the nonuniform effects of the cycle-by-cycle depletion analyses (plutonium composition changes, control rod movements, refueling scheme, power redistribution, and changes in local spectra associated with these), and on the conditions for reusing the bred fuel. Two interpretations of the doubling time are usually considered:

1. The simple doubling time ($T_s$), which is a measure of fissile fuel doubling without reuse of the bred fuel. This would occur if the reactor is continuously refueled with fresh fuel composition:

$$\frac{1}{T_s} = \frac{1}{M_{f_i}} \overline{\frac{dM_f}{dt}}^{t} , \qquad (1)$$

where

$T_s$ = simple doubling time

$M_{f_i}$ = initial (beginning-of-cycle) fuel mass

$\overline{(dM_f/dt)}^{t}$ = cycle-time-averaged rate of surplus fuel mass production.

2. The compound doubling time ($T_c$) is a measure of the fissile fuel doubling with instantaneous reuse of the bred fuel. Under these conditions one expects an exponential increase in fuel mass, $M_{f_t} = M_{f_i} \exp(\ln 2 \cdot t/T_c)$, where for $t = T_c$ the fuel mass is doubled. This may be written in terms of the logarithmic derivative as

$$\frac{\ln 2}{T_c} = \frac{1}{M_f} \frac{dM_f}{dt} . \qquad (2)$$

If it is assumed that the fissile fuel mass at any point in time is not significantly different from the initial fissile fuel mass ($M_f \simeq M_{f_i}$ at all $t$), then $T_c = (\ln 2)\, T_s$. The compound doubling time would be observed if the reactor could be operated for long periods of time without refueling (e.g., if the core conversion ratio were near unity for a small reactivity loss with time, and if the mechanical properties of the fuel or structure were not limiting).

In practice, for realistic fast reactor systems with 6- or 12-month refueling intervals, it is expected that the actual doubling time will more closely approximate the compound doubling time, although it should always lie between the two definitions. With a scatter refueling scheme (multibatch fuel management) only about 20 to 30% of the core is refueled each cycle, in equilibrium, and half of this amount for the radial blanket. Thus, a considerable amount of the bred fuel is effectively reused in succeeding fuel cycles.

## SIMPLIFIED ANALYSIS OF BREEDING AND DOUBLING

It is beneficial to review the simple methods of calculating breeding ratio and doubling time to determine the most important parameters which influence these quantities. As shown by Okrent,[1] the conventional point-in-time breeding ratio may be written, in terms of neutron balance, as

$$\text{BR} = \frac{(\nu - 1) - \alpha - P - L + (\nu' - 1)\delta}{1 + \alpha} \qquad (3a)$$

or

$$BR = \eta - 1 - \frac{P + L - (\eta' - 1 + \alpha'\eta')\delta}{1 + \alpha} \quad , \qquad (3b)$$

where

$\alpha$ = capture to fission rate ratio for the fissile material

$P$ = parasitic capture to fissile fission rate ratio

$L$ = leakage to fissile fission rate ratio

$\delta$ = fertile to fissile fission rate ratio

$\nu$ = average number of neutrons per fissile fission

$\nu'$ = average number of neutrons per fertile fission

$\eta$ = neutron production to absorption rate ratio for fissile material

$\eta'$ = neutron production to absorption rate ratio for fertile material.

The numerator of Eq. (3a) multiplied by the fissile fission rate is the production rate of fissile fuel obtained by way of neutron balance; the neutrons produced from all fissions, less those necessary to maintain criticality and those which are lost in a nonproduction manner (do not produce fissile fuel), must necessarily produce fissile fuel. The denominator multiplied by the fissile fission rate is the destruction rate of fissile fuel. From Eq. (3b), assuming the last term to be small, the breeding gain varies roughly as $BG \approx \eta - 2$.

The simple doubling time may be computed, following Golden,[2] as

$$\frac{1}{T_s\ (\text{year})} = \frac{\text{kg fissile material accumulated/year}}{\text{initial fissile loading (kg)}, M}$$

$$= \frac{1}{M\ (\text{kg})} \left[ BG \frac{\text{fissile atoms produced}}{\text{fissile atoms destroyed}} \right.$$

$$\cdot P[\text{MW(th)}] \cdot 10^6 \frac{\text{W}}{\text{MW}} \cdot 2.903$$

$$\times 10^{10} \frac{\text{fissions}}{\text{W} \cdot \text{sec}} \cdot 3.1536 \times 10^7 \frac{\text{sec}}{\text{year}}$$

$$\cdot C \frac{\text{full power days}}{\text{day}}$$

$$\cdot \frac{1}{1 + \delta} \frac{\text{fissile fissions}}{\text{fission}}$$

$$\cdot (1 + \alpha) \frac{\text{fissile absorptions}}{\text{fissile fission}}$$

$$\left. \cdot \frac{W_{\text{fiss}} \times 10^{-3}}{6.023 \times 10^{23}} \frac{\text{kg}}{\text{atom}} \right]$$

$$T_s\ (\text{year}) = \frac{2.75\, M(\text{kg})\ (1 + \delta)}{BG(1 + \alpha) C\ P[\text{MW(th)}]} \quad , \qquad (4)$$

where the $2.903 \times 10^{10}$ fissions/(W sec) is based on 215 MeV/fission (used in many fast reactor computer codes, see Ref. 6), and

$C$ = capacity factor-fraction of calendar time that the reactor is at full power

$P$ = nominal reactor power in thermal megawatts

$M$ = initial fissile loading in kg

$W_{\text{fiss}}$ = mass number of fissile material (taken to be 239).

All other quantities have been defined previously.

The main quantities of interest affecting the doubling time are the breeding gain and the specific power (power per unit mass of initial fissile loading). An increase in either quantity will decrease the simple doubling time.

Of particular interest in this discussion is the conclusion that the breeding gain varies roughly as $\eta - 2$. Ott[4] proposed that isotopic $\eta$ weighting be used in breeding gain calculations. He showed that such a weighting procedure makes the breeding gain nearly insensitive to plutonium composition changes. This procedure is examined in detail in the later sections.

## ISOTOPIC REACTIVITY WORTHS AND CORRELATION OF REACTIVITY VARIATION TO BREEDING GAIN

Employing one-group perturbation theory neglecting leakage, it is found that

$$\rho = \frac{\delta k}{k} = \frac{f + a}{i}$$

where

$$i = \frac{1}{k} \int dV\ \phi \nu \Sigma_f \phi \quad ,$$

$$f = \frac{1}{k} \int dV\ \phi \delta (\nu \Sigma_f) \phi \quad ,$$

and

$$a = - \int dV\ \phi \delta (\Sigma_a) \phi \quad .$$

Consider any particular nuclide $i$ in any particular reactor zone $n$ where the cross sections are constant over any particular zone. Also, consider small perturbations about criticality:

$$\rho = \frac{\sum_n \sum_i \delta N_i^n (\nu \sigma_f - \sigma_a)_i^n\ \phi_n^2 V_n}{\sum_n \sum_i \nu_i^n F_i^n\ \phi_n} \qquad (5)$$

with $F_i^n = \Sigma_{f\,i}^n \phi_n V_n$, and where it has been assumed that the perturbations are due to changes in fuel composition and not to changes in the one-group microscopic cross sections. In the perturbation denominator it is assumed that $\nu_i^n$ is a constant, equal to $\nu$ of $^{239}$Pu ($\nu_9$). The denominator can be rewritten as

denominator = $\nu_9 \omega F$, with $F = \sum_n \sum_i F_i^n$ (the total fission rate) and $\omega = \sum_n \sum_i F_i^n \phi_n / F^4$ (a fission averaged importance function or weighting function).

In one-group, the adjoint flux is the direct flux, is the flux, and $\omega$ measured the averaged flux weighting.

It can be shown that the atom density after a burnup period is given by

$$N_i^n/N_{HM}^n = \varepsilon_i^n + 0.9956 \times 10^{-6} B^n \frac{W_{HM}^n}{W_{\text{fiss}}^n} \frac{C_{i-1}^n - A_i^n}{F^n} \tag{6a}$$

$$N_{FP}^n/N_{HM}^n = \varepsilon_{FP}^n + 0.9956 \times 10^{-6} B^n \frac{W_{HM}^n}{W_{\text{fiss}}^n} \left(1 - \frac{A_{FP}^n}{F^n}\right) \tag{6b}$$

where a lumped fission product model is assumed. The $C_{i-1}^n$ is the capture rate in nuclide $i$ - 1 in region $n$ and represents the production rate of nuclide $i$; $A_i^n$ is the absorption rate of nuclide $i$ in region $n$; $F^n$ is the fission rate in region $n$; and $B^n$ is the burnup (MWd/MT) in region $n$ for some given time interval. An energy release of 215 MeV/fission has been used. $W_{HM}^n$ and $W_{\text{fiss}}^n$ are the mass numbers of the heavy metal and fissile material in region $n$, where $W_{\text{mixture}} = \sum_i^{\text{mix}} a_i W_i$, $a_i$ = atom fraction of nuclide $i$ in the mixture and $W_i$ = the mass number of nuclide $i$. $N_{HM}^n$ is the initial atom density [atoms/(b cm)] of heavy metal (U + Pu) in region $n$; $N_i^n$ is the atom density [atoms/(b cm)] of nuclide $i$ in region $n$ after a burnup interval of $B^n$ (MWd/MT); and $N_{FP}^n$ is the atom density of fission product pairs in region $n$ after a burnup interval of $B^n$ (MWd/MT).

$\varepsilon_i^n$ = initial atom fraction of nuclide $i$ in heavy metal in region $n$

$$\varepsilon_i^n = \begin{cases} e^n (W_{HM}/W_{\text{Pu}}) a_i^n & \text{, Pu isotopes} \\ (1 - e^n)(W_{HM}/W_{\text{U}}) a_i^n & \text{, U isotopes} \end{cases},$$

where $e^n$ is the initial plutonium weight fraction enrichment [Pu/(U + Pu)] in region $n$, $a_i^n$ is the atomic abundance of isotope $i$ in region $n$. $W_{\text{Pu}}$ and $W_{\text{U}}$ are the mass numbers of the plutonium in the fuel and uranium in the fuel, respectively.

$\varepsilon_{FP}^n$ = initial atom fraction of fission product paris in heavy metal in region $n$

$\varepsilon_{FP}^n = e_{FP}^n (W_{HM}/W_{FP})$, where $W_{FP}$ is the mass number of fission product pairs ($W_{FP} \simeq 236$)

$e_{FP}^n$ = initial fission product weight fraction in heavy metal [$FP$/(U + Pu)] in region $n$.

If the heavy metal is defined to include the fission product pairs, then the heavy metal is nearly constant independent of time (burnup).

Using the simplified depletion analysis, $\delta N_i$ is given as

$$\delta N_i^n = 0.9956 \times 10^{-6} B^n \frac{W_{HM}^n}{W_{\text{fiss}}^n} \frac{C_{i-1}^n - A_i^n}{F^n} N_{HM}^n ,$$

for fuel isotopes

$$\delta N_{FP}^n = 0.9956 \times 10^{-6} B^n \frac{W_{HM}^n}{W_{\text{fiss}}^n} \left(1 - \frac{A_{FP}^n}{F^n}\right) N_{HM}^n ,$$

for fission products .

The reactivity variation becomes

$$\rho = \frac{0.9956 \times 10^{-6}}{\nu_9 \omega F} \sum_n \phi_n^2 V_n \frac{W_{HM}^n}{W_{\text{fiss}}^n} \times \left[ \sum_i (\nu\sigma_f - \sigma_a)_i^n (C_{i-1}^n - A_i^n) \frac{B^n N_{HM}^n}{F^n} - \sigma_{a_{FP}}^n \left(1 - \frac{A_{FP}^n}{F^n}\right) B^n N_{HM}^n \right] . \tag{7}$$

The following simplifications are made:

1. $0.9956 \times 10^{-6} \frac{B^n N_{HM}^n V_n}{F^n} \frac{W_{HM}^n}{W_{\text{fiss}}^n} \equiv \Delta t\,(\text{sec})\, 10^{-24}$ where $\Delta t$ is the time in full power seconds corresponding to some given burnup interval or to a fuel cycle.
2. $\phi_n^2$ is large and nearly spatially flat in the core and small in the blankets.

Then,

$$\rho = K \sum_n^{\text{core}} \left[ \sum_i (\nu\sigma_f - \sigma_a)_i^n \frac{C_{i-1}^n - A_i^n}{F} - \sigma_{a_{FP}}^n \left(1 - \frac{A_{FP}^n}{F^n}\right) \frac{F^n}{F} \right] \tag{8}$$

and

$$K = \frac{\phi_{\text{core}}^2 \Delta t(\text{sec}) \times 10^{-24}}{\nu_9 \omega} ,$$

where $\phi_{core}\,\Delta t(\text{sec})$ is the neutron fluence for the given time interval.

Neglecting the fission products for the moment, two very important conclusions are obtained:

1. The term $(C^n_{i-1} - A^n_i)$ is the isotopic surplus production rate. It should be weighted by the quantity $(\nu\sigma_f - \sigma_a)^n_i$ to predict the correct isotopic reactivity variation. Thus, the proper reactivity weights are given in terms of this quantity.

2. The reactivity variation is given in terms of the isotopic surplus production rate in the core to the total reactor fission rate weighted by the isotopic reactivity worth. This is equivalent to the fractional breeding gain of the core in the British definition as will be shown later.

From the form of the equation for the reactivity variation, it appears that the effects of fission products can be included by rewriting the equation, neglecting the term $A^n_{FP}/F^n$ (nonsaturating fission product pairs) and noting that $\sum_i (C^n_{i-1} - A^n_i) \simeq -F^n$:

$$\rho = K \sum_n^{\text{core}} \left\{ \sum_i \left[ (\nu\sigma_f - \sigma_a)^n_i + \sigma^n_{a_{FP}} \right] \frac{C^n_{i-1} - A^n_i}{F} \right\} \qquad (9)$$

Now the isotopic breeding gain in each core region is weighted by the isotopic reactivity worth adjusted to include the production of fission product pairs. For core regions which are depleted in place without refueling, this may be a reasonable approach.

It is imperative to point out an alternate interpretation of Eqs. (8) or (9). If the reactivity variation of two different fuel cycles are being compared using, for example, the actual compositions and cross sections at the beginning of each cycle in two separate calculations, then the $\Delta t(\text{sec})$ which appears in the factor $K$ is the time interval in full power seconds for each fuel cycle. If the cycle time is the same for each cycle, then $K$ varies only as $\phi^2_{core}/\omega$ between the two cycles, and differences in the cycle reactivity variation are given approximately in terms of differences in breeding performance and fission product poisoning.

### General Definitions

The simplified definitions of breeding gain and doubling time are very useful for understanding the important interrelationships between variables and the influence of the various reactor parameters, but the simplified definitions are not useful for actual design purposes. The effects in multizoned reactors of local isotopic redistribution in plutonium, fission product accumulation, control rod movements, power spatial redistribution, and the local changes in spectra are important but outside the capabilities of the simple models (which tend to deal just with lumped fissile and fertile material). The simpler models must be replaced with calculational methods which account explicitly for the various fuel nuclides and the various zones in the reactor.

A number of methods have been proposed in the literature[4,5] for calculating the reactor breeding gain. These generally involve some form of isotopic and zone-dependent weighting of the surplus production and destruction rates.

$$\text{Standard: } BG_{stan} = \frac{\sum_n \sum_i \gamma^n_i (C^n_{i-1} - A^n_i)}{\sum_n \sum_i \gamma^n_i A^n_i} \qquad (10a)$$

$$BR_{stan} = 1 + BG_{stan} \qquad (10b)$$

$$\text{British: } BG_{Brit} = \frac{\sum_n \sum_i \gamma^n_i (C^n_{i-1} - A^n_i)}{\sum_n \sum_i F^n_i} \quad . \qquad (10c)$$

The breeding ratio may be defined to conform with the conventional definition as:

$$BR_{Brit} = \frac{\sum_n \sum_i \gamma^n_i C^n_{i-1}}{\sum_n \sum_i \gamma^n_i A^n_i} \quad . \qquad (10d)$$

It has been shown that only the breeding gain is the quantity of physical interest, affecting the doubling time and fuel cycle reactivity variation. Thus, the breeding ratio is of little physical interest, although the standard definition should be maintained. The quantities $C$, $A$, and $F$ describe the capture, absorption, and fission rates, respectively. The index $i$ denotes the nuclide type (isotope) and $n$ denotes the reactor region: $i$ = 5, 6, 8, 9, 0, 1, 2 denotes $^{235}$U, $^{236}$U, $^{238}$U, $^{239}$Pu, $^{240}$Pu, $^{241}$Pu, $^{242}$Pu as defined by Goldschmidt.[5] The $\gamma^n_i$ are weights, by nuclide and zone, which should be chosen to give the proper interpretation of the breeding gain and doubling time.

The compound doubling time Eq. (2) is written as

$$\frac{\ln 2}{T_c} = \frac{1}{N_f} \frac{dN_f}{dt} \qquad (11)$$

where $N_f$ is the total number of fuel atoms in the reactor. It has been assumed that the atomic mass number of fuel does not vary with time. In a quasi-equilibrium sense, the surplus production rate of fuel atoms is given as

$$\frac{dN_f}{dt} = \sum_n \sum_i \gamma^n_i (C^n_{i-1} - A^n_i)$$

and the total number of fuel atoms is given as

$$N_f = \sum_n \sum_i \gamma_i^n N_i^n V_n \quad ,$$

where

$N_i^n$ = atom density of nuclide $i$ in region $n$

$V_n$ = volume of region $n$.

The total fuel atoms must be weighted in the same way as the surplus production of fuel atoms to have a correct meaning of the fuel doubling time.

Ott[4] pointed out that, in equilibrium, the accumulated fuel ($N_f$) is the direct result of the surplus fuel production rate ($dN_f/dt$) and the two quantities have the same isotopic composition. Thus, in this case, the two quantities are related by a constant, or the equilibrium doubling time is a constant independent of the weighting factors $\gamma_i^n$. However, this case is never one of practical interest since an equilibrium situation, in which succeeding fuel cycles exhibit identical performance, is never observed. In practice, the term "equilibrium" is used to represent the average over later fuel cycles, where each fuel cycle may fluctuate about this average. Of considerable interest in fast reactor analysis is the operation over the first few fuel cycles, where the plutonium isotopic composition changes appreciably. In this nonequilibrium situation, the choice of weighting factors is of considerable importance. It is assumed, of course, that this nonequilibrium process can be treated sufficiently accurately by a quasi-equilibrium (or quasi-static) analysis for each fuel cycle within a given time period.

The resulting expression for the compound doubling time may be rewritten in terms of the breeding gain:

$$\text{Standard: } \frac{\ln 2}{T_c} = \frac{\sum_n \sum_i \gamma_i^n A_i^n}{\sum_n \sum_i \gamma_i^n N_i^n V_n} (BG_{\text{stan}}) \qquad (12a)$$

$$\text{British: } \frac{\ln 2}{T_c} = \frac{\sum_n \sum_i F_i^n}{\sum_n \sum_i \gamma_i^n N_i^n V_n} (BG_{\text{Brit}}) \quad . \qquad (12b)$$

It is observed that the doubling time is independent of the denominator of the breeding gain. Insofar as the doubling time is concerned, the denominator used in the breeding gain definition is arbitrary.

The correlation of fuel cycle reactivity variation with the cycle-time-averaged breeding gain can be given using Eq. (9). In terms of any weights $\gamma_i^n$, this becomes

$$\rho = K \frac{\overline{\sum_n^{\text{core}} \sum_i \gamma_i^n (C_{i-1}^n - A_i^n)}^t}{\overline{\sum_n \sum_i F_i^n}^t} \quad , \qquad (13)$$

where $K$ is defined in Eq. (8), and the cycle-time-average of each quantity is indicated.

Let the internal conversion gain (ICG) and the fractional breeding gain (FBG) of the core be defined as follows for the two definitions:

$$\text{Standard: } \text{ICG}_{\text{stan}} = \frac{\sum_n^{\text{core}} \sum_i \gamma_i^n (C_{i-1}^n - A_i^n)}{\sum_n^{\text{core}} \sum_i \gamma_i^n A_i^n} \qquad (14a)$$

$$\text{FBG}_{\text{stan}}^{\text{core}} = \frac{\sum_n^{\text{core}} \sum_i \gamma_i^n (C_{i-1}^n - A_i^n)}{\sum_n \sum_i \gamma_i^n A_i^n} \qquad (14b)$$

$$\text{British: } \text{ICG}_{\text{Brit}} = \frac{\sum_n^{\text{core}} \sum_i \gamma_i^n (C_{i-1}^n - A_i^n)}{\sum_n^{\text{core}} \sum_i F_i^n} \qquad (14c)$$

$$\text{FBG}_{\text{Brit}}^{\text{core}} = \frac{\sum_n^{\text{core}} \sum_i \gamma_i^n (C_{i-1}^n - A_i^n)}{\sum_n \sum_i F_i^n} \quad . \qquad (14d)$$

Assuming that the cycle-time-averaged values may be replaced by the known values at the start of a fuel cycle, to avoid performing a depletion analysis, the fuel cycle reactivity variation is given as

$$\rho \approx (\text{ICG}_{\text{stan}}) \frac{\sum_n^{\text{core}} \sum_i \gamma_i^n A_i^n}{\sum_n \sum_i F_i^n} \qquad (15a)$$

$$\rho \approx (\text{FBG}_{\text{stan}}^{\text{core}}) \frac{\sum_n \sum_i \gamma_i^n A_i^n}{\sum_n \sum_i F_i^n} \qquad (15b)$$

$$\rho \approx (\text{ICG}_{\text{Brit}}) \frac{\sum_n^{\text{core}} \sum_i F_i^n}{\sum_n \sum_i F_i^n}$$

$$= (\text{ICG}_{\text{Brit}}) \times \text{the core power fraction} \qquad (15c)$$

$$\rho \approx (\text{FBG}_{\text{Brit}}^{\text{core}}) \quad . \qquad (15d)$$

The British definition is the most convenient to use since the fuel cycle reactivity variation is proportional to very simple quantities. These are always obtained in the output edit from statics analysis as, for example, from the 2DB code.[6]

It is also seen, from Eq. (9), that the weights $\gamma_i^n$ should be proportional to $(\nu\sigma_f - \sigma_a)_i^n + \sigma_{a_{FP}}^n$ in order to obtain the correct reactivity variation. This conclusion is shown to have important consequences in the numerical analysis section.

### Choice of Weights and Interpretation

The weights are chosen for the most meaningful interpretation of the breeding gain or doubling time. They are generally normalized such that $\gamma_9^n = 1$ in any zone. The $^{238}U$ weight is always assumed to be zero ($\gamma_8^n = 0$), reflecting the low physical importance associated with the small loss of this nuclide with burnup. Four different choices of weights are described and discussed below.

*Standard:* Zero fertile and unit fissile weights.

$$\gamma_i^n = \begin{cases} 1 & i = 9, 1, 5 \\ 0 & i = 0, 2, 8 \end{cases} .$$

Interpretation: Doubling time of fissile material with equal weighting of the fissile nuclides. It provides a relative figure of merit of fissile mass accumulation and may be quite useful as a measure of the economic doubling time if the price of each type of fissile nuclide is the same.

*Ott $\eta$ Weighting*[4].

$$\gamma_i^n = \begin{cases} \eta_i^n/\eta_9^n & i = 9, 0, 1, 2 \\ 0 & i = 5, 8 \end{cases}$$

where

$$\eta_i^n = \nu\sigma_{f_i}^n/\sigma_{a_i}^n .$$

Interpretation: Doubling time of total plutonium which, according to Ott,[4] is somewhat insensitive to changes in the isotopic composition of plutonium. This definition is potentially useful for obtaining an estimate of the equilibrium breeding ratio and doubling time, from static reactor calculations using, for example, start-of-life plutonium composition.

*Alternate $\eta$ Weighting:* By defining

$$\gamma_i^n = \begin{cases} \eta_i^n/\eta_9^n & i = 9, 1, 5 \\ 0 & i = 0, 2, 8 \end{cases} ,$$

a measure of the accumulation of fissile mass may be obtained within the $\eta$ weighting procedure. This may then be compared directly with the predictions of the standard procedure.

By defining

$$\gamma_i^n = \begin{cases} \eta_i^n/\eta_9^n & i = 9, 0, 1, 2, 5 \\ 0 & i = 8 \end{cases} ,$$

a measure of the accumulation of all nuclides, except for $^{238}U$, is obtained. This may be compared directly with the predictions of the British weighting procedure described below.

*British Reactivity Weighting:* The isotopic reactivity weights, from Eq. (9), are given as $(\nu\sigma_f - \sigma_a)_i^n$. Baker and Ross[3] choose to normalize the weights such that the conditions $\gamma_9^n = 1$ and $\gamma_8^n = 0$ are simultaneously satisfied.

$$\gamma_i^n = \frac{(\nu\sigma_f - \sigma_a)_i^n - (\nu\sigma_f - \sigma_a)_8^n}{(\nu\sigma_f - \sigma_a)_9^n - (\nu\sigma_f - \sigma_a)_8^n} , \quad \text{all } i .$$

Interpretation: Doubling time of critical mass material, i.e., the time necessary to make a second, similar reactor critical independent of the specific plutonium isotopic composition.

This definition is also useful for gauging the reactivity variation over a fuel cycle. Equation (8) may be rewritten as follows (again neglecting the the term $A_{FP}^n/F^n$):

$$\rho = K \sum_n^{\text{core}} \left\{ [(\nu\sigma_f - \sigma_a)_9^n - (\nu\sigma_f - \sigma_a)_8^n] \sum_i \gamma_i^n \frac{C_{i-1}^n - A_i^n}{F} - [(\nu\sigma_f - \sigma_a)_8^n + \sigma_{a_{FP}}^n] \frac{F^n}{F} \right\} , \qquad (16)$$

where

$$\sum_i \gamma_i^n \frac{C_{i-1}^n - A_i^n}{F} = \text{FBG}_{\text{Brit}}^n ,$$

the fractional breeding gain of region $n$ in the British definition. It is evident that the reactivity variation, for the given choice of wieghts, is not given simply in terms of the fractional breeding gain for the core in the British definition as in Eq. (15d). However, it is shown in a later section that the cycle-to-cycle trends predicted by Eqs. (16) and (15d) are the same, although the magnitude of the cycle-to-cycle change is somewhat different.

### Other Weighting Schemes

Following Eq. (9), it is possible to define a set of weights which appears to include the effect of accumulating fission product pairs. Such a set would be

$$\gamma_i^n \approx (\sigma\nu_{f_i}^n - \sigma_{a_i}^n + \sigma_{a_{FP}}^n) .$$

However, when normalized in the same manner as the British definition, the $\sigma_{a_{FP}}^n$ does not appear in the $\gamma_i^n$ and this approach reverts to the British definition.

It seems that there is no simple way of including a practical fuel management scheme in the weights. It has been shown that, for a practical multibatch refueling scheme with scatter replacement of spent fuel assemblies, the enrichment of the fresh replacement fuel must increase to compensate for the accumulation of fission products and for the isotopic redistribution of the

partially depleted plutonium fuel (net loss of the valuable $^{241}Pu$). There is obviously no way in which the weights can be made to anticipate this enrichment increase, which is totally dependent on the fuel management scheme chosen. Thus, it is virtually impossible to predict "equilibrium" performance from start-of-life statics analysis. In fact, it is difficult to define the equilibrium cycle itself, because of variations in the number of assemblies replaced as well as variations in the feed enrichments in the later fuel cycles. The term "equilibrium" is currently taken to refer to the average behavior of later fuel cycles, when cycle-by-cycle fuel depletion and refueling analyses are performed over the operating lifetime of the reactor.

There appears to be no alternative to establishing the actual equilibrium composition, from which the equilibrium cycle breeding gain, doubling time, and reactivity variation may be computed. This does not necessarily imply that an explicit detailed depletion analysis must be performed to establish an equilibrium composition. An approximate, but computationally rapid, method of calculating the equilibrium composition is given in the concluding section. It may be sufficiently accurate for use in optimization studies and conceptual design studies which are based on the equilibrium cycle performance.

## ANALYSIS AND RESULTS

The various schemes described above for calculating the breeding gain, doubling time, and fuel cycle reactivity variation are evaluated through numerical analysis. The reactor studied is the Westinghouse demonstration plant design.[7] It is a dilute, liquid metal fast breeder reactor [300 MW(e)] using a mixed oxide fuel. This reactor exhibits nuclear characteristics similar to those of the larger [1000 MW(e)] fast breeder reactors and, therefore, any forthcoming conclusions regarding the accuracy of the proposed calculational methods will be applicable to the larger reactors as well. The nuclear data used for the calculations is the Westinghouse modified ABBN (Russian) data,[8] with modified fission and capture cross sections of $^{239}Pu$ to incorporate the higher groupwise $\alpha$-values of $^{239}Pu$, modifed fission and capture cross sections for $^{241}Pu$ and $^{235}U$, modified capture cross sections for Fe, and the $^{240}Pu$ data replaced by that from the ENDF/B file. A comparison of this data set with others currently in use, for a benchmark fast reactor calculation, was recently compiled by Baker and Hammond.[9]

The reactor described above is completely analyzed in the conventional manner using fuel cycle depletion analysis. The code[6] 2DB is used to perform the depletion analysis, employing two-dimensional ($R$-$Z$) diffusion theory and zonewise depletion within small regions of the core, radial blanket, and axial blankets. The fuel cycle analysis is performed both for the startup fuel cycle and the equilibrium fuel cycle and accounts for control rod movements over each fuel cycle. The only assumption employed is that the residence time of the radial blanket fuel assemblies is twice that of the core fuel assemblies. The nonuniform effects of local changes in fuel composition, local fission product accumulation, power redistribution, control poison removal, and changes in the zone-dependent spectra with time are taken into account in the fuel cycle analysis.

The fuel cycle analysis shows that a higher plutonium enrichment is necessary in the equilibrium cycle, when compared with the startup cycle, to offset the accumulation of fission products and the isotopic redistribution of the plutonium fuel (net loss of $^{241}Pu$). The fissile plutonium mass is found to increase by 21% from the start of the first cycle to the start of the equilibrium cycle. The fissile plutonium simple doubling time is computed from

$$\frac{1}{T_s\ (\text{year})} = \frac{\text{surplus production of fissile plutonium per fuel cycle}}{\text{initial mass of fissile plutonium}} \times \frac{\text{number of fuel cycles}}{\text{calendar year}} .$$

The simple doubling time is computed both for the startup fuel cycle and the equilibrium fuel cycle. The fuel cycle reactivity variation is also computed during the fuel cycle analysis for the startup and equilibrium reactors.

The pertinent data from the fuel cycle analysis is given in Table I. Given for the startup and equilibrium fuel cycles are the observed simple

TABLE I

Data From Fuel Cycle Analysis

| Item | Case | |
|---|---|---|
| | Startup Cycle | Equilibrium Cycle |
| Net fissile Pu produced per fuel cycle (kg/half year) | 29.0 | 20.0 |
| Initial fissile Pu mass (kg) | 971 | 1168 |
| Fissile Pu simple doubling time (year) | 16.7 | 29.2 |
| Fuel cycle reactivity variation (% $\Delta k/k$) | 2.13 | 2.00 |
| Relative breeding gain inferred from observed doubling times and initial fissile Pu masses [Eq. (4)] | 1.00 | 0.69 |

doubling times and the observed reactivity variations over both cycles. Using Eq. (4) it is possible to infer, in relative terms, how much the breeding gain should decrease (from startup to equilibrium) to match the observed increase in simple doubling time and the increase in initial fissile plutonium loading. The 21% increase in initial fissile plutonium loading and the 75% increase in doubling time require a 31% decrease in breeding gain from startup to equilibrium. This is shown as a relative effect (Table I).

The results presented in Table I consider only fissile plutonium. This represents a departure from the commonly accepted definition, wherein the total fissile mass ($^{239}Pu + ^{241}Pu + ^{235}U$) is considered. In the depletion analysis the $^{235}U$ burnout was considered, as it must be, and the doubling time of total fissile mass could have been quoted. However, the only purpose of the depletion analysis was to test the validity of the results from statics analysis using the various definitions of the breeding gain. In these definitions not only is the $^{235}U$ effect small, but also its contribution is almost completely offset by the small contribution from the fertile plutonium nuclides ($^{240}Pu$ and $^{242}Pu$). These breeding gain definitions tend to gauge the production or doubling of fissile plutonium. Therefore, to evaluate these definitions, the effects only of fissile plutonium are extracted from the fuel cycle analysis.

The $\eta$ weights for the Ott definition and the $\rho$ weights for the British definition of the breeding gain were calculated once for the beginning of reactor life spectrum and were assumed to remain constant for all time. These weights are given in Table II, where the following notation is used:

UICZ = upper inner core zone—low enrichment core region above the core midplane

LICZ = lower inner core zone—low enrichment core region below core midplane

UOCZ = upper outer core zone—high enrichment core region above core midplane

LOCZ = lower outer core zone—high enrichment core region below core midplane

RB1 = first assembly row of radial blanket (height same as core)

TABLE II

Weights in Breeding Gain Calculations — Start of First Cycle

| Nuclide | Reactor Zone | | | | | | | | | | |
|---|---|---|---|---|---|---|---|---|---|---|---|
| | UICZ | LICZ | UOCZ | LOCZ | RB1 | RB2,3 | RBE | UAX1 | LAX1 | UAX2 | LAX2 |
| Standard: Equal Fissile Weights, Zero Fertile Weights | | | | | | | | | | | |
| 9 | 1.0 | 1.0 | 1.0 | 1.0 | 1.0 | 1.0 | 1.0 | 1.0 | 1.0 | 1.0 | 1.0 |
| 0 | 0 | 0 | 0 | 0 | 0 | 0 | 0 | 0 | 0 | 0 | 0 |
| 1 | 1.0 | 1.0 | 1.0 | 1.0 | — | — | — | — | — | — | — |
| 2 | 0 | 0 | 0 | 0 | — | — | — | — | — | — | — |
| 5 | 1.0 | 1.0 | 1.0 | 1.0 | 1.0 | 1.0 | 1.0 | 1.0 | 1.0 | 1.0 | 1.0 |
| 8 | 0 | 0 | 0 | 0 | 0 | 0 | 0 | 0 | 0 | 0 | 0 |
| Ott: $\eta$ Weighting | | | | | | | | | | | |
| 9 | 1.0 | 1.0 | 1.0 | 1.0 | 1.0 | 1.0 | 1.0 | 1.0 | 1.0 | 1.0 | 1.0 |
| 0 | 0.620 | 0.616 | 0.640 | 0.638 | 0.402 | 0.192 | 0.143 | 0.251 | 0.198 | 0.251 | 0.184 |
| 1 | .11 | 1.11 | 1.11 | 1.11 | — | — | — | — | — | — | — |
| 2 | 0.491 | 0.487 | 0.511 | 0.508 | — | — | — | — | — | — | — |
| 5 | 0.792 | 0.793 | 0.792 | 0.793 | 0.822 | 0.860 | 0.881 | 0.847 | 0.865 | 0.850 | 0.869 |
| 8 | 0 | 0 | 0 | 0 | 0 | 0 | 0 | 0 | 0 | 0 | 0 |
| British: Reactivity Weighting | | | | | | | | | | | |
| 9 | 1.0 | 1.0 | 1.0 | 1.0 | 1.0 | 1.0 | 1.0 | 1.0 | 1.0 | 1.0 | 1.0 |
| 0 | 0.178 | 0.176 | 0.190 | 0.189 | 0.050 | 0 | 0 | 0 | 0 | 0 | 0 |
| 1 | 1.43 | 1.43 | 1.43 | 1.43 | — | — | — | — | — | — | — |
| 2 | 0.099 | 0.097 | 0.107 | 0.106 | — | — | — | — | — | — | — |
| 5 | 0.742 | 0.744 | 0.740 | 0.742 | 0.821 | 0.911 | 0.918 | 0.874 | 0.890 | 0.874 | 0.892 |
| 8 | 0 | 0 | 0 | 0 | 0 | 0 | 0 | 0 | 0 | 0 | 0 |

RB2, 3 = second and third assembly rows of radial blanket (height same as core)

RBE = radial blanket extensions beyond core axial boundaries

UAX1 = upper axial blanket above inner core zone

LAX1 = lower axial blanket below inner core zone

UAX2 = upper axial blanket above outer core zone

LAX2 = lower axial blanket below outer core zone.

These were not the regions used in the explicit depletion analysis—many sub-zones of each of the above regions were used in the depletion analysis. There are enough regions here, however, to yield sufficiently accurate results for the breeding gain analysis, including essentially the same space-energy effects as in the explicit depletion analysis.

Of some interest in Table II is the reactivity worth of $^{241}Pu$ and $^{235}U$ relative to $^{239}Pu$. Plutonium-241 is worth 43% more than $^{239}Pu$, while $^{235}U$ is worth 26% less than $^{239}Pu$ in the fast energy spectrum of the oxide fuel composition considered here.

Table III gives the surplus production, absorption, and fission rates from statics analysis for the start of the first fuel cycle. These results are combined with the weights in Table II to generate the breeding gains and doubling times given in Table IV. The isotopic and zonewise breakdown of the breeding gain is given, as well as the total breeding and associated doubling time for each of the standard, Ott, and British definitions.

Three different types of Ott $\eta$ weighting are considered, each described earlier, for testing the sensitivity of the breeding gain to the $\eta$ weighting procedure. The first type is equivalent to that originally studied by Ott.[4] It gives a result, in terms of the doubling time, which is comparable to the standard definition, and both of these are much too low when compared with the doubling time from the fuel cycle analysis in Table I. All three types of $\eta$ weighting give a rather narrow grouping of predicted doubling times, and all of these are too low.

The British definition gives a breeding gain which is significantly lower than the other definitions. Correspondingly, the doubling time is significantly longer and is very close to that from the fuel cycle analysis. This is the first indication that the British definition, using reactivity weighting, is superior to the conventional definition or any combination of Ott $\eta$ weighting.

TABLE III

Fission, Absorption, and Surplus Production Rates — Start of First Cycle ($\times 10^{-18}$)

| Nuclide | Reactor Zone | | | | | | | | | | |
|---|---|---|---|---|---|---|---|---|---|---|---|
| | UICZ | LICZ | UOCZ | LOCZ | RB1 | RB2,3 | RBE | UAX1 | LAX1 | UAX2 | LAX2 |
| Surplus Production Rate | | | | | | | | | | | |
| 9 | -0.353 | -0.350 | -1.45 | -1.46 | 4.46 | 3.37 | 1.01 | 1.67 | 1.68 | 1.00 | 1.00 |
| 0 | 0.321 | 0.333 | 0.250 | 0.257 | 0 | 0 | 0 | 0 | 0 | 0 | 0 |
| 1 | -0.960 | -0.972 | -0.772 | -0.778 | 0 | 0 | 0 | 0 | 0 | 0 | 0 |
| 2 | 0.064 | 0.065 | 0.049 | 0.050 | 0 | 0 | 0 | 0 | 0 | 0 | 0 |
| 5 | -0.077 | -0.078 | -0.043 | -0.043 | -0.083 | -0.068 | -0.023 | -0.031 | -0.034 | -0.019 | -0.021 |
| 8 | -5.23 | -5.29 | -2.92 | -2.94 | -4.80 | -3.47 | -1.04 | -1.73 | -1.74 | -1.04 | -1.04 |
| Absorption Rate | | | | | | | | | | | |
| 9 | 4.91 | 4.97 | 3.95 | 3.98 | 0 | 0 | 0 | 0 | 0 | 0 | 0 |
| 0 | 0.618 | 0.625 | 0.509 | 0.513 | 0 | 0 | 0 | 0 | 0 | 0 | 0 |
| 1 | 1.28 | 1.30 | 1.03 | 1.04 | 0 | 0 | 0 | 0 | 0 | 0 | 0 |
| 2 | 0.094 | 0.095 | 0.078 | 0.079 | 0 | 0 | 0 | 0 | 0 | 0 | 0 |
| 5 | 0.077 | 0.078 | 0.043 | 0.043 | 0.083 | 0.068 | 0.023 | 0.031 | 0.034 | 0.019 | 0.021 |
| 8 | 5.23 | 5.29 | 2.92 | 2.94 | 4.80 | 3.47 | 1.04 | 1.73 | 1.74 | 1.04 | 1.04 |
| Fission Rate | | | | | | | | | | | |
| 9 | 3.97 | 4.01 | 3.19 | 3.21 | 0 | 0 | 0 | 0 | 0 | 0 | 0 |
| 0 | 0.298 | 0.299 | 0.253 | 0.253 | 0 | 0 | 0 | 0 | 0 | 0 | 0 |
| 1 | 1.12 | 1.14 | 0.902 | 0.910 | 0 | 0 | 0 | 0 | 0 | 0 | 0 |
| 2 | 0.036 | 0.036 | 0.031 | 0.031 | 0 | 0 | 0 | 0 | 0 | 0 | 0 |
| 5 | 0.059 | 0.060 | 0.033 | 0.033 | 0.061 | 0.048 | 0.016 | 0.022 | 0.024 | 0.014 | 0.015 |
| 8 | 0.673 | 0.671 | 0.415 | 0.413 | 0.344 | 0.095 | 0.028 | 0.066 | 0.065 | 0.043 | 0.042 |

TABLE IV

Breeding Gains and Doubling Times — Start of First Cycle

| Nuclide | Reactor Zone | | | | | | | | | | | |
|---|---|---|---|---|---|---|---|---|---|---|---|---|
| | UICZ | LICZ | UOCZ | LOCZ | RB1 | RB2,3 | RBE | UAX1 | LAX1 | UAX2 | LAX2 | TOT |
| Standard: Equal Fissile Weights, Zero Fertile Weights | | | | | | | | | | | | |
| 9 | -0.015 | -0.015 | -0.063 | -0.063 | 0.194 | 0.147 | 0.044 | 0.073 | 0.073 | 0.044 | 0.044 | 0.460 |
| 0 | 0 | 0 | 0 | 0 | 0 | 0 | 0 | 0 | 0 | 0 | 0 | 0 |
| 1 | -0.042 | -0.042 | -0.034 | -0.034 | — | — | — | — | — | — | — | -0.152 |
| 2 | 0 | 0 | 0 | 0 | — | — | — | — | — | — | — | 0 |
| 5 | -0.003 | -0.003 | -0.002 | -0.002 | -0.004 | -0.003 | -0.001 | -0.001 | -0.001 | -0.001 | -0.001 | -0.023 |
| 8 | 0 | 0 | 0 | 0 | 0 | 0 | 0 | 0 | 0 | 0 | 0 | 0 |
| Total | -0.061 | -0.061 | -0.099 | -0.099 | 0.190 | 0.144 | 0.043 | 0.071 | 0.071 | 0.043 | 0.043 | 0.286 |
| Doubling Time | Simple: 12.3 year | | | Compound: 8.5 year | | | | | | | | |
| Ott: $\eta$ Weighting for Plutonium Nuclides, Zero Uranium Weights | | | | | | | | | | | | |
| 9 | -0.014 | -0.014 | -0.059 | -0.059 | 0.181 | 0.137 | 0.041 | 0.068 | 0.068 | 0.041 | 0.041 | 0.430 |
| 0 | 0.008 | 0.008 | 0.007 | 0.007 | 0 | 0 | 0 | 0 | 0 | 0 | 0 | 0.030 |
| 1 | -0.043 | -0.044 | -0.035 | -0.035 | — | — | — | — | — | — | — | -0.158 |
| 2 | 0.001 | 0.001 | 0.001 | 0.001 | — | — | — | — | — | — | — | 0.005 |
| 5 | 0 | 0 | 0 | 0 | 0 | 0 | 0 | 0 | 0 | 0 | 0 | 0 |
| 8 | 0 | 0 | 0 | 0 | 0 | 0 | 0 | 0 | 0 | 0 | 0 | 0 |
| Total | -0.048 | -0.049 | -0.086 | -0.087 | 0.181 | 0.137 | 0.041 | 0.068 | 0.068 | 0.041 | 0.041 | 0.307 |
| Doubling Time | Simple: 12.7 year | | | Compound: 8.8 year | | | | | | | | |
| Ott: $\eta$ Weighting for Fissile Nuclides, Zero Fertile Weights | | | | | | | | | | | | |
| 9 | -0.015 | -0.015 | -0.062 | -0.062 | 0.191 | 0.144 | 0.043 | 0.071 | 0.072 | 0.043 | 0.043 | 0.452 |
| 0 | 0 | 0 | 0 | 0 | 0 | 0 | 0 | 0 | 0 | 0 | 0 | 0 |
| 1 | -0.046 | -0.046 | -0.037 | -0.037 | — | — | — | — | — | — | — | -0.165 |
| 2 | 0 | 0 | 0 | 0 | — | — | — | — | — | — | — | 0 |
| 5 | -0.003 | -0.003 | -0.002 | -0.002 | -0.003 | -0.003 | 0 | -0.001 | -0.001 | 0 | 0 | -0.018 |
| 8 | 0 | 0 | 0 | 0 | 0 | 0 | 0 | 0 | 0 | 0 | 0 | 0 |
| Total | -0.063 | -0.064 | -0.100 | -0.101 | 0.188 | 0.141 | 0.042 | 0.070 | 0.070 | 0.042 | 0.042 | 0.268 |
| Doubling Time | Simple: 13.0 year | | | Compound: 9.0 year | | | | | | | | |
| Ott: $\eta$ Weighting all Nuclides, Zero $^{238}$U Weight | | | | | | | | | | | | |
| 9 | -0.014 | -0.014 | -0.058 | -0.058 | 0.178 | 0.135 | 0.040 | 0.067 | 0.067 | 0.040 | 0.040 | 0.452 |
| 0 | 0.008 | 0.008 | 0.006 | 0.006 | 0 | 0 | 0 | 0 | 0 | 0 | 0 | 0.029 |
| 1 | -0.043 | -0.043 | -0.034 | -0.035 | — | — | — | — | — | — | — | -0.155 |
| 2 | 0.001 | 0.001 | 0.001 | 0.001 | — | — | — | — | — | — | — | 0.005 |
| 5 | -0.002 | -0.003 | -0.001 | -0.001 | -0.003 | -0.002 | -0.001 | -0.001 | -0.001 | -0.001 | -0.001 | -0.017 |
| 8 | 0 | 0 | 0 | 0 | 0 | 0 | 0 | 0 | 0 | 0 | 0 | 0 |
| Total | -0.050 | -0.050 | -0.086 | -0.087 | 0.176 | 0.132 | 0.040 | 0.066 | 0.066 | 0.039 | 0.039 | 0.285 |
| Doubling Time | Simple: 13.8 year | | | Compound: 9.6 year | | | | | | | | |
| British: Reactivity Weighting all Nuclides, Zero $^{238}$U Weight | | | | | | | | | | | | |
| 9 | -0.015 | -0.015 | -0.063 | -0.064 | 0.194 | 0.147 | 0.044 | 0.073 | 0.073 | 0.044 | 0.044 | 0.461 |
| 0 | 0.003 | 0.003 | 0.002 | 0.002 | 0 | 0 | 0 | 0 | 0 | 0 | 0 | 0.009 |
| 1 | -0.060 | -0.061 | -0.048 | -0.049 | — | — | — | — | — | — | — | -0.217 |
| 2 | 0 | 0 | 0 | 0 | — | — | — | — | — | — | — | 0.001 |
| 5 | -0.003 | -0.003 | -0.001 | -0.001 | -0.003 | -0.003 | -0.001 | -0.001 | -0.001 | -0.001 | -0.001 | -0.018 |
| 8 | 0 | 0 | 0 | 0 | 0 | 0 | 0 | 0 | 0 | 0 | 0 | 0 |
| Total | -0.075 | -0.076 | -0.110 | -0.111 | 0.191 | 0.144 | 0.043 | 0.072 | 0.072 | 0.043 | 0.043 | 0.236 |
| Doubling Time | Simple: 16.7 year | | | Compound: 11.6 year | | | | | | | | |

Since a detailed fuel cycle analysis is performed for the purpose of comparison with theory, it is possible to examine the equilibrium core as well as the startup core. In this case, however, the Ott $\eta$ weighting procedure is not considered because of its less than successful prediction of the doubling time for the startup core. It gives results comparable with the standard definition; therefore, only the standard and British definitions are compared for the equilibrium core.

Ott[4] cited, as a strong advantage of the $\eta$ weighting procedure, that the breeding gain was insensitive to change in plutonium isotopic composition. This is clearly not an advantage in terms of the actual fuel cycle analysis, which showed that the breeding gain should decrease substantially, reflecting the enrichment increase necessary to offset the accumulation of fission products and the net loss of $^{241}$Pu. In the actual cycle-by-cycle depletion analysis, the changes in plutonium isotopic composition are important and should influence significantly the breeding gains. The reactor, after refueling, must have sufficient excess multiplication to operate for another fuel cycle. Changes in plutonium isotopic composition affect the feed enrichment; for example, the net loss of $^{241}$Pu requires that the feed enrichment must increase in later cycles. These changes in feed enrichment, in turn, affect the space-dependent flux level and spectrum and thus affect the breeding gain and doubling time.

From Ott's analysis, one infers that $\eta$ weighting possesses the ability to predict the equilibrium breeding gain and doubling time from start-of-life statics analysis. If such were the case, using Table IV, the equilibrium doubling time would be predicted to be 12.7 year, when this is really a factor of $2\frac{1}{2}$ low when compared with the actual value of 29.2 year.

One of the important conclusions of this study is that the equilibrium performance cannot be predicted from start-of-life statics analysis using any simple weighting procedure. The equilibrium cycle is obtained after several fuel cycles, where small errors propagated through many cycles can result in large errors for the equilibrium cycle. In each cycle, there are nonuniform burnup effects caused by local changes in fuel composition and fission product buildup, control rod movements, power redistribution, and changes in the zone-dependent spectra with time. In addition, a multibatch fuel management scheme with scatter replacement of spent assemblies contributes to the eventual characteristics of the equilibrium cycle. It is asking a great deal, indeed, to expect a simple weighting procedure to anticipate all these effects and give the equilibrium cycle characteristics from startup core statics analysis.

In the study of the equilibrium core performed here, the statics analysis uses the composition at the start of the equilibrium cycle which is obtained from the fuel cycle depletion analysis. The various reaction rates are given in Table V for the start of the equilibrium cycle. These include, of course, the power redistribution which occurs since the beginning-of-life, and all the nonuniform burnup effects which occur in all cycles preceding this one. For simplicity, the British reactivity weights are assumed to remain the same as for the startup core; although the weights will change with time and a new set of weights should be computed to correspond to the point in time for which the breeding gain is being calculated. Due to the enrichment increase in the equilibrium cycle, the spectra is hardened in the core regions. Also, the spectra in the blanket regions hardens appreciably, particularly in the radial blanket regions due to the production of fission material in these regions. However, because of the normalization to $^{239}$Pu, it seems that the weights would not be significantly affected and the use of the startup core weights is justified.

The weights of Table II are combined with the reaction rates of Table V to obtain the results for the breeding gain and doubling time of the equilibrium core given in Table VI. These results are checked by using the conclusion, given in the discussion of Table I, that the breeding gain should decrease by 31% from the startup core to the equilibrium core. Based on this, the standard definition should give an equilibrium core breeding gain of 0.197 and the British definition should give 0.162. These compare very well with the actual values obtained of 0.198 and 0.164, respectively. The equilibrium doubling time from the British definition is in good agreement with that from the fuel cycle analysis (Table I), whereas the standard definition again gives results which are too low. The British definition predicts an equilibrium doubling time which is 3.4% low when compared with the depletion analysis. However, even this discrepancy is due to the use of weights from the startup core studies. Small discrepancies of this type are avoided by recomputing the weights at each point in time for which a breeding gain is desired.

The final test of the various definitions is the computation of the fuel cycle reactivity variation, both for the startup core and for the equilibrium core. The results pertaining to this effect are given in Table VII. The fractional breeding gain in the core and the internal (core) conversion gain are also given. Equation (16) is used to compute a relative reactivity variation ($\rho/K$) for the two fuel cycles, and the actual reactivity variation from fuel cycle analysis is also given. The uncertainty

TABLE V

Fission, Absorption, and Surplus Production Rates — Start of Equilibrium Cycle ($\times 10^{-18}$)

| Nuclide | Reactor Zone | | | | | | | | | | |
|---|---|---|---|---|---|---|---|---|---|---|---|
| | UICZ | LICZ | UOCZ | LOCZ | RB1 | RB2,3 | RBE | UAX1 | LAX1 | UAX2 | LAX2 |
| Surplus Production Rate | | | | | | | | | | | |
| 9 | -0.791 | -0.799 | -1.57 | -1.59 | 3.62 | 3.24 | 0.945 | 1.43 | 1.26 | 0.922 | 0.885 |
| 0 | 0.264 | 0.273 | 0.194 | 0.201 | 0.176 | 0.086 | 0.030 | 0.039 | 0.065 | 0.018 | 0.030 |
| 1 | -0.649 | -0.656 | -0.622 | -0.628 | — | — | — | — | — | — | — |
| 2 | 0.025 | 0.025 | 0.027 | 0.027 | — | — | — | — | — | — | — |
| 5 | -0.052 | -0.053 | -0.034 | -0.034 | -0.066 | -0.063 | -0.021 | -0.026 | -0.026 | -0.017 | -0.018 |
| 8 | -4.52 | -4.59 | -2.69 | -2.72 | -4.79 | -3.70 | -1.08 | -1.64 | -1.55 | -1.03 | -1.03 |
| Absorption Rate | | | | | | | | | | | |
| 9 | 4.73 | 4.80 | 3.88 | 3.93 | 0.759 | 0.300 | 0.095 | 0.142 | 0.220 | 0.063 | 0.096 |
| 0 | 0.631 | 0.643 | 0.544 | 0.550 | 0.007 | 0.002 | 0.001 | 0.001 | 0.003 | 0 | 0.001 |
| 1 | 0.974 | 0.989 | 0.894 | 0.904 | — | — | — | — | — | — | — |
| 2 | 0.095 | 0.096 | 0.083 | 0.084 | — | — | — | — | — | — | — |
| 5 | 0.052 | 0.053 | 0.034 | 0.034 | 0.066 | 0.063 | 0.021 | 0.026 | 0.026 | 0.017 | 0.018 |
| 8 | 4.52 | 4.59 | 2.69 | 2.72 | 4.79 | 3.70 | 1.08 | 1.64 | 1.55 | 1.03 | 1.03 |
| Fission Rate | | | | | | | | | | | |
| 9 | 3.83 | 3.89 | 3.15 | 3.18 | 0.577 | 0.212 | 0.064 | 0.103 | 0.152 | 0.045 | 0.065 |
| 0 | 0.306 | 0.309 | 0.272 | 0.274 | 0.002 | 0 | 0 | 0 | 0 | 0 | 0 |
| 1 | 0.855 | 0.868 | 0.784 | 0.793 | — | — | — | — | — | — | — |
| 2 | 0.036 | 0.036 | 0.033 | 0.033 | — | — | — | — | — | — | — |
| 5 | 0.040 | 0.040 | 0.026 | 0.026 | 0.048 | 0.044 | 0.014 | 0.019 | 0.018 | 0.012 | 0.013 |
| 8 | 0.581 | 0.582 | 0.385 | 0.385 | 0.407 | 0.157 | 0.040 | 0.071 | 0.075 | 0.047 | 0.048 |

TABLE VI

Breeding Gains and Doubling Times — Start of Equilibrium Cycle

| Nuclide | Reactor Zone | | | | | | | | | | | |
|---|---|---|---|---|---|---|---|---|---|---|---|---|
| | UICZ | LICZ | UOCZ | LOCZ | RB1 | RB2,3 | RBE | UAX1 | LAX1 | UAX2 | LAX2 | TOT |
| Standard: Equal Fissile Weights, Zero Fertile Weights | | | | | | | | | | | | |
| 9 | -0.034 | -0.035 | -0.068 | -0.069 | 0.156 | 0.140 | 0.041 | 0.062 | 0.054 | 0.040 | 0.038 | 0.326 |
| 0 | 0 | 0 | 0 | 0 | 0 | 0 | 0 | 0 | 0 | 0 | 0 | 0 |
| 1 | -0.028 | -0.028 | -0.027 | -0.027 | — | — | — | — | — | — | — | -0.110 |
| 2 | 0 | 0 | 0 | 0 | 0 | 0 | 0 | 0 | 0 | 0 | 0 | 0 |
| 5 | -0.002 | -0.002 | -0.001 | -0.001 | -0.003 | -0.003 | -0.001 | -0.001 | -0.001 | -0.001 | -0.001 | -0.018 |
| 8 | 0 | 0 | 0 | 0 | 0 | 0 | 0 | 0 | 0 | 0 | 0 | 0 |
| Total | -0.064 | -0.065 | -0.096 | -0.097 | 0.153 | 0.137 | 0.040 | 0.060 | 0.053 | 0.039 | 0.037 | 0.198 |
| Doubling Time Simple: 22.8 year Compound: 15.8 year | | | | | | | | | | | | |
| British: Reactivity Weighting all Nuclides, Zero $^{238}U$ Weight | | | | | | | | | | | | |
| 9 | -0.035 | -0.035 | -0.069 | -0.069 | 0.158 | 0.141 | 0.041 | 0.062 | 0.055 | 0.040 | 0.039 | 0.329 |
| 0 | 0.002 | 0.002 | 0.002 | 0.002 | 0 | 0 | 0 | 0 | 0 | 0 | 0 | 0.008 |
| 1 | -0.040 | -0.041 | -0.039 | -0.039 | — | — | — | — | — | — | — | -0.159 |
| 2 | 0 | 0 | 0 | 0 | — | — | — | — | — | — | — | 0 |
| 5 | -0.002 | -0.002 | -0.001 | -0.001 | -0.002 | -0.002 | -0.001 | -0.001 | -0.001 | -0.001 | -0.001 | -0.014 |
| 8 | 0 | 0 | 0 | 0 | 0 | 0 | 0 | 0 | 0 | 0 | 0 | 0 |
| Total | -0.074 | -0.075 | -0.107 | -0.108 | 0.156 | 0.139 | 0.040 | 0.061 | 0.054 | 0.040 | 0.038 | 0.164 |
| Doubling Time Simple: 28.2 year Compound: 19.5 year | | | | | | | | | | | | |

in the latter quantity is due to the convergence criterion on the total fission source rate employed in the depletion analysis.

TABLE VII

Fractional Breeding Gain in Core, Internal Conversion Gain, and Fuel Cycle Reactivity Variation

| Quantity | Startup Cycle | Equilibrium Cycle |
|---|---|---|
| Fractional breeding gain in the core | | |
| Standard definition | -0.319 | -0.323 |
| British definition | -0.372 | -0.364 |
| Internal conversion gain | | |
| Standard definition | -0.323 | -0.352 |
| British definition | -0.387 | -0.403 |
| Quantity proportional to fuel cycle Reactivity variation [$\rho/K$ from Eq. (16)] | -1.48 | -1.44 |
| Reactivity variation over fuel cycle from depletion analysis (% $\Delta k/k$) | -2.13 ± 0.03 | -2.00 ± 0.03 |

The commonly accepted indicator of the fuel cycle reactivity variation, the internal conversion gain, gives an incorrect trend for both the standard and British definitions. The fractional breeding gain of the core again gives the wrong trend in the standard definition, but gives the right trend in the British definition as expected from Eq. (16). However, the magnitude of the reduction is not quite correct, giving 2.2% as compared with the actual 6.1% reduction in the nominal values of fuel cycle reactivity variation. The reactivity variation is also computed using Eq. (16) where the result is given in terms of $\rho/K$ and $K$ is defined in Eq. (8). The quantity $K$ involves the fuel cycle time which is the same for both the startup and equilibrium cycles. In addition, it involves the core average flux which is not the same in both cycles. The quantity $\omega$, given as

$$\omega = \sum_n F_n \phi_n / F \approx \phi_{\text{core}} \quad ,$$

is very nearly the core average flux since the fission rates in the blanket regions are very low. Therefore $\phi^2_{\text{core}}/\omega \simeq \phi_{\text{core}}$, and $K$ varies directly as $\phi_{\text{core}}$. It is assumed, in addition, that $\phi_{\text{core}}$ varies as the core power fraction. This is a reasonable approximation since each cycle was required to have the same initial multiplication factor, which implies that the average macroscopic fission cross section of the core was nearly the same in both cases. By this assumption, $\phi_{\text{core}}$ is found to decrease by 6.1% from the startup cycle to the equilibrium cycle. The magnitude of $\rho/K$ is shown in Table VII to decrease by 2.7% from startup to equilibrium, and the analysis just performed shows that $K$ itself decreases by 6.1%. The net effect is that the magnitude of the negative reactivity variation decreases by about 8.8%, where the observed change in the nominal value is 6.1%. This is exceptionally good agreement considering some of the assumptions made regarding the variation in the quantity $K$. It appears, therefore, that the simple calculation of the fuel cycle reactivity variation, using Eq. (16) and the British definition of the breeding gain, gives very good results for the observed fuel cycle reactivity variation. This, of course, is obtained from statics analysis but gives results comparable with those from the explicit fuel cycle depletion analysis.

The conceptual difficulties associated with the use of the internal conversion gain in the standard definition are resolved by using Eq. (16) and the British definition of the core fractional breeding ratio. In fact, the correct trend is observed just from the core fractional breeding gain in the British definition, even without Eq. (16). Equation (16) serves to give the correct magnitude of the change in fuel cycle reactivity variation. The explanation for the failure of the standard definition and the success of the British definition is simply the change in the plutonium isotopic composition and the method of treating the higher plutonium isotopes in each case. The general trend toward isotopic redistribution with burnup in the core, for a reactor initially fueled with commercial grade plutonium, is to decrease the fraction of 239 and 241 (241 fraction decreases more rapidly than 239) and to increase the fraction of 240 and 242 (240 fraction increases much more rapidly than 242). Second, the total plutonium enrichment must increase with time (or with burnup) to compensate both for the buildup of fission products and the net loss of the valuable $^{241}$Pu. The effects of this isotopic redistribution on the breeding gain with time, in each of the standard and British definitions, are seen by comparing Tables IV and VI for the startup core and equilibrium core, respectively. The only significant difference between the two definitions, in just the core regions, is the treatment of $^{241}$Pu. The treatment of $^{239}$Pu is nearly the same since a unit weight is ascribed to this nuclide in both cases. The only difference for $^{239}$Pu occurs because of the difference in the denominator of the two definitions for the breeding gain. The considerably greater wieght given to $^{241}$Pu in the British definition (43% greater than that of the standard definition) results in an overall decrease

in the magnitude of the negative core fractional breeding gain with time due to the $^{241}Pu$ depletion, whereas in the standard definition an increase in the magnitude with time is observed. Thus, the difference in weighting of the higher plutonium isotopes (for this case just $^{241}Pu$) is solely responsible for obtaining an entirely different prediction of the trend for the reactivity variation with time.

The same type of anomaly that was observed with the use of the standard definition to compare the performance of two similar reactors, one fueled with commercial grade plutonium and the other fueled with weapons grade plutonium, is also removed when using the British definition. This example is discussed in the Introduction. The resolution of this difficulty is also a consequence of the proper weighting (reactivity weighting) of the higher plutonium isotopes.

## CONCLUSIONS

There are four significant conclusions which result from the foregoing analysis and numerical studies:

1. The British definition of a point-in-time breeding gain is the best prescription to use in statics calculations. The fissile plutonium doubling times predicted by the British definition are in very good agreement with those from explicit depletion analysis and are much better than those predicted by the standard definition or any possible $\eta$ weighting combination in the Ott method. It is recommended that this definition be included in static diffusion theory analysis.

2. The reactivity weights in the British definition should be recomputed at each point in time for which the breeding gain, doubling time, and fuel cycle reactivity variation is desired.

3. The British definition of the breeding gain gives the proper trend regarding the reactivity variation with burnup where changes in the isotopic composition of fuel are involved. This is a direct consequence of the isotopic reactivity weighting, particularly for the higher plutonium isotopes. The British definition in conjunction with Eq. (16) gives not only the proper trend but also the proper magnitude of the reactivity variation. The conceptual difficulties encountered in the past using the standard definition, where the incremental changes in the magnitude of the core conversion gain and the magnitude of the fuel cycle reactivity variation were in opposite directions, are alleviated by the British definition and Eq. (16).

4. For realistic reactor systems involving a complex multibatch fuel management scheme with scatter replacement of spent fuel assemblies, involving explicit control rod movements over each fuel cycle, and involving a significant power redistribution with time, it is virtually impossible to predict the equilibrium cycle breeding performance from startup core statics analysis. The nonuniform burnup effects throughout the core and blankets give rise to locally different changes in plutonium isotopic composition, locally different fission product accumulation, and a power redistribution. These, coupled with control rod movements over the fuel cycle, give rise to changes in the zone-dependent spectra with time, which are particularly pronounced in the radial blanket due to the accumulation of fissile material. In addition, in a multibatch refueling scheme, the net loss of $^{241}Pu$ and the accumulation of fission products dictate that the plutonium enrichment must increase with time. These effects cause significant changes in the local and overall breeding gains and in the doubling time, which are very difficult to predict from start-of-life statics analysis.

In this study, depletion analysis was used to determine the start of equilibrium cycle compositions. These were then used in statics analysis to obtain the predictions of breeding gains, doubling times, and fuel cycle reactivity variations in the various definitions for comparison with the results of the explicit equilibrium fuel cycle analysis.

A simple alternative to this procedure, which would eliminate the need for a detailed depletion analysis, is to use Eqs. (6a) and (6b) to determine the approximate compositions at the middle of equilibrium cycle (defined as half the maximum average burnup of the fuel assemblies in the core). The time in full power days necessary to attain this burnup is easily computed, knowing the constant reactor power level and the core power fraction. The radial blanket composition is obtained by assuming that the residence time of the radial blanket is twice that of the core and that the start-of-life power fraction remains unchanged. The composition of the upper and lower axial blankets is obtained using the same residence time as the core and assuming that the start-of-life power fraction remains unchanged. Such a procedure would allow the determination of the burnup in all reactor regions from the start-of-life to the middle of the equilibrium fuel cycle. Also, the regionwise incremental burnup for one fuel cycle is known once the fuel cycle time is specified, employing the assumption that the regionwise power fractions remain unchanged over one cycle. Knowing the regionwise burnup to the

middle of the equilibrium fuel cycle, and the regionwise incremental burnup over the cycle, the burnup to the start or end of the equilibrium fuel cycle is obtained, and the compositions at either of these time points may be computed using Eqs. (6a) and (6b). The composition at the end of the equilibrium cycle is of particular importance for evaluating the one remaining quantity needed in in Eqs. (6). The reaction rates are obtained from the startup core statics analysis and assumed to remain constant with time. However, not known is the initial plutonium enrichment, which must be chosen such that the reactor is just critical ($k = 1$) at the end of the equilibrium cycle. Thus, one or two iterations on Eqs. (6) may be necessary, picking the initial enrichment, using the known burnups and reaction rates to compute the new composition at the end of the equilibrium cycle, and then performing statics analysis to determine the multiplication constant. Success is achieved when the initial enrichment yields critically at the end of the equilibrium cycle. Of course, all the above assumes that all control rods are withdrawn. If desired, after the reactor is made just critical at the end of equilibrium cycle, the proper amount of control poison may be inserted to make the reactor critical at any other point in time during the equilibrium cycle.

With the compositions at the middle of equilibrium cycle now known, the breeding gain, doubling time, and equilibrium fuel cycle reactivity variation may be computed by statics analysis. Even though this procedure is approximate (not accounting for power redistribution and local spectra changes) it may be sufficiently accurate for conceptual design studies and optimization studies, where an extremely rapid computational technique is needed precluding a detailed depletion analysis. Any final design analysis would normally employ a detailed fuel cycle analysis anyway, no matter how accurate the above scheme is shown to be.

## ACKNOWLEDGMENTS

The author gratefully acknowledges the significant contribution of Colin Durston of the Westinghouse Advanced Reactors Division, who provided much help in preparing the depletion analysis calculations, which used his revised version of the 2DB code. Numerous helpful discussions of the methods and results with both Colin Durston and M. W. Dyos of the Advanced Reactors Division are gratefully acknowledged.

This work was performed while the author was on academic leave of absence for one year at the Westinghouse Electric Corporation, Advanced Reactors Division, Madison, Pennsylvania 15663.

## REFERENCES

1. D. OKRENT, "Neutron Physics Considerations in Large Fast Reactors," *Power Reactor Technol.*, **1**, 107 (1964).

2. G. H. GOLDEN, "Elementary Neutronics Considerations in LMFBR Design," ANL-7532, Argonne National Laboratory (1969).

3. P. V. EVANS, Ed., "Appendix: Definitions of Fast Reactor Breeding and Inventory," *Proc. London Conf. Fast Breeder Reactors*, p. 947, Pergamon Press, New York (1967).

4. K. O. OTT, "An Improved Definition of the Breeding Ratio for Fast Reactors," *Trans. Am. Nucl. Soc.*, **12**, 719 (1969).

5. P. GOLDSCHMIDT, "Breeding Ratio for Fast Reactors," *Nucl. Appl. Technol.*, **9**, 450 (1970).

6. W. W. LITTLE, Jr. and R. W. HARDIE, "2DB User's Manual—Revision 1," BNWL-831, Rev. 1, Battelle Memorial Institute Pacific Northwest Laboratories (1969).

7. W. M. JACOBI, "Westinghouse Liquid Metal Fast Breeder Reactor Demonstration Plant Design," *Proc. Am. Power Conf.*, Chicago (April 1971).

8. I. I. BONDARENKO, Ed., *Group Constants for Nuclear Reactor Calculations*, Consultants Bureau Enterprises, Inc., New York (1964).

9. A. R. BAKER and A. D. HAMMOND, "Calculations for a Large Fast Reactor: A Comparison of Results Organized by the International Working Group on Fast Reactors of the International Atomic Energy Agency," TRG-2133(R), United Kingdom Atomic Energy Authority, Risley (1971).

# MODELS FOR THE SAFE STORAGE OF FISSILE METAL

REACTORS

**KEYWORDS:** *uranium, enrichment, plutonium-239, metals, storage, safety, criticality, numerical solutions, mockup, configuration, plutonium-240*

S. J. ALTSCHULER and C. L. SCHUSKE
*Dow Chemical U.S.A., Rocky Flats Division, P.O. Box 888*
*Golden, Colorado 80401*

Received August 4, 1971
Revised October 12, 1971

*Two models are described for calculating critically safe storage configurations for uranium (93.4% $^{235}U$) and plutonium (96% $^{239}Pu$, 4% $^{240}Pu$) metal. The first model deals with conventional arrays in air of fissile units surrounded by concrete walls. The model uses the concepts of surface density and unit surface-to-volume ratio to define safe-array parameters.*

*The second model makes use of thick internal moderators (i.e., water) enclosing each storage unit in an array. These arrays are also surrounded by concrete walls. The internal moderators partially isolate adjacent storage units from one another and thus, in some cases, permit extremely high surface densities and vault loading.*

*Several factors that influence the storage model are shape and density of the individual storage units and the degree of reflection of arrays of units.*

## INTRODUCTION

Methods are needed for determining critically safe storage arrays for fissile metal. The methods should be simple and applicable to the wide variety of unit shapes that occur in practice. The methods described approximately satisfy both requirements.

The first method involves correlating the surface density of the array, defined as the mass of fissile material per unit floor area, with the surface-to-volume ratio of the individual units in the array. Refer to the definitions of terms at the end of this report. The correlation of the surface density with surface-to-volume ratios dates to about 1957 from earlier work (unpublished) done by Schuske. Figure 1 contains the original experimental data. Since 1957, several authors have explored this method.[1-4] The current report significantly advances the previous work and provides guidance for use of the first method.

The second method makes use of water as an internal moderator to partially isolate adjacent units in the storage arrays. Much higher surface densities can be developed for storage structures of this type.

In addition to the discussion of the storage models and examples, a comparison is presented of the calculational method used in deriving these models with pertinent experimental arrays. A calculational study follows of the factors, such as unit shapes and densities and array reflection, that influence the storage models.

Because of the requirements for fire protection, the discussion relates also to effects on the neutron multiplication factor ($k_{eff}$) of water sprays.

## DESCRIPTION OF CALCULATIONS AND RESULTS

A series of KENO[5] calculations has been made to supplement the existent experimental data.[6-8] KENO is a multigroup Monte Carlo criticality code. The errors for the quoted $k_{eff}$s are $\sigma$ (one standard error) or

$$\sigma = \left[ \frac{\sum_{i=1}^{N} (k_{eff}^{i} - \bar{k}_{eff})^2}{N(N-1)} \right]^{1/2} ,$$

where

$$\bar{k}_{eff} = \frac{1}{N} \sum_{i=1}^{N} k_{eff}^{i} .$$

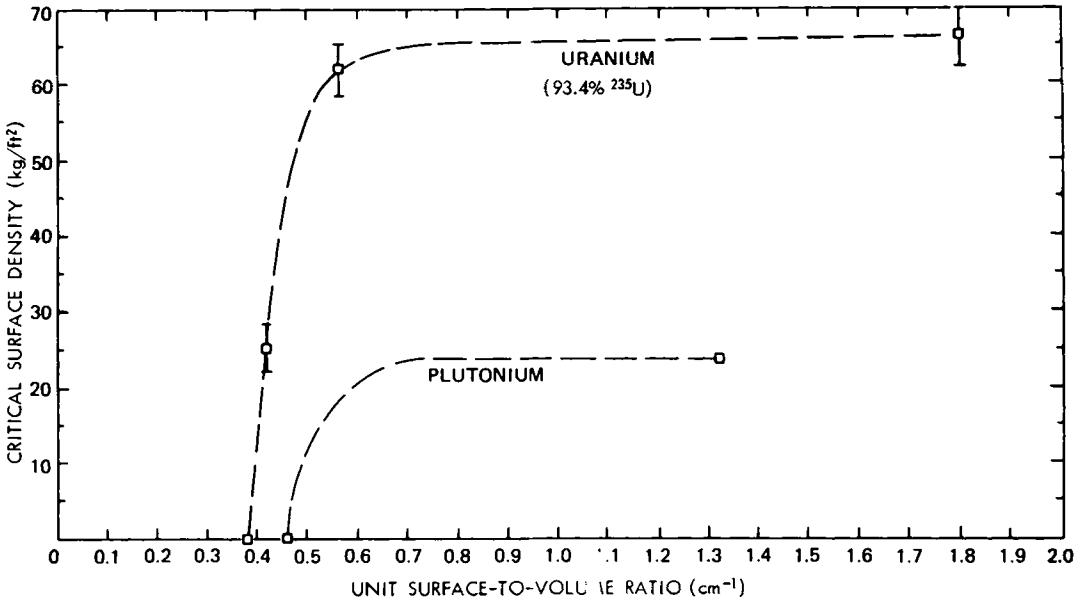


Fig. 1. Original experimental data of critical surface density and unit surface-to-volume ratio.

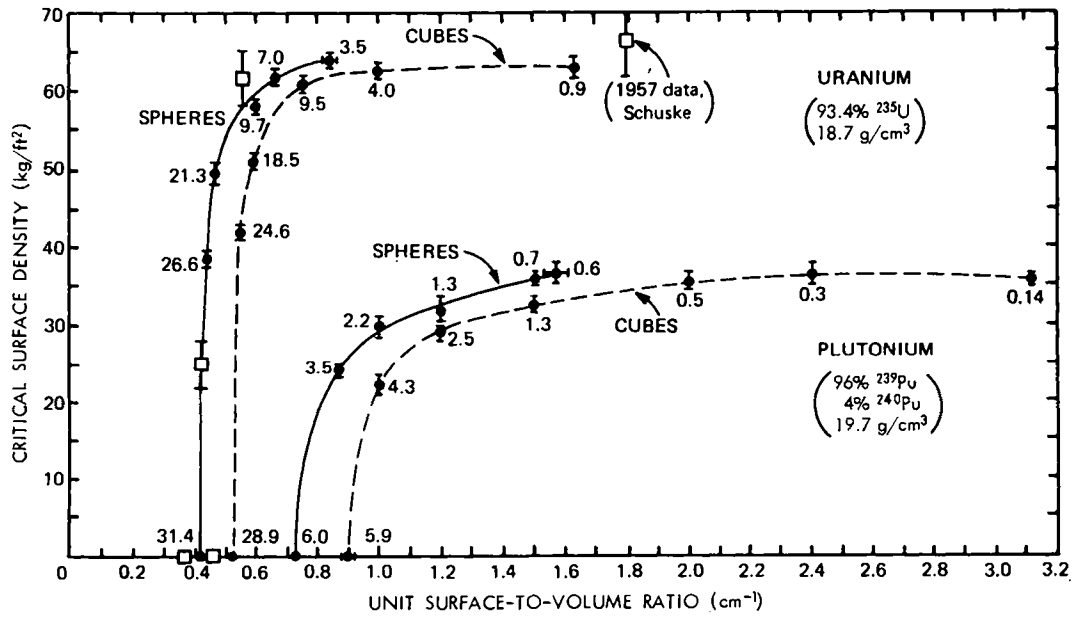


Fig. 2. Critical surface density and unit surface-to-volume ratio for a nearly infinite square lattice array on a concrete slab.

The cross sections used were the Hansen-Roach B sets,[9] with the exception of calcium and silicon which were obtained from Whitesides of Oak Ridge. All nuclides except hydrogen were treated as isotropic scatterers. The plutonium used in all calculations for the storage models was 96% $^{239}$Pu and 4% $^{240}$Pu with unit densities ranging from 4.43 to 19.7 g/cm$^3$. The enriched uranium was 93.4% $^{235}$U and 6.6% $^{238}$U with densities from 5.46 to 18.6 g/cm$^3$. The concrete composition used in these calculations was 02-A given in the handbook, *Reactor Physics Constants*.[10]

Calculational data are presented in five basic parts. The first part is a comparison between KENO results and experimental data. The comparisons are given in Table I and Figs. 1 and 2. The experimental data are critical, except for the 1957 data and that given in Ref. 7.

TABLE I

Comparison of Calculations with Experimental Results

| Number of Array Units | Description of Experiments | $k_{eff} \pm \sigma$ [c] | Reference |
|---|---|---|---|
| 3 × 3 × 3 | 3-kg plutonium metal units | 0.993 ± 0.009 | 6 |
| 4 × 4 × 4 | 3-kg plutonium metal units, 1.27-cm moderators | 0.988 ± 0.009 | |
| 4 × 4 × 4 | 3-kg plutonium metal units, 2.55-cm moderators | 1.019 ± 0.008 | |
| 4 × 4 × 6 | 2.03-kg plutonium metal units in steel cans on a large concrete slab | 0.999 ± 0.011 | 7 |
| 5 × 5 × 3 [a] | 2.03-kg plutonium metal units in steel cans on a large concrete slab | 0.973 ± 0.008 | |
| 5 × 5 × 4 [b] | 2.03-kg plutonium metal units in steel cans on a large concrete slab | 1.037 ± 0.010 | |
| 2 × 2 × 2 | ~21-kg uranium (93.2) cylinders in 0.635-cm Lucite box | 1.006 ± 0.010 | 8 |
| 2 × 2 × 2 | ~21-kg uranium (93.2) cylinders in 1.27-cm Lucite box | 0.990 ± 0.008 | |

[a]The system was subcritical at an approximate multiplication of 40.
[b]The KENO calculation was used to bracket the critical value; the experiment indicated that this assembly would be supercritical.
[c]Calculations based on ~11,000 neutron histories.

The second part of the calculational data shows how to develop the relationship between the critical surface density, $SD$, and the surface-to-volume ratio, $s/v$, of the individual arrayed units for several variables. These variables are the shape of a stored unit, the density of the unit, and the degree of reflection of an array of units. Concrete was used as the reflector in all cases. All curves can be represented by the following empirical relationship:

$$SD = SD_0 - a \exp\left\{-b\left[\left(\frac{s}{v}\right) - \left(\frac{s}{v}\right)_0\right]\right\}$$

$SD$ = critical surface density

$SD_0$ = surface density for an infinite slab

$\frac{s}{v}$ = surface-to-volume ratio of individual units

$a, b, \left(\frac{s}{v}\right)_0$ = constants.

The primary purpose for the curve fitting was to determine if all the curves were of the same form and to determine if any of the parameters could be simply calculated and had physical significance. The surface density, $SD_0$, is for an infinite slab of the fissile material and is independent of the fissile unit shape and density. It is dependent on the degree of reflection, for example, whether the array is bare, reflected on one surface, or on both surfaces. All other constants $[a, b, (s/v)_0]$ do not have simple physical significance.

The third part concerns the development of a safe-storage model for conventional arrays in air surrounded by concrete walls.

The fourth part concerns the development of a safe-storage model that assumes a water moderator which partially isolates one interacting storage unit from another.

The final part includes a discussion of special internally moderated systems, where the moderator is concrete or Plexiglas, and comparisons are made with the water-moderated systems.

## CALCULATIONAL RESULTS RELATING SURFACE DENSITY AND UNIT SURFACE-TO-VOLUME RATIO

### Bare Planar Arrays

Figure 3 shows the critical surface density versus individual unit surface-to-volume ratio curves for large arrays of uranium and plutonium bare spheres and cubes. Figure 4 shows this relationship for right circular cylinders with height-to-diameter ($H/D$) ratios of 2, 4, and 8.

The surface-to-volume ratio at zero surface density is that for a single critical unit. It is the largest single unit of academic interest and has the lowest surface-to-volume ratio. Since such a unit is critical by itself, the surface density is approximately zero when its mass is averaged over a near infinite area (vault floor).

The limiting maximum surface density, for large arrays, occurs for an infinite slab. All other critical surface densities, regardless of unit shape, are less than this value. For all units, the highest value of surface density occurs when the units touch. This accounts for the abrupt ending of the curves for spheres and not for cubes.

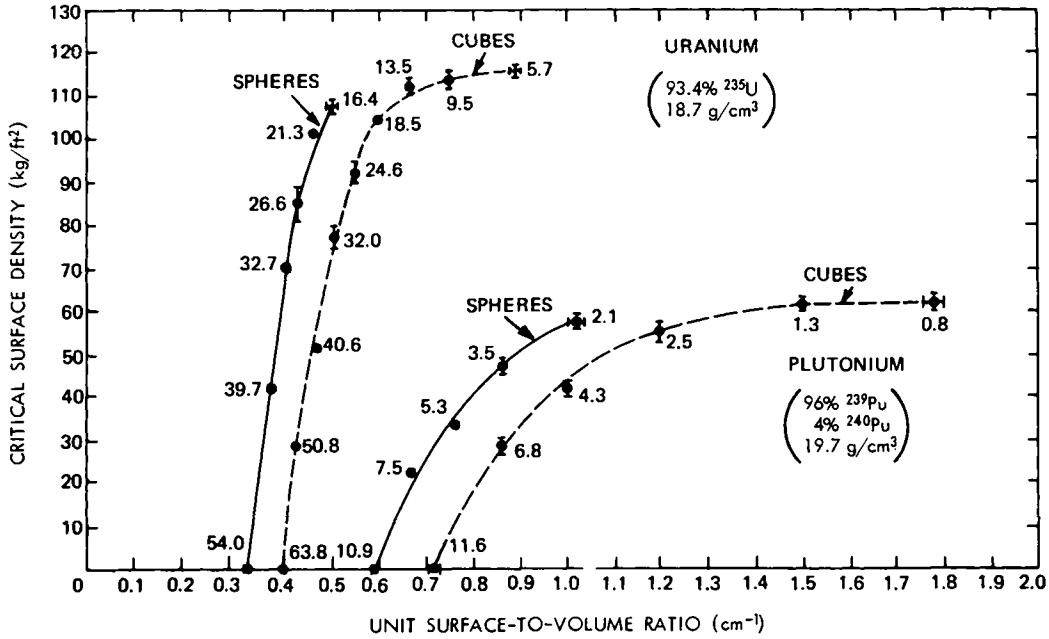


Fig. 3. Critical surface density and unit surface-to-volume ratio for unreflected, nearly infinite square lattice arrays (values on curves are weights of units in kilograms).

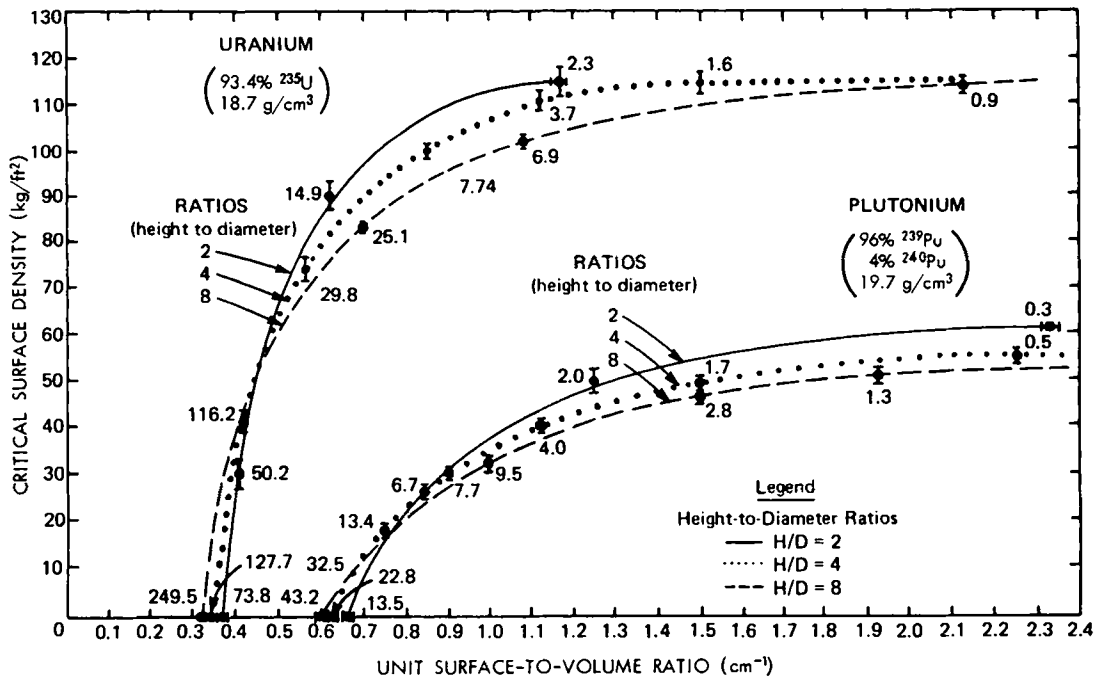


Fig. 4. Critical surface density and unit surface-to-volume ratio of unreflected, nearly infinite square lattice arrays of right circular cylinders.

#### Semireflected Planar Arrays

Figure 2 shows the surface density versus surface-to-volume ratio relationship for semireflected arrays of plutonium and uranium spheres and cubes. These arrays are placed on a 6-in. (15.24-cm) thick, 20- × 20-m concrete slab which, in this case, is much larger than the array itself.

Also plotted in Fig. 2 are the original points by Schuske (shown in Fig. 1). The agreement between the calculated and the experimental points for uranium pieces is good. The plutonium points were only estimates.

As the amount of reflection for each unit is increased, the size of a single critical unit will decrease. The curves will shift downward and to the right. Critical conditions will occur at lower surface densities and higher surface-to-volume ratios, i.e., smaller units separated by larger distances.

#### Sandwiched Planar Arrays

Figure 5 shows the critical surface density versus surface-to-volume ratio for cubes sandwiched between two 6-in.-thick concrete slabs. To minimize edge leakage, the arrays have been made large. Twenty meters was chosen as a large practical limit.

From Figs. 2, 3, and 5, it appears that the curves for uranium units, particularly cubes, tend to be flatter above the knee than those for plutonium.

#### The Effects of Reflection on Slab Thickness

This material was included as an observation that surface density ($SD_0$) is approximately a linear function (within $2\sigma$) of the degree of reflection for large arrays. Previous work[11] confirms this linear relationship.

Figure 6 gives the relationship between critical slab thickness and the number of slab sides reflected by concrete.

#### Planar Arrays in Storage Facilities

A third and the most common storage condition would be in a vault with walls, floor, and ceiling of concrete. This case is not realistically described by the semireflected or sandwiched arrays. Since the sandwiched case is an extreme one and gives conservative results, the vault size chosen was large, i.e., 20 ×20 ×3 m. The value was selected to obtain some contrast with the sandwiched case. The storage facility chosen is not so large as to be totally impractical. The critical surface density versus surface-to-volume ratio relationships for this storage facility are shown in Fig. 7, along with those for sandwiched cubes to allow comparison.

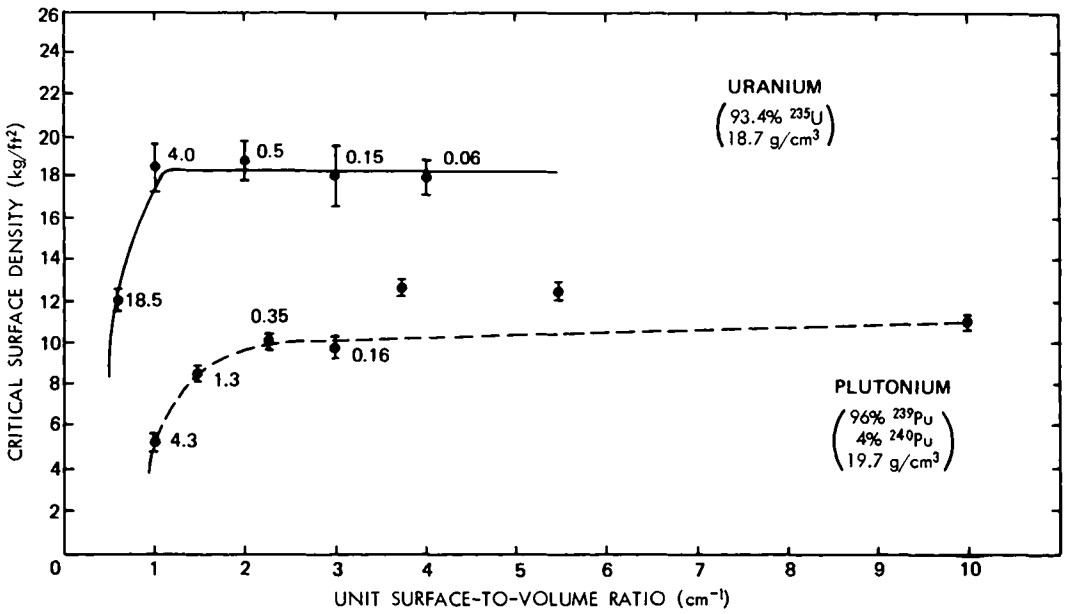


Fig. 5. Critical surface density and unit surface-to-volume ratio for a nearly infinite square lattice of cubes sandwiched between two concrete slabs.

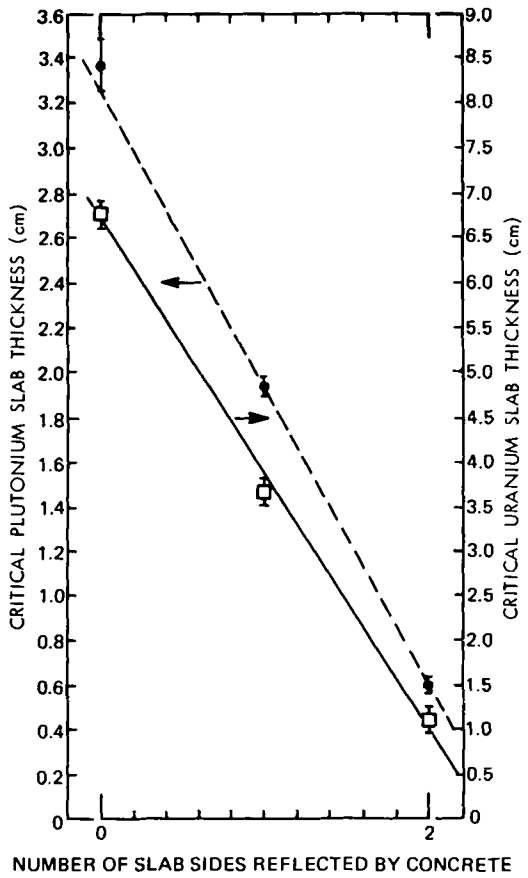


Fig. 6. Critical slab thickness and number of reflected sides.

A series of calculations was performed to gain insight on the effect of vault height on $k_{eff}$. A fixed floor loading was assumed for each of the three data values given in Fig. 8.

### Three-Dimensional Arrays in Vaults

A number of calculations were done to investigate the effect on $k_{eff}$ of redistributing spherical fissile units from a critical planar array on the vault floor into three-dimensional arrays. The systems investigated were 7- and 21-kg uranium spheres, 4.3-kg plutonium cubes, and 0.04-, 0.28-, 2.23-, 3.54-, and 5.28-kg plutonium spheres. In approximately cubic lattices, none of these systems was more reactive than when in a planar array on the floor of the vault.

The requirement for uniform spacing in three dimensions is not a stringent one, as shown in Table II. The lattice spacings for these arrays in the $z$ direction will differ from those in the $x$ or $y$ directions by as much as 20%, while $k_{eff}$ is essentially constant. Figures 9 and 10 show the variation of $k_{eff}$ with lattice spacing in the $z$ direction. Even when several units are stacked on each other, $k_{eff}$ does not exceed 1.08.

### Reduced Density

A series of calculations was performed on arrays of low density cubes. The data for the specific densities ($\rho$) are presented in Fig. 11.

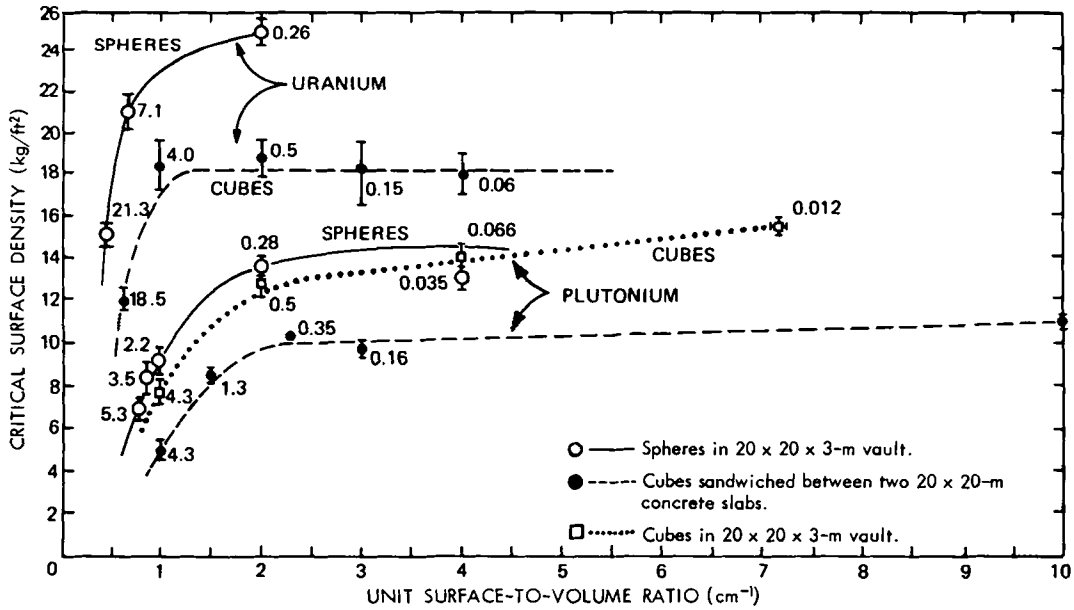


Fig. 7. Critical surface density and unit surface-to-volume ratio in square lattice arrays.

The curves have the typical shapes observed in previous sections.

### Water Sprinklers

Under current consideration is the installation of water sprinkler systems as a fire control method in fissile material handling facilities.

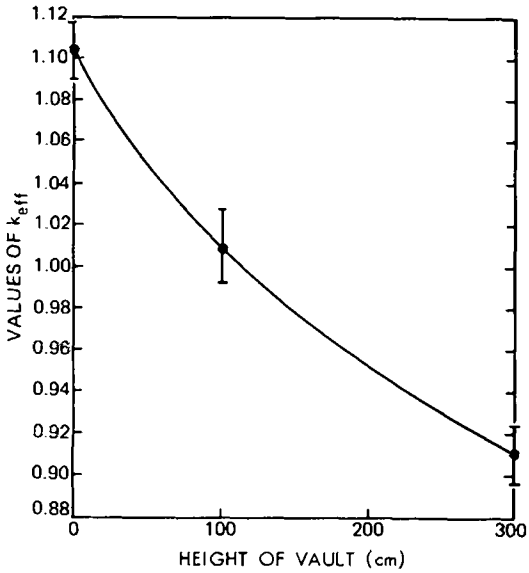


Fig. 8. Height of vault versus $k_{eff}$ values.

Calculations indicate that a sprinkler flow of 1 gal/(ft$^2$ min) has a negligible effect on an array reactivity. The flow rate is a factor of ~4 higher than for a standard sprinkler.[12]

### Variation of Multiplication Factor ($k_{eff}$) with Vault Size

Table III contains a brief study of $k_{eff}$ as a function of the internal vault dimensions. The surface densities have been held constant. It can be seen, as expected, that $k_{eff}$ decreases when dimensions are decreased from a 66.8- × 66.8- × 9.8-ft structure to a 10- × 10- × 10-ft structure.

## STORAGE MODEL FOR ARRAYS IN AIR

### Basic Assumptions

The graph of the critical surface density ($SD$) of an array versus the surface-to-volume ratio ($s/v$) of an individual fissile unit has a form independent of unit shapes, degree of reflection, or unit densities. This relationship is used to develop a safe-storage model, one for plutonium and one for enriched uranium, for a variety of unit shapes, masses, and densities. Five assumptions were used:

1. A concrete storage structure with internal dimensions of 66.8 × 66.8 × 9.8 ft with 1-ft-thick

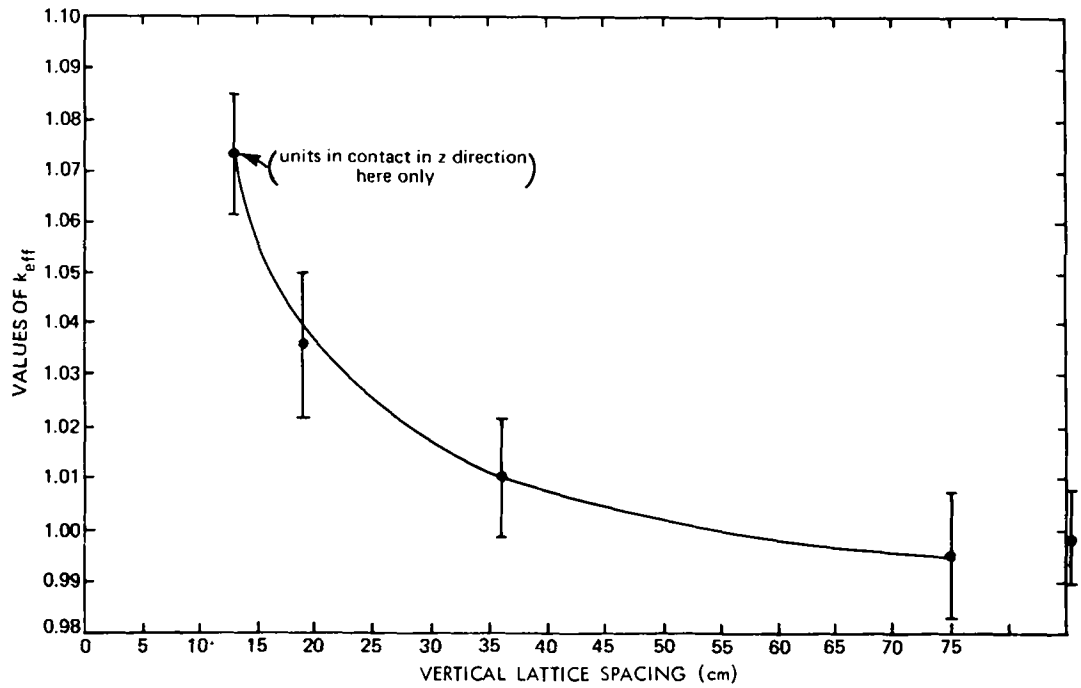


Fig. 9. Vertical lattice spacing versus $k_{eff}$ values.

concrete[13] walls was chosen as the maximum size that could be accommodated by the storage model. [Larger structures could be constructed using this model, if subdivided by an isolation thickness[14] of concrete (~1 ft) into individual adjacent structures no greater than 66.8 × 66.8 × 9.8 ft.] Any structure smaller than these dimensions would also be acceptable, provided that the height is not less than 9.8 ft. The height can be greater than 9.8 ft. See Table III for $k_{eff}$ as a function of vault size.

2. All containers or shelving must provide positive protection against double batching. If this cannot be accomplished, reduce masses accordingly.

3. Sprinkling of storage facility with water is permitted provided the flow rate does not exceed 1 gal/(ft$^2$ min). If more water is needed, verification calculations would be needed.

4. Finely divided or compressed metal turnings must be protected against internal moderation because of sprinkler action or other water sources.

5. All storage configurations permitted by the model are far subcritical ($k_{eff} + 4\sigma \leq 0.90$).

### Rules Defining the Model

1. Maximum individual cube, sphere, or equilateral cylinder masses permitted for full density are 22.0 kg for enriched uranium and 5.0 kg for plutonium.

2. The maximum permissible masses of single cubes, spheres, or equilateral cylinders of re-

TABLE II

Variation of $k_{eff}$ with Distance between Units

| Array Size in Storage Units | Unit Radius ($R$) (cm) | Unit Mass ($M$) (kg) | Lattice Spacing ($l_x = l_y$) ($l_z$) (cm) | | $k_{eff} \pm \sigma$ | Notes and Comments | Identifying Figure |
|---|---|---|---|---|---|---|---|
| **Uranium (93.4) Metal Spheres:** | | | | | | | |
| 56 × 56 × 1 | 6.50 | 21.28 | 36.36 | – | 0.999 ± 0.009 | Spheres in a plane array on floor of vault | Plotted as Fig. 9 |
| 28 × 28 × 4 | | | 72.72 | 75.0 | 0.995 ± 0.012 | Spheres evenly spaced | |
| | | | | 36.4 | 1.010 ± 0.012 | | |
| | | | | 19.0 | 1.036 ± 0.014 | | |
| | | | | 13.0 | 1.073 ± 0.012 | Spheres in contact | |
| 116 × 116 × 1 | 4.50 | 7.06 | 17.55 | – | 1.005 ± 0.009 | Spheres in a plane array on floor of vault | Plotted as Fig. 10 |
| 41 × 41 × 8 | | | 49.66 | 37.5 | 0.989 ± 0.013 | Spheres evenly spaced | |
| 44 × 44 × 7 | | | 46.28 | 42.9 | 1.000 ± 0.010 | Spheres evenly spaced | |
| 48 × 48 × 6 | | | 42.42 | 50.0 | 0.984 ± 0.015 | Spheres evenly spaced | |
| | | | 42.42 | 19.0 | 1.020 ± 0.015 | | |
| | | | 42.42 | 9.0 | 1.065 ± 0.015 | Spheres in contact | |
| **Plutonium Metal Spheres and Cubes:** | | | | | | | |
| 1252 × 1252 × 1 | 0.75 | 0.0348 | 1.60 | – | 0.982 ± 0.014 | Spheres | None for Plutonium |
| 223 × 223 × 33 | 0.75 | 0.0348 | 8.98 | 9.09 | 0.962 ± 0.016 | | |
| 455 × 455 × 1 | 1.5 | 0.278 | 4.40 | – | 1.003 ± 0.013 | | |
| 102 × 102 × 20 | 1.5 | 0.278 | 19.64 | 15.0 | 1.014 ± 0.015 | | |
| 133 × 133 × 1 | 3.0 | 2.228 | 15.0 | – | 0.999 ± 0.011 | | |
| 50 × 50 × 8 | 3.0 | 2.228 | 40.00 | 37.5 | 1.000 ± 0.014 | | |
| 102 × 102 × 1 | 3.5 | 3.54 | 19.64 | – | 1.015 ± 0.016 | | |
| 42 × 42 × 6 | 3.5 | 3.54 | 47.40 | 50.0 | 1.009 ± 0.014 | | |
| 77 × 77 × 1 | 4.0 | 5.28 | 26.0 | – | 1.018 ± 0.017 | | |
| 34 × 34 × 5 | 4.0 | 5.28 | 58.9 | 60.0 | 1.017 ± 0.010 | | |
| 87 × 87 × 1 | 6.0 | 4.26 | 23.0 | – | 0.988 ± 0.013 | Cubes | |
| 36 × 36 × 6 | 6.0 | 4.26 | 55.66 | 50.0 | 0.977 ± 0.018 | Cubes | |

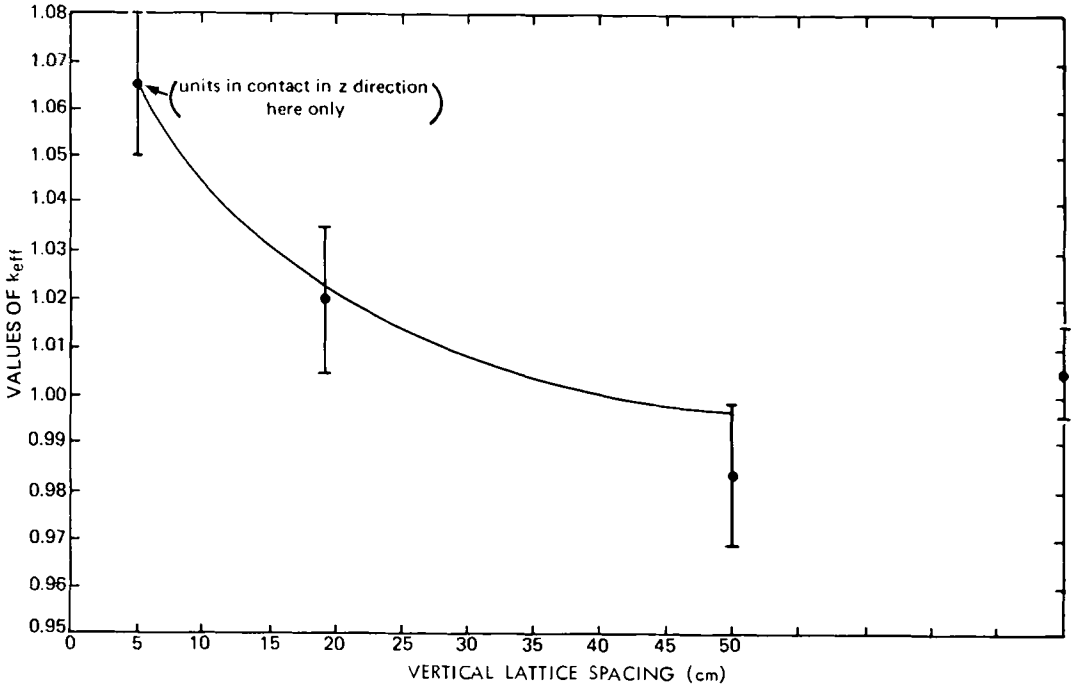


Fig. 10. Vertical lattice spacing versus $k_{eff}$ values.

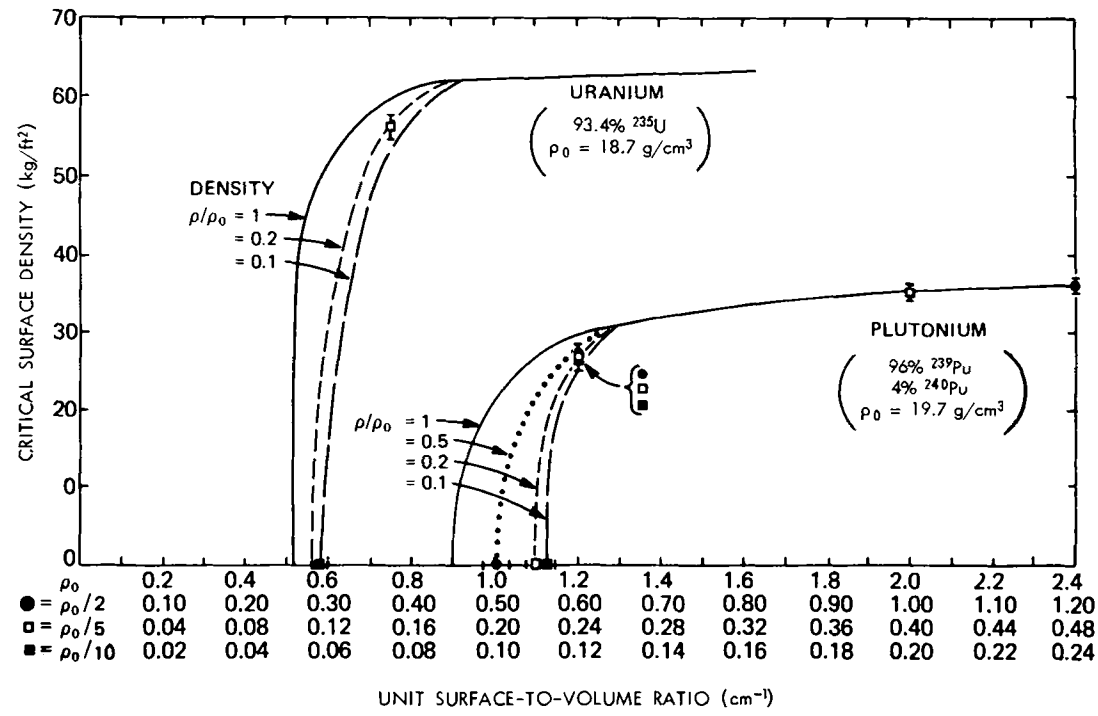


Fig. 11. Effect of varying the density of units on the relationship between critical surface density and surface-to-volume ratio of nearly infinite square lattice arrays on a concrete slab.

TABLE III

Variation of $k_{eff}$ with Vault Size. (All vaults have 1-ft-thick concrete walls.)

| Unit Diameter ($D$) (cm) | Unit Height ($H$) (cm) | Unit Mass ($M$) (kg) | Surface Density ($SD$) (kg/ft$^2$) | Inside Vault Dimensions (ft) | $k_{eff} \pm \sigma$ |
|---|---|---|---|---|---|
| **Plutonium Metal:** | | | | | |
| 12.0 | 3.15 | 7.02 | 2.04 | 66.8 X 66.8 X 9.8 | 0.873 ± 0.009 |
| | | | | 16.7 X 16.7 X 9.8 | 0.851 ± 0.008 |
| | | | | 9.3 X 9.3 X 9.8 | 0.848 ± 0.007 |
| 7.05 | 6.5 | 5.00 | 1.01 | 66.8 X 66.8 X 9.8 | 0.842 ± 0.011 |
| | | | | 17.8 X 17.8 X 9.8 | 0.857 ± 0.010 |
| | | | | 8.9 X 8.9 X 9.8 | 0.842 ± 0.007 |
| 4.8 | 19.0 | 6.77 | 2.55 | 66.8 X 66.8 X 9.8 | 0.853 ± 0.010 |
| | | | | 9.8 X 9.8 X 9.8 | 0.770 ± 0.011 |
| **Uranium (93.4) Metal:** | | | | | |
| 38.0 | 3.104 | 65.13 | 6.44 | 66.8 X 66.8 X 9.8 | 0.845 ± 0.012 |
| | | | | 19.1 X 19.1 X 9.8 | 0.814 ± 0.008 |
| 12.3 | 11.3 | 24.8 | 3.20 | 66.8 X 66.8 X 9.8 | 0.867 ± 0.010 |
| | | | | 16.7 X 16.7 X 9.8 | 0.859 ± 0.009 |
| | | | | 11.1 X 11.1 X 9.8 | 0.846 ± 0.011 |
| 7.818 | 46.0 | 40.9 | 2.97 | 66.8 X 66.8 X 9.8 | 0.747 ± 0.010 |
| | | | | 11.1 X 11.1 X 9.8 | 0.690 ± 0.008 |

duced density are given in Fig. 12 and discussed as item 1, following the rules (see Table IV also).

3. Any single storage unit must be subcritical when fully water-flooded. For guidance, use Eqs. (1) and (2) in item 2 following the rules.

4. Maximum individual masses permitted, regardless of density, are 65 kg for enriched uranium and 30 kg for plutonium.

5. Any enriched uranium mass that exceeds 40.0 kg must not exceed a surface density of 6.0 kg/ft$^2$ in a storage array. Any plutonium unit mass that exceeds 15.0 kg must not exceed a surface density of 3.0 kg/ft$^2$ in a storage array.

6. Spacing of storage positions for individual units must be selected in such a manner as to distribute units nearly uniformly throughout the structure. See Table II for guidance. A 20% deviation in vertical spacing from uniform spacing is permissible.

7. Plutonium and enriched uranium can be stored in the same structure, provided that the different materials are approximately alternately mixed.[15]

8. Aisles and material transfer routes must be subtracted from the total floor area on which material can be stored because these aisles will also contain material during transfer. Total vault capacity can be maximized by minimizing aisle area.

The aisle correction is done as follows:

Step 1: Assume that all aisles extend from floor to ceiling. Calculate the volume occupied by aisles.

Step 2: Assume all storage units permitted by the model are uniformly distributed about the total vault volume.

Step 3: Subtract the number of units occupied by the aisle volume, step 1, from the total number in step 2.

9. Units of different shapes and masses can be stored in the same structure provided that the safe surface densities are observed for each individual unit. This is more easily accomplished if sections of the structure are set aside for similar masses and shapes rather than randomly storing the units. The rule is based on the concepts of coupled reactors.[16-18]

10. Figure 13 and Table V can be used to calculate safe-storage configurations ($k_{eff} + 4\sigma \leq 0.90$) provided that rules 1 through 9 are used.

#### Item 1. Reduced Density

The data on reduced density units required for application of rule 2 of the model are provided in

TABLE IV

Vault Calculations for Reduced Density

| Array Size in Storage Unit | Unit Diameter ($D$) (cm) | Unit Height ($H$) (cm) | Unit Mass ($M$) (kg) | Density Ratio ($\rho/\rho_0$) | Surface Density ($SD$) (kg/ft$^2$) | $k_{eff} \pm \sigma$ | ($k_{eff} + 4\sigma$) | Notes |
|---|---|---|---|---|---|---|---|---|
| 30 X 30 X 1 | 7.05 | 6.5 | 5.00 | 1.00 | 1.01 | 0.842 ± 0.011 | 0.886 | Plutonium[a] |
| 67 X 67 X 1 | 9.07 | 8.38 | 5.00 | 0.4686 | 5.03 | 0.823 ± 0.013 | 0.875 | Plutonium[a] |
| 25 X 25 X 1 | 11.8 | 10.87 | 21.99 | 1.00 | 3.08 | 0.833 ± 0.010 | 0.873 | Uranium[a] |
| 45 X 45 X 1 | 14.12 | 13.04 | 21.99 | 0.5822 | 9.98 | 0.840 ± 0.013 | 0.892 | Uranium[a] |
| 30 X 30 X 1 | 7.05 | 6.5 | 5.00 | 1.00 | 1.01 | 0.842 ± 0.011 | 0.886 | Plutonium[a] |
| 11 X 11 X 1 | 22.56 | 20.8 | 36.85 | 0.225 | 1.00 | 0.689 ± 0.009 | 0.725 | Plutonium[b] |
| 19 X 19 X 1 | 22.56 | 20.8 | 36.85 | 0.225 | 2.98 | 0.779 ± 0.012 | 0.827 | Plutonium[b] |
| 25 X 25 X 1 | 22.56 | 20.8 | 36.85 | 0.225 | 5.17 | 0.878 ± 0.014 | 0.934 | Plutonium[b,c] |
| 25 X 25 X 1 | 11.8 | 10.87 | 21.99 | 1.00 | 3.08 | 0.833 ± 0.010 | 0.873 | Uranium[a] |
| 11 X 11 X 1 | 30.2 | 27.83 | 108.80 | 0.295 | 2.95 | 0.727 ± 0.011 | 0.814 | Uranium[b] |
| 20 X 20 X 1 | 30.2 | 27.83 | 108.80 | 0.295 | 9.75 | 0.863 ± 0.010 | 0.903 | Uranium[b,c] |
| 21 X 21 X 1 | 38.0 | 3.104 | 65.13 | 1.00 | 6.44 | 0.845 ± 0.012 | 0.893 | Uranium[b] |
| 12 X 12 X 1 | 76.0 | 6.208 | 216.22 | 0.415 | 6.98 | 0.842 ± 0.010 | 0.882 | Uranium[b] |

$\frac{d_M}{M_0} = \left(\frac{\rho}{\rho_0}\right)^{4/3}$

[a]Complies with rules of model.
[b]Not acceptable according to model; violates rule 3.
[c]Not acceptable according to model; does not meet rule 4, surface density is too high.
The calculations for b and c were to gain insight on the latitude of safe values of $k_{eff}$ permitted by the model.
[d]The equation gives the relationship of maximum mass ($M_0$) to density ($\rho_0$) of a single unit to other unit masses and densities.

Fig. 12. A test of Fig. 12 has been made and reported in Table IV.

*Caution*: Some common sense is also required in applying data in the figure. The density correction applies to a uniform density change, not a change brought about by averaging out, for example, a hole drilled in a unit.

### Item 2. Safe Individual Storage Units with Full Water Reflection

The lower limit for surface-to-volume ratio is set by the requirement that a single unit be safe when water reflected. In the works by Gwin and Mee[19] and by Goodwin and Schuske[20] equations are given of hyperbolas for critical cylinders of uranium and plutonium metal reflected by hydrogenous material. For the current report, these equations have been modified by reducing their asymptotes. The critical diameter of an infinitely long cylinder was decreased 10%. The critical thickness of an infinite diameter cylinder was decreased 15%. The remaining constant was then adjusted to correspond to a cylinder of optimum height-to-diameter ratio whose mass was about 15% lower than the critical value. The plutonium equation was also adjusted for the difference in density between those reported by Goodwin and Schuske to high density.

TABLE V

Specifications for Model

| Fissile Material | Range of Surface-to-Volume Ratio ($s/v$) (cm$^{-1}$) | Safe Surface Density ($SD$) (kg/ft$^2$) |
|---|---|---|
| Uranium (93.4) (18.7 g/cm$^3$) | 0.000 to 0.487 | 0.0 |
| | 0.488 to 0.649 | 3.0 |
| | 0.650 to 0.749 | 6.0 |
| | >0.750 | 10.0 |
| Plutonium (96.0) (19.7 g/cm$^3$) | 0.000 to 0.822 | 0.0 |
| | 0.823 to 0.969 | 1.0 |
| | 0.970 to 1.099 | 2.0 |
| | 1.100 to 1.449 | 3.0 |
| | >1.450 | 5.0 |

The resulting equations are:

1. $(D - 3.623)(H - 0.433) = 20.80$ for plutonium
2. $(D - 6.606)(H - 1.564) = 48.35$ for enriched uranium,

where $H$ and $D$ are the height and diameter of the cylinder in centimeters.

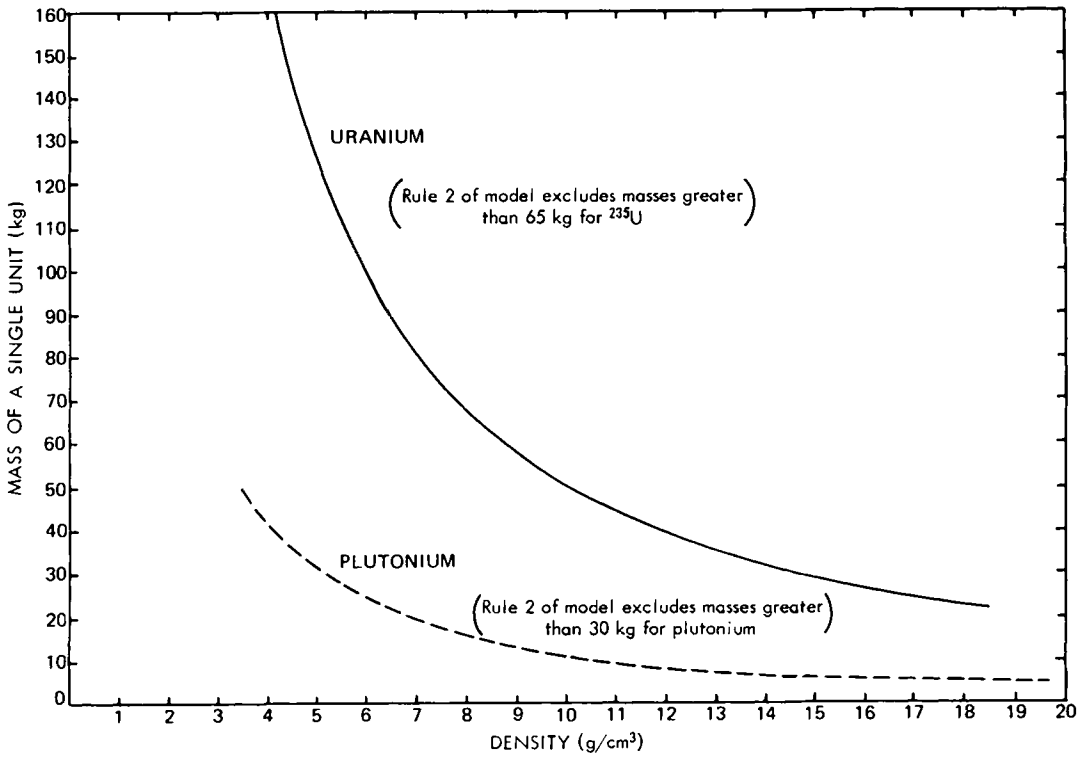


Fig. 12. Relationship between the mass of a single unit and the density assuming an inverse power law of 4/3.

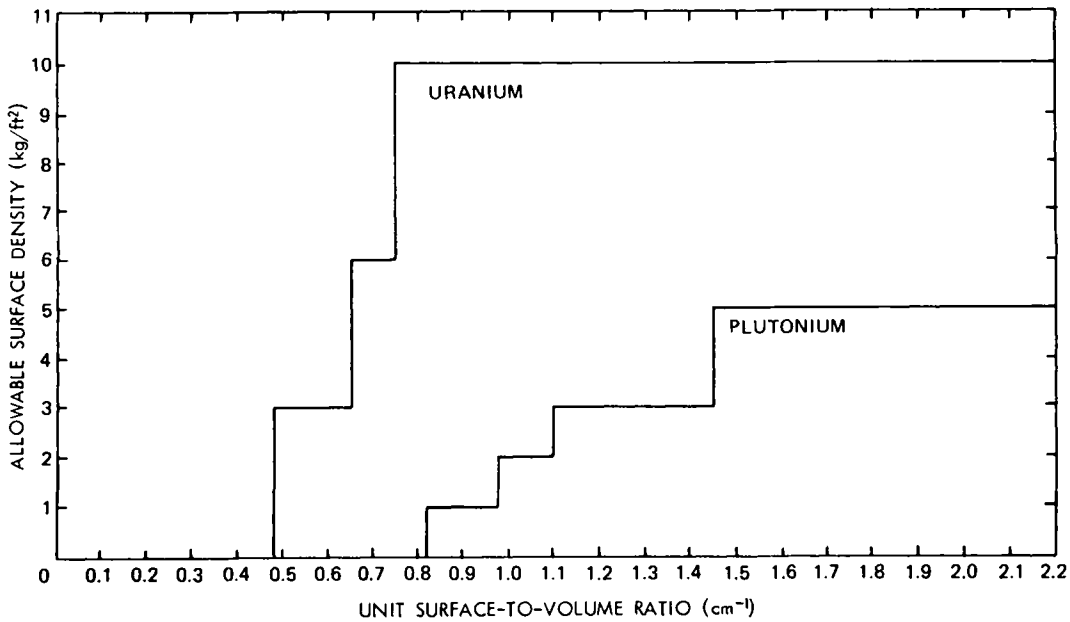


Fig. 13. Permissible values from model for arrays in air.

### Calculational Verification of the Model

Most of the test data presented in Table V represent cases where unit dimensions, mass, and surface density are in excess of those permitted by the model.

The test data provide a designer with knowledge of the safety factors involved in the model, as well as suggest some latitude for storage facility design. All cases tested are subcritical ($k_{eff} < 0.95$). Any specific data in Table VI where $k_{eff} + 4\sigma \leq 0.90$ can be used for design considerations.

TABLE VI

Results of Calculations to Test Model

| Array Size in Storage Units | Unit Diameter ($D$) (cm) | Unit Height ($H$) (cm) | Unit Mass ($M$) (kg) | Surface-to-Volume Ratio ($s/v$) ($cm^{-1}$) | Surface Density ($SD$) ($kg/ft^2$) | | Multiplication Factor ($k_{eff} \pm \sigma$) | $k_{eff} + 4\sigma$ | Comments |
|---|---|---|---|---|---|---|---|---|---|
| | | | | | Permitted by Model | of Actual Array | | | |
| **Plutonium Metal** | | | | | | | | | |
| 30 X 30 X 1 | 7.05 | 6.5 | 5.00 | 0.875 | 1.0 | 1.01 | 0.842 ± 0.011 | 0.886 | Permitted |
| 29 X 29 X 1[b] | 7.2 | 6.6 | 5.29 | 0.859 | 1.0 | 1.00 | 0.868 ± 0.012 | 0.916 | Not permitted |
| 36 X 36 X 1[b] | 7.2 | 6.6 | 5.29 | 0.859 | 1.0 | 1.54 | 0.901 ± 0.010 | 0.941 | Not permitted |
| 54 X 54 X 1 | 6.626 | – | 3.00 | 0.905 | 1.0 | 1.96 | 0.767 ± 0.007 | 0.794 | Safe but not permitted[a] |
| 45 X 45 X 1 | 7.584 | – | 4.50 | 0.7911 | 1.0 | 2.00 | 0.895 ± 0.013 | 0.947 | Not permitted |
| 41 X 41 X 1 | 4.8 | 19.0 | 6.77 | 0.939 | 1.0 | 2.55 | 0.853 ± 0.010 | 0.893 | Safe but not permitted |
| 36 X 36 X 1 | 12.0 | 3.15 | 7.02 | 0.968 | 2.0 | 2.04 | 0.873 ± 0.009 | 0.909 | Not permitted |
| 36 X 36 X 1 | 12.0 | 3.25 | 7.24 | 0.948 | 2.0 | 2.04 | 0.889 ± 0.012 | 0.937 | Not permitted |
| 40 X 40 X 1 | 15.0 | 2.4 | 8.36 | 1.100 | 3.0 | 3.00 | 0.862 ± 0.010 | 0.902 | Not permitted |
| 44 X 44 X 1 | 20.0 | 1.83 | 11.36 | 1.29 | 3.0 | 4.93 | 0.888 ± 0.010 | 0.928 | Not permitted |
| 43 X 43 X 1 | 21.5 | 1.717 | 13.28 | 1.350 | 3.0 | 5.50 | 0.882 ± 0.008 | 0.914 | Not permitted |
| 63 X 63 X 1 slab | 21.2 X 21.2 | 1.016 | 9.00 | 2.157 | 5.0 | 8.00 | 0.936 ± 0.016 | 1.000 | Not permitted |
| 36 X 36 X 10 | 4.5 | cube | 1.80 | 1.333 | 3.0 | 5.21 | 0.868 ± 0.015 | 0.928 | Not permitted |
| 41 X 41 X 1 | 24.0 | 1.50 | 13.34 | 1.498 | 5.0 | 5.02 | 0.875 ± 0.010 | 0.915 | Not permitted |
| 34 X 34 X 1[b] | 32.0 | 1.2 | 19.01 | 1.792 | 3.0 | 4.92 | 0.827 ± 0.011 | 0.871 | Safe but not permitted[a] |
| 39 X 39 X 1[b] | 32.0 | 1.2 | 19.01 | 1.792 | 3.0 | 6.48 | 0.891 ± 0.013 | 0.943 | Not permitted |
| 25 X 25 X 1 | 52.0 | 0.863 | 36.11 | 2.394 | 5.0 | 5.06 | 0.813 ± 0.016 | 0.877 | Safe but not permitted[a] |
| **Uranium (93.4) Metal** | | | | | | | | | |
| 25 X 25 X 1 | 11.8 | 10.87 | 21.99 | 0.523 | 3.0 | 3.08 | 0.833 ± 0.010 | 0.873 | Permitted |
| 24 X 24 X 1[b] | 12.3 | 11.3 | 24.8 | 0.502 | 3.0 | 3.20 | 0.867 ± 0.010 | 0.907 | Not permitted |
| 27 X 27 X 1[b] | 12.3 | 11.3 | 24.8 | 0.502 | 3.0 | 4.06 | 0.886 ± 0.009 | 0.922 | Not permitted |
| 18 X 18 X 1 | 7.818 | 46.0 | 40.9 | 0.555 | 3.0 | 2.97 | 0.747 ± 0.010 | 0.787 | Permitted |
| 26 X 26 X 1[c] | 26.5 | 4.0 | 40.81 | 0.651 | 6.0 | 6.18 | 0.862 ± 0.011 | 0.906 | Not permitted |
| 13 X 13 X 4[c] | 26.5 | 4.0 | 40.81 | 0.651 | 6.0 | 6.18 | 0.841 ± 0.012 | 0.889 | Safe but not permitted |
| 22 X 22 X 1 | 32.0 | 3.773 | 56.5 | 0.655 | 6.0 | 6.13 | 0.882 ± 0.008 | 0.914 | Not permitted |
| 22 X 22 X 1[b] | 32.0 | 3.8 | 56.54 | 0.651 | 6.0 | 6.13 | 0.897 ± 0.009 | 0.933 | Not permitted |
| 24 X 24 X 1[b] | 32.0 | 3.8 | 56.54 | 0.651 | 6.0 | 7.30 | 0.910 ± 0.010 | 0.950 | Not permitted |
| 28 X 28 X 1[b] | 32.0 | 3.8 | 56.54 | 0.651 | 6.0 | 9.93 | 0.948 ± 0.011 | 0.992 | Not permitted |
| 21 X 21 X 1 | 34.0 | 3.62 | 60.78 | 0.670 | 6.0 | 6.01 | 0.879 ± 0.013 | 0.931 | Not permitted |
| 21 X 21 X 1[b,c] | 38.0 | 3.104 | 65.13 | 0.750 | 6.0 | 6.44 | 0.845 ± 0.012 | 0.893 | Safe but not permitted |
| 12 X 12 X 3[c] | 38.0 | 3.104 | 65.13 | 0.750 | 6.0 | 6.30 | 0.805 ± 0.010 | 0.845 | Safe but not permitted |
| 26 X 26 X 1[b] | 38.0 | 3.104 | 65.13 | 0.750 | 6.0 | 9.87 | 0.903 ± 0.009 | 0.939 | Not permitted |
| 17 X 17 X 1[b,c] | 46.0 | 3.02 | 92.9 | 0.749 | 6.0 | 6.02 | 0.870 ± 0.010 | 0.910 | Not permitted |
| 12 X 12 X 2[c] | 46.0 | 3.02 | 92.9 | 0.749 | 6.0 | 6.00 | 0.869 ± 0.010 | 0.909 | Not permitted |
| 22 X 22 X 1[b] | 46.0 | 3.02 | 92.9 | 0.749 | 6.0 | 10.07 | 0.927 ± 0.012 | 0.975 | Not permitted |

[a] *Safe but not permitted* indicates that this system is not permitted by the model but does comply with $k_{eff} \pm 4\sigma \leq 0.90$.
[b] Shows effect of varying surface density.
[c] Shows effect of rearranging units.

Vault is 12-in. thick concrete, 66.8 × 66.8 × 9.8-ft inside dimensions.

#### Example 1. Two-Layer Array of Annular Cylinders

The unit is an annular cylinder of plutonium ($\rho$ = 15.6 g/cm$^3$) with dimensions $R_1$ = 2 cm, $R_2$ = 4 cm, $H$ = 10.2 cm (mass = ~6 kg). Find the horizontal center-to-center spacing for a two-layer array of these units.

$$s = 2\pi R_2^2 + 2\pi R_2 H = 356.88 \text{ cm}^2$$

$$v = \pi(R_2^2 - R_1^2) H \times \frac{\rho}{\rho_{max}} = 304.50 \text{ cm}^2$$

$$\frac{s}{v} = 1.17 \text{ cm}^{-1}, \text{ safe } SD = 3 \text{ kg/ft}^2$$

$R_1$ = inside radius of annular cylinder

$R_2$ = outside radius of cylinder

$\rho$ = density of plutonium

$H$ = height of cylinder.

Therefore, 12 kg (two 6-kg units) require 4 ft$^2$ of area, or 2-ft centers are required for an array 2 layers high.

The KENO calculation gave $k_{eff} \pm \sigma$ = 0.761 ± 0.012 for ~11,000 histories.

## STORAGE MODEL FOR ARRAYS IN WATER

Greatly increased storage densities and resulting economies can be achieved if moderators are used inside the vault to decrease interaction between the individual units. The model described here makes use of water as the moderator.

### Basic Assumptions

Each plutonium storage unit is placed in a bucket which has a 7.5-in. inner diameter and 10-in. inner height. Each bucket is surrounded by a water jacket 3 in. thick. The enriched uranium containers have 10-in. inner diameter ($D$) and 13.5-in. inner height ($H$) and are surrounded by 3 in. of water. All array calculations were based on an in-contact 20 × 20 × 20 array of these containers.

All arrays are surrounded by 12-in.-thick concrete walls.

### Rules

1. A storage unit is to be subcritical when fully water reflected.

2. The following equations may be used for guidance. Other shaped units must follow rule 1.

For uranium:

$$(D - 6.24)(H - 1.47) = 41.8 \ .$$

For plutonium:

$$(D - 3.42)(H - 0.40) = 17.6 \ .$$

3. All containers must provide positive protection against double batching.

4. Low density fissile materials, such as metal turnings, etc., must be protected against internal moderation by sprinklers or other sources of water.

5. A means of assuring that the water jackets are full is required. (Jelled water should be used to minimize loss of water in jackets from possible small leaks.)

6. Water sprinklers may be used to control fires.

### Calculational Verification of Storage Model for Arrays in Water

Table VII contains a calculational verification of arrays of several units taken from the equations in rule 2, assuming a 20 × 20 × 20 array of these units. One foot of concrete surrounded the arrays.

Larger unit shapes, such as tall thin cylinders or thin slabs, could be stored in this manner if the inside dimensions of the buckets were increased proportionally.

#### Example 1. A Cubic Array in Contact

This example makes use of the annular cylinder unit used previously, i.e., plutonium metal ($\rho$ = 15.6 g/cm$^3$) with dimensions $R_1$ = 2 cm, $R_2$ = 4 cm, $H$ = 10.2 cm (mass ~6 kg). A unit was placed upright on the bottom of a 7.5-in. inside diameter, 10-in. inside height, and 3-in.-thick bucket of water. The walls of the bucket were 0.063-in. iron, inside and out. The bucket had a top of similar material and thickness. The covered buckets were then placed in contact with each other in a 20 × 20 × 20 array, which was in turn enclosed by 12 in. of concrete.

A KENO calculation for this case gave a $k_{eff} \pm \sigma$ = 0.762 ± 0.012 for ~11,000 histories. The $k_{eff} \pm \sigma$ = 0.860 ± 0.011 for a single water flooded unit.

## SPECIAL STORAGE ARRAYS USING INTERNAL MODERATORS

Plexiglas, concrete, and water are used as internal moderators. These cases are not arrived at by the previous two models, but are presented

TABLE VII

Verification of Model for Units in Water-Jacketed Buckets
(The 20 × 20 × 20 array is enclosed by a 12-in.-thick concrete vault.)

| Material | Unit Diameter ($D$) (cm) | Unit Height ($H$) (cm) | Unit Mass ($M$) (kg) | $k_{eff} \pm \sigma$ | $k_{eff} + 4\sigma$ | Notes |
|---|---|---|---|---|---|---|
| Plutonium | 18.732 | 1.81 | 9.83 | 0.853 ± 0.009 | 0.889 | Safe but not permitted |
| | 18.732 | 1.555 | 8.44 | 0.814 ± 0.009 | 0.850 | Permitted |
| | 4.51 | 24.24 | 7.94 | 0.812 ± 0.009 | 0.848 | Safe but not permitted |
| | 7.046 | 6.509 | 5.00 | 0.883 ± 0.009 | 0.919 | Not permitted |
| | 6.54 | 6.042 | 4.00 | 0.803 ± 0.008 | 0.835 | Permitted |
| Uranium | 11.8 | 10.87 | 21.99 | 0.876 ± 0.008 | 0.904 | Safe but not permitted |
| | 11.03 | 10.19 | 18.01 | 0.831 ± 0.009 | 0.867 | Permitted |
| | 25.08 | 4.18 | 38.20 | 0.907 ± 0.009 | 0.943 | Not permitted |
| | 25.08 | 3.689 | 33.72 | 0.886 ± 0.008 | 0.918 | Permitted |
| | 8.11 | 33.71 | 32.22 | 0.838 ± 0.008 | 0.870 | Safe but not permitted |

Note: Jacket is 3-in.-thick water, 0.063-clad iron inside and out.
Plutonium bucket is 7.5-in. inside diameter and 10-in. inside height.
Uranium bucket is 10-in. inside diameter and 13.5-in. inside height.

TABLE VIII

Plutonium Units in Plexiglas Buckets

| Array Size in Storage Units | Unit Mass ($M$) (kg) | Plexiglas Bucket Thickness (in.) | Spacing and Notes | $k_{eff} \pm \sigma$ |
|---|---|---|---|---|
| 124 X 8 X 14 | 3 | 2 | No tops or clad | 0.798 ± 0.009 |
| 1 | 3 | 2 | No tops or clad | 0.740 ± 0.010 |
| 124 X 8 X 14 | 6 | 2 | No tops or clad | 0.987 ± 0.009 |
| 1 | 6 | 2 | No tops or clad | 0.891 ± 0.008 |
| 124 X 8 X 14 | 5 | 2 | No tops or clad | 0.902 ± 0.015 |
| 1 | 5 | 2 | No tops or clad | 0.844 ± 0.009 |
| 124 X 8 X 14 | 5 | 2 | No tops | 0.896 ± 0.010 |
| 1 | 5 | 2 | No tops | 0.849 ± 0.011 |
| 124 X 8 X 14 | 5 | 3 | | 0.861 ± 0.009 |
| 124 X 8 X 14 | 5 | 3 | In contact | 0.882 ± 0.012 |
| 1 | 5 | 3 | | 0.869 ± 0.009 |
| 124 X 8 X 14 | 3 | 3 | | 0.798 ± 0.009 |
| 124 X 8 X 14 | 3 | 3 | In contact | 0.841 ± 0.014 |

Note: Vault is 6-in.-thick concrete; internal dimensions are 300 ft long by 20 ft wide by 34 ft high. The 3-kg units are 3.32-cm radius spheres; other units have cylinders with $H/D = 1$. Single unit in array is placed in vault corner for maximum reactivity. Buckets are spaced 29 in. center-to-center, except when in contact with each other. All buckets have tops and are clad inside and out with 0.063 in. of iron, except where noted.

to provide a comparison of the effectiveness of the three moderators.

Table VIII lists the results of a series of calculations made to simulate a possible storage facility. The plutonium units are placed on the bottom of the bucket which has an inside diameter of 7.5 in. and an inside height of 10 in. The center-to-center spacing of the buckets is 29 in. Calculations show that the presence or absence of 0.063-in. stainless cladding of the buckets inside and out does not appreciably change $k_{eff}$.

Cladding may be necessary for fire safety. Plexiglas buckets, 2 in. thick, provide sufficient isolation for 5-kg units to be stored on 29-in. centers. This amounts to a surface density of about 14 kg/ft$^2$. If the Plexiglas bucket is made 3 in. thick and provided with 3-in.-thick tops, sufficient decoupling is provided to allow them to be placed in contact with each other and still be safely subcritical while containing a 5-kg unit of plutonium metal. The safe surface density is then 70 kg/ft$^2$.

Table IX presents the results of replacing the Plexiglas buckets with concrete ones because of economy and increased fire safety. Three inches of concrete is not as efficient at neutronic isolation as the same thickness of Plexiglas.

Plutonium metal units of slightly less than 4 and 3 kg, respectively, may be safely arrayed and in contact, in concrete buckets, under the same conditions as stated above for Plexiglas.

Table X lists the results of calculations of in-contact arrays of buckets of concrete, Plexiglas, or water. The arrays are cubic, 20 × 20 × 20, and surrounded on all 6 surfaces by 12 in. of concrete with no intervening space. The plutonium metal units are cylinders with the optimum height-to-

TABLE IX

Plutonium Units in Concrete Buckets

| Array Size in Storage Units | Unit Mass ($M$) (kg) | Concrete Bucket Thickness (in.) | Spacing and Other Notes | $k_{eff} \pm \sigma$ |
|---|---|---|---|---|
| 124 X 8 X 14 | 5 | 3 | | 0.927 ± 0.012 |
| 1 | 5 | 3 | | 0.859 ± 0.009 |
| 124 X 8 X 14 | 4 | 3 | | 0.880 ± 0.007 |
| 124 X 8 X 14 | 3 | 3 | In contact | 0.890 ± 0.008 |
| 124 X 8 X 14 | 3 | 2 | In contact | 1.028 ± 0.009 |

Note: All buckets have tops and are clad inside and out with 0.063 in. of iron. Buckets are spaced 29 in. center-to-center, except when in contact with each other. The 3-kg units are 3.32-cm radius spheres; other units are cylinders with height-to-diameter ratio of 1. Vault is 6-in.-thick concrete, 300 ft long by 20 ft wide by 34 ft high inner dimensions. Single unit in array is placed in vault corner for maximum reactivity.

TABLE X

Buckets in Edge-to-Edge Contact

| Unit Mass ($M$) (kg) | Bucket Material | $k_{eff} \pm \sigma$ | Notes and Comments |
|---|---|---|---|
| 2.5 | Concrete | 1.062 ± 0.011 | Buckets fit around unit with no space between them. Bucket is filled by unit. |
| 2.0 | Concrete | 0.977 ± 0.011 | |
| 4.0 | Plexiglas | 0.976 ± 0.012 | |
| 3.0 | Plexiglas | 0.889 ± 0.007 | |
| 3.0 | Water | 0.875 ± 0.012 | |
| 3.0 | Plexiglas | 0.758 ± 0.012 | Buckets are 7.5 inches inner diameter and 10-inch inner height. Units do not fill bucket but rest on the bottom of the bucket. |
| 3.0 | Water | 0.739 ± 0.010 | |
| 5.0 | Water | 0.883 ± 0.009 | |
| 3.0 | Concrete | 0.817 ± 0.009 | |

Note: The 12-in.-thick concrete vault surrounds the 20 × 20 × 20 array of 3 in. thick, 0.063-in. iron clad (inside and out) buckets, in contact with each other, with tops. The units are right circular cylinders of optimum height-to-diameter ratio (0.9238).

diameter ($H/D$) ratio = 0.9238, rather than spheres or equilateral cylinders, $H/D = 1$.

The conclusion to be drawn from the table is that, if the buckets fit tightly around the units with no intervening space, only Plexiglas and water buckets are safe and then only for 3-kg units. If the buckets are standardized to some reasonable size (i.e., the 7.5-in. inner diameter and 10-in. inside height used previously), 3-kg units in Plexiglas, concrete, or water buckets all have a large margin of safety.

Thus, hydrogenous materials can be used effectively in high density storage configurations.

## DEFINITIONS

### Loading

The loading is the total mass of fissile metal which can be safely stored in a vault. It equals the product of the usable area and the surface density. For mixtures of material of different sizes, shapes, and compositions, the loading equals the sum of the products of the safe surface density for each type of material and the usable area occupied.

### Usable Area

The usable area includes the largest surface area, whether wall or floor, of the rectangular parallelepiped constituting the storage facility minus corrections to allow for aisle space.

### Surface Density

Surface density refers to the mass of an array of units divided by the area over which distributed (units are kilograms per square foot).

### Surface-to-Volume Ratio

The surface-to-volume ratio is defined as the quotient of the unit surface area and its fissile volume.

### Surface

Surface refers to the surface of a single unit from which neutrons may escape the unit. It is the smallest surface area which encloses the unit.

### Volume

The volume is the space occupied by the mass of fissile metal in a single unit when calculated at maximum theoretical density (18.7 g/cm$^3$ for enriched uranium and 19.7 g/cm$^3$ for plutonium).

### ACKNOWLEDGMENTS

The authors acknowledge the helpful suggestions of Deanne Dickinson, Donald R. Ferguson, Douglas C. Hunt, and John D. McCarthy for thorough reviews of the report. Acknowledgment is given also to Deanne Dickinson for the two examples used with the text. We also wish to acknowledge Fritzie Laner for her helpful editorial suggestions.

This work was performed under U.S. Atomic Energy Commission Contract AT(29-1)-1106.

## REFERENCES


1. NORMAN KETZLACH, "Bases for Establishing Nuclear Safety Criteria," *Chem. Eng. Prog. Symp. Ser.*, **28**, 56 (1960).

2. H. C. PAXTON, "Correlations of Experimental and Theoretical Critical Data," LAMS-2537, p. 11, Los Alamos Scientific Laboratory (1961); also, "Criticality Control in Operations with Fissile Material," LA-3366, p. 39, Los Alamos Scientific Laboratory (1966).

3. T. GUTMAN, "A Surface-Density Evaluation of Critical Array Data," *Nucl. Appl.*, **2**, 121 (1968).

4. R. L. STEVENSON and R. H. ODEGAARDEN, "Studies of Surface Density Spacing Criteria Using KENO Calculations," *Trans. Am. Nucl. Soc.*, **12**, 890 (1969).

5. G. E. WHITESIDES and N. F. CROSS, "KENO, A Multigroup Monte Carlo Criticality Program," CTC-5, Computing Technology Center Nuclear Division, Union Carbide Corporation (1969).

6. H. F. FINN and N. L. PRUVOST, "Livermore Plutonium Array Program," *Proc. Livermore Array Symp.*, CONF-680909, Lawrence Radiation Laboratory (1968).

7. C. L. SCHUSKE, C. L. BELL, G. H. BIDINGER, and D. F. SMITH, "Industrial Criticality Measurements on Enriched Uranium and Plutonium, Part II," RFP-248, The Dow Chemical Company, Rocky Flats Division (1962).

8. J. T. THOMAS, "Critical Arrays of U(93.4) Metal Cylinders," Neutron Physics Division Annual Progress Report, ORNL-3499, Oak Ridge National Laboratory (1963).

9. *Reactor Physics Constants*, 2nd ed., ANL-5800, p. 558, Argonne National Laboratory, Argonne (1963).

10. *Reactor Physics Constants*, 2nd ed., ANL-5800, p. 659, Argonne National Laboratory (1963).

11. R. E. ROTHE, C. L. SCHUSKE, and E. E. HICKS, "The Criticality of a Uranium Solution Slab Under Various Reflector Conditions," *Nucl. Appl. Technol.*, **7**, 505 (1969).

12. C. YAO and A. S. KALELKAR, "Effects of Drop Size on Sprinkler Performance," *Fire Technol.*, p. 254 (1970).

13. *Reactor Physics Constants*, 2nd ed., ANL-5800, Argonne National Laboratory (1963).

14. C. L. SCHUSKE, "Neutron Multiplication Measurements of Parallel Arrays of Oralloy Units," RFP-59, The Dow Chemical Company, Rocky Flats Division (1956).

15. C. LEE SCHUSKE and DONALD C. COONFIELD, "Mixtures of Plutonium and Enriched Uranium in Slab Geometry," RFP-1489, The Dow Chemical Company, Rocky Flats Division (1971).

16. R. AVERY, "Coupled Fast-Thermal Power Breeder," *Nucl. Sci. Eng.*, **3**, 129 (1958).

17. R. AVERY, "Theory of Coupled Reactors, P/1858, *Proc. U.N. Intern. Conf. Peaceful Uses At. Energy, 2nd, Geneva*, **12**, 151 (1958).

18. R. AVERY et al., "Coupled Fast-Thermal Power Breeder Critical Experiment," P/2160, *Proc. U.N. Intern. Conf. Peaceful Uses At. Energy, 2nd, Geneva*, **12**, 151 (1958).

19. R. GWIN and W. T. MEE, "Critical Assemblies of Uranium 235," Y-A2-124, Radiation Control Group, Y-12 Plant, Oak Ridge, Tennessee (1953).

20. A. GOODWIN, Jr. and C. L. SCHUSKE, "Plexiglas and Graphite Moderated Plutonium Assemblies," Parts A and B, Reactor Science and Technology, *J. Nucl. Energy*, **15**, 120 (1961).

# THE CUSP PROCESS FOR PREPARING CONCENTRATED, CRYSTALLINE URANIA SOLS BY SOLVENT EXTRACTION

CHEMICAL PROCESSING

KEYWORDS: *uranium dioxide, preparation, solvent extraction, amines, hydrocarbons, sols, nitric acid*

J. P. McBRIDE, K. H. McCORKLE, Jr., W. L. PATTISON, and B. C. FINNEY *Oak Ridge National Laboratory, P.O. Box X, Oak Ridge, Tennessee 37830*

Received November 24, 1969
Revised October 13, 1971

*Urania sol is used for preparing uranium oxide microspheres for nuclear reactor fuels. A new process for producing concentrated, 1 M U or more, crystalline urania sols by solvent extraction has been developed. This process is based on a time-temperature conductivity-controlled extraction of nitric acid from a hydrolyzing U(IV) nitrate-formate solution using an amine-in-hydrocarbon extractant. The sols contain predominantly crystalline urania, and are more resistant to rapid, spontaneous gelation and other variations in properties than earlier sols made by solvent extraction. Also, earlier solvent extraction processes produced dilute (0.2-0.3 M U) sols that required concentration to 1 M before making the spheres.*

*The preparation of a satisfactory sol depends on ensuring crystallization of the urania, minimizing uranium oxidation, and having a stable U(IV) nitrate-formate feed solution. Feed solutions were made by reducing uranyl nitrate-formate solution with platinum-catalyzed hydrogen at atmospheric pressure. The reduction requires vigorous agitation of the solution and continuous electrometric monitoring of the U(IV)/U(VI) redox potential to minimize harmful side reactions.*

*The studies include both laboratory development and an engineering-scale demonstration.*

## I. INTRODUCTION

The development of sol-gel processes at the Oak Ridge National Laboratory to make dense thoria and thoria-urania for use as nuclear fuels[1-6] led to the search for colloid processes for other metal oxides, as well as for carbides and carbonitrides, with nuclear applications. The starting point in all sol-gel processes is the preparation of a metal oxide sol. The next step is the formation of spherical sol drops, which are gelled by extracting water and electrolyte in a fludizing column of a drying solvent.[5-7] The gelled spheres are then dried and fired. This report describes the concentrated urania sol preparation (CUSP) process for making urania sol to be used in the preparation of dense urania microspheres for nuclear fuels.

Sols of 1-1.4 *M* crystalline urania are prepared directly by solvent extraction in the CUSP process. This process avoids the handling of radioactive solids, as required in some earlier urania sol processes, while eliminating or minimizing the sol concentration step inherent in the earlier solvent extraction process for the preparation of dilute sols.[7-14] Further, it lends itself to closer control than can be easily imposed on the previous processes. In general, the sols prepared by the CUSP process have better reproducibility and longer "shelf life" (the interval between preparation of the sol and spontaneous gelation of 1 *M* U) than urania sols prepared previously by solvent extraction. Earlier urania sols typically had shelf lives of several days to a few weeks, whereas properly prepared CUSP urania sols have shelf lives exceeding four months.

The CUSP process has been tested in engineering-scale equipment, and the suitability of the sols for forming dense microspheres has been demonstrated.

## II. SOL SPECIFICATIONS AND DEVELOPMENTAL STUDIES

The available chemical analyses were not sufficiently complete or reproducible for determining the "goodness" of a sol. The better-quality sols were characterized by longer shelf lives and

higher gelling concentrations, i.e., the highest concentration to which a sol may be concentrated without the occurrence of gelation. These latter characteristics average the effects of many subsidiary variables such as electrolyte content, amorphous urania content, oxidation state, and oxidation rate. Ultimately, it might be desirable to specify sols by their microsphere-forming behavior; however, variability in the microsphere-forming process is now too great to define "formability" as if it were a sol property only.

Considerations leading to the development of the CUSP process stemmed from aging and digestion studies of dilute sols prepared by the multistage extraction-digestion process.[7-14] The conductivity (free nitric acid concentration) of these sols increased rapidly with age (100% in four weeks), and the decreasing concentration at which these sols gelled while undergoing evaporation was associated with this increase in free acid. A large fraction of the urania in these sols was amorphous (determined by the method described in Sec. VII), and the amorphous urania tended to crystallize and release nitric acid with aging. This amorphous fraction was typically about 65% initially but decreased to 35% after two weeks. Figure 1 shows the changes in the amount of crystallized urania in these sols at various stages in the multistage solvent extraction process and with aging.

Digestion, at 61°C, of hydrolyzed U(IV) nitrate-formate solution, 0.2 $M$ $[U(OH)_{2.5}]^{1.5+}(NO_3^-)(CHO_2^-)_{0.5}$, from the first extractor led to the crystallization of about 25% of the urania after 1 h, but longer times did not promote further crystallization. Figure 2 shows changes in crystallinity and in the U(VI) content of the uranium during digestion. The similarity between the curves in Fig. 2 suggested that, in general, U(VI) impedes crystallization and that a uranium concentration of about 20% U(VI) blocks crystallization. Another portion of this solution, held at room temperature, where the rate of uranium oxidation was slow, attained 90% crystallinity in two days. The total amount of nitrate retained in the sols at any single free acid content (conductivity) was affected by changes in the relative amounts of the nitric acid removed in each of the three extraction stages. This behavior suggested that the rate of extraction is an important process variable needing further optimization for uranium ion hydrolytic kinetics, and it led to the concept of extracting nitrate continuously at a controlled rate following a prescribed time-temperature-conductivity path, as embodied in the CUSP process.

Problems involved in controlling the hydrolytic kinetics, oxidation, and crystallization are interrelated. Nitrate must be extracted to promote hydrolysis, and the level to which the total nitrate concentration must be reduced slightly exceeds that needed to prevent gelation. The nitric acid promotes oxidation, but some must be present to prevent gelation. Temperatures that promote crystallization of the urania also accelerate oxidation of the urania by the nitrate. Nitrate that is associated with the amorphous urania inhibits rapid crystallization.

The amount of nitrate present in the amorphous urania at any particular conductivity depends on the previous rate of extraction. When the extraction rate was too rapid, the concentration of retained nitrate increased and made crystallization

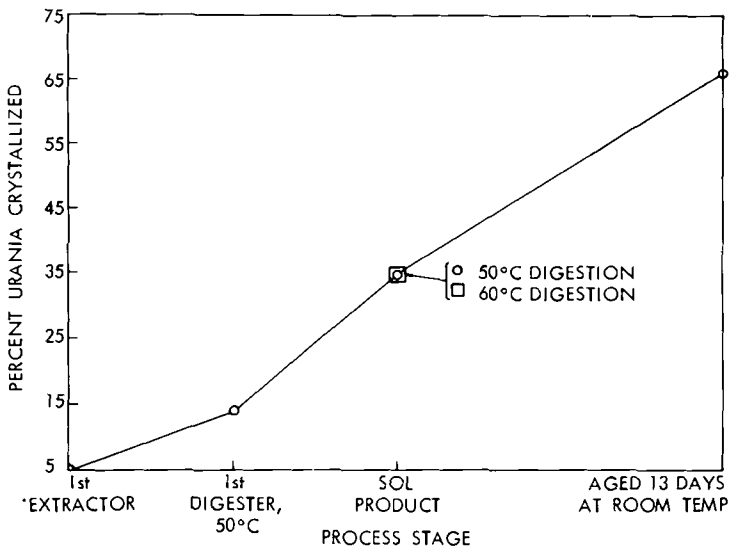


Fig. 1. Crystallization of urania during the three-stage solvent extraction process for dilute sol.

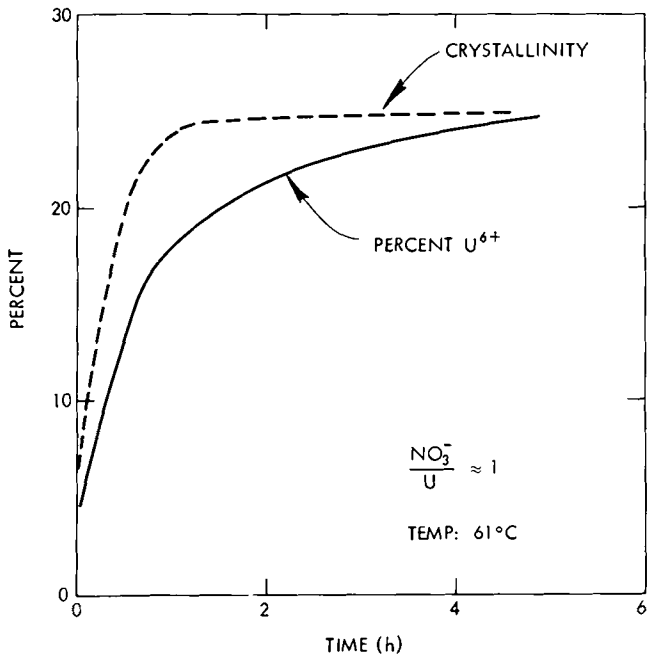


Fig. 2. Effect of digestion on the first extractor product of the solvent extraction process for dilute sol.

slow, erratic, and incomplete at the crystallization point. Exact specifications for the CUSP process involve conflicts among chemical requirements, costs, and operating convenience.

## III. THE PREPARATION OF U(IV) FEED SOLUTIONS

Feed solutions for the laboratory development studies and the engineering demonstration of the CUSP process were made from 1 to 1.25 *M* uranyl nitrate solution to which formic acid was added immediately before reduction. The formate/U mole ratio was 0.5. The uranyl species was reduced batchwise to the uranous form with hydrogen at atmospheric pressure using a commerically available platinum catalyst ($PtO_2$, "Adams Catalyst"). This catalyst settles and filters rapidly in the reduced solution. Hydrogen was injected through a porous gas-diffuser immersed in the solution, which was agitated with 3W/liter stirring power. The extent of reduction was monitored by the U(IV)/U(VI) redox potential using platinum versus glass electrodes. When uranium reduction approaches completion, the potential versus time graph has a sharply increased slope which decreases to zero abruptly at completion.

Batch reduction with a slurry catalyst was necessary to permit intense, uniform agitation of the solution and to permit the hydrogen flow to be stopped quickly after the uranium reduction was complete. Continuing the hydrogen flow in the absence of uranyl ions produces ammonia. More than about 0.01 mole of ammonia per mole of uranium promotes early gelation and falsifies the conductivity, which is the major process control variable in the extraction steps.

Ammonia is not the only deleterious side-reaction product. Preliminary tests suggest that nitrites and/or organonitrite derivatives are produced during reduction if agitation is not both uniform and intense. The U(IV) species appear to be more labile toward oxidation by nitrites than by nitrates. The available analyses [U, U(IV), nitrate, total nitrogen, formate, ammonia, total carbon, conductivity, pH, and density] are not sufficiently accurate or specific for determining these nitrite-derived species by difference.

The stoichiometry of the aqueous U(IV) feed solution is 1 to 1.3*M* $[U(OH)_{1.5}]^{2.5+}(NO_3^-)_2(CHO_2^-)_{0.5}$. The actual chemical species present are not known in detail, but most of the formate and some of the nitrate are complexed to the partially hydrolyzed U(IV) species.

## IV. LABORATORY DEVELOPMENT

A schematic equipment flow sheet for the laboratory CUSP process is shown in Fig. 3. The extractant, 0.25 *M* Amberlite LA-2[a] in 75% diethylbenzene—25% *n*-$C_{12}$ paraffin diluent,[b] was circulated around a closed loop through the batch of U(IV) solution in the extractor. The extractant, Amberlite LA-2, is a secondary amine with convenient solubility and basicity properties; however, neither it nor its molarity in the diluent is uniquely essential. The composition of the diluent may be varied from 50 to 100% diethylbenzene without affecting the properties of the sol or the system operation more than marginally with respect to crud formation, phase separation, and uranium losses. When the diethylbenzene concentration falls below 50%, crud and emulsification problems (in the simple stirred-pot extractor) increase. Below 25% diethylbenzene, these problems render the system practically inoperable.

In the laboratory development studies, extractant was pumped through a pipette tip near the bottom of the flask into 2.5 liters of U(IV) feed solution contained in a 5-liter round-bottom flask. Extractant-aqueous contact was enhanced with a paddle-blade stirrer adjusted to the maximum speed which would not emulsify aqueous solution

[a]Amberlite LA-2, Rohm and Haas Company.

[b]*n*-$C_{12}$ paraffin, Sourth Hampton Company. The $C_{12}$ represents an average molecular weight of a mixture.

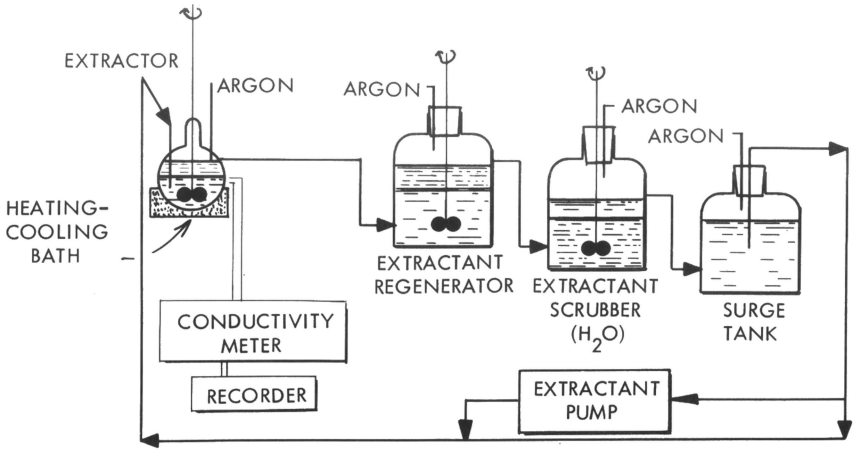


Fig. 3. CUSP solvent extraction laboratory apparatus.

into the supernatant layer of extractant. Extractant was regenerated with a stirred aqueous solution of 1 *M* NaOH - 1 *M* $Na_2CO_3$. The water scrubber guarded against possible carryover of entrained caustic carbonate into the sol. The extraction rate was controlled by varying the extractant flow rate. The extraction temperature was controlled by an external oil bath for the extractor.

Figure 4 shows an idealized time-temperature-conductivity history for converting the feed solution to a sol. Solution conductivity starts at about 70 mmho/cm at 25°C. As extraction proceeds at a rate less than 1 mole of $HNO_3$ per mole of uranium per hour, the temperature is increased to 35°C. Extraction continues to point one, where it is stopped and heatup is resumed. The increase in conductivity after point one is made to parallel the "gel line" by supplying slight and varying additional extraction as needed. The gel line is the electrolyte-temperature boundary between the fluid sol state and the soft-solid gel state of the aqueous phase when the boundary is approached from above (before crystallization). At 58 to 62°C, the aqueous phase darkens and evolves gas, mostly nitric oxide. The evolution of gas is closely related to both crystallization and oxidation of the urania. If oxidation is properly minimized during the other processing steps, most of the oxidation occurs during the gas evolution.

Extraction is restarted at point two to promote crystallization. Once crystallization has been initiated, it proceeds spontaneously, releasing a large amount of nitric acid. At this point, extraction is increased to prevent excessive urania oxidation. After 10 to 15 min, the rates of gas evolution and nitric acid release diminish, and continued extraction causes the conductivity to decrease. The initial portion of the path from two to three is shown as a region because the problem of balancing off a high, varying rate of nitric acid release against extractant holdup and flow rate causes the path to wander. This wandering is not very significant if the conductivity does not exceed 55 mmho/cm and the temperature does not exceed

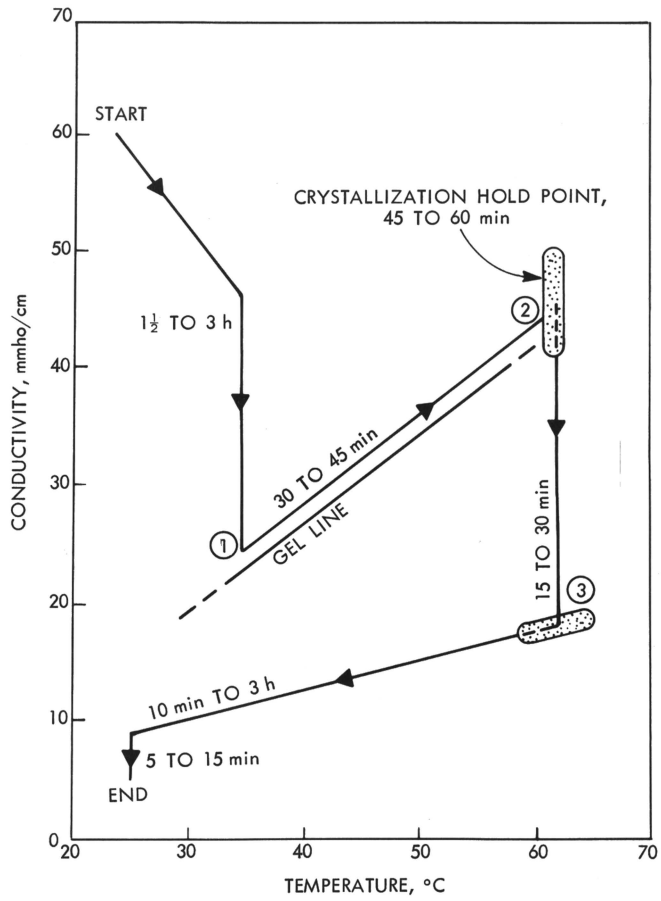


Fig. 4. Idealized CUSP operating path.

65°C. When the conductivity decreases to about 16 mmho/cm, extraction is stopped and the sol is cooled to 25°C. At this temperature, the conductivity of the sol is about 5 to 8 mmho/cm. A slight loss of temperature control at point three, where the high flow rate of cool extractant to the 62°C extractor ceases abruptly, was encountered. The conductivity at point three is deliberately set slightly high because of practical problems in stopping the rapid, 62°C extraction precisely at a value that would give 4 mmho/cm on cooling to 25°C (the optimum for sol stability). The final adjustment of the conductivity to 4 mmho/cm is made by a slow extraction at 25°C.

Table I shows the effect of the initial extraction rate on total nitrate in the urania polymer solution

TABLE I

Effect of Extraction Rate on Total Nitrate Content of Urania Polymer Solution

| Run No. | Extraction Rate $\frac{\text{moles } HNO_3}{\text{mole U-h}}$ | Conductivity at 35°C (mmho/cm) | Nitrate/U Mole Ratio |
|---|---|---|---|
| CUSP-3 | 0.46 | 24 | 0.5 |
| CUSP-9 | 1.1 | 26 | 0.7 |
| CUSP-10 | 1.4 | 27 | 0.6 |
| CUSP-11 | 2.4 | 25.5 | 0.9 |

at point one of Fig. 4. Although the discrepancy between the results for runs CUSP-9 and -10 might indicate either process nonreproducibility or an artifact of the chemical analysis, the general trend of nitrate content with extraction rate is clear. The mixture of strong reductants [U(IV) and formic acid] with strong oxidants (nitrate and possibly nitrite) is only marginally metastable during a number of standard analytical manipulations.

## V. CHARACTERIZATION OF LABORATORY-PREPARED URANIA SOLS

The sols were characterized by chemical constituent analyses, conductivity, x-ray diffraction, electron microscopy, Brunauer-Emmett-Teller nitrogen adsorption area (BET area) measurements, and, in some instances, by making urania microspheres.

The sols contained predominantly crystalline urania (>80%); their average crystallite size was determined to be 39 ± 1 Å by x-ray diffraction. They remained fluid for several months at a urania concentration of 1 to 1.4 *M* and could be concentrated without gelation to greater than 3 *M* urania by vacuum evaporation when fresh.

Selected data for the properties of the various sols are given in Table II. Not all of these sols were made by the recommended operating path shown in Fig. 4. Much of the variation in the data in Table II was caused by exploratory flow sheet changes. Runs CUSP-4 through -7 represent attempts to reproduce a single operating procedure, while runs CUSP-8 and -9 had different crystallizing temperatures, runs CUSP-9 and -10 had different rates of extraction, and run CUSP-12 had a different feed concentration.

The effect of oxidation on crystallization, as suggested by the data in Fig. 2, is qualitatively well-confirmed by the U(IV) and crystallinity data in Table II. Linear least-squares extrapolation of the data in Table II to the final crystallinity and oxidation states in Fig. 2 gives a surprisingly good quantitative confirmation, considering that oxidation is not the only variable important to crystallization.

Table III shows the effect of aging on the conductivity of CUSP sols. In instances where the sol is 100% crystalline (CUSP-7) or where the ni-

TABLE II

Selected Properties of Urania Sols Prepared in the Laboratory by the CUSP Process

| Run No. | Uranium Concentration (*M*) | U(IV) Content (% U) | Nitrate/U Mole Ratio | Formate/U Mole Ratio | Crystallinity[a] (% U) |
|---|---|---|---|---|---|
| CUSP-4 | 1.34 | 82 | 0.14 | 0.47 | – |
| CUSP-5 | 1.39 | 84 | 0.14 | 0.44 | – |
| CUSP-(5-6)[b] | 1.39 | 82 | 0.12 | 0.36 | – |
| CUSP-7 | 1.38 | 89 | 0.11 | 0.48 | 100 |
| CUSP-8 | 1.32 | 85 | 0.15 | 0.41 | 79 |
| CUSP-9 | 1.42 | 82 | 0.19 | 0.35 | 46 |
| CUSP-10 | 1.39 | 81 | 0.14 | 0.42 | 33 |
| CUSP-11 | 1.47 | 84 | 0.21 | 0.36 | 77 |
| CUSP-12 | 0.93 | 89 | 0.13 | 0.43 | 81 |

[a]Average crystallite size: 39 ± Å.

[b]Composite mixture.

trate/U mole ratio is not higher than 0.15 (CUSP-8, -10, -12), changes in conductivity are slow and the sols do not thicken rapidly. In cases where the sols contain a significant amorphous fraction and the $NO_3^-$/U mole ratio is high (CUSP-9, -11), conductivities greater than 11 mmho/cm are reached at aging times of one to two months and the sols become thixotropic gels.

Figure 5 shows the effect of the vacuum off-gassing temperature (part of the BET procedure) on the surface area of CUSP gels prepared by drying sols at room temperature under argon. The maximum specific surface area is obtained by off-gassing at 85 to 100°C; a sharp decrease in area is seen between 100 and 200°C. The area then remains nearly constant up to a temperature of 400°C, above which another decrease in area occurs. The loss of area in the temperature range 100 to 200°C may partially result from surface chemical reactions between the faces of adjacent crystallites; above 400°C, however, the usual solids-diffusion crystal-growth sintering processes probably dominate.

The CUSP-7 gel had a maximum surface area of 136 $m^2/g$, which is close to the value of 139

TABLE III

Effect of Aging on the Conductivity of Laboratory-Prepared CUSP Sols

| Run No. | Conductivity[a] as Prepared (mmho/cm) | Aging Time (months) | Conductivity[a] After Aging (mmho/cm) |
|---|---|---|---|
| CUSP-7 | 7.7 | 5.3 | 9.3 |
| CUSP-8 | 5.9 | 3.7 | 9.8 |
| CUSP-9 | 4.9 | 2.0 | 11.2 |
| CUSP-10 | 6.0 | 1.6 | 9.4 |
| CUSP-11 | 7.2 | 1.3 | 11.9 |
| CUSP-12 | 4.4 | 1.0 | 6.4 |

[a]Conductivities were measured at temperatures from 23.2 to 33.1°C and were normalized to 25°C, assuming an increase in conductivity of 1.9% per degree.

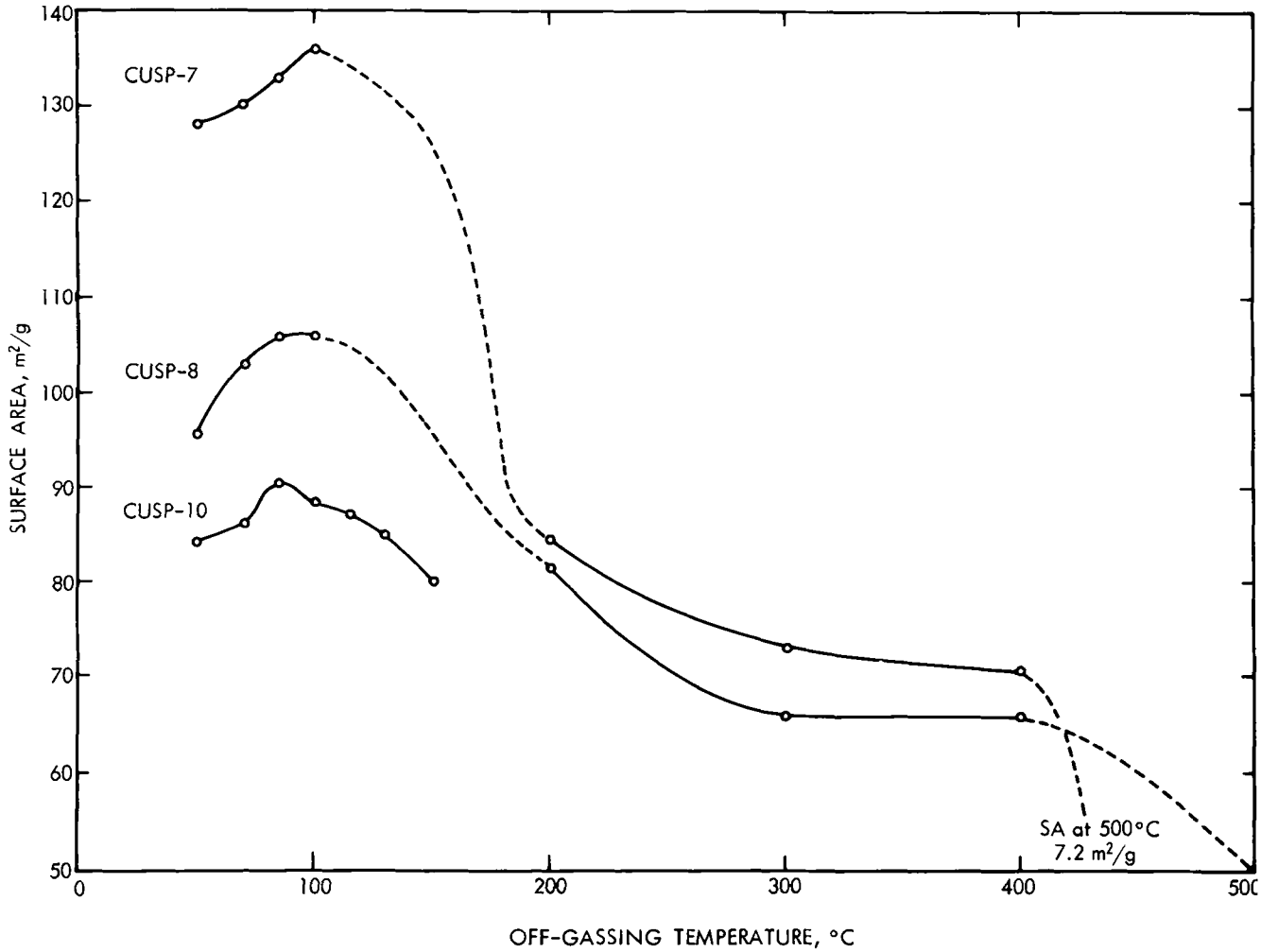


Fig. 5. Surface areas of CUSP urania gels.

$m^2/g$ calculated by assuming the urania particles to be cubes with 39-Å edges (the experimental x-ray crystallite size). This sol was 100% crystalline as determined by the x-ray method described in Sec. VII. The sols prepared in runs CUSP-8 and -10 had amorphous fractions of 21 and 67%, respectively, and lower specific surface areas.

Although microsphere-forming studies are not yet complete, preliminary experience shows that the sphere-forming behavior of the sols is satisfactory. Some properties of the final urania microspheres are given in Table IV.

TABLE IV

Properties of Urania Microspheres Made from Laboratory-Prepared CUSP Sols, after Firing at 1150°C in 4% $H_2$-96% Ar

| Run No. | O/U Atom Ratio | BET Surface Area ($m^2/g$) | Density[a] (% of Theoretical) | Porosity[b] (%) |
|---|---|---|---|---|
| CUSP-4 | 2.02 | 0.0059 | 97.3 | 0.96 |
| CUSP-5 | 2.01 | 0.0074 | 97.3 | 0.84 |
| CUSP-6 | 2.01 | 0.0053 | 96.9 | 0.33 |

[a]Measured by Hg intrusion at 15 psi.

[b]Measured by Hg intrusion at 15,000 psi.

## VI. ENGINEERING DEMONSTRATION

An engineering-scale demonstration of the CUSP process was carried out in equipment designed for making dilute urania and dilute $ThO_2$-$UO_3$ sols by continuous-flow three-stage extraction and digestion.[6,7,15] The main equipment adaptations were confined to one extraction stage of the system (Fig. 6), where the aqueous surge tank, pump, conductivity instrumentation, and piping for aqueous recycle have been added. The chemical flow sheet for the engineering-scale operation is shown in Fig. 7. Operating time was about 5 h per batch of 15 liters of 1 *M* urania sol (~$\frac{3}{4}$ kg of urania produced per hour of operation).

Ten runs were made to test equipment and develop routine operating procedures. Problems associated with crud and emulsification were less severe in the engineering extractor than in the laboratory extractor, and process control by conductivity was simple after run ES-1. In run ES-1, the conductivity instrument readings were falsely high because the probes were placed in near-stagnant regions of the equipment, and gelation occurred when the sol conductivity crossed the gel line shown in Fig. 4. Sol recirculation was reestablished and processing continued after about 16 h, but an inferior sol (with a shelf life of only four months) resulted. Stable, fluid sols were made in runs ES-2, -3, -4, and -7.

Table V contains chemical data for sols made in these runs. Feed solutions for runs ES-1 through -7, with the exception of ES-5, were made in a baffled, stirred tank whose height was about equal to its diameter (1 ft).

Feed solution for run ES-5 was made in a 5-in.-diam tank that is critically safe for $^{235}U$, but has a liquid depth-to-diameter ratio of about 11 for 15 liters. The shape of this reductor led to less vigorous stirring than was employed in the first reductor. The properties of the sol produced in run ES-5 were inferior (a gelling concentration of only 2.3 *M* U, and a shelf life at 1 *M* U of only two months). The poor results were caused by the inadequate stirring, which permitted ammonia and other undesirable side-reaction products to form.

In the feed solution for run ES-6, instrument failure led to severe overreduction, and hence to the formation of ammonia. The ammonia caused gelation during final extraction at 25°C. Runs ES-8, -9, and -10 were made with feed from the critically safe reductor after the stirring in it was somewhat improved by installing more stirrer blades. Although the average shelf life of these last three sols was longer than that of the sol from run ES-5, these last sols were inferior to those from runs ES-2, -3, -4, and -7, in which feed was obtained from the 1-ft-diam reductor. The feeds from the two reductors were not distinguishable by the available chemical analyses.

Gel microspheres were made from sol ES-2 at two urania concentrations: 1 *M* and 3 *M*. The 3 *M* sample was prepared by vacuum evaporation at 35 to 40°C after the total nitrate/U mole ratio had been increased to 0.105 with nitric acid. This electrolyte-adjusted 3 *M* sol had a shelf life of five months. Some properties of the final, fired urania microspheres from sol ES-2 are given in Table VI.

After the ten engineering-development runs had been completed, sol 1 *M* in U and containing more than 200 kg of urania was prepared in 4-kg (urania) batches. The first 25 batches were prepared mainly as a production demonstration, while the second 25 batches were produced for specific needs and for investigation of equipment performance. This production experience confirmed that the CUSP process is reproducibly controllable, and that fluid 1 *M* urania sols with shelf lives of three months or more can be produced at the rate of 4 kg of urania per 8-h shift on a two-shift per day, 5-day-week basis. To ensure reproducibility of sol product properties, it was necessary to drain the system of residual sol and flush with two water washes after each batch was prepared.

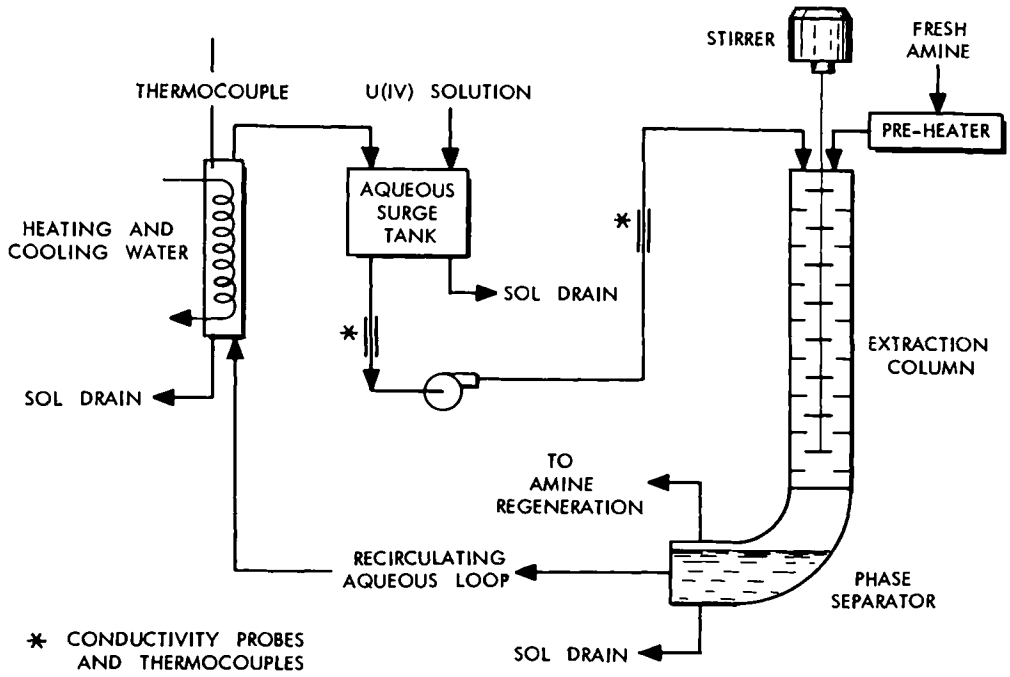


Fig. 6. Schematic diagram of sol preparation section of the engineering-scale CUSP solvent extraction equipment.

TABLE V

Properties of $UO_2$ Sols Prepared in an Engineering-Scale Demonstration of the CUSP Process

| Run No. | U(IV) Content (% U) | $NO_3^-/U$ Mole Ratio | $NH_4^+/U$ Mole Ratio[a] | Conductivity, 25°C (mmho/cm) | Crystallinity (%) | Aging Time to Gelation at 1 *M* Urania (months) |
|---|---|---|---|---|---|---|
| ES-1 | 82 | 0.14 | – | 6.60 | 100 | 4 |
| ES-2 | 86 | 0.09 | 0.0017 | 3.50 | 100 | 18 |
| ES-3 | 90 | 0.11 | – | 2.25 | 100 | 12 |
| ES-4 | 86 | 0.14 | – | 4.25 | – | 14 |
| ES-5 | 83 | 0.08 | 0.020 | 3.75 | – | 2 |
| ES-6 | – | 0.08 | 0.029 | 5.00[b] | – | 0[b] |
| ES-7 | 88 | 0.12 | 0.0017 | 3.02 | – | 12 |
| ES-8 | 85 | 0.11 | 0.0019 | 3.75 | – | 2 |
| ES-9 | 87 | 0.09 | 0.0015 | 3.10 | – | 4 |
| ES-10 | 86 | 0.10 | 0.0017 | 3.10 | – | 3 |

[a]The $NH_4^+/U$ mole ratio was determined for the uranous nitrate feed and should be essentially the same in the completed sol since $NH_4^+$ does not extract.

[b]Gelled during final nitric acid extraction because of high $NH_4^+$ content of feed solution.

TABLE VI

Selected Properties of Fired Urania Microspheres Made from Sol ES-2

| Molarity of Urania Sol | Final O/U Atom Ratio | C (%) | Density ($g/cm^3$)[a] | | Bead Size ($\mu$m) | Average Crush Strength (g) |
|---|---|---|---|---|---|---|
| | | | 15 psi | 15,000 psi | | |
| 1 *M* | 2.003 | <0.002 | 10.78 | 10.81 | 300-350 | 614 |
| 3 *M* | 2.005 | 0.003 | 10.53 | 10.60 | 350-400 | 746 |

[a]Measured by Hg intrusion.

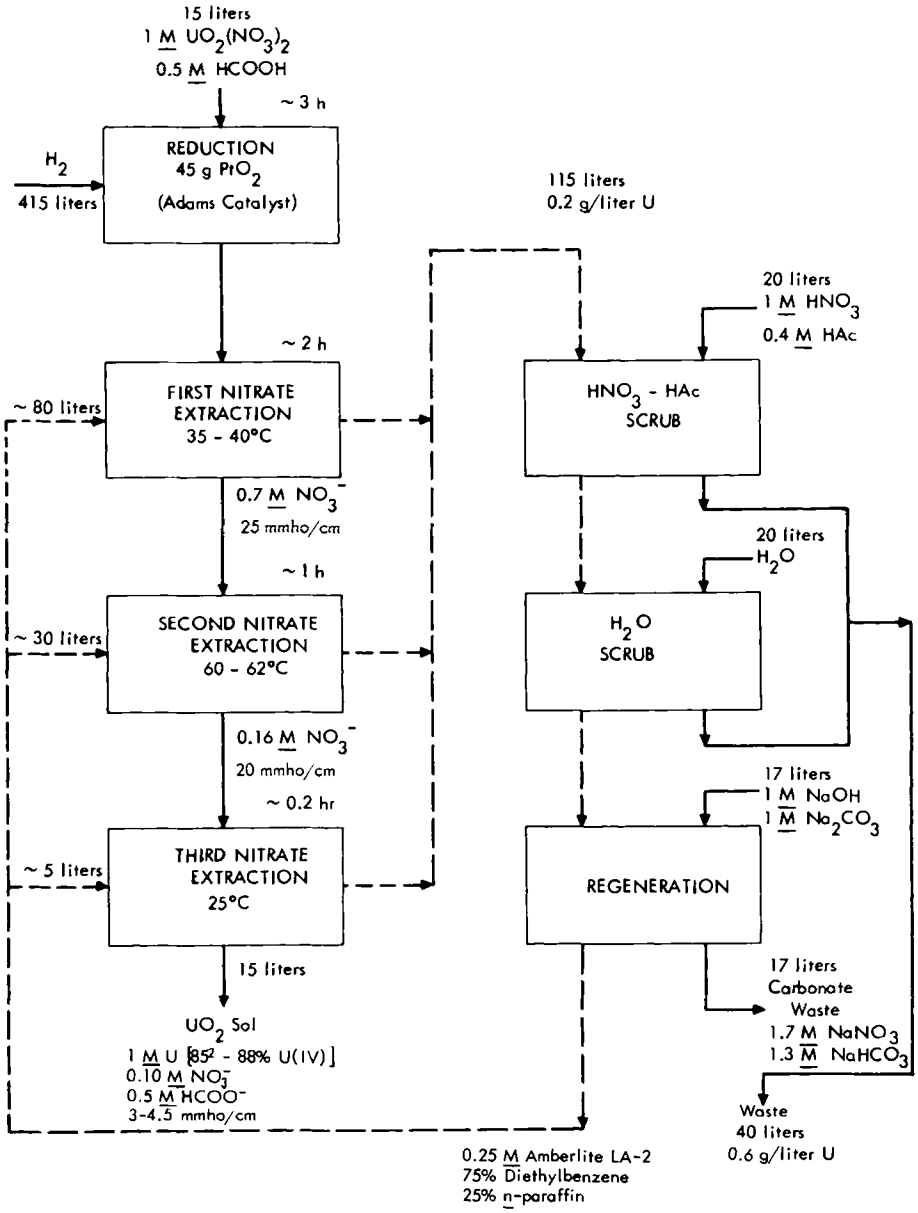


Fig. 7. Flow sheet for the engineering-scale preparation of urania sol by the CUSP process.

Figure 8 is an electron photomicrograph of the colloidal urania particles of sols prepared from a 1 *M* U feed solution in the engineering-scale demonstration. X-ray diffraction showed that the 250- to 350-Å-diam agglomerates consist of 40-Å urania crystallites with little or no amorphous urania present.

## VII. DETERMINATION OF AVERAGE CRYSTALLINE SIZE AND OF CRYSTALLINE URANIA FRACTION OF SOLS

The average urania crystallite size in the sols was calculated from x-ray diffractometer line-broadening data by standard procedures.[16,17] Broadening of the (111), (220), and (311) lines usually gave the same apparent crystallite size within normal experimental error and never indicated greatly differing sizes. When the three lines did not give the same size, the sizes were averaged.

The amount of crystalline urania present was determined by two methods:

1. Comparison of the x-ray diffractometer trace for the (111) line of the sample with the diffractometer trace for the (111) line of a urania sol which was shown to be 100% crystalline by agreement between the x-ray diffraction line-broadening particle size and the BET gas adsorption area, assuming the crystallites to be approximately

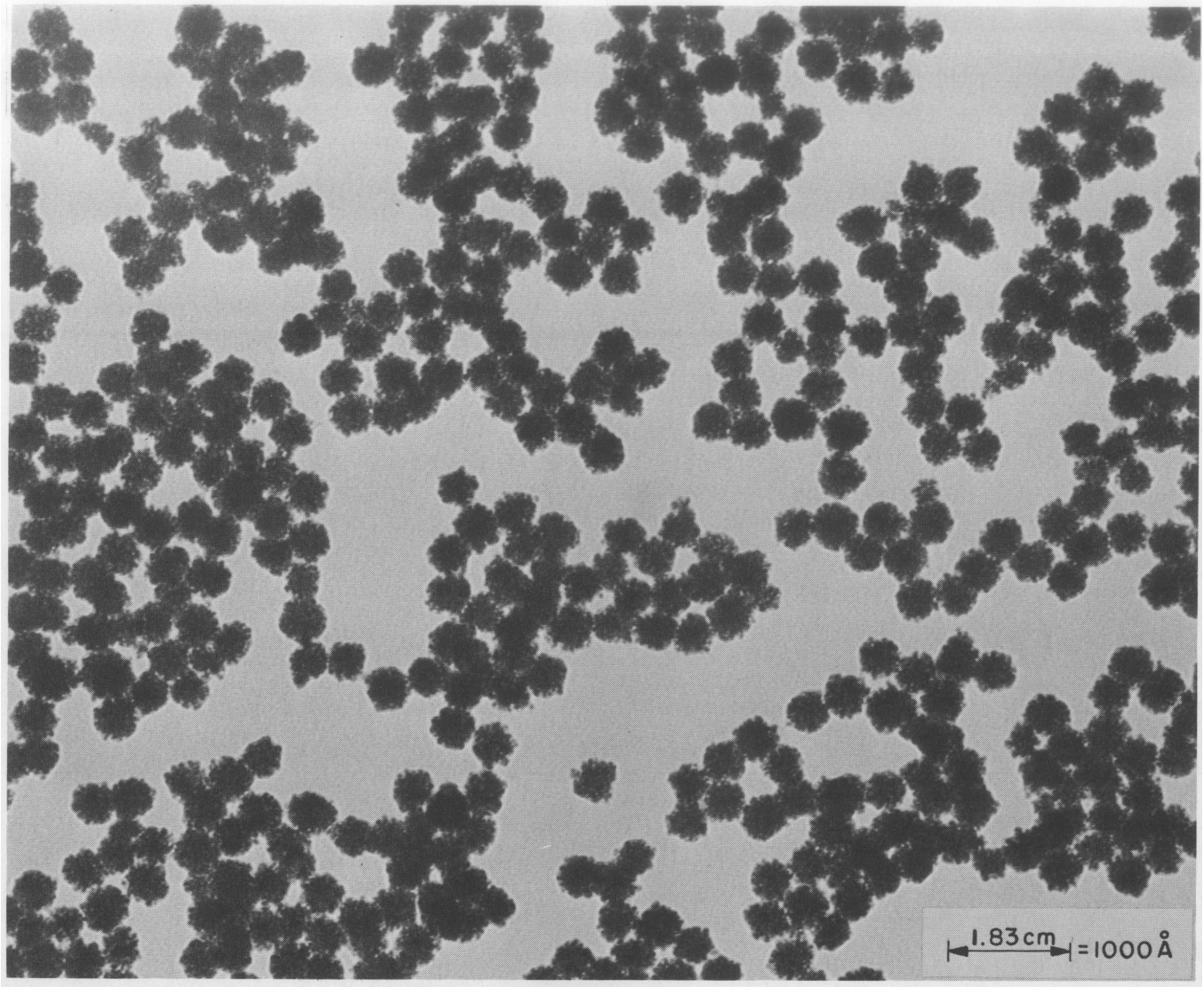


Fig. 8. Electron photomicrograph of sol particles made in CUSP engineering equipment.

spherical cubo-octahedra of crystal-density urania.

2. Comparison of the x-ray diffractometer trace for the (111) line of the sample with the diffractometer trace for the (111) line of a thoria sol which was shown to be fully crystalline by the method above.

The parameter chosen for correlation with crystallinity was the ratio of net peak height of the (111) line to the scattered background radiation level (P/B). Peak area is the theoretically preferred measure of crystallinity, and the use of peak area to determine crystalline MgO in Portland cement has been reported.[18] For our particular equipment and samples, however, we found empirically that peak height and background level were less subject to variation and bias than was the location of a base line for peak area. No corrections were made for effects of amorphous urania or of soluble species on the calibrations, but these interferences should not be significant in the particular concentration and crystallinity ranges which were used. Rigid standardization of all handling and operating procedures was required for about ±5% reproducibility.

#### ACKNOWLEDGMENTS

This research was sponsored by the U.S. Atomic Energy Commission under contract with the Union Carbide Corporation.

## REFERENCES


1. K. H. McCORKLE, O. C. DEAN, and C. E. SCHILLING, "Preparation of Dense Millimeter Size Thorium and Thorium-Uranium Oxide for Fuel Element Fabrication," *Trans. Am. Nucl. Soc.*, **3**, 376 (1960).

2. K. H. McCORKLE, A. T. KLEINSTEUBER, C. E. SCHILLING, and O. C. DEAN, "Preparation of High Density Compactable Thorium Oxide Particles," U.S. Patent No. 3,035,895, U.S. Atomic Energy Commission (May 22, 1962).

3. O. C. DEAN, C. C. HAWS, A. T. KLEINSTEUBER, and J. W. SNIDER, "The Sol-Gel Process for Preparation of Thoria Base Fuels," *Proc. Symp. Thorium Fuel Cycle Gatlinburg, Tennessee, December 5-7, 1962*, TID-7650, U.S. Atomic Energy Commission, Division of Technical Information.

4. C. C. HAWS, J. L. MATHERNE, F. W. MILES, and J. E. VAN CLEVE, "Summary of Kilorod Project—A Semiremote 10 kg/day Demonstration of $^{233}UO_2$-$ThO_2$ Fuel Element Fabrication by the ORNL Sol-Gel Vibratory Compaction Method," ORNL-3681, Oak Ridge National Laboratory (1965).

5. D. E. FERGUSON, O. C. DEAN, and D. A. DOUGLAS, "The Sol-Gel Process for the Remote Preparation and Fabrication of Recycle Fuels," *U.N. Intern. Conf. Peaceful Uses At. Energy, 3rd*, Geneva, **10**, 307; CONF. 2.6/P/237, U.S. Atomic Energy Commission.

6. P. A. HAAS, C. C. HAWS, F. G. KITTS, and A. D. RYON, "Engineering Development of Sol-Gel Processes at the Oak Ridge National Laboratory," ORNL-TM-1978, Oak Ridge National Laboratory (1968).

7. R. G. WYMER, "Laboratory and Engineering Studies of Sol-Gel Processes at Oak Ridge National Laboratory," in *Proc. Panel on Sol-Gel Processes for Ceramic Fuels*, p. 131, International Atomic Energy Agency, Vienna (1968); also ORNL-TM-2205, p. 9, Oak Ridge National Laboratory (1968).

8. D. E. FERGUSON, "Sol-Gel Technology in the Nuclear Reactor Fuel Cycle," *Progress in Nuclear Energy, Series III, Process Chemistry*, Vol. 4, p. 37, Pergamon Press, New York (1969).

9. J. P. McBRIDE, "Preparation of $UO_2$ Microspheres by a Sol-Gel Technique," ORNL-3874, p. 2, Oak Ridge National Laboratory (1968).

10. J. P. McBRIDE, K. H. McCORKLE, and W. L. PATTISON, in "Laboratory Studies of Sol-Gel Processes at the Oak Ridge National Laboratory," J. P. McBRIDE (Compiler), ORNL-TM-1980, p. 25, Oak Ridge National Laboratory (1967).

11. L. E. MORSE, in "Laboratory Studies of Sol-Gel Processes at the Oak Ridge National Laboratory," J. P. McBRIDE (Compiler), ORNL-TM-1980, p. 32, Oak Ridge National Laboratory (1967).

12. D. E. FERGUSON et al., "Chemical Technology Division Annual Progress Report for Period Ending May 31, 1966," ORNL-3945, p. 157, Oak Ridge National Laboratory (1966).

13. D. E. FERGUSON et al., "Chemical Technology Division Annual Progress Report for Period Ending May 31, 1967," ORNL-4145, p. 180, Oak Ridge National Laboratory (1967).

14. D. E. FERGUSON et al., "Chemical Technology Division Annual Progress Report for Period Ending May 31, 1968," ORNL-4272, p. 142, Oak Ridge National Laboratory (1968).

15. J. W. SNIDER, "The Design of Engineering-Scale Solex Equipment," ORNL-4256, Oak Ridge National Laboratory (1969).

16. H. P. KLUG and L. E. ALEXANDER, *X-Ray Diffraction Procedures*, John Wiley and Sons, New York (1954).

17. H. S. PEISER, H. P. ROOKBY, and A. J. C. WILSON, *X-Ray Diffraction of Polycrystalline Materials*, Reinhold Publishing Corporation, New York (1960).

18. S. S. REHSI and A. J. MAJUINDAR, "Quantitative Determination of Uncombined MgO in Portland Cement Clinker by X-Ray Diffractometry," *J. Appl. Chem.*, **18**, 297 (1968).

# RADIOLYSIS OF HANFORD B PLANT HDEHP EXTRACTANT

CHEMICAL PROCESSING

**KEYWORDS:** *radiolysis, butyl phosphates, kerosene, strontium, DEHPA, solvent extraction, efficiency, reprocessing, fuels, reactors, Purex process*

WALLACE W. SCHULZ *Atlantic Richfield Hanford Company*
*P.O. Box 769, Richland, Washington 99352*

Received August 25, 1971

*Irradiation ($^{60}Co$ source) tests were performed to determine effects of radiolysis of HDEHP [bis(2-ethylhexyl)phosphoric acid] solvents. (An HDEHP-TBP-kerosene extractant is used in the Hanford B Plant to extract $^{90}Sr$ from Purex process high-level waste). Irradiation to 230 to 350 Wh/liter destroys only small (~6%) amounts of HDEHP; the principal radiolytic effect is a two- to threefold decrease in strontium extraction capacity. This effect is ascribed to polymerization of HDEHP with itself and/or with $H_2MEHP$ [mono(2-ethylhexyl)phosphoric acid], a primary radiolysis product. Dilute NaOH and $Na_2CO_3$ solutions wash $H_2MEHP$ from irradiated HDEHP extractants; however, only with solvents irradiated in the absence of any aqueous phase do such washes improve strontium extraction properties. Addition of unirradiated HDEHP to irradiated HDEHP solvents increases their ability to extract strontium; this simple procedure is used to maintain the strontium extraction capacity of the B Plant solvent at a suitable level. Performance and properties of plant solvent are in general agreement with those anticipated from $^{60}Co$ irradiation tests.*

## INTRODUCTION

Previous papers have described the scope and objectives of the comprehensive Waste Management Program currently being implemented at Hanford.[1,2] An important part of this program involves solvent extraction removal of long-lived $^{90}Sr$ from Purex acid waste (PAW) solution. Purex acid waste solution is the high-level, concentrated and denitrated, radioactive waste solution resulting from reprocessing of irradiated aluminum-clad uranium metal fuel elements; its composition is listed in the paper by Larsen.[3]

Bis(2-ethylhexyl)phosphoric acid (HDEHP) diluted with tri-n-butyl phosphate (TBP) and normal paraffin hydrocarbon (NPH) is used as the strontium extractant. (NPH is a mixture of alkanes in the $C_{10}$ to $C_{14}$ range.) A simplified version of the chemical flow sheet presently employed in the Hanford B Plant for extraction of $^{90}Sr$ from PAW solution is depicted in Fig. 1; details of this and earlier flow sheets for HDEHP extraction of strontium from Hanford waste have been given by Beard et al.[1] and Larsen.[3]

The HDEHP extractant receives radiation at the rate of about 3 Wh/liter per solvent extraction cycle under the flow sheet conditions of Fig. 1. By way of comparison, in one cycle of Hanford Purex plant operation the TBP solvent receives a dose of only about 0.006 to 0.01 Wh/liter.[4] Such a comparison can be misleading, however, without taking into account the much greater tolerance of the B Plant extraction system to massive doses of radiation.

Prior to B Plant startup, extensive laboratory studies were performed to evaluate the effects of radiation on physical and chemical properties of the HDEHP-TBP extractant. Solvents were irradiated not only in the absence of any aqueous phase but also under cyclic conditions simulating contact of the extractant with various flow sheet aqueous solutions. Results of these studies are presented and correlated with measurements of actual B Plant solvent over the first two years operation. That the studies discussed here were largely empirical is emphasized; their objective was to estimate the expected performance and life of HDEHP extractants under typical plant conditions rather than determination of the fundamental

radiation chemistry of HDEHP and its solutions. The only studies of the latter type have been performed by Wagner and Towle[5] and by Kuzin, Semushin, and Romanovskii[6] who determined $G$ values for many of the gaseous and liquid species produced during radiolysis of undiluted HDEHP.

## EXPERIMENTAL DETAILS

### Materials

Impure HDEHP (93% HDEHP) was purchased from the Union Carbide Company; composition of this material is listed in a paper by Partridge and Jensen.[7] HDEHP, free of all impurities, was prepared by their procedure. Less pure (98.4% HDEHP) material was obtained by the purification procedure of Schmitt and Blake.[8]

Both as-received and vacuum-distilled TBP (Commercial Solvents Corporation) were used to dilute the HDEHP. Hydrocarbon diluents used were Soltrol-170 (Phillips Petroleum Company), consisting of 100% branched chain paraffins; and two NPH solutions (hereafter NPH-1 and NPH-2) from the South Hampton Refining Company. The latter contained only normal paraffins and differed slightly in relative amounts of the $C_{10}$ to $C_{14}$ components.

Samples of actual B Plant solvent were procured as needed after plant startup. Prior to use in distribution ratio tests, plant solvent was washed with successive portions of 6 $M$ $HNO_3$ and water to convert completely to the hydrogen-form and to remove fission product activity.

Hydroxyacetic acid (HAcOH) was obtained as an 11.5 $M$ solution from the E. I. du Pont de Nemours Company. Trisodium N-hydroxyethylethylenediamineacetate ($Na_3HEDTA$) was obtained as a 1.57 $M$ stock solution. Trisodium nitrilotriacetate ($Na_3NTA$) was obtained as a 1.8 $M$ stock solution from the Geigy Chemical Company. All other chemicals were of reagent grade quality.

### Irradiation Procedures

Aside from a special set of experiments, $^{60}Co$ irradiations of HDEHP extractants and extractant components were of two general types. In one case various organic solutions were irradiated to desired exposure levels at 26 to 29°C and in the absence of any aqueous phase. In cyclic irradiation experiments, HDEHP-TBP-diluent solutions

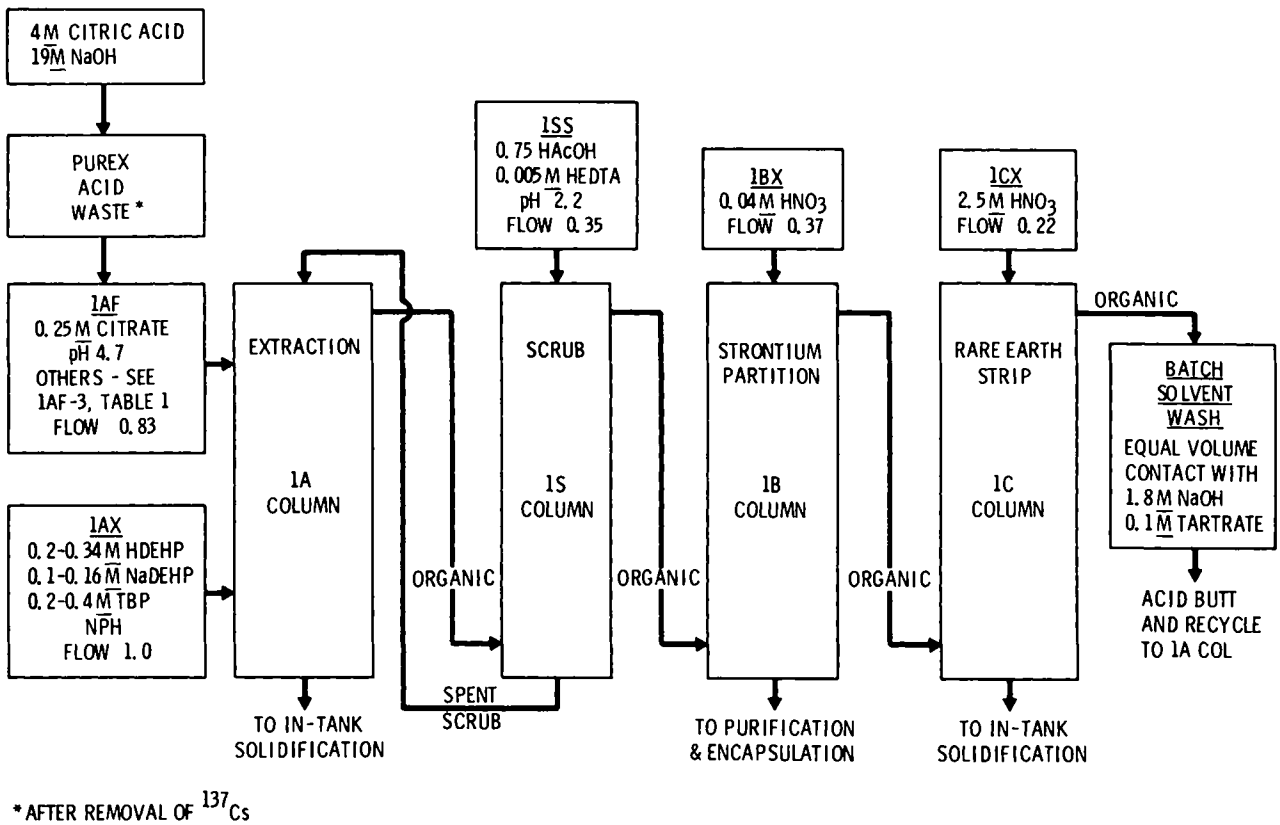


Fig. 1. Hanford B plant Strontium extraction flowsheet.

were irradiated while in intimate (stirred) contact with a sequence of different aqueous solutions The sequence and compositions of the aqueous solutions and the irradiation periods used in each contact are described subsequently. Conditions in the cyclic tests were chosen to simulate those anticipated for various proposed B Plant flow sheets. Temperatures of the solutions in the cyclic irradiations were kept in the range 35 to 40°C. Also in these tests aqueous and organic phases were separated outside the $^{60}Co$ facility.

Portions of highly purified HDEHP were irradiated in the absence of any aqueous phase and also while in stirred contact with an equal volume of either water or 1 *M* $HNO_3$. Solutions during irradiation were maintained at 26°C.

All organic and, when present, aqueous phases were irradiated in air. Conventional ceric sulfate dosimetry techniques[9] were used to calibrate the dose rate of the $^{60}Co$ source which ranged from 1.1 to 1.8 Mrad/h in this work. Following Stieglitz,[10] doses received by organic solutions were calculated by the relation

$$W = 2.78 \times 10^{-9} D_r T F D_o$$

where

$W$ = dose absorbed by organic solution (Wh/liter).

$2.78 \times 10^{-9}$ = factor for converting rads to Wh/g

$D_r$ = dose rate $^{60}Co$ source (rad/h)

$T$ = irradiation time (h)

$F$ = volume fraction organic phase in test mixture

$D_o$ = density (g/liter) of organic phase if irradiated alone or average density (g/liter) of aqueous-organic mixtures.

### Solvent Quality Tests

Tri-n-butyl phosphate (TBP) and HDEHP concentrations were determined by gas chromatographic procedures.[11] A Sargent Company automatic titrator operated in the derivative mode was also used to measure HDEHP and $H_2MEHP$ [mono(2-ethylhexyl)phosphoric acid] concentrations of various unirradiated and irradiated extractants. Organic acid concentrations were obtained by titrating with alcoholic KOH in a 50 vol% water-50 vol% isopropanol solvent. In all cases the amounts of HDEHP and $H_2MEHP$ were calculated assuming that these were the only acids present, that the equivalents of base added to the first end point represented the number of moles of HDEHP and $H_2MEHP$, and that the equivalents of base from the first to the second end point represented the number of moles of $H_2MEHP$. This calculation procedure was considered completely satisfactory for all unirradiated extractants and for those irradiated solvents not containing TBP. Less reliable titration data were obtained with irradiated HDEHP-TBP solutions because the calculation procedure did not take into account small concentrations of (H)BP (dibutylphosphoric acid) which were probably present. Titration errors introduced by ignoring the presence of (H)BP did not appear large, however, since in all cases gas chromatographic and titration methods yielded HDEHP concentrations which agreed to within 3 to 5%.

The Signer method[12] was used to determine molecular weights of HDEHP extractants after irradiation in stirred contact with either water or 1 *M* $HNO_3$; in this procedure azobenzene was used as a reference material and cyclohexane as a carrier solvent. Prior to use in the Signer method the HDEHP irradiated while in contact with 1 *M* $HNO_3$ was washed with water; all cyclohexane-HDEHP solutions were dried free of water.

Capacity of various HDEHP extractants for extracting strontium and/or Ce(III) was measured by contacting (mechanical stirring) them 10 min at 25°C with an equal volume of appropriately traced synthetic extraction column feedstock (Table I).

TABLE I

Chemical Composition of Simulated Extraction Column Feed Solutions

| Constituent | Molarity 1AF-1 Solution[a,b] |
|---|---|
| $NaNO_3$ | 0.60 |
| NaAcOH | 0.20 |
| $Na_3HEDTA$ | 0.18 |
| $Na_2SO_4$ | 0.079 |
| $Na_2C_4H_6O$[c] | 0.014 |
| $Fe(NO_3)_3$ | 0.072 |
| $Al(NO_3)_3$ | 0.036 |
| $Cr(NO_3)_3$ | 0.014 |
| $Ni(NO_3)_2$ | 0.0072 |
| $La(NO_3)_3$ | 0.0024 |
| $Ce(NO_3)_3$ | 0.0012 |
| $Sr(NO_3)_2$ | 0.0009 |
| $Ca(NO_3)_2$ | 0.0006 |
| pH | 3.5 |

[a] 1AF-2 solution: Same except 0.15 *M* $Fe(NO_3)_3$, 0.25 *M* $Na_3HEDTA$; and pH = 4.3.

[b] 1AF-3 solution: Same except 0.19 *M* $Fe(NO_3)_3$, 0.37 *M* $Na_2SO_4$, 0.26 *M* $Na_3NTA$ and no $NaNO_3$ or $Na_3HEDTA$; and pH = 4.3.

[c] Tartrate.

Aqueous phase pH's after contact of extractants with 1AF-1 and 1AF-2 solutions were about 3.2 to 3.3 and 3.6 to 3.8, respectively. All plant solvent samples were contacted with 1AF-2. The Ce(IV) extraction capacity of certain of the HDEHP solvents was estimated by contacting them 1 h at 25°C with an equal volume of an aqueous solution of the composition 1.96 *M* $HNO_3$-0.014 *M* $La(NO_3)_3$-0.0071 *M* $Ce(NO_3)_3$-0.020 *M* $(NH_4)_2S_2O_8$-0.02 *M* $AgNO_3$ and containing $^{144}Ce$(IV). Distribution ratios ($E_a^o$) for strontium, Ce(III), and Ce(IV) were calculated from radiometric analyses of aqueous and organic phases.

## RESULTS AND DISCUSSION

### Solvent Radiolysis in the Absence of an Aqueous Phase

*Extractant Composition Effects.* Various HDEHP-TBP extractants were irradiated in the absence of any aqueous phase to an exposure of about 240 Wh/liter.

Three predominant radiolytic effects were observed (Table II) in these experiments:

1. most significantly, a two- to threefold decrease in strontium extraction capacity

2. irradiation to 240 Wh/liter destroyed only small amounts (~6%) of HDEHP

3. decreases in Ce(IV) extraction capacity, the extent of which varied with the nature of the kerosene diluent.

The large decrease in strontium extraction capacity of irradiated extractants does not correlate with the small decrease in HDEHP concentration of such solutions. Rather the decrease in Sr extraction $E_a^o$ is ascribed to interaction (hydrogen bonding) of $H_2$MEHP, a primary radiolysis product, with HDEHP. HDEHP is known to exist as a hydrogen-bonded dimeric species in unirradiated kerosene solutions.[13] Hydrogen bonding with $H_2$MEHP in irradiated solutions is believed to produce even more complex entities, making HDEHP molecules either unavailable or, at least, less available for bonding strontium. The great propensity of $H_2$MEHP for intramolecular hydrogen bonding has been reported by Ferraro and Peppard[14]; in n-hexane, for example, $H_2$MEHP exists as a polymer with a molecular weight about 15 times the formula weight. Also, Schulz[15] has recently shown that addition of small amounts of $H_2$MEHP to unirradiated HDEHP solvents has a severe depressing effect on strontium distribution ratios. Antagonistic effects in other systems involving $H_2$MEHP have also been reported.[13]

The decreased strontium extraction capacity of irradiated HDEHP solvents was essentially independent of either the type or history of the hydrocarbon diluent. The source of the unirradiat-

TABLE II

Variation of Radiolysis Effects with Extractant Composition

(All solvents were irradiated to about 240 Wh/liter in absence of any aqueous phase)

| | Composition | | | | | | | Distribution Ratios | | | |
|---|---|---|---|---|---|---|---|---|---|---|---|
| | HDEHP | | | $H_2$MEHP Molarity | | | | Sr[a] | | Ce(IV) | |
| | | Molarity | | | | TBP | Kerosene | | | | |
| Solvent | Source[b] | UnIr[c] | Ir[d] | UnIr | Ir | Source[b,e] | Diluent | UnIr | Ir | UnIr | Ir |
| 1 | P-1 | 3.10 | 2.82 | 0.0 | 0.33 | NP | NP | [f] | [f] | [f] | [f] |
| 2 | P-2 | 0.293 | 0.279 | 0.0 | 0.041 | NP | Soltrol-170 | 2.97 | 1.45 | [f] | [f] |
| 3 | P-2 | 0.275 | 0.261 | 0.0 | 0.058 | NP | NPH-1 | 3.86 | 1.24 | [f] | [f] |
| 4 | P-2 | 0.309 | 0.288 | 0.0 | 0.032 | VD | Soltrol-170 | 5.16 | 2.39 | [f] | [f] |
| 5 | P-2 | 0.315 | 0.286 | 0.0 | 0.033 | VD | NPH-1 | 4.78 | 1.97 | [f] | [f] |
| 6 | AR | 0.313 | 0.301 | [f] | 0.045 | AR | Soltrol-170 | 4.06 | 2.12 | 900 | 100 |
| 7 | AR | 0.313 | 0.290 | [f] | [f] | AR | NPH-1 | 4.16 | 1.60 | 2100 | 330 |
| 8 | AR | 0.305 | 0.291 | 0.013 | 0.052 | AR | NPH-2 | 4.10 | 1.75 | 1000 | 290 |

[a]Measured with 1AF-1 solution (Table I).

[b]P-1 = purified by method of Ref. 6.
P-2 = purified by method of Ref. 7.
NP = not present.
AR = as-received.
VD = vacuum distilled.

[c]UnIr = unirradiated.

[d]Ir = irradiated.

[e]0.2 *M* when present.

[f]Not measured.

ed HDEHP; i.e., as-received or specially purified, used in these experiments also appeared to have little effect on the decrease in Sr $E_a^o$. Strontium extraction by both unirradiated and irradiated HDEHP solvents was significantly (F ratio test) affected, however, by the presence or absence of TBP. This latter result is to be expected from the synergistic effect of TBP on HDEHP extraction of strontium reported previously in a paper by McDowell.[16]

The third main effect noted in these experiments—decreased Ce(IV) extraction capacity—is ascribed to the presence of radiolytically produced reducing agents in the organic extractant. Such reducing agents originate principally from radiolytic attack of the hydrocarbon diluent. Less reducing materials are generated from radiolysis of NPH than from Soltrol-170; this is shown by the results in Table II and was also noted in another study.[2] Cerium(IV) extraction capacity of irradiated HDEHP extractants, containing either NPH or Soltrol-170, can be largely restored by washing with $HNO_3$-$KMnO_4$ solutions.

*Removal of $H_2MEHP$.* Ethylene glycol and NaOH and $Na_2CO_3$ solutions effectively wash $H_2MEHP$ from irradiated (no aqueous phase) HDEHP extractants (Table III). Concomitant with removal of the $H_2MEHP$ is a marked increase in strontium extraction capacity. Indeed, dilute (0.5 to 0.75 *M*) NaOH and $Na_2CO_3$ washes restore strontium extraction capacity nearly to that of unirradiated solvent. The contention that interaction between $H_2MEHP$ and HDEHP in such irradiated solvents is largely responsible for their decreased strontium extraction capacity is strongly supported by these data.

TABLE III

Removal of $H_2MEHP$ from Irradiated HDEHP Extractant

[Portions of an irradiated HDEHP-TBP solvent (solvent No. 8, Table II), contacted 10 min at 25°C with indicated volumes of various washes.]

| Wash Solution | | Volume Ratio[a] | Washed Solvent | | |
|---|---|---|---|---|---|
| Reagent | Molarity | | HDEHP *M* | $H_2MEHP$ *M* | Sr $E_a^{o}$[b] |
| None | | - | 0.291 | 0.052 | 4.41[c] |
| NaOH | 0.75 | 1 | [d] | <0.01 | 7.99 |
| NaOH | 1.4 | 0.5 | [e] | <0.01 | 7.67 |
| NaOH | 2.0 | 1 | [e] | <0.01 | 6.94 |
| NaOH | 3.8 | 1 | [e] | 0.013 | 6.21 |
| NaOH | 5.4 | 1 | [e] | 0.024 | 4.86 |
| $Na_2CO_3$ | 0.5 | 1 | 0.295 | <0.01 | 7.44 |
| $Na_2CO_3$ | 0.75 | 1 | [d] | <0.01 | 6.48 |
| $Na_2CO_3$ | 1.0 | 1 | 0.286 | 0.019 | 6.82 |
| Ethylene glycol | | 0.2 | 0.291 | 0.043 | 5.33 |
| Ethylene glycol | | 0.5 | 0.294 | 0.024 | 5.36 |
| Ethylene glycol[d] | | 1 Contact 1 | 0.283 | 0.021 | 6.30 |
| | | 1 Contact 2 | 0.278 | <0.01 | 7.10 |
| | | 1 Contact 3 | 0.274 | <0.01 | 7.18 |

[a]Volume wash liquid/volume HDEHP extractant.

[b]With 1AF-2 solution (Table II).

[c]$E_a^o$ for unirradiated solvent was 8.89.

[d]Three successive contacts.

[e]Not determined.

Preferential solubility of $H_2MEHP$ over HDEHP in ethylene glycol was used earlier by Stewart and Crandall[17] to develop a procedure for purifying commercial grade HDEHP. Similarly, the much greater solubility of $Na_2MEHP$ over NaDEHP in aqueous NaOH and $Na_2CO_3$ solution was noted previously by Oak Ridge National Laboratory investigators.[18] These latter workers established that aqueous phase solubility of $Na_2MEHP$ increases with decreased aqueous phase sodium concentration; this effect is operative in the results in Table III.

Dilute NaOH and $Na_2CO_3$ solutions are superior to ethylene glycol for washing $H_2MEHP$ from irradiated extractant. Ethylene glycol also solubilizes significant amounts of HDEHP, another disadvantage to its use.

*Addition of HDEHP to Irradiated Extractants.* Strontium extraction capacity of both washed and unwashed irradiated HDEHP extractants responds in a regular fashion to changes in HDEHP concentration (Fig. 2). Solvents for these experiments were prepared by addition of appropriate amounts of NPH, purified HDEHP,[7] and TBP to portions of washed and unwashed irradiated extractant. (The carbonate-washed solvent was also washed with 6 *M* $HNO_3$ and water prior to addition of HDEHP.)

Logarithmic plots of Sr $E_a^o$ versus HDEHP molarity in Fig. 2 are straight, nearly parallel lines for both unirradiated and irradiated extractants. The curve for unwashed, irradiated solvent is displaced by almost a constant amount (about a factor of 2 in Sr $E_a^o$) from that for unirradiated extractant, however. The curve for the washed extractants is displaced only slightly from that for unirradiated solvent demonstrating further the beneficial effects of removal of $H_2MEHP$. (As can be seen in Fig. 2, a single carbonate wash was nearly as effective as two ethylene glycol washes in restoring strontium extraction capacity.)

For various reasons (e.g., highly complex nature of aqueous phase, etc.) slopes of the curves in Fig. 2 cannot be interpreted as rigorously establishing extractant dependencies. Qualitatively, however, the nearly equal slopes imply that both unirradiated and unwashed, irradiated (200 wh/liter) HDEHP solvents extract strontium by the same mechanism. But, because of hydrogen-bonding with $H_2MEHP$, the effective HDEHP con-

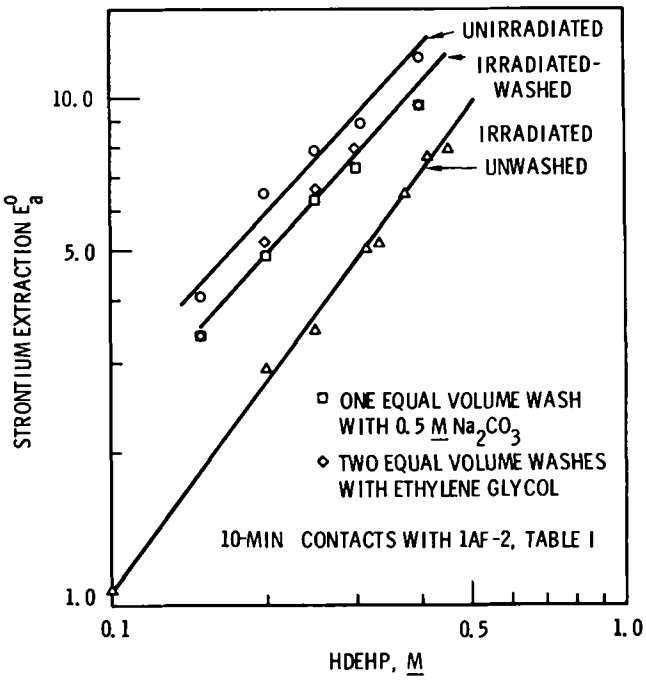


Fig. 2. Addition of HDEHP to irradiated extractants. All irradiated extractants were prepared from Solvent 8, Table II. All extractants were 0.2 *M* TBP.

centration available for reaction with strontium is less in the irradiated solvent.

### Solvent Radiolysis in Presence of an Aqueous Phase

*Cyclic Irradiation Tests*. The sequence and composition of the various aqueous solutions with which a HDEHP extractant was contacted in a typical irradiation test are listed in Table IV. Conditions of this particular cyclic test approximated chemical flow sheet conditions used in present-day B Plant operation (Fig. 1). (An important exception is that citrate rather than a mixture of HAcOH and $Na_3NTA$ is now used as both a buffering and complexing agent in the extraction column feed.) This flow sheet involves coextraction of strontium and rare earths (1A column), scrubbing of small amounts of coextracted sodium and other impurities (1S column), partitioning of strontium (1B column), and stripping of trivalent rare earths (1C column). Under present flow sheet conditions for processing PAW solution, the plant HDEHP receives radiation at the rate of about 3 Wh/liter per solvent extraction cycle. This dose rate is about one-third that used in the cyclic $^{60}Co$ irradiation test outlined in Table IV.

Current plant practice is to batch wash the HDEHP extractant every cycle with an equal volume of 1.8 *M* NaOH-0.1 *M* sodium tartrate solution. The primary purpose of this wash is to remove $^{90}Y$ and $^{91}Y$ (which contribute to the radiation dose received by the extractant) and other radioactive and inert (e.g., iron) impurities; solvent wash conditions are also designed to remove, at least partially, radiolytically generated $H_2MEHP$. Solvent wash steps were incorporated in all cyclic irradiation tests. Also simulating plant practice, washed solvents were butted each cycle with 12 *M* $HNO_3$ to the desired NaDEHP to HDEHP ratio.

Results of a typical cyclic irradiation test are summarized in Table V. Easily the most distinguishing feature of this and other cyclic irradiation tests was the gradual fall-off in the capacity of the HDEHP solvent to extract strontium. Periodic washing of the extractant with dilute NaOH solution did not prevent diminution of the strontium extraction $E_a^o$. Strontium extraction capacity was maintained at or near initial levels by periodic additions of HDEHP but, as noted in Table V, only at the expense of ever-increasing extractant HDEHP concentration. Singularly, Ce(III) extraction capacity was little changed by solvent radiolysis; small differences in Ce(III) $E_a^o$ values listed in Table V likely represent experimental errors involved in determining distribution ratios greater than 100.

Throughout this and other cyclic irradiation tests the concentration of $H_2MEHP$ in the irradiated solvent was below the detection limit (~0.01 *M*) of the titration method used for its analysis. This result complicates understanding of deterioration of strontium extraction capacity which

TABLE IV

Conditions Employed in Cyclic Irradiation Test

(Initial extractant was 0.19 *M* HDEHP-0.11 *M* NaDEHP-0.2 *M* TBP-NPH)

| Contact Type | Aqueous Phase | Aqueous / Organic Volume Ratio | Solvent Exposure (Wh/liter) |
|---|---|---|---|
| 1A column | 1AF-2[a] | 1.0 | 0.83 |
| 1S column | 1SS-2[b] | 0.2 | 1.70 |
| 1B column | 0.04*M* $HNO_3$ | 0.2 | 1.33 |
| 1C column | 2.0 *M* $HNO_3$ | 0.2 | 0.78 |
| 1CW receiver | None | 0.0 | 0.63 |
| Solvent wash | 10S-2[c] | 0.5 | 0.63 |
| Acid butt | 12*M* $HNO_3$ | 0.016 | 0.0 |
| | | Dose/cycle = 8.5 Wh/liter | |

[a] Listed in Table I.

[b] 0.75 *M* $AcOH^-$-0.01 *M* $NTA^{-3}$-0.036 *M* NaOH.

[c] 1.4 *M* NaOH-0.1 *M* sodium tartrate.

occurs under cyclic irradiation conditions. One possibility may be that even in this case periodic solvent washing with dilute NaOH solution removes $H_2MEHP$ and that the diminished strontium extraction occurs because of some mechanism other than polymerization of $H_2MEHP$ and HDEHP molecules. Alternatively, in the presence of an aqueous phase, reaction of HDEHP and $H_2MEHP$ may proceed either more rapidly or more completely (or both) with the result that some of the $H_2MEHP$ is not available for either titration or removal by solvent washes.

TABLE V

Typical Cyclic Irradiation Test Results

(Test conditions listed in Table IV)

| Cycle | Cumulative Solvent Exposure (Wh/liter) | Irradiated Extractant | | |
|---|---|---|---|---|
| | | HDEHP[a] ($M$) | $Sr^{b,c}$ ($E_a^o$) | $Ce(III)^{b,c}$ ($E_a^o$) |
| 0 | 0.0 | 0.305 | 3.60 | 260 |
| 3-A | 25.6 | 0.302 | 3.27 | 210 |
| 6-A | 51.1 | 0.297 | 2.70 | 240 |
| 6-B[d] | 51.1 | 0.310 | 2.85 | 250 |
| 9-A | 76.6 | 0.297 | 2.48 | 220 |
| 9-B[d] | 76.6 | 0.410 | 3.48 | 280 |

[a]After washing with equal volumes of 6 $M$ $HNO_3$ and water.

[b]With 1AF-3, Table I.

[c]Solvents not washed prior to distribution ratio contacts.

[d]After butting with unirradiated HDEHP.

*Radiolysis of HDEHP-Aqueous Phase Mixtures.* Substantive evidence that the presence of an aqueous phase during irradiation increases the molecular complexity of irradiated HDEHP is provided by the results in Table VI. Molecular weight data show polymerization of HDEHP increases in the order: unirradiated HDEHP < HDEHP irradiated neat (no aqueous phase) <HDEHP irradiated with water <HDEHP irradiated with 1 $M$ $HNO_3$. Strontium extraction capacity for both washed and unwashed solvents prepared from the irradiated HDEHP solutions decreases in the same order.

Radiolytic destruction of HDEHP also increases when an aqueous phase is present during irradiation. The increase is slight with water but substantial when HDEHP is irradiated in contact with 1 $M$ $HNO_3$. $A$ - $G_m$ (number of HDEHP molecules destroyed per 100 electron volts absorbed) value of 2.84 was calculated for irradiation of HDEHP in the absence of an aqueous phase; this compares with a value of 3.42 found by Wagner and Towle[5] for as-received HDEHP irradiated to 2055 Wh/liter.

## PLANT-SCALE SOLVENT PERFORMANCE

The Hanford B Plant HDEHP solvent inventory is nominally 10,000 gal. Mechanical losses (which occur chiefly in the batch washing operation) amount to about 80 to 100 gal/day; the loss is replaced when the inventory has decreased by about

TABLE VI

Radiolysis of HDEHP-Aqueous Phase Mixtures

| System | Properties of Irradiated HDEHP[a] | | | | | |
|---|---|---|---|---|---|---|
| | HDEHP ($M$) | Molecular Weight[b] / Formula Weight | $H_2MEHP$, $M$ | | Sr Extraction $E_a^o$[c] | |
| | | | Unwashed | Washed[d] | Unwashed | Washed |
| Unirradiated HDEHP | 3.10<br>0.300[e] | 2.0 | 0.0<br>0.0 | | 8.93 | |
| HDEHP-neat | 2.70<br>0.305[e] | 2.2 | 0.236<br>0.0253 | 0.007 | 6.66 | 7.95 |
| 50 vol% HDEHP-50 vol% $H_2O$ | 2.67<br>0.304[e] | 2.4 | 0.268<br>0.0316 | 0.007 | 5.29 | 6.44 |
| 50 vol% HDEHP-50 vol% 1 $M$ $HNO_3$ | 2.53<br>0.300[e] | 2.6 | 0.354<br>0.0420 | 0.0127 | 3.92 | 4.81 |

[a]All HDEHP solvents irradiated to 350 Wh/liter.

[b]Isopiestic method of Signer.[12]

[c]With 1AF-2, Table I.

[d]Washed with one-half volume of 1.4 $M$ NaOH and then with equal volumes of 6 $M$ $HNO_3$ and water.

[e]After dilution with NPH and TBP; all were 0.2 $M$ TBP.

10%. With feed prepared from PAW solution, the solvent exposure per cycle is about 3 Wh/liter and the steady-state exposure is about 200 Wh/liter.

Performance and properties of the B Plant extractant over the first two years of operation have conformed generally to those expected from cyclic irradiation ($^{60}$Co) studies. The plant started up with an 0.32 *M* HDEHP-0.2 *M* TBP solvent; within three months strontium extraction capacity decreased about twofold although the HDEHP concentration had decreased only about 6% (Fig. 3). Addition of HDEHP at that time (to 0.39 *M*) partially restored strontium extraction capacity but, as observed in the cyclic irradiation studies, not to that of the original unirradiated extractant.

The pattern of falling strontium extraction $E_a^o$ and restoration of extraction capacity by butting the plant solvent with HDEHP (and TBP) has now been repeated several times. This method of operation has enabled maintenance of adequate extraction recovery from PAW solution. The plant is currently operating with nominal 0.5 *M* HDEHP-0.4 *M* TBP solvent. Hydraulic operations have not been sensibly affected by the increased density and viscosity of the extractant. Extraction recovery of cerium and other rare earths has been excellent throughout also. Periodic butting of the plant solvent with virgin HDEHP and TBP will continue, it is anticipated, until physical properties become limiting.

According to derivative-mode acid-base titration data, the concentration of $H_2$MEHP in plant solvent has remained at or below 0.01 *M* throughout. This observation is consistent with the results of the cyclic $^{60}$Co irradiation test cited earlier and indicates the NaOH washing step is performing as expected. Just as in the cyclic tests, however, absence of appreciable concentrations of $H_2$MEHP in the plant solvent makes it difficult to account for the decreased strontium extraction capacity.

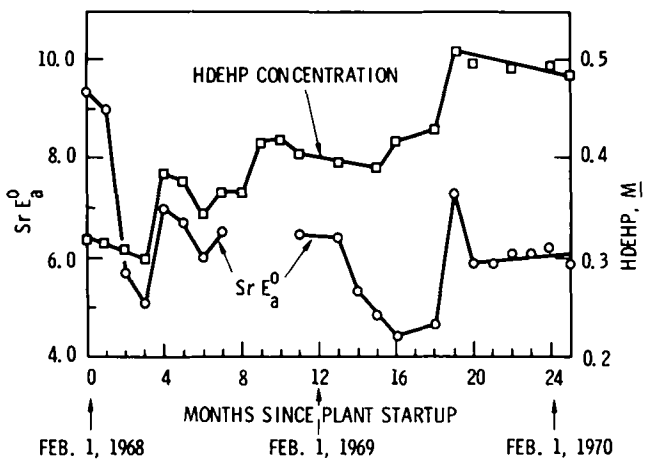


Fig. 3. Properties of B Plant extractant.

With reference to Fig. 3, Sr $E_a^o$ data are not available for the eighth through tenth months of plant operation. Also, the time period encompassed in Fig. 3 includes times when the plant was either not operating or operating with feeds derived from sources other than PAW solution; solvent radiolysis is essentially negligible in both cases.


## ACKNOWLEDGMENTS

Grateful acknowledgment is made to Louise C. Neil and G. E. Smedberg, Pacific Northwest Laboratory, for their assistance in performing the experimental portion of this work. I am also indebted to G. F. Schiefelbein, Pacific Northwest Laboratory, for permission to quote molecular weight data for irradiated HDEHP solutions.


## REFERENCES


1. S. J. BEARD, R. J. KOFOED, J. J. SHEFCIK, and P. W. SMITH, "Waste Managment Program—Chemical Processing Department," HW-81481, General Electric Company (1964).

2. R. L. MOORE, L. A. BRAY, and F. P. ROBERTS, in *Solvent Extraction Chemistry of Metals*, H. A. C. McKay, T. V. Healy, I. L. Jenkins, and A. Naylor, Eds., p. 401, CRC Press, Cleveland, Ohio (1967).

3. D. E. LARSEN, "Atlantic Richfield Hanford Company Radioactive Waste Management Program," ARH-2185, Atlantic Richfield Hanford Company (1971).

4. G. L. RICHARDSON, "Application of Aqueous Technology to LMFBR Separations Processes. Program Plan for Task T-1: Solvent Performance," WHAN-FR-32, WADCO Corporation (1970).

5. R. M. WAGNER and L. H. TOWLE, "Radiation Stability of Organic Liquids—Semi-Annual Report No. 3 for January-June, 1957," AECU-4053, Stanford Research Institute (1958).

6. I. A. KUZIN, A. M. SEMUSHIN, and V. N. ROMANOVSKII, "Stability of Di(2-ethylhexyl) Hydrogen Phosphate Against Radiation," *Khim. Vysokikh Énerg.*, **3**, 275 (1969).

7. J. A. PARTRIDGE and R. C. JENSEN, "Purification of Di(2-ethylhexyl)phosphoric Acid by Precipitation of Copper (II) Di(2-ethylhexyl)phosphate," *J. Inorg. Nucl. Chem.*, **31**, 2588 (1969).

8. J. M. SCHMITT and C. A. BLAKE, Jr., "Purification of Di(2-ethylhexyl)phosphoric Acid," ORNL-3548, Oak Ridge National Laboratory (1964).

9. J. W. T. SPINKS and R. J. WOOD, *An Introduction to Radiation Chemistry*, p. 112, John Wiley and Sons, New York (1964).

10. L. STIEGLITZ, Personal Communication (June 1970).

11. M. H. CAMPBELL, "Gas Chromatographic Analysis of Solvent Used in Reactor Fuel Reprocessing and Fission Product Recovery," *Anal. Chem.*, **38**, 237 (1966).

12. E. P. CLARK, "The Signer Method for Determining Molecular Weights," *Anal. Chem.*, **13**, 820 (1941).

13. D. F. PEPPARD and G. W. MASON, "Some Mechanisms of Extraction of M(II), (III), (IV), and (VI) Metals by Organophosphorus Extractions," *Nucl. Sci. Eng.*, **16**, 382 (1963).

14. J. R. FERRARO and D. F. PEPPARD, "Structural Aspects of Organophosphorus Extractants and Their Metallic Complexes as Deduced from Spectral and Molecular Weight Studies," *Nucl. Sci. Eng.*, **16**, 389 (1963).

15. W. W. SCHULZ, "Effects of Some Synergistic and Antagonistic Agents on HDEHP Extraction of Strontium," BNWL-759, Pacific Northwest Laboratory (1968).

16. H. J. McDOWELL, "Synergistic and Solvent Effects in the Extraction of Strontium and Sodium by Di(2-ethylhexyl)phosphate," *J. Inorg. Nucl. Chem.*, **30**, 1037 (1968).

17. D. C. STEWART and H. W. CRANDALL, "The Separation of Mixtures of Mono- and Di-Substituted Alkyl Phosphoric Acids," *J. Am. Chem. Soc.*, **73**, 1377 (1951).

18. K. B. BROWN et al., "Progress Report; Uranium Chemistry of Raw Materials Section January 1, 1952 to March 31, 1952," ORNL-1308, Oak Ridge National Laboratory (1952).

# STUDIES OF FUEL-CLAD MECHANICAL INTERACTION AND THE RESULTING INTERACTION FAILURE MECHANISM

FUELS

**KEYWORDS:** *fuel elements, performance, power, burnup, control elements, mockup, uranium dioxide, fuel cans, reaction kinetics, radiation effects, operation, fuel rods, deformation, expansion*

E. ROLSTAD and K. D. KNUDSEN *Institutt for Atomenergi, P.O. Box 173 N-1751 Halden, OECD Halden Reactor Project, Halden, Norway*

Received June 4, 1971
Revised September 17, 1971

*Fuel performance studies at the Halden reactor have given valuable information on how various design parameters affect the mechanical interaction between fuel and cladding. The experiments have also indicated how the interaction is dependent on burnup and on the actual power history of the fuel rod.*

*This information was obtained by means of differential transformer type of detector, measuring the changes in length and diameter of fuel rods while operating at power in the reactor.*

*Based on this experience, a simple graphical model has been proposed for the prediction of interaction between fuel and cladding as a function of power history and burnup. This concept, referred to as "iso-gap curves," clearly demonstrates the importance of avoiding an increase in power at high burnup and could be useful when planning reactor operations with respect to fuel management schemes, i.e., power changes, control rod movement, fuel shuffling, and loading.*

## INTRODUCTION

There is experimental evidence that high burnup fuel has a tendency to fail from the clad strain produced by mechanical interaction if the power is suddenly increased beyond its normal operating value. Whether a failure will occur depends not only on the original fuel rod design, burnup level, power level, and magnitude of the power increase, but also on the complete previous operation history of the fuel rod. This failure mechanism therefore appears to be very complex and more difficult to predict than any of the more commonly known power limitations, burnout, for example. The amount of experimental evidence related to this phenomenon is also very limited, and therefore we have not been able, so far, to build up a quantitative correlation that can predict interaction failures. It is therefore difficult to judge whether this failure mechanism will impose serious limitations on the operation of today's power reactors.

## GENERAL DESCRIPTION OF THE FUEL-CLAD MECHANICAL INTERACTION MECHANISM

When operated in a reactor, the diameter of the $UO_2$ fuel pellets will increase relative to their unirradiated value for two reasons:

1. thermal expansion effects, including thermal shape distortion and fuel cracking
2. irradiation induced swelling and fuel relocation effects.

The thermal expansion effects are approximately proportional to power and therefore apply directly from startup. The swelling is an increasing function of burnup and becomes gradually more important toward the end of the irradiation lifetime. Consider an unirradiated fuel rod which is gradually brought to full power. Its fuel pellets will start off as right circular cylinders but will expand thermally and distort to hourglass shaped bodies with convex ends. At a relatively low power level, the thermal hoop stress will generate radial cracks which will open, causing mechanical interaction with the clad. The magnitude of the interaction forces will be dependent on the power level and on design parameters, for example, the size of the fuel-clad clearance. The length of the pellets will also increase, and the pellets therefore slide upward

relative to the clad. Friction forces will oppose the sliding and build up a tensile force system in the clad and an equal axial force system compressing the pellet stack. As power is increased the interaction forces will also increase and more cracks will form both radially and across the pellet length. This progressive fuel cracking is, of course, an irreversible process. The interaction behavior of a fuel rod during the first startup is therefore very different from its later behavior, when the pellet already is cracked into a number of smaller pieces.

As explained, most of the interaction forces will be applied locally at the pellet ends resulting in local strain concentrations. Each of these strains is very small but add up to give measurable increases in the clad length and diameter ("bamboo ridges") at the pellet interfaces.

If the power is maintained steady at maximum, no further strain will be produced by thermal expansion but the fuel diameter will start to increase gradually from fuel swelling and will strain the clad. Under these conditions the interaction forces will, however, also compress the fuel so that part of the volume increase from swelling will be accommodated by plastic flow and fuel densification in the hot part of the fuel. If, however, the power history is more irregular, the swelling induced strain will not be applied continuously but as strain increments during power peaks.

The magnitude of the strain increment occurring during a power peak will be dependent on the maximum power level and on the amount of fuel swelling that has occurred since the last power peak that strained the clad. The amount of strain will also be dependent on how fast the power was increased. A large number of in-reactor experiments at Halden, using differential transformer types of instruments to measure the length change of the fuel rod and pellet stack and also the complete diameter profile of a fuel rod, support this general description.

As an example of these measurements some results from the IFA-118 series of experiments[1] are presented.

The rig, IFA-118, carried two four-rod fuel clusters, one above the other. The length change of each of the eight fuel rods was measured by means of differential transformer elongation detectors. The fuel rods were supported in the rig so that they could be removed and replaced by new ones after the scheduled irradiation period. The same rig, IFA-118 was used with three different fuel rod loadings so that a total of 24 rods took part in the experiments. The three different loadings were called IFA-118 I, II, and III in the same order as they were irradiated. Each of the loadings stayed in the reactor for one irradiation period of ~3 months.

The design parameters of the 24 fuel rods were systematically varied to study the effect of the following on the fuel rod elongation and bamboo-ridge formation during startup phase and low burnup operation:

| | |
|---|---|
| pellet length | 7, 14, 20, and 30 mm |
| gap size | 40 and 100 $\mu$m |
| pellet end shape | flat, dished, and dished-chamfered. |

Figure 1 shows typical elongation behavior which is qualitatively representative for all 24 rods. This was recorded during the first power cycle starting at a positive power ramp from zero to full power, immediately followed by a negative ramp back to zero power. The complete cycle took place over 15 to 20 h. The figure shows that during the positive ramp the rod elongated by ~0.45% and that when the power was reduced to zero again, approximately two-thirds of this remained as a permanent strain. Next time the power was increased, the elongation followed the same curve as for the first negative ramp of the first cycle, and the rod continued to operate along this curve until it was removed from the reactor at a burnup of 1200 MWd/t $UO_2$. The elongation behavior during the first positive ramp is therefore completely different from all the later power ramps. We believe that this difference comes partly from the fact that the fuel has expanded the clad and created ridges etc., so that it fits to the pellet stack at maximum power. Another difference which is probably even more important is

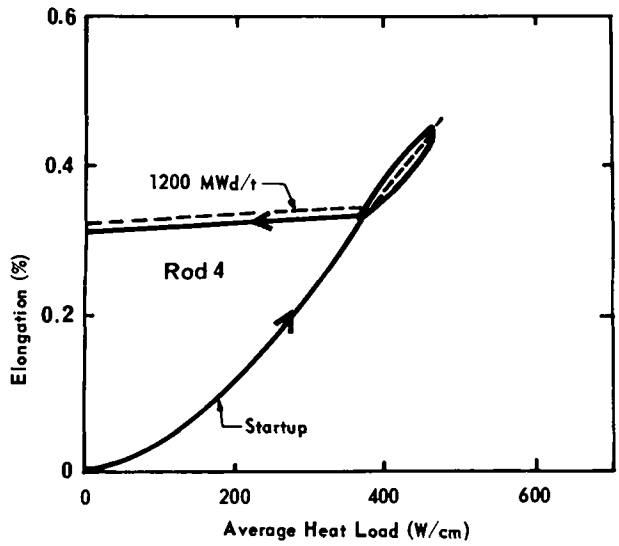


Fig. 1. Typical rod elongation behavior during startup phase.

that during the first power ramp the pellets start as uncracked pellets, and that they gradually crack up as power is increased. A pellet that has been at high power and therefore is heavily cracked does not distort thermally at lower power as much as it did during the first startup. During later operation, before the fuel swelling becomes important, the fuel rod is therefore free from interaction up to ~85% of the maximum power it has seen before.

Even if all the 24 pins of the IFA-118 experiments showed a qualitatively similar behavior, their quantitative elongation would vary substantially depending on the design parameters used.

Figure 2 shows the effect of pellet length, Fig. 3 the effect of varying the pellet end shape, and Fig. 4 the effect of the gap size.

The heights of the bamboo ridges were measured after the rods were removed from the reactor. The conclusions from these measurements were:

1. There was no influence of gap size on ridge height.
2. Dished pellets produce ridges larger than flat ended pellets by a factor 2.
3. The dished and chamfered pellet gave approximately the same ridge height as the flat-ended pellets.
4. The 14-, 20-, and 30-mm-long pellets gave the same ridge height, but the 7-mm-long ones had 50% smaller ridges.

These results form a good basis for designing fuel that will give small ridges and a small axial startup strain. The experiments have also given

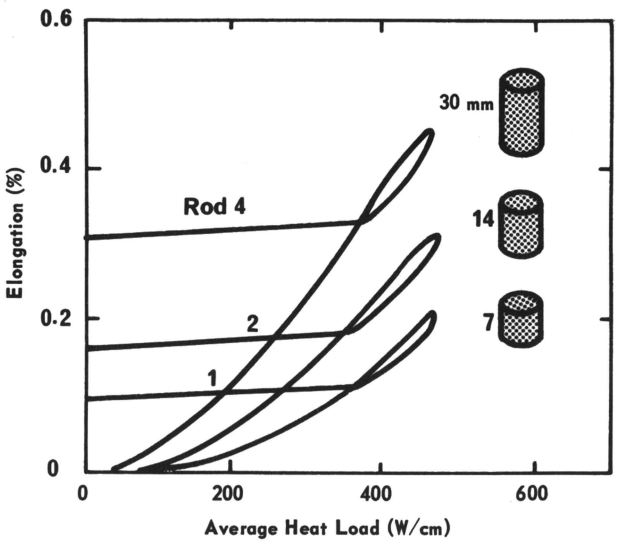


Fig. 2. Influence of pellet length on rod elongation.

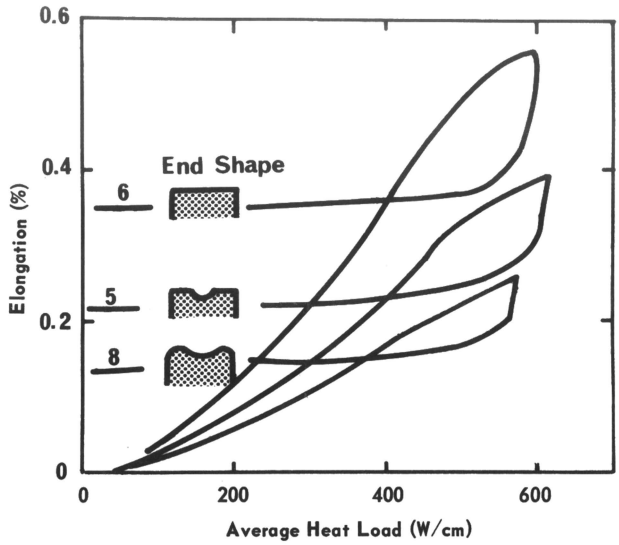


Fig. 3. Influence of pellet end shape on rod elongation.

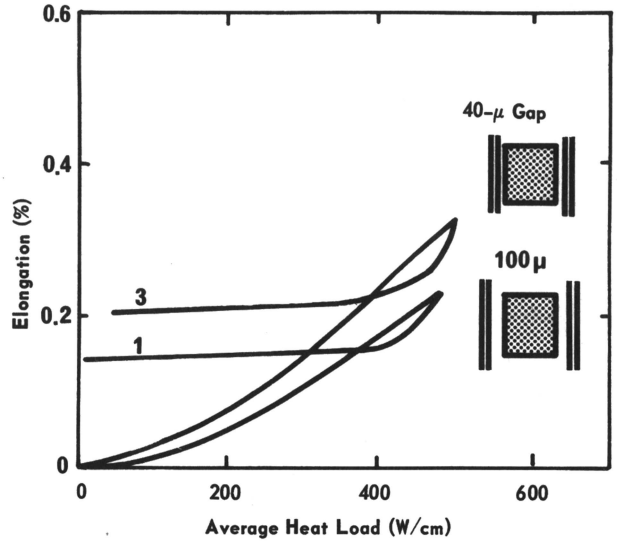


Fig. 4. Influence of gap size on rod elongation.

indication about how to reduce the strain by adopting special startup procedures.

We do not, however, know how important it is to reduce the startup strain because this apparently does not result in failures even with the most unfavorable design and mode of operation, and most of the elongation differences between long or short, flat or dished pellets seem to disappear after the first positive ramp.

If the fuel is operated so that the clad is strained late in its irradiation life, for example by a power excursion, then the risk of failure is appreciably higher. The reason for this is that the clad ductility has been reduced by neutron bombardment and chemical attack to such an extent

that it is unable to accommodate even a moderate strain, which would have caused no harm early in the irradiation period. The change in the clad ductility with burnup and the swelling induced change in fuel diameter are the most important phenomena related to the interaction failure mechanism. These two phenomena are therefore discussed briefly.

## CHANGE IN CLAD DUCTILITY WITH IRRADIATION

There are three general effects of neutron irradiation on the properties of Zircaloy:

1. increase in yield and tensile strength
2. decrease in ductility, and especially the uniform elongation to fracture
3. decrease of the work hardening capability.

The rate of embrittlement is dependent on temperature, spectrum, and fabrication variable. Appreciable recovery of radiation damage does not occur at temperatures below ~300°C. The damage-fluence relationships are fairly well established and seem to follow an inversed exponential function. The embrittlement rate is thus expected to decrease with increasing fluence and finally result in saturation. The fluence needed for saturation is subject to disagreement. Fluence values in the range $5 \times 10^{19}$ n/cm$^2$ to $10^{21}$ n/cm$^2$ have been reported. This disagreement probably reflects differences in materials and spectra. There are indications, however, that the more ductile materials retain their ductility to larger fluences than the harder and stronger materials. In addition, texture effects probably are important factors.[2-4]

Figure 5 shows strain-to-failure measurements performed on some of the cladding tubes irradiated in the Halden reactor. The results are plotted against burnup of the contained fuel.

## CHANGE IN OUTSIDE FUEL DIAMETER FROM FISSION PRODUCT SWELLING AND FUEL RELOCATION

The fuel volume will increase with burnup due to the solid and gaseous fission products produced.[5,6] During the initial phase the fuel will swell inward and little will be seen on the outside diameter. From some threshold value in burnup, however, the swelling will also affect the fuel diameter and make it increase approximately linearly with burnup. The threshold burnup at which this occurs and also the rate of swelling will be dependent on power and fuel design parameters.[7] The degree of constraint from the clad will also influence the rate of swelling and relocation.

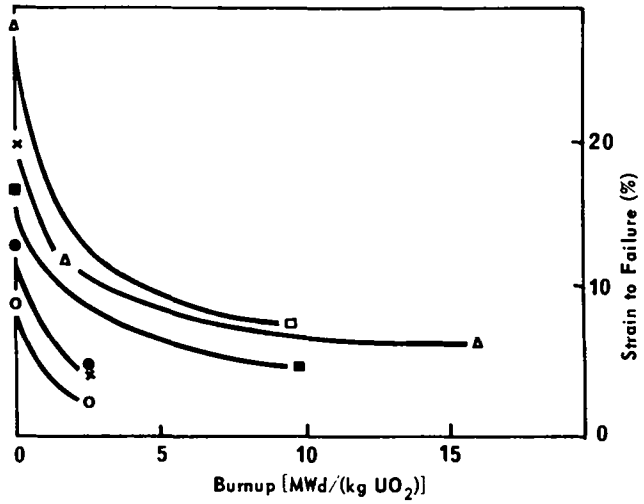


Fig. 5. Change in clad ductility with burnup.

## A GRAPHICAL PRESENTATION OF THE FUEL-CLAD MECHANICAL INTERACTION LIMIT AS A FUNCTION OF BURNUP

Figure 6 shows a type of plot developed to illustrate how the interaction limit will change with burnup. The $Y$ axis of this plot is a power axis. The plot to the left of this axis shows diametral clad strain, with the initial clearance as parameter. The $X$ axis to the right is a burnup axis. This plot shows a number of iso-gap (or iso-strain) curves. These curves are so designed that if the power of the fuel rod follows one of these lines, no change in the gap size will take place, or if the fuel already is in contact, no further diametral strain will be produced.

When building up the iso-gap curves, it has been assumed that for this particular rod design no diametral swelling takes place up to a burnup of 5 MWd/(kg $UO_2$) but that from this burnup level the fuel diameter will increase linearly with burnup. If we consider a fuel rod with a clearance of 0.15 mm, the diametral strain plots show that the power can be brought up to 650 W/cm before hard interaction takes place and the clad is strained. The iso-gap curves which correspond to this power level are defined as the "original interaction limit" for this rod. The fully drawn line represents an imagined power history. At a burnup of ~12 MWd/(kg $UO_2$) the original interaction limit is exceeded and the fuel interacts with the clad and strains it plastically. The interaction limit is therefore lifted upward. The "new interaction limit" is defined as that one of the iso-gap curves which is a tangent to the previous operation history. At point B this new interaction limit is again touched and at point C it is exceeded and a failure is imagined to have taken place.

The strain increments produced each time the interaction limit is exceeded can be found by moving backward along the actual iso-strain curve to the power axis and over to the diametral strain curve corresponding to the initial clearance of the rod. The strain increments found by this method should be regarded as maximum values because the plastic flow in the $UO_2$ is ignored, which tends to reduce the strain especially if the interaction limit is exceeded gradually. The amount by which the interaction limit can be exceeded before the rod fails will in some way be coupled to the strain-to-failure curves shown in Fig. 5, so that at low burnup the interaction limit can be exceeded drastically without a failure; at high burnup, however, even a small overpower can be detrimental.

Note that the interaction plot is specific for one rod design so that, for example, if the fuel density is changed, then a different interaction plot must be designed.

When using the interaction plot, it should also be remembered that it works with local values of heat load and burnup. This is illustrated in Fig. 7. The axial power distribution along a fuel rod is assumed here to change gradually through the operation period from a top-heavy flux at startup, through a more symmetric one midway in the period (dotted curve), and end with a bottom-heavy flux as shown in the small inserted picture.

Three points along the fuel rod are considered. Point 2, representing the midpoint of the rod, has been assumed to follow the line marked 2 in the interaction plot. Point 1 starts at high power but falls off strongly with burnup and therefore moves very favorably in the interaction plot. For point 3, however, the power starts off low but increases with burnup and the iso-gap curves are crossed in the wrong direction and the gap thus decreases. The initial clearance of the rod will decide whether interaction and possibly also failure will take place. This example shows that it is not always sufficient to monitor that part of the fuel which sees the highest power.

From the interaction plots one may get the impression that the interaction problem can be avoided simply by increasing the gap size sufficiently. This, however, has the negative effect that the heat impedance from fuel to clad will increase. Figure 8 shows how the relationship between the heat load corresponding to fuel melting for a new fuel rod is dependent on the gap size. The gap size is expressed here as a percentage of outer fuel diameter. From this figure, it can be seen that if the gap exceeds 1.5%, then the fuel will melt at a lower power than when using a smaller gap. The margin to center melting is therefore reduced, at least during the first part of the irradiation period. Figure 8 was computed by means of a fuel temperature calculation program in use at the Halden project.[8]

## EXPERIMENTAL RESULT

As a concrete example, Fig. 9 shows interaction plots for the instrumented fuel assembly, IFA-21, which we believe failed by mechanical interaction.

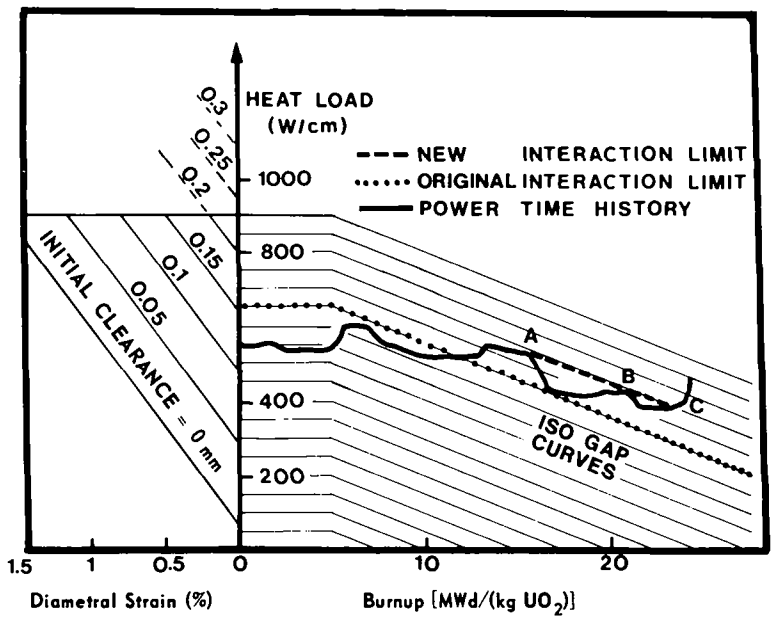


Fig. 6. The iso-gap curve concept.

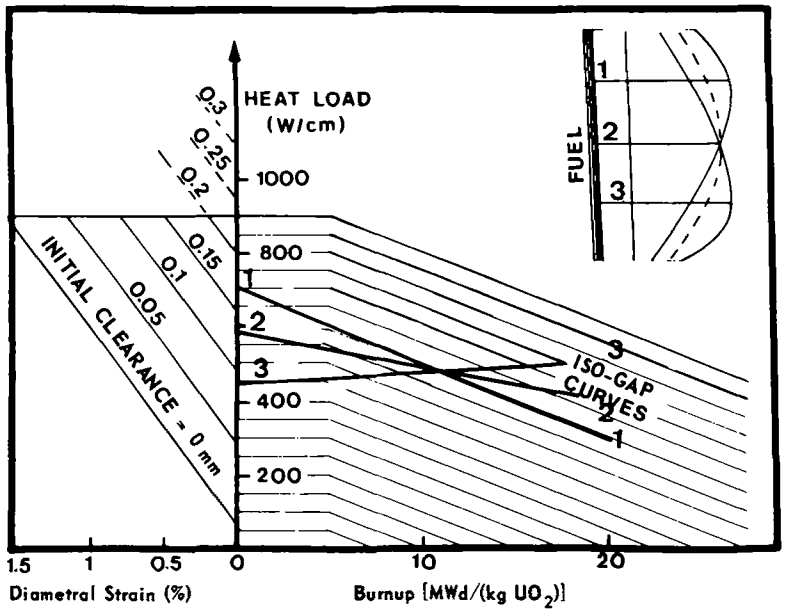


Fig. 7. Influence of a change in axial power distribution on interaction.

This assembly contained five fuel rods. Four of these rods had a very small gap of 0.05 mm. The gap of the fifth rod was 0.16 mm.

The rods were operated at a maximum power of ~600 W/cm up to a burnup of 5 MWd/(kg $UO_2$). The power was then reduced to 450 W/cm and irradiation continued. At a burnup of 10 MWd/(kg $UO_2$) the power was again increased to little more than 600 W/cm. The consequence of this was that all the four low clearance rods failed but the large clearance rod was intact. Postirradiation examination showed a large number of axial cracks in the clad. From the smallest of these, it could be seen that the cracks had started from the ridge positions and from the inside of the clad.

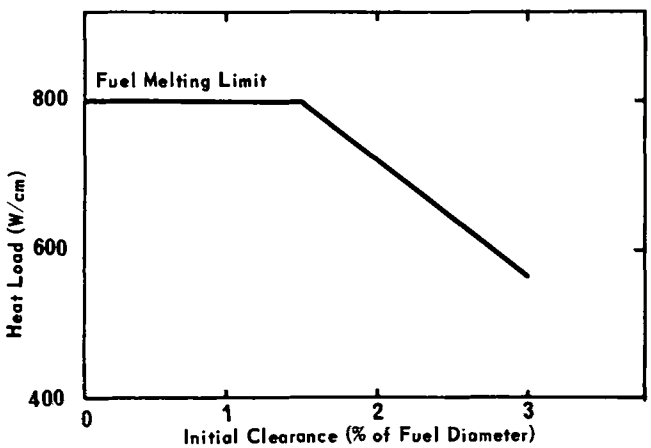


Fig. 8. Influence of gap size on fuel melt limitation.

Small incipient cracks were also found in the large clearance rod but these had not penetrated through the clad. This rod obviously had an advantage of the larger gap relative to the four others, but if the power excursion had been somewhat larger, this rod would have failed also.

Figure 9 shows an interaction plot for the low clearance rods and Fig. 10 for the large clearance rod. These experiments were repeated in the R-2 reactor in Sweden using similar rods and operation history. The results from these experiments agreed well with the Halden experiments.

Another piece of experimental evidence is coming from a series of interaction failure experiments being performed as a joint effort between AB Atomenergy and ASEA-ATOM, Sweden and Institutte for Atomenergy Norway. Six fuel rods from one of the first Halden instrumented fuel assemblies IFA-4, which was loaded during Autumn 1963, and unloaded during Spring 1970, have been transported to Sweden for interaction failure experiments. Two of these tests were made during April 1971. One of the rods failed at ~500 W/cm maximum heat load and the other at ~570 W/cm.[9]

Figure 11 shows the approximate power burnup history, representative of the upper end of these rods. The rods were operated in the lower half of the Halden core. The axial power distribution to which the rods were exposed during the failure test in the R-2 reactor is, of course, different from the distribution in the Halden reactor. This complicates the evaluation of the results. The initial diametral clearance is in the tolerance range 0.11 to 0.25 mm. The plot shows that the

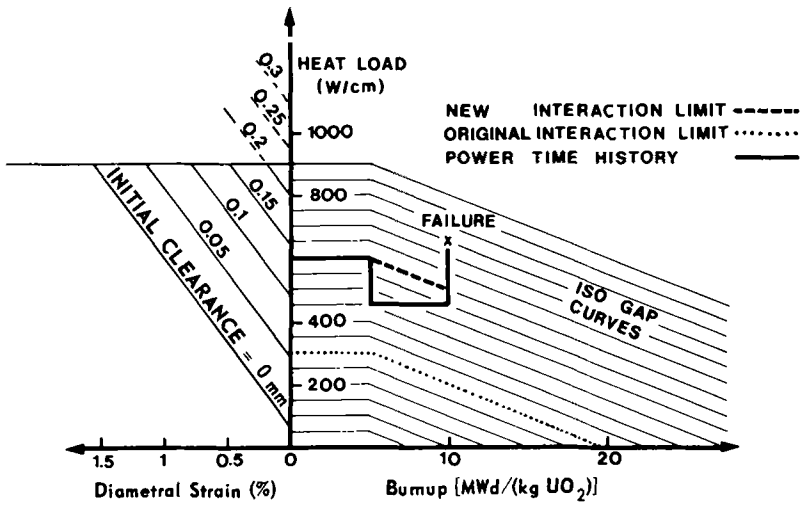


Fig. 9. Interaction plot for the 0.05-mm clearance rod in IFA-21.

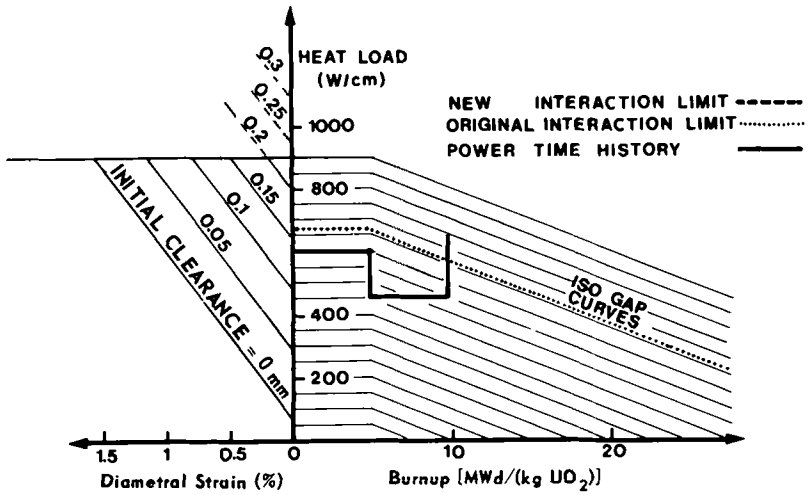


Fig. 10. Interaction plot for the 0.16-mm clearance rod in IFA-21.

rods also must have been very close to failure during the last high power operation in the Halden reactor at ~20 MWd/(kg $UO_2$), and postirradiation showed that, in fact, one rod had failed.

## FUTURE DEVELOPMENT WORK

The interaction plot illustrates the basic ideas of fuel-clad mechanical interactions and how these develop with burnup. The present plot, however, is based on a number of simplified assumptions and should therefore not be used too quantitatively. For example, the thermal expansions are computed by a simple model which ignores the thermal hourglassing and cracking of the fuel pellets. In-core measurements have shown that the fuel even for large clearance rods (0.2 to 0.3 mm) interacts sufficiently hard with the clad already at 400 to 500 W/cm during first startup to produce both bamboo ridges and axial permanent strain. This is in disagreement with the interaction plot and indicates that the power scale of the plots is too optimistic.

Also, the swelling model is too simple and, for example, takes no account of the influence of power level on the rate of diametral swelling with burnup.

If a more realistic thermal expansion and swelling model were applied, the iso-gap lines would probably not be straight and parallel but would be curved.

As a contribution to the development of more realistic interaction plots, it would be useful to do

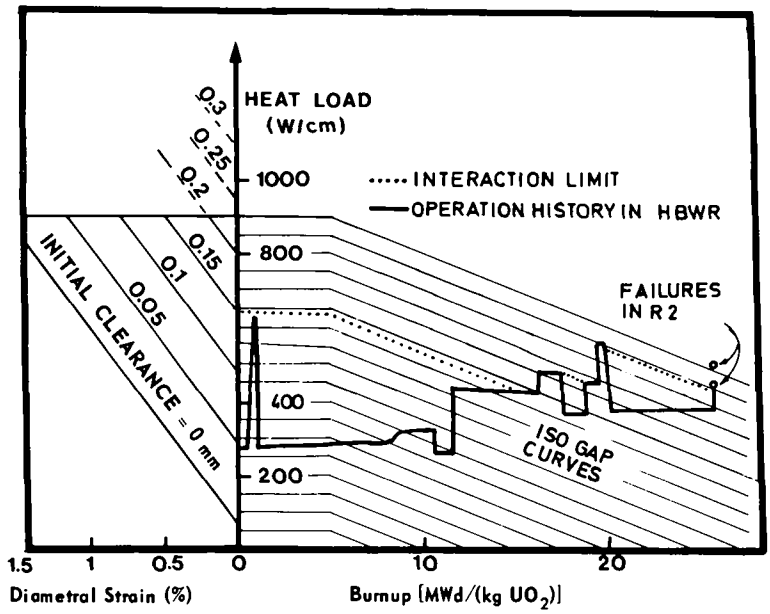


Fig. 11. Interaction plot for the IFA-4 rods.

a series of experiments corresponding to the one illustrated in Fig. 12. In this experiment fuel rods equipped with elongation detectors should be brought to predetermined power level during startup, and the elongation curve registered. The power should then be dropped by ~20% and the irradiation continued for ~2 MWd/(kg $UO_2$). The power should then again be increased until the elongation detector indicates hard interaction. This power level should be plotted as a point on the iso-strain curve. The power should then be reduced again and the same procedure repeated a number of times until the wanted maximum burnup level is reached.

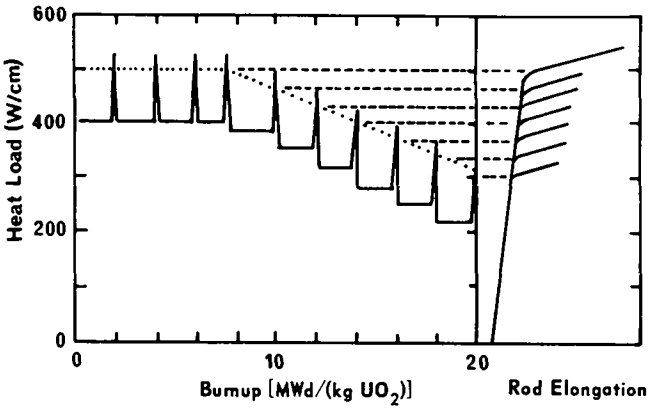


Fig. 12. A possible experiment to determine the interaction limit.

These experiments will make it possible to design more realistic interaction plots that can be used to predict at what power level a fuel rod will start to interact. The second step will be to determine how much the interaction limit can be exceeded before a failure takes place. This will, in some way, be coupled to the strain-to-failure limitation for the clad material as illustrated by Fig. 5. Some rods therefore will be taken out of this interaction limit experiment at different burnup levels and be subjected to a power increase until they fail. The properties of the unirradiated clad material, the rate of power increase during the failure experiment and previous strain history of the clad, are also important parameters. A total strain arrived at by adding the strain-increments algebraically independent on the burnup level at which they occurred will definitely not be a good failure criterion. Some function which weights the strain increments at high burnup more heavily than the startup and low burnup strain must be applied.

## CONCLUSIONS

Clad strain from mechanical interaction generally does not result in failures during startup or early operation because the clad then has sufficient ductility to take the strain. The clad ductility, however, decreases due to neutron bombardment and chemical attack so that at high burnup even a small interaction strain may be sufficient to make the clad crack in a brittle manner.

Two methods to avoid the interaction failures can be considered:

1. development of clad materials that have sufficient ductility even at high burnups.
2. design and operation of fuel so that excessive interaction at high burnup is avoided.

The first method would definitely be the most convenient one, but a large number of reactors have been committed with Zr-2 or Zr-4 clad and no great improvement in these alloys is expected. Also, there does not seem to be any serious competitor to the zirconium alloys as clad material. It therefore seems necessary to make use of the second method and try to operate the reactors so that excessive interaction at high burnup is avoided. This will mean that we first must learn how to avoid interaction from experiments as explained and proposed in this paper where the interaction behavior is studied by means of in-core instruments. Interaction and failure experiments without in-core elongation or diameter measurements are not able to give sufficiently detailed information to contribute positively to this very complicated phenomenon.

To operate a complete reactor core so that interaction failures are avoided will demand a good power distribution evaluation system. The power burnup history for every piece of fuel in the core must be stored by a computer. This information must then be used in connection with the daily operation of the reactor and the fuel management program for giving advice to the operators about, for example, how to load fuel, shuffle fuel, and manipulate the control rods to avoid excessive interaction on the high burnup fuel.

The reduced operational flexibility which may be a consequence of the limits imposed by the interaction failure may result in increased fuel cycle cost. If, however, the limits used are well optimized with respect to failure probability and increased cost, then the reduced number of failures and improved reactor availability should compensate for this and give improved total plant economy.

Finally, we will mention that the work presented is based on experiments with typical BWR fuel rods with a strong freestanding clad. Fuel with a "weaker" clad that collapses onto the fuel, either instantaneously or due to creep, will have a different interaction behavior.

## REFERENCES

1. E. ROLSTAD and K. D. KNUDSEN, "In-Core Study of the Influence of Important Fuel Design Parameters on the Elongation and 'Bamboo-Ridge' Formation of Zircaloy-2 Clad $UO_2$ Fuel Rods," Reaktortagung, Bonn, 3/3 - 2/4 (1971).

2. A. L. BEMENT, Jr., HW-74955, General Electric Company, Hanford Atomic Products Operation (1963).

3. A. L. BEMENT, Jr., *AIME Symposium on Irradiation Effects*, Asheville, Gordon and Breach Science Publishers, New York (1965).

4. G. ÖSTBERG and H. P. MYERS, "Aspects of Swedish Studies of Cladding Materials for Water Cooled Reactors," *U.N. Intern. Conf. Peaceful Uses At. Energy*, 3rd, Geneva, Vol. 9 (1964).

5. R. C. DANIEL et al., "Effects of High Burn-up on Zircaloy-Clad, Bulk $UO_2$, Plate Fuel Element Samples," WAPD-263, Westinghouse Electric Corporation (1962).

6. H. B. MEIERAN, "History of the NRX Reactor X-1-q and X-3-N Tests and the Non-Destructive Examination of their Plate Type Ceramic Fuel Elements," WAPD-TM-455, Westinghouse Electric Corporation (1966).

7. S. AAS, "Mechanical Interaction between Fuel and Cladding," Advanced Course on Limiting Aspects of Fuel Element Performance in Water Cooled Power Reactors at Kjeller, Norway (August 1970).

8. G. KJAERHEIM and E. ROLSTAD, "In-Pile Determination of $UO_2$ Thermal Conductivity Density Effects and Gap Conductance," HPR-80, Institute for Atomenergy, Halden Reactor Project, Lillestrøm.

9. H. MOGARD et al., "Power Increases and Fuel Defection," *U.N. Intern. Conf. Peaceful Uses At. Energy*, 4th, Geneva (1971).

# INSTRUMENTED CAPSULE FOR MEASURING FISSION-INDUCED CREEP OF OXIDE FUELS

FUELS

**KEYWORDS:** *capsules, instruments, design, fission, creep, uranium dioxide, neutrons, strain, shear, testing, operation*

A. A. SOLOMON and R. H. GEBNER
*Argonne National Laboratory, Argonne, Illinois 60439*

Received June 15, 1971
Revised October 4, 1971

*The design, testing, and operation of an instrumented capsule used to study fission-induced creep of stoichiometric enriched $UO_2$ helices are described. Preliminary data are reported for a specimen of 1.82% $^{235}U$ enrichment that was irradiated in the General Electric Test Reactor. A large primary creep component was observed under a load of 211 g (equivalent to an outer fiber shear stress of 2890 psi) at a fission rate of $2.6 \times 10^{12}$ fissions/(cm$^3$ sec) and a maximum specimen temperature of 103°C. Extrapolation of the strain-time creep data yielded a steady-state shear strain rate of $\sim 6 \times 10^{-6}$/h at the outer fibers. Anelastic strain was also observed when the specimen was unloaded and subsequently irradiated.*

## INTRODUCTION

Recent experimental evidence[1-4] indicates that fissioning oxide fuel materials exhibit significantly enhanced plasticity because of the fission event. This enhanced plasticity is especially important at low temperatures where normal thermal creep cannot occur. Enhanced plasticity will affect both the stress level in the cladding generated by the swelling fuel and the fracture[5] and resintering or densification of the fuel.

These problems led to an investigation of in-reactor creep of enriched $UO_2$ at temperatures below 500°C where thermal creep is negligible. A specimen configuration in the form of a helical spring was selected to optimize heat dissipation and to magnify the expected small specimen strains. High heat dissipation resulted from a large surface-to-volume ratio for this configuration, a liquid metal heat-transfer medium surrounding the specimen, close proximity of the specimen to the capsule coolant, and single capsule containment. The specimen strains were magnified 516 times by measuring spring deflection. This greatly increased the resolution of the strain measurement and reduced the reactor time necessary to obtain reliable deformation data.

## CAPSULE DESIGN

The capsule design is shown schematically in Fig. 1. All the capsule structural members were constructed of Type 304 stainless steel unless otherwise specified. The unloaded $UO_2$ spring was held between zirconium grips so that the upper end was fixed in space and the lower end was loaded by the weight of the pushrod assembly. The pushrod transferred the deflections of the loaded spring to a radiation-resistant linear variable differential transformer (LVDT) located outside the high flux region of the General Electric Test Reactor (GETR), where the first irradiation was performed. The bellows system was used to support the pushrod so that the load could be applied to the specimen after the reactor had attained steady-state operation. A second enriched $UO_2$ spring was positioned above the loaded spring to study the effects of irradiation under no-load conditions. Self-powered neutron detectors were used to monitor the flux level and to maintain a constant and equal flux level at both springs during the irradiation. Chromel-Alumel thermocouples at both the LVDT and the loaded and unloaded springs completed the capsule instrumentation. The capsule was filled with the eutectic composition of 78 wt% potassium and 22 wt% sodium (NaK) to the level shown in Fig. 1.

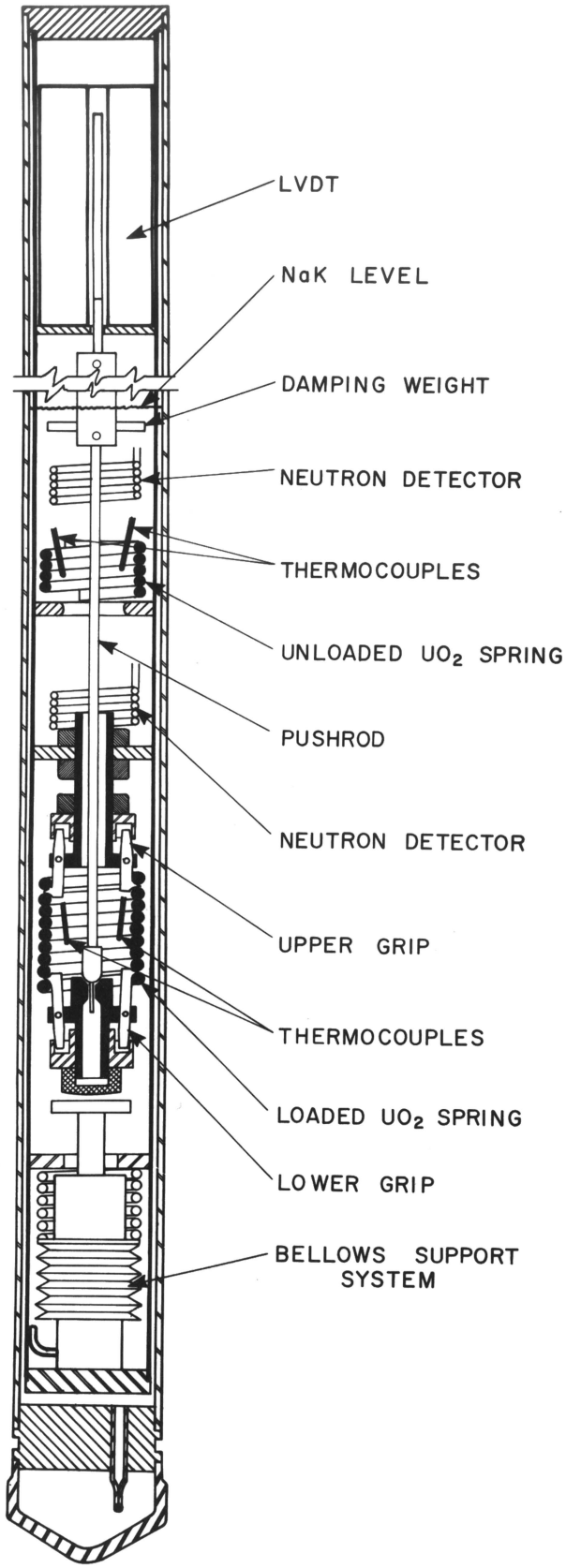


Fig. 1. Instrumented creep capsule.

### LVDT

A radiation-resistant Schaevitz No. 500XS-ZRT LVDT was used to measure spring deflection. Pre-irradiation calibrations indicated that the sensitivity of the LVDT did not vary more than 1% from room temperature to 400°C and was constant with time at any temperature in that range. From neutron flux measurements made by GE at various positions in the GETR, the estimated fast neutron flux at the LVDT was $4 \times 10^9$ n/(cm$^2$ sec), or $\sim 10^6$ n/cm$^2$, for an expected irradiation of 30 days. This was well below the rated LVDT life of $3 \times 10^{20}$ n/cm$^2$.

### Bellows System

The bellows system was designed to operate against a preloaded spring made of Inconel X so that normal operation was from a positive pressure of 25 psig to atmospheric pressure for 2.5 mm of travel. In the event of a pressure loss in the bellows system, the bellows would automatically retract and thereby prevent accidental fracture of the specimen. The operation of the bellows could be observed from the LVDT output as the pushrod load was transferred to the $UO_2$ spring. After ~2-mm elastic deflection of the $UO_2$ spring, the load was completely transferred, and the bellows was retracted the remaining ~23 mm of travel by reducing the bellows pressure to 0 psig.

### Enriched $UO_2$ Spring Specimens

A typical enriched $UO_2$ spring specimen is shown in Fig. 2. An extrusion technique[6] was used to fabricate helices with a circular cross section, thus greatly simplifying the stress and strain analysis. The enrichment of 1.82% $^{235}U$ was uniformly distributed by deflocculation of fully enriched and depleted $UO_2$ powders. Sintering was performed at 1800°C for 2 h in flowing hydrogen, which yielded $UO_{2.000 \pm 0.002}$ with 96% TD, closed porosity, and 22-$\mu$m grain size. The overall spring geometry was 24 ± 0.4-mm o.d. and 1.75 ± 0.17-mm "wire" diameter.

The fabricated springs were x rayed and sections were examined metallographically to reveal microstructural flaws. A typical microstructure (Fig. 3) exhibited equiaxed grain structure and closed porosity. The $UO_2$ springs were proof tested by applying a load 60% greater than the load used for capsule 1. None of the springs fractured during these tests. Several springs were intentionally loaded until fracture occurred at a maximum tensile stress of ~15,000 psi. In addition, out-of-reactor creep tests were performed on the

$UO_2$ springs at 120°C and 7000 psi maximum shear stress. At a sensitivity of $10^{-4}$ cm, no measurable permanent deformation was observed after one week.

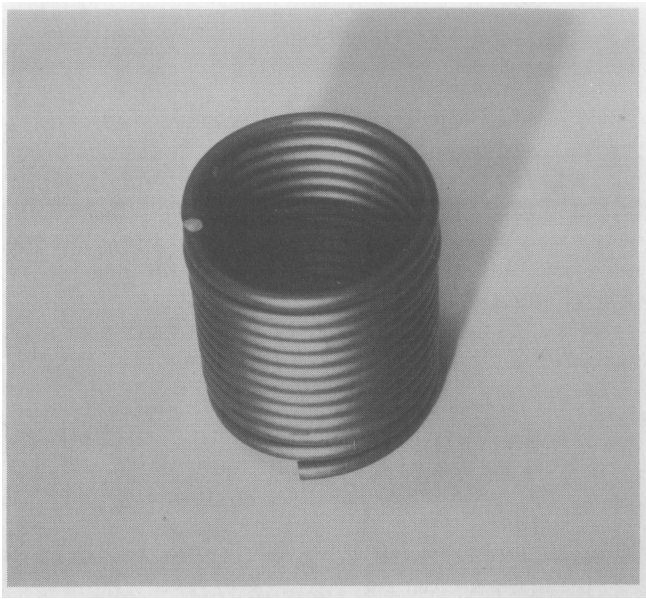

Fig. 2. Typical extruded $UO_2$ specimen.

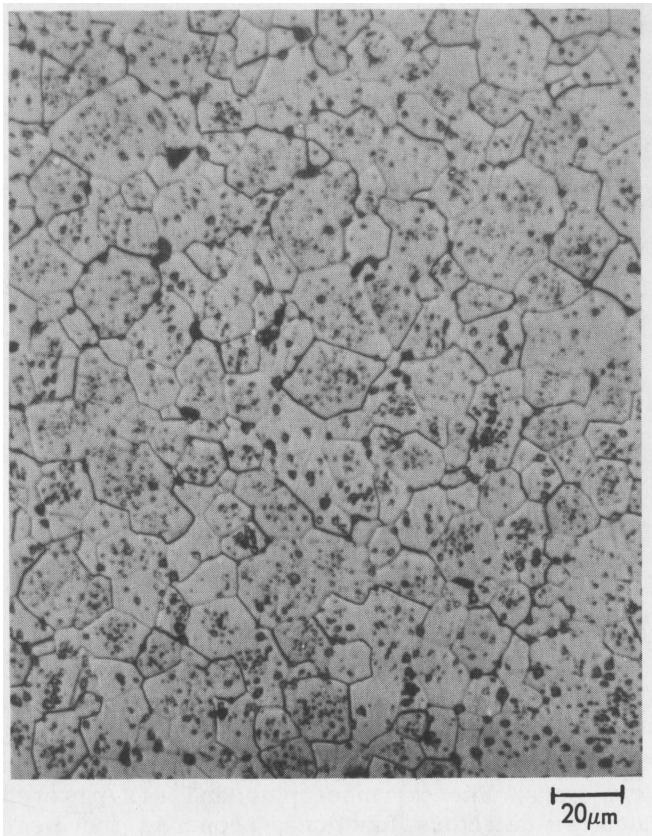


Fig. 3. Typical etched microstructure of enriched stoichiometric $UO_2$ helix.

#### Pushrod

A long hollow tube, sufficiently rigid to prevent buckling and friction during deformation of the $UO_2$ spring, was used to fabricate the pushrod. Damping weights were affixed to the pushrod to load the specimen and to provide damping of the pushrod motion in the NaK pool.

#### Self-Powered Neutron Detectors

Reuter-Stokes Model RSN-202-FL self-powered neutron detectors were selected because of their high sensitivity of $5.63 \times 10^{-20}$ A/n/(cm$^2$ sec) and acceptable burnout rate of 0.23%/month at a neutron flux of $10^{13}$ n/(cm$^2$ sec). The detectors were coiled into an ~2.5-cm-o.d. helix (~1.2 cm long) to optimize the output at a particular capsule location. The flux calculated from the self-powered neutron detector measurements agreed within ~20% with the calculated flux values.[7]

### CAPSULE PROOF TESTING

A number of proof tests were performed to check capsule design, operation, and calibration. The technique[8] used to braze all the thermocouples, self-powered neutron detectors, LVDT, and NaK fill and evacuation tubes simultaneously was evaluated by helium leak testing and subsequent sectioning to examine the braze compound wetting and joint integrity. Brazing was performed in flowing hydrogen at 1180°C using Coast Metal 60 braze alloy and induction heating. The braze-joint configuration (Fig. 4) allowed braze alloy to flow

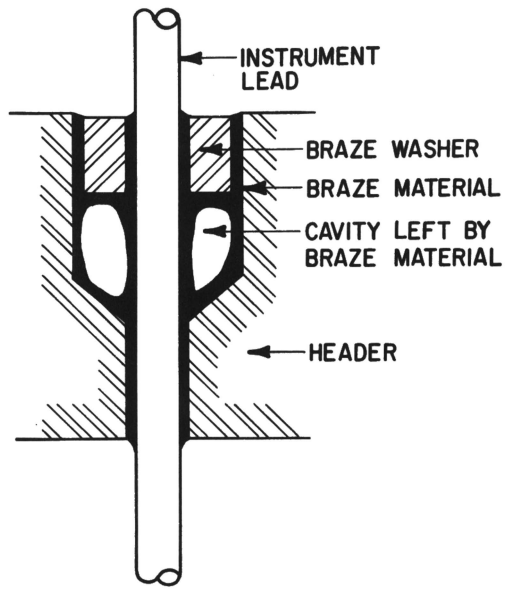


Fig. 4. Typical braze joint geometry.

upward around the washer and form a strong mechanical joint and double containment. Component materials were either Type 304 stainless steel or Inconel 600.

Since the thermocouples could not be allowed to obstruct the deforming $UO_2$ spring, it was necessary to relate thermocouple readings obtained at a distance from the spring with the actual surface temperature of the spring. This was done by filling a mockup capsule with NaK, employing a heater to simulate the fissioning $UO_2$ spring, and positioning thermocouples around the heater. An x ray of the mockup is shown in Fig. 5 and the results of this calibration are shown in Fig. 6. If these results are extrapolated to a fission rate of $1 \times 10^{13}$ fissions/(cm sec), which corresponds to a total power of ~885 W for the loaded spring, the difference between the temperature $\frac{1}{16}$ in. away (thermocouple 2) from the heater, and a temperature $\frac{1}{8}$ in. away (thermocouple 3) was only 7°C. The axial temperature differences (thermocouples 4, 5, and 6), which reflect the NaK convection currents, were 20°C at the same power level. The mockup test was used to predict the capsule temperatures by correcting for the differences in cooling water temperature in the two cases. A predicted temperature of 157°C was obtained at 885 W.[9] This was in good agreement with the temperature of 150°C measured during the first irradiation at the same power level.

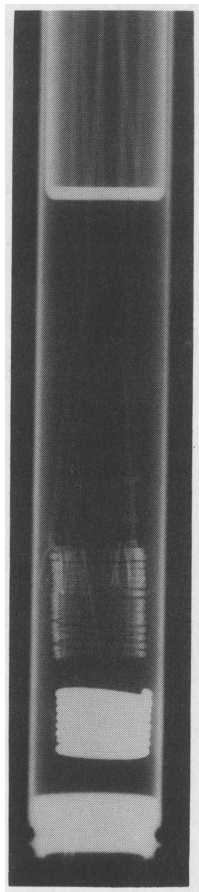

Fig. 5. X ray of capsule mockup.

The $UO_2$ spring that was also included in this mockup (Fig. 5) was used to study the effects of NaK on the spring at capsule operating temperatures. The capsule was soaked for four days at 300°C. When the spring was exposed, the brownish surface color indicated that oxidation had occurred. To avoid this problem, ultra-high purity triple-distilled NaK and high purity He-6% $H_2$ cover gas were used for the first capsule. Special care was taken during NaK filling to maintain a low oxygen potential.

Other tests performed on a second complete capsule mockup verified the following:

1. Capsule temperature changes due to variations in reactor power had a negligible effect on the LVDT output.
2. Deformation of the $UO_2$ springs was coaxial with the centerline of the capsule.
3. Bubbles did not cling to the $UO_2$ spring during NaK filling.
4. Welding and NaK filling could be performed without breaking the springs.

### NaK Fill System

The NaK fill system (Fig. 7) was designed to prevent oxygen contamination and to achieve good wetting of the $UO_2$ helix. All system components were constructed of Type 304 stainless steel and glass. The system, including the NaK pot, was flushed three times with purified He-6% $H_2$ then outgassed at 400°C for 18 h at $10^{-5}$ Torr. The capsule was NaK filled at 200°C with the $UO_2$ specimen loaded so that the coils would be separated and maximum wetting achieved. Subsequent x-ray examination showed excellent wetting by the NaK and the absence of detectable entrapped bubbles in the NaK.

## CAPSULE OPERATION AND RESULTS

The capsule was inserted in pool position X2 of the GETR and located in a low flux position with the specimen supported by the bellows system. Capsule movement was provided by the Vertical-Radial Adjustable Facility Tube (V-RAFT) transport mechanism. The reactor was brought to full power and achieved steady-state operation after two days. The thermocouples and self-powered neutron detectors functioned properly; the measured temperature at the loaded spring was 102 ± 2°C, (or a maximum specimen temperature of

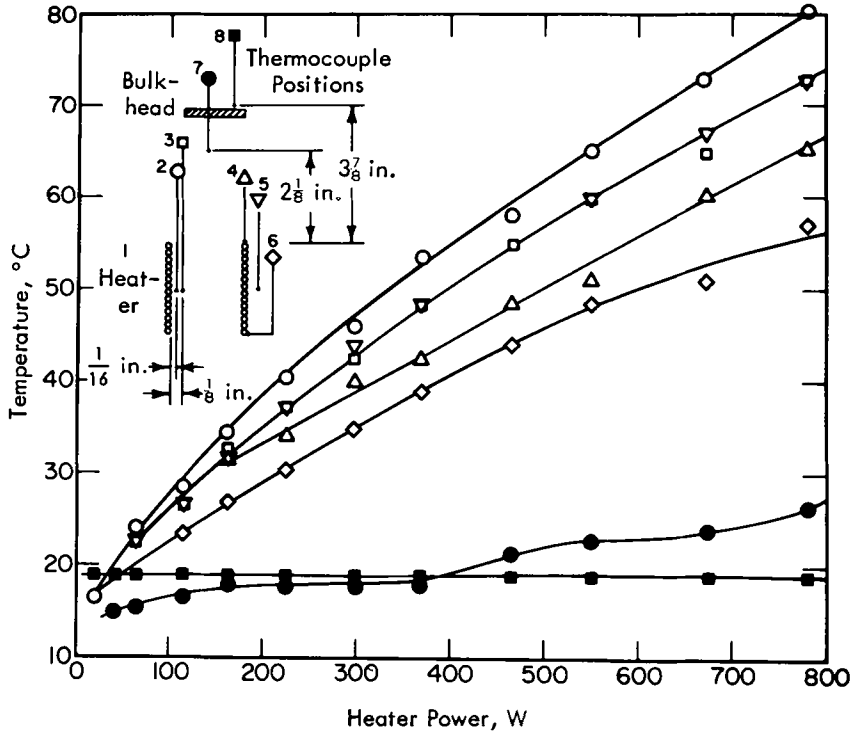


Fig. 6. Thermocouple calibration.

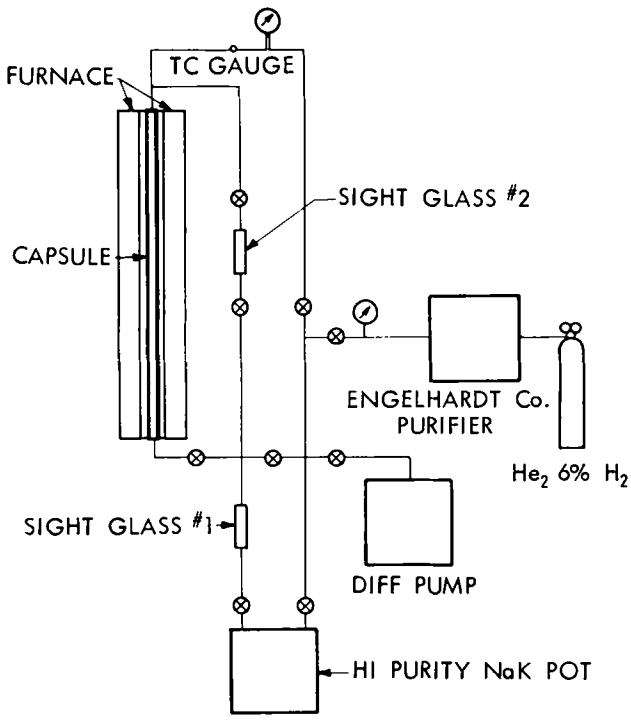


Fig. 7. NaK fill system.

103°C) the measured flux was $1.6 \times 10^{13}$ n/(cm$^2$ sec), and the calculated[7] fission rate was $2.6 \times 10^{12}$ fissions/(cm$^3$ sec).

The spring was then loaded for two days with 211 g,[a] which corresponded to a maximum shear stress of 2890 psi. A total deflection of 5 mm was measured during this time. The creep curve (Fig. 8) obtained under these conditions showed a large primary creep component that was even more evident when the strain rate was plotted as a function of shear strain, as shown in Fig. 9. The extrapolated steady-state shear strain rate was $\sim 6 \times 10^{-6}$/h. After obtaining this creep curve, an attempt was made to increase the fission rate by moving the capsule to a higher flux position, but a sudden movement of the transport mechanism caused the loaded spring to break.

Because of the malfunction in the transport mechanism, two changes were made in the capsule

[a] Calculated by adding the weight of the pushrod, lower grip, and one-half the weight of the specimen and subtracting the buoyancy force from the NaK. The buoyancy force was determined by measuring the volume of water displaced by the pushrod, lower grip, and one-half the spring using an immersion technique and calculating the buoyant force from the same volume of NaK displaced.

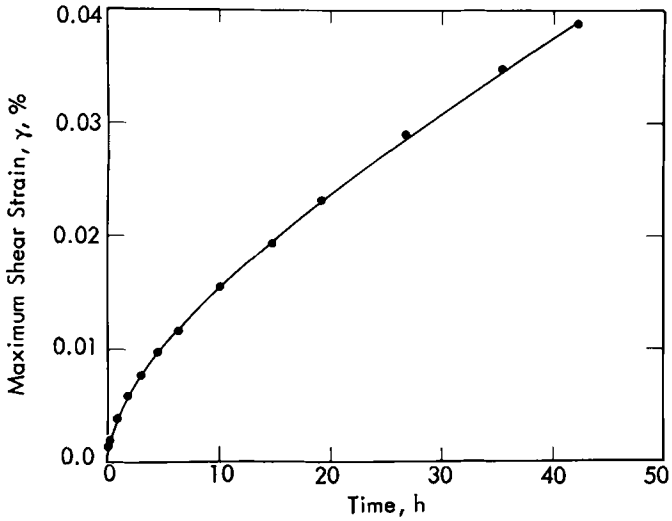


Fig. 8. Maximum shear strain $\gamma_p$ as a function of time.

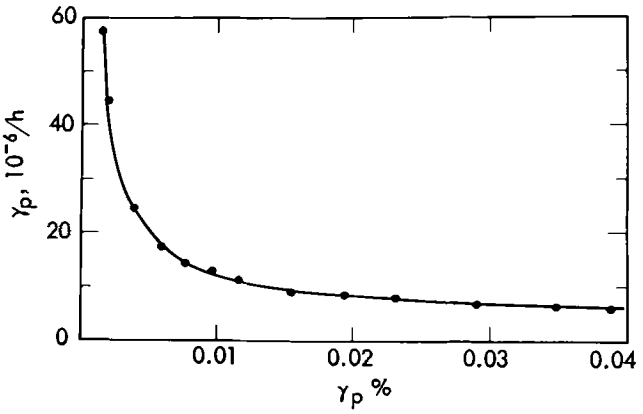


Fig. 9. Variation of maximum shear strain rate $\dot{\gamma}_p$ with maximum shear strain.

design and transport mechanism for subsequent irradiations. First, it was decided to support the spring before any capsule movement so that sudden motion would not cause breakage of the specimen. To make the bellows movement as controllable as possible during the critical support procedure, a bellows guide was added to prevent lateral motion. By measuring the displacement of the pushrod when it was in contact with the bellows, it was determined that bellows motion was controllable within ±0.002 cm. Second, a new transport mechanism was built and carefully aligned and tested to minimize sticking.

After the loaded spring fractured, the reactor cycle was completed by calibrating the thermocouples and neutron detectors with respect to the V-RAFT motions. The capsule was accordingly first moved downward to the peak flux and then radially to the position nearest the reactor core (full-in). After this calibration, the springs were left in the full-in position for two days, until the end of the reactor cycle, to study the swelling and integrity of the $UO_2$ springs at high [$2 \times 10^{13}$ fissions/(cm$^3$ sec)] fission rates. During this calibration and high flux exposure, the bellows support was raised so that the lower fragment of the broken spring would be returned to the position it occupied before fracture occurred. This adjustment was made so that more realistic capsule temperatures would be obtained.

The relation between measured fluxes using the self-powered neutron detectors and the calculated values is shown in Fig. 10. The initial nonlinearity at low flux probably originates from errors

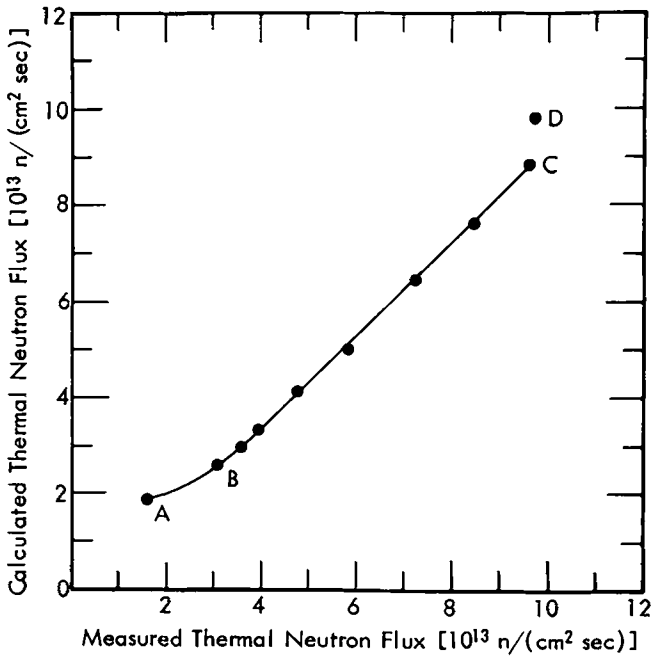


Fig. 10. Relation between measured and calculated thermal neutron flux.

in the calculated fluxes for the full-up position A and the peak flux position B. The linearity from B to C corresponds to radial capsule motion. The deviation at D could have resulted from the capsule arriving at the full-in position before anticipated, or from binding in the transport mechanism. Most important, however, the self-powered neutron detectors yielded good relative flux values that could be used to study the effect of fission rate on the creep rate.

Pre-irradiation and postirradiation neutrographs of the capsule (Fig. 11) revealed several

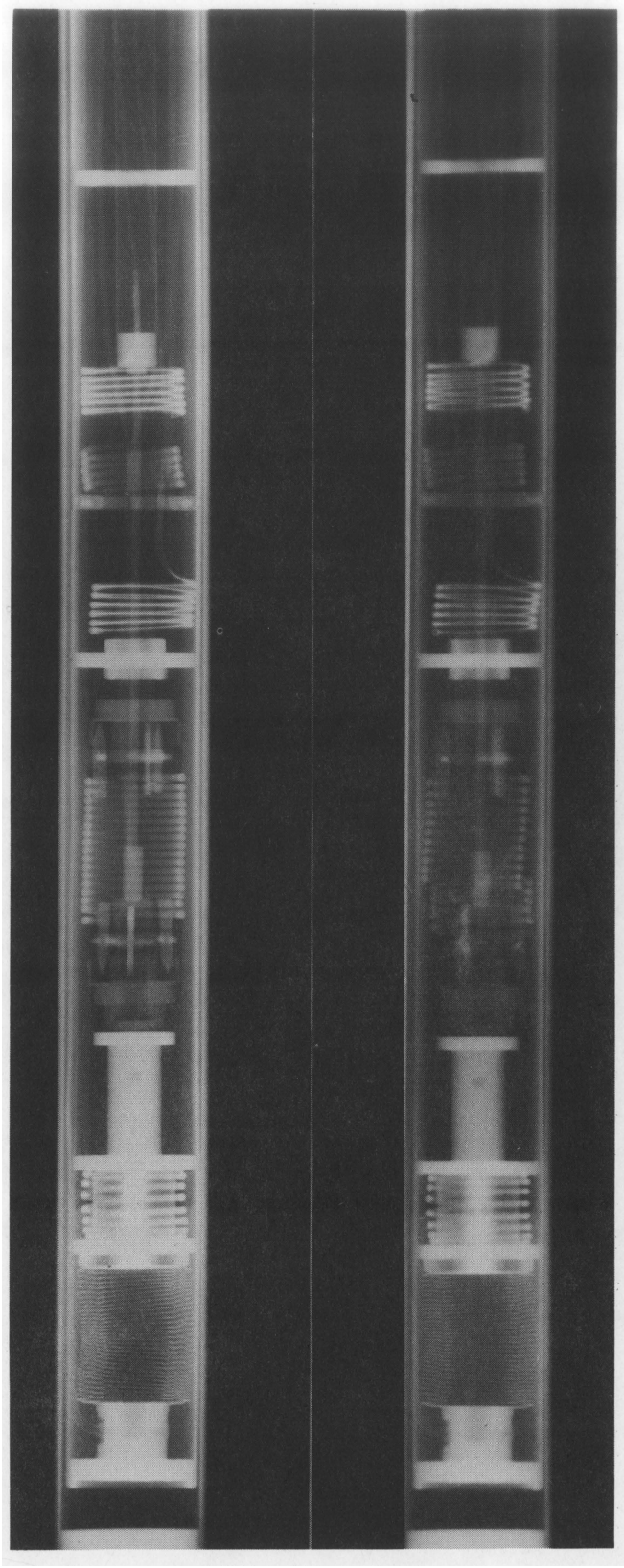

Fig. 11. (a) Pre-irradiation and (b) postirradiation neutron radiographs of creep capsule.

important results. The specimen had failed in two places away from the stress concentrations in the grips. No indication of damage due to high flux was apparent. No measurable swelling occurred in the loaded or unloaded springs. By determining the distance between coils on the unbroken pieces of the spring, it was found that 25% of the measured 5-mm total spring extension was recovered and therefore only 75% of the strain was permanent. It is assumed that additional plastic deformation did not occur during the rapid fracture of the $UO_2$ spring.

## DISCUSSION

The preliminary result that deformation can occur at 103°C in oxide fuels undergoing fission suggests an important conclusion concerning the mechanism of deformation. If the mechanism is controlled by the motion of point defects[1,2] there must be a means of moving the point defects. Calculations[1,2] of the defect mobility in fissioning oxides show that the motion of defects to fixed sinks and Frenkel-pair recombination, which can lead to higher defect mobility under irradiation, becomes insignificant at 100°C.[b] Only the release of thermal energy from thermal rods and spikes[1] can enable the defects to move at such a low temperature. Therefore any mechanism of deformation controlled by defect mobility must be coupled to the release of thermal energy from the fission event.

The fact that no creep deformation was obtained out-of-reactor for the enriched $UO_2$ springs, under approximately the same stresses and temperatures as for the in-reactor creep test, underscores the importance of the fission event in triggering a deformation mechanism. It is unlikely that fracture is the deformation mechanism because the fracture tensile stress measured out-of-reactor was five times greater than the maximum tensile stress for the loaded $UO_2$ spring in the first capsule. Moreover, if local fracturing occurred as the result of the thermoelastic stresses generated when the reactor was brought to power, it would either have led to immediate fracture of the specimen at the time the load was subsequently applied or would have altered the elastic deflection slightly when the load was applied. In neither case, however, would it lead to time-dependent creep deformation.

[b] Using the relation suggested by Brucklacher et al.[1] for the enhancement of diffusivity in $UO_2$ from recombination events, and the material and test conditions of the present investigation, a diffusivity of $\sim 10^{-34}$ is found at 100°C.

## SUMMARY AND CONCLUSIONS

The instrumented creep capsule used to study low-temperature fission-induced creep in oxide fuel materials has been shown to operate successfully. In-reactor creep was measured at a maximum specimen temperature of 103°C for a fission rate of $2.6 \times 10^{12}$ fissions/($cm^3$ sec) and a maximum shear stress of 2890 psi.

Future capsules will be designed to study the important effects of fission rate and stress on fission-induced creep phenomenon.

### ACKNOWLEDGMENTS

The authors would like to express their appreciation to R. F. Canon, who suggested the conceptual design for the capsule and to H. C. Stevens for his assistance in performing the calculations for the irradiations in GETR. The assistance of the staff of the General Electric Company in performing the irradiation is also gratefully acknowledged.

This work was performed under the auspices of the U.S. Atomic Energy Commission.

### REFERENCES

1. D. BRUCKLACHER, W. DIENST, and F. THUMMLER, KFK-817/EUR 3975(d), GFK Karlsruhe (1968).

2. D. BRUCKLACHER and W. DIENST, *J. Nucl. Mater.*, **36**, 244 (1970).

3. D. J. CLOUGH, Meeting on *Fast Reactor Fuel and Fuel Elements*, Paper 6, Karlsruhe, September 28-30, 1970.

4. E. C. SYKES and P. T. SAWBRIDGE, RD/B/N 1489, Central Electricity Generating Board (1969).

5. A. A. SOLOMON, J. L. ROUTBORT, and J. C. VOGLEWEDE, "Fission-Induced Creep of $UO_2$ and Its Significance to Fuel-Element Performance," ANL-7857, Argonne National Laboratory (to be published).

6. J. T. DUSEK and G. D. WHITE, "Fabrication of Uranium Dioxide Helices for Irradiation Creep Measurements," *J. Am. Ceram. Soc.* (to be published).

7. W. A. ERWIN, Private Communication (August 7, 1970).

8. D. WALKER, Private Communication (March 6, 1970).

9. A. A. SOLOMON and R. H. GEBNER, Reactor Development Program Progress Report, ANL-7726, p. 109, Argonne National Laboratory (July 1970).

# ELEVATED-TEMPERATURE DAMAGE FUNCTIONS FOR NEUTRON EMBRITTLEMENT IN PRESSURE VESSEL STEELS

MATERIALS

KEYWORDS: *high temperature, steel-ASTM-A350, embrittlement, pressure vessels, PM-2A, SM-1A, radiation effects, irradiation, neutrons*

C. Z. SERPAN, Jr. *Reactor Materials Branch, Code 6390*
*Naval Research Laboratory, Washington, D. C. 20390*

W. N. McELROY *WADCO Corporation, P.O. Box 1970*
*Richland, Washington 99352*

Received July 21, 1971

*Damage functions, represented here as multigroup cross sections for neutron-induced radiation damage production, were derived for irradiation of two A350-series ferritic steels at temperatures of 510 and 430°F (266 and 221°C), representing the PM-2A and SM-1A reactor pressure vessels. The functions were derived using the SAND-II computer code with the neutron spectra and resulting increases in transition temperature from a series of irradiations in different reactor locations.*

*The derived damage functions effected a best correlation of available data and on that basis are considered good through comparison of total fluence values determined both from experimental measurements and from the damage-function calculation technique. Trends are suggested for the magnitude of damage function cross-section values as a function of energy at low vs elevated temperatures. However, the present experimental data are not sufficiently definitive to draw positive conclusions about the specific contributions of neutrons of all energy levels to the neutron embrittlement process.*

## INTRODUCTION

The primary containment vessels of most commercial, light water moderated reactors in the U. S. are fabricated from low alloy, ferritic steel that characteristically exhibits a nil-ductility transition (NDT) temperature which, during reactor operation, is increased by neutron bombardment. Accordingly, limits are placed on the permissible NDT increase for reactor vessel steels, thus underlining the importance of establishing trends in NDT increase and of continuing to unravel the causes of the increase.[1-3]

Most of the available trend data are developed from test reactor irradiations which have dose rate and neutron spectra conditions different from operating power reactors. Although current evidence[4-6] suggests that no dose-rate effect exists for notch ductility characteristics for the range of fluxes and fluences typical for light water thermal reactors, effects are observed resulting from neutron spectra differences. Accounting for differences in damage resulting from differences in neutron-energy spectra is the major concern of this work. Some early work to account for neutron energy differences in radiation effects studies involved calculation of damage cross-section values from theoretical considerations,[7-10] but more recently, computer techniques are being used to generate energy-dependent damage cross sections[11-13] which are designated damage functions, $G(E)$.

## COMPUTATIONAL TECHNIQUE

Damage functions are simply a series of cross-section values corresponding to the energy-level grouping in a neutron spectrum for a specific change in mechanical properties; multiplication of each cross section times the corresponding flux value yields a series of responses which, when summed and divided into the magnitude of the mechanical property change, yields the fluence value to cause that change. Derivation requires a consistent set of mechanical property change and corresponding neutron fluence data from reactor irradiations in known neutron spectra, and an initial approximation of the damage function.

The method involves the use of the SAND-II iterative unfolding technique[14] developed originally

for neutron spectra and reaction cross-section determination. The SAND-II code is used to obtain a damage function solution[11] for a set of integral equations of the form

$$S_j = \int\int G(E)\ \phi_j(E,t)\ dEdt \quad (j = 1, 2, \ldots n) \quad , \quad (1)$$

where $S_j$ is a measured integral property change for a specified material, irradiated for a time $t$ in the $j$'th neutron environment (at constant temperature $T$), and $\phi_j(E,t)$ is the corresponding $j$'th neutron differential spectrum. For this study, the following assumptions were made:

1. $\phi_j(E,t)$ is separable in energy and time and can be represented as $t \cdot \phi_j(E)$.
2. For a specified band of temperatures about $T$, $G(E)$ and $\phi_j(E)$ can be represented by time-averaged values $\overline{G}(E)$ and $\overline{\phi}_j(E)$.

Using these assumptions and notation, Eq. (1) is rewritten

$$S_j = S_j^{(K)} \quad (j = 1, 2, \ldots n) \quad , \quad (2)$$

where

$$S_j^{(K)} = t \cdot \int \overline{G}^{(K)}(E) \cdot \overline{\phi}_j(E)dE \quad (3)$$

and the superscript refers to the $K$'th iteration cycle. As a convenience, the bars over $\overline{G}^{(K)}(E)$ and $\overline{\phi}_j(E)$ are omitted in the text.

Given $S_j$ and $\phi_j(E)$ as the measured property change and neutron spectrum, respectively, as input data, together with the initial approximation $G^{(0)}(E)$ for the true shape of the damage function, the SAND-II code will generate appropriate iterative solutions $G^{(K)}(E)$ for Eq. (2). An appropriate solution is obtained when the standard deviation of the ratios of the measured-to-calculated values $S_j/S_j^{(K)}$ reaches a lower value which is consistent with experimental uncertainties. Using this method, damage functions were derived for neutron irradiation of two low alloy steels, A350-LF3 and A350-LF1 (modified) at temperatures of 510 and 430°F (266 and 221°C), respectively, temperatures higher than those of previous $G(E)$ studies of low alloy ferritic steels.[11-12]

## EXPERIMENTAL DATA

This report presents an analysis of the increase in transition temperature, $\Delta TT$,[a] measured at the 30 ft-lb energy level with Charpy V-notch specimens, for irradiation at 510°F (266°C) of A350-LF3 steel ring forgings representing the PM-2A reactor vessel, and at 430°F (221°C) of A350-LF1 (modified) steel plate and ring forgings representing the SM-1A reactor vessel. The experimental irradiation data[15,16] for both steels are presented in Figs. 1 and 2, and summarized in Table I.

Details in Table I include the experiment irradiation location in reactors. The Low Intensity Test Reactor (LITR) data are identified by the prefix $C$ followed by the core lattice position; the Union Carbide Research Reactor (UCRR) data are identified by the prefix $T$, and the core location. In-reactor positions including the $\frac{1}{4}$ and $\frac{3}{4}$ thickness locations (measured from the inner vessel surface) within the PM-2A reactor vessel wall, and an above-core surveillance location in the SM-1A reactor are also listed. Each location has an arbitrarily numbered spectrum, with the u representing an unfolded spectrum; this is discussed below. Multigroup neutron spectra were calculated at Battelle-Northwest for each reactor position[7,17] using one- and two-dimensional transport theory codes, Program S and 2DXY, respectively.

The measured neutron fluence values >1 MeV in Table I are based on a fission-spectrum-averaged cross section ($\overline{\sigma}_{fs}$) of 68 mb for the $^{54}Fe(n,p)^{54}Mn$ reaction; these values are included for reference only. Neutron fluences, $\Phi^{cs} > 0.5$ MeV in Table I are termed calculated-measured values. This term arises from the practice of (a) obtaining measured activation of a flux detector material from the reactor location of interest, and (b) using that value to fix the absolute magnitude of the flux for energies >0.5 MeV in that specific reactor location as determined by a reactor physics spectrum calculation. These fluences are based on a set of energy-dependent activation cross sections for the $^{54}Fe(n,p)^{54}Mn$ reaction with a $\overline{\sigma}_{fs}$ of 82.6 mb.[18]

The total fluences, $\Phi^{cs}$ total, in Table I were derived using measured activation of both thermal and fast neutron detectors in the following manner and are termed calculated-measured values. Activation rates at saturation from bare and cadmium-covered cobalt flux detectors (Al-0.1% Co alloy) for thermal and epithermal neutrons and rates from iron detectors for fast neutrons were input into the SAND-II code along with the reactor physics spectrum calculation. The code was used to adjust the magnitudes of both fast and thermal components in the spectrum calculation to agree with the activation measurements in an operation called "unfolding." The actual value of total fluence for a given irradiation, as listed in Table I,

[a] A transition temperature increase requires selection of a Charpy-V energy absorption level, preferably based on an average correlation point representative of the drop-weight NDT value for that class of steel, and translation along that energy level from the unirradiated-condition curve to the irradiated-condition curve.

TABLE I

Summary of Experimental Data for Development of A350 Steel Damage Functions

| Reactor Steel | No. | Experimental Core Position | Spectrum | $\Delta T_T$ $C_v$ 30 ft-lb | | $\Phi^{fs} > 1$ MeV $\bar{\sigma}^{fs}$ = 68 mb | $\Phi^{cs} > 0.5$ MeV $\bar{\sigma}^{cs}$ = 82.6 mb | $\Phi^{cs}$ total $>10^{-10}$ MeV |
|---|---|---|---|---|---|---|---|---|
| | | | | °F | °C | $^{54}Fe(n,p)^{54}Mn$ | | |
| PM-2A[15] | 12 | C18 | 6u | 320 | 178 | $2.7 \times 10^{19}$ | $4.07 \times 10^{19}$ | $1.80 \times 10^{20}$ |
| $3\frac{5}{8}$-in. | 31 | C55 | 7u | 270 | 150 | 1.4 | 2.40 | 2.19 |
| A350-LF3 | 34 | C55 | 7u | 365 | 203 | 2.9 | 4.97 | 4.54 |
| forging | 13A | TC3 | 82u | 115 | 64 | 0.46 | 0.59 | 0.297 |
| | PM-2A | $\frac{3}{4}$t | 16u | 135[a] | 75 | 0.40 | 0.38 | 0.249 |
| | PM-2A | $\frac{1}{4}$t | 17u | 195[a] | 108 | 0.73 | 0.64 | 0.818 |
| SM-1A[16] | 93HA | C53 | 3u | 320 | 178 | $2.0 \times 10^{19}$ | 3.41 | $1.81 \times 10^{20}$ |
| $2\frac{5}{8}$-in. | 92 | C18 | 6u | 275 | 153 | 1.3 | 1.96 | 0.866 |
| A350-LF1 | 37 | C18 | 6u | 330[b] | 183 | 2.0 | 3.01 | 1.33 |
| (modified) | 37 | C18 | 6u | 340 | 189 | 2.0 | 3.01 | 1.33 |
| forging | 52 | C18 | 6u | 380 | 211 | 2.8 | 4.22 | 1.87 |
| | 11 | C18 | 6u | 395[b] | 219 | 3.1 | 4.67 | 2.07 |
| | 38 | C55 | 7u | 415[b] | 231 | 2.8 | 4.80 | 4.39 |
| | 22 | C55 | 7u | 440[b] | 244 | 3.1 | 5.32 | 4.86 |
| | 93 | C43 | 21u | 195 | 108 | 0.64 | 1.03 | 0.476 |
| | 59 | C43 | 21u | 400 | 222 | 3.0 | 4.83 | 2.23 |
| | 14B | TD3 | 83u | 90 | 50 | 0.26 | 0.33 | 0.134 |
| | SM-1A | above | 81u | 80[b] | 44 | 0.26 | 0.16 | 0.125 |
| | SM-1A | above | 81u | 115[b] | 64 | 0.48 | 0.30 | 0.230 |

[a]2.4-in. A350-LF3 vessel ring forging.

[b]$3\frac{5}{8}$-in. A350-LF1 (modified) test plate.

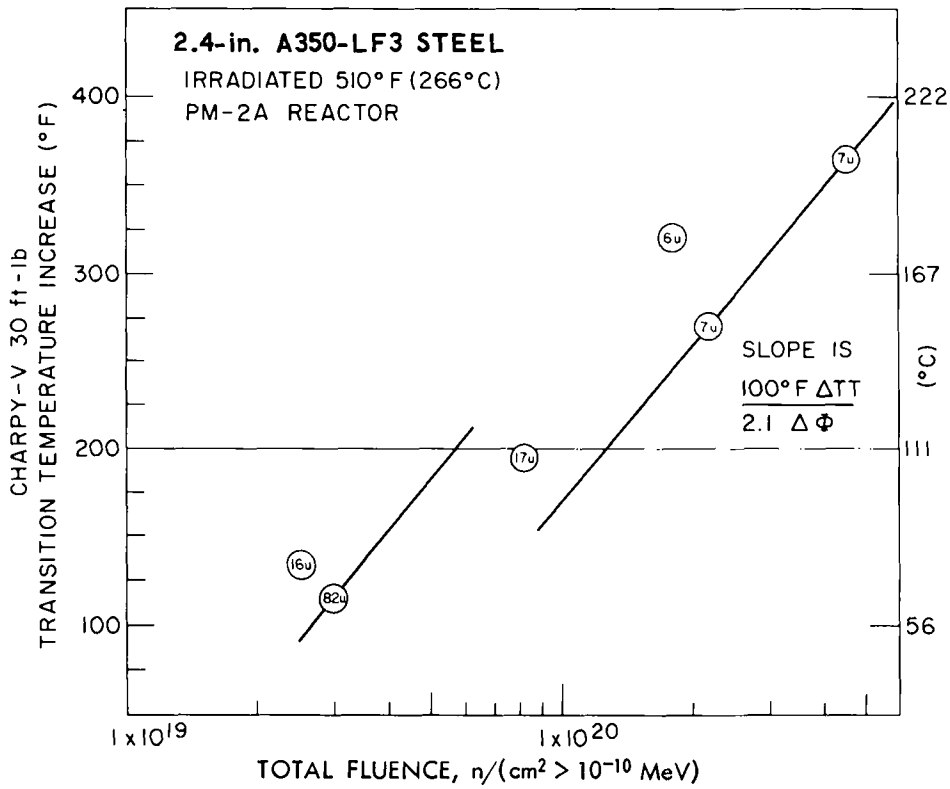


Fig. 1. Charpy-V 30 ft-lb transition temperature increases versus total neutron fluence for 510°F (266°C) irradiations of A350-LF3 steel. The trend lines having the indicated slope permit extrapolation of the data points to total fluence for a 200°F (111°C) increase in transition temperature.

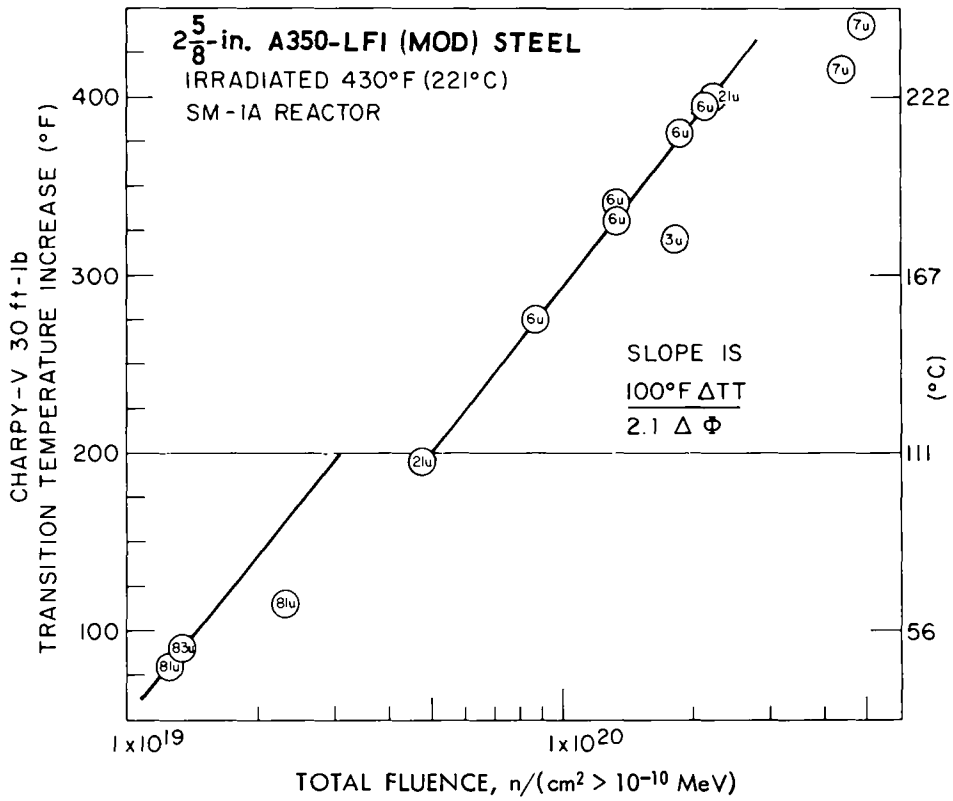


Fig. 2. Charpy-V 30 ft-lb transition temperature increases versus total neutron fluence for 430°F (221°C) irradiations of A350-LF1 (modified) steel. The trend lines having the indicated slope permit extrapolation of the data points to total fluence for a 200°F (111°C) increase in transition temperature.

was then determined by dividing the calculated-measured fluence >0.5 MeV (as described above) by the percentage of neutrons >0.5 MeV determined for the unfolded spectrum. These total fluences are also referred to as calculated-measured values in this report to differentiate them from subsequent damage function-calculated total fluence values.

In Figs. 1 and 2, the data points are identified only by spectrum number for reference to Table I. This convention was followed because the radiation responses were observed to be spectrum dependent, not simply fluence-level dependent.[11,12] In the figures, it is observed that the data points for each spectrum conform to a line that has the same slope in each case, but a different intercept on the horizontal axis; this was observed and discussed previously.[11,12] The slope shown in Fig. 1, 100°F $\Delta TT/2.1\ \Delta\Phi$, was determined simply from the two spectrum 7u data points. The same value of slope in Fig. 2 was derived by a least squares fit of the data from both spectrum 6u and 21u.

The above-noted slope in data points means that the total fluence increased by a factor of 2.1 for each 100°F (56°C) increase in transition temperature. This is surprising since another low alloy steel, A302-B, showed total fluence to increase by a factor of 4 for the same 100°F (56°C) increase in transition temperature over approximately the same fluence range of data but at irradiation temperatures <240°F (116°C).[11] In this connection, it is well known that neutron irradiation of ferritic low alloy steels will produce greater $\Delta TT$ at temperatures <240°F (116°C) than at ~450°F (232°C) and above. Since the two A350-series steels required such low total fluences to generate the 100°F (56°C) $\Delta TT$ for irradiation at the higher temperatures wherein thermal annealing can reduce the damage rate, it was considered important to study the radiation embrittlement response of these steels at temperatures <240°F (116°C) for comparison. This was accomplished, and while the data are not presented herein, they show clearly that a 100°F (56°C) $\Delta TT$ would require an ~1.4-fold increase in total fluence for the A350-LF3 steel (of Fig. 1) and a <2-fold increase in total fluence for the A350-LF1 (modified) steel (of Fig. 2). Thus, the total fluences for $\Delta TT$ at low and higher temperatures were in proper relation to experimental observations for the two A350-series steels but clearly disagreed with the observations from the A302-B steel. Radiation

response differences emanating from variations in chemical composition and microstructure appear to be largely responsible for such differences (see Refs. 1, 2, and 3 for additional discussion of this point).

## DAMAGE FUNCTION DERIVATION

$G(E)$'s were derived using the SAND-II code with total neutron fluences listed in Table II (calculated-measured values) with a mechanical property change of 200°F (111°C) $\Delta TT$ both in A350-LF3 steel irradiated at 510°F (266°C) and in A350-LF1 (modified) steel irradiated at 430°F (221°C). The total fluence in each spectrum for $\Delta TT$ of 200°F (111°C) was determined from the plots of Figs. 1 and 2. The previously discussed slope was fitted to the data points of each spectrum, and the intercept of this line with the 200°F $\Delta TT$ abscissa gave the total fluence. [Some spectra listed in Table I and shown in Fig. 2 were not used in the final derivation of the damage function for A350-LF1 (modified) steel for reasons explained below.]

The new damage functions are shown graphically as the smooth curves in Figs. 3 and 4 for A350-LF3 and A350-LF1 (modified) steel, respectively. Absolute values of the functions for the 200°F (111°C) $\Delta TT$, and the histograms, corresponding to the group structure used for the reactor physics spectrum calculations, are listed in Table III.

The damage function in Fig. 4 for the A350-LF1 (modified) steel was first developed with data from all locations noted in Table I for that steel. The initial interim results, however, suggested that the mechanical property and fluence data of spectrum 83u (UCRR core location T-D3) and spectrum 81u (the SM-1A above-core surveillance location) were apparently inconsistent relative to the other spectra in the data set. Omission of these two spectra and reevaluation of the remaining data resulted in the damage function of Fig. 4, derived in just one iteration.

## RESULTS AND DISCUSSION

The two damage functions are generally similar in the high energy region and in the intermediate energy range between $10^{-4}$ and $10^{-2}$ MeV. [The sharp discontinuities in this intermediate energy range are simply a reflection of the $(n,\gamma)$ responses in iron for the input model and are not necessarily to be taken as real structure in the damage function.[11,12]] Because of experimental uncertainties, particularly in the flux-spectral data, differences between the two damage functions are not considered significant, but rather are introduced by the iterative procedure to effect

TABLE II

Total Fluences, n/(cm$^2$ >$10^{-10}$ MeV), to Produce a 200°F (111°C) $\Delta TT$ in A350 Steels by Measurements and $G(E)$ Calculations

| | PM-2A $G(E)$ | | | | |
|---|---|---|---|---|---|
| | Reactor position | | | | |
| | LITR C-18 | LITR C-55 | PM-2A $\frac{1}{4}$T | PM-2A $\frac{3}{4}$T | UCRR T-C3 |
| | Spectrum | | | | |
| | 6u | 7u | 17u | 16u | 82u |
| Calculated-measured | $6.9 \times 10^{19}$ | $12.4 \times 10^{19}$ | $8.5 \times 10^{19}$ | $4.2 \times 10^{19}$ | $5.9 \times 10^{19}$ |
| $G(E)$ – calculated | $5.5 \times 10^{19}$ | $5.8 \times 10^{19}$ | $9.1 \times 10^{19}$ | $7.0 \times 10^{19}$ | $4.8 \times 10^{19}$ |

| | SM-1A $G(E)$ | | | |
|---|---|---|---|---|
| | Reactor position | | | |
| | LITR C-18 | LITR C-55 | LITR C-53 | LITR C-43 |
| | Spectrum | | | |
| | 6u | 7u | 3u | 21u |
| Calculated-measured | $5.2 \times 10^{19}$ | $9.7 \times 10^{19}$ | $8.0 \times 10^{19}$ | $4.8 \times 10^{19}$ |
| $G(E)$ – calculated | $5.1 \times 10^{19}$ | $5.9 \times 10^{19}$ | $5.8 \times 10^{19}$ | $4.9 \times 10^{19}$ |

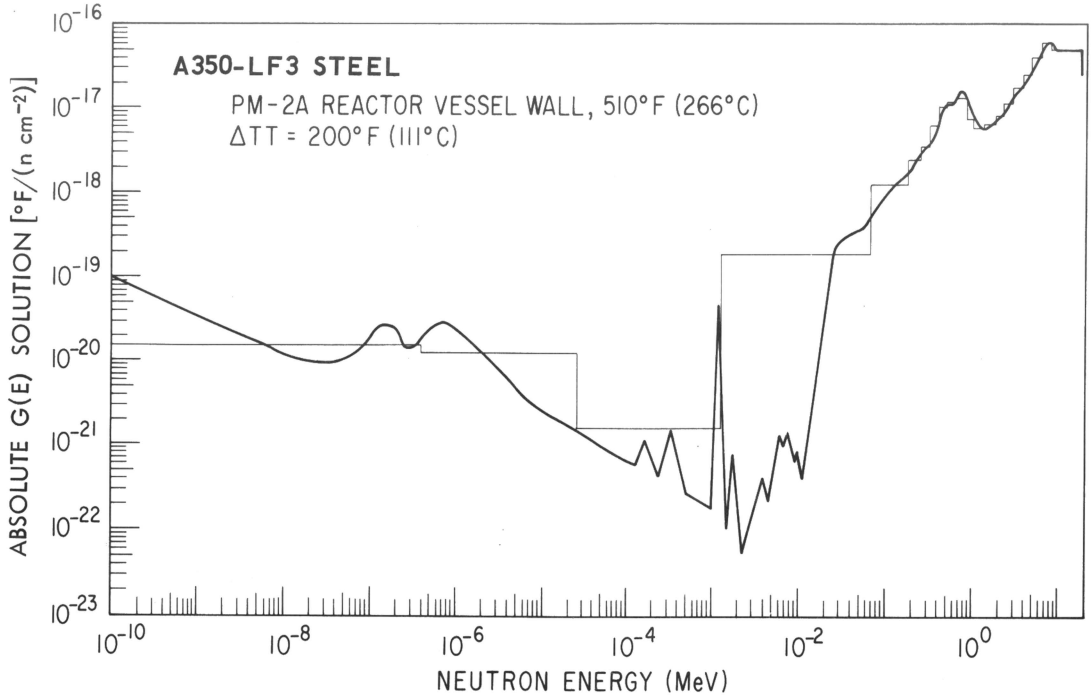


Fig. 3. Absolute damage function for a 200°F (111°C) transition temperature increase in A350-LF3 steel irradiated at 510°F (266°C). The histogram represents averaged values corresponding to the reactor physics spectrum group structure.

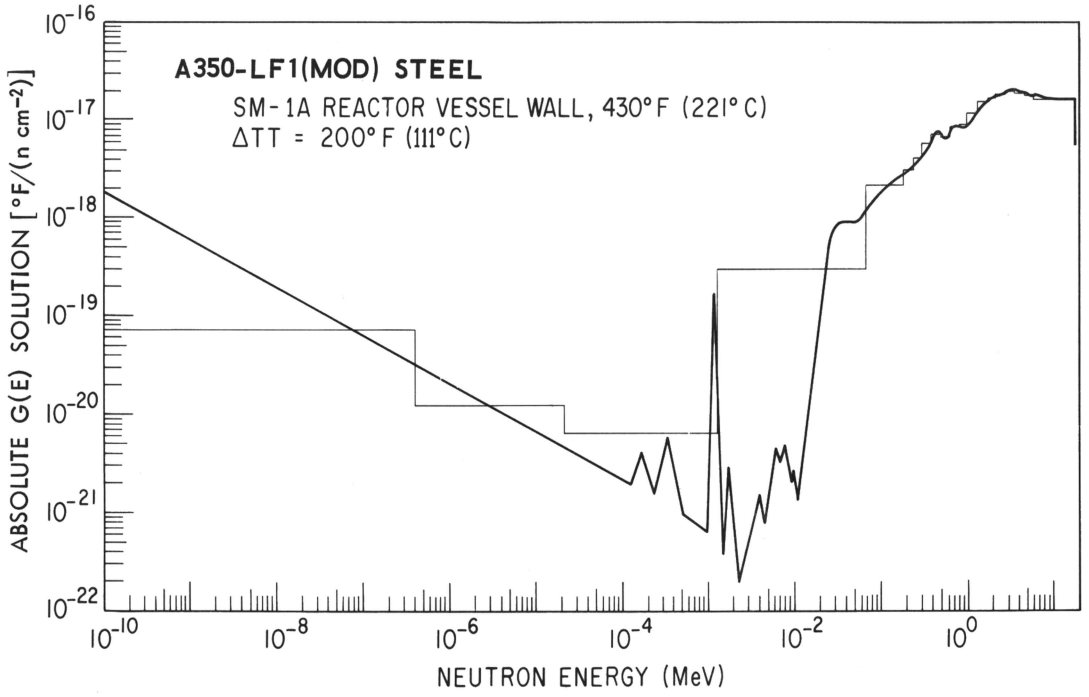


Fig. 4. Absolute damage function for a 200°F (111°C) transition temperature increase in A350-LF1 (modified) steel irradiated at 430°F (221°C). The histogram represents averaged values corresponding to the reactor physics spectrum group structure.

proper correlation of the available data. For instance, in Fig. 3 the structure below $10^{-6}$ MeV for the A350-LF3 steel is necessary to satisfy the system of equations with the relatively high thermal-neutron flux for the two PM-2A reactor locations, spectra 16u and 17u of 61.9 and 70.1% thermal neutrons, respectively. By contrast, the SM-1A vessel wall spectrum has a much lower thermal-neutron population of only about 14.7% and a solution can be obtained with little or no structure. Low energy range discontinuities are observed in Fig. 3 and similar discontinuities have been observed in the low-energy values of a preliminary damage function for A302-B steel irradiated at a temperature of about 550°F (288°C).[19,20] In both instances, the significance of the discontinuities cannot be considered established.

TABLE III

Group-Averaged Values for Absolute $G(E)$'s for a 200°F (111°C) $\Delta TT$ in Two A350 Steels

| Lower Energy Limit for Group (MeV) $E_l$ | Lower Lethargy Limit for Group $u_l$ | Group-Averaged Values, $\bar{G}i$, °F/(n cm$^{-2}$) × $10^{-18}$ | |
|---|---|---|---|
| | | PM-2A A350-LF3 510°F (266°C) | SM-1A A350-LF1 (modified) 430°F (221°C) |
| 7.79 | 0.25 | 45.70 | 15.80 |
| 6.07 | 0.50 | 51.22 | 16.53 |
| 4.72 | 0.75 | 34.00 | 17.24 |
| 3.68 | 1.00 | 21.62 | 18.18 |
| 2.87 | 1.25 | 15.08 | 18.43 |
| 2.23 | 1.50 | 9.947 | 17.13 |
| 1.74 | 1.75 | 7.071 | 16.15 |
| 1.35 | 2.00 | 5.552 | 14.27 |
| 1.05 | 2.25 | 4.940 | 11.41 |
| 0.821 | 2.50 | 6.352 | 8.518 |
| 0.639 | 2.75 | 11.69 | 8.097 |
| 0.498 | 3.00 | 10.56 | 6.651 |
| 0.388 | 3.25 | 8.963 | 6.853 |
| 0.302 | 3.50 | 5.333 | 5.325 |
| 0.235 | 3.75 | 3.063 | 3.808 |
| 0.183 | 4.00 | 2.097 | 2.937 |
| $1.17\times10^{-2}$ | 6.75 | 1.110 | 2.139 |
| $1.23\times10^{-2}$ | 9.00 | 0.0937 | 0.1585 |
| $1.01\times10^{-4}$ | 11.50 | 0.001047 | 0.003845 |
| $6.83\times10^{-7}$ | 16.50 | 0.0117 | 0.01317 |
| $4.14\times10^{-7}$ | 17.00 | 0.00158 | 0.00155 |
| $1.0\times10^{-10}$ | 20.72 | 0.0155 | 0.07378 |

The appearance or absence of a low-energy contribution to damage resulting from thermal neutrons places importance on the accurate determination of the percentage of these neutrons in any given spectrum. The thermal-neutron flux values for the three spectra under consideration here, spectra 16u and 17u for the PM-2A and 38 for the SM-1A pressure vessel, are all subject to more than a nominal amount of error. For spectra 16u and 17u, the reaction $^{59}Co(n,\gamma)^{60}Co$ occurring in the alloyed cobalt of the steel was used as an indicator of the epithermal flux,[15] and by inference, the thermal-neutron flux. For spectrum 38, several bare and cadmium-covered cobalt flux wire measurements were available although their spatial relationship to one another and to the iron flux measurements could not be accurately established. It is, therefore, possible that these thermal-neutron flux values could be in error by a factor of 2 or more. In spite of the attention given here to the possible role of thermal neutrons, it should be noted from Table III that the absolute value of the thermal-neutron energy-range damage function cross sections are small and thus contribute little to the respective total embrittlement unless the thermal to fast flux ratio is high (i.e., such as $>>$ 10:1).

Despite the uncertainty in some of the input flux spectra, the resulting damage functions are, from an engineering standpoint, the best available for the irradiation temperatures indicated. A useful means to gauge the limits of correlation accuracy of these functions is to compare the total measured fluence for a 200°F (111°C) $\Delta TT$ in the steel with $G(E)$-calculated values. In Table II, the measured and calculated total fluences are compared for the two damage functions for the spectra used in this study. The agreement between the experimentally derived calculated-measured and the $G(E)$-calculated total fluences is considered sufficient to assure the acceptability of the damage functions for use with most neutron spectra of practical interest. Details of the technique for engineering application of these damage functions is considered elsewhere.[12]

A critical comparison of specific damage function values at each energy level between the present two elevated-temperature functions and the ones developed previously for lower temperatures[11] is not realistic at this time. The main reason is that all functions refer to different steels with responses to neutron irradiation known to be different. In general, however, for these different $G(E)$'s, all the cross-section values corresponding to each neutron energy level appear to be within the same order of magnitude. This is reasonable since all four steels show basically the same nature of embrittlement increase with increasing neutron fluence. Because of the differences which do exist between the $G(E)$'s, however, it will be of continuing interest to develop additional damage functions of these same steels but for different irradiation temperatures.

## SUMMARY AND CONCLUSIONS

Damage functions, defined as multigroup cross sections for production of neutron-induced radiation damage, have been derived for the 510°F (266°C) irradiation behavior of A350-LF3 steel representative of the PM-2A reactor pressure vessel, and for the 430°F (221°C) irradiation behavior of A350-LF1 (modified) steel representative of the SM-1A reactor pressure vessel. The analysis was based on two independent sets of data relating measured increases in Charpy V-notch 30 ft-lb transition temperature ($\Delta TT$) with neutron fluences from many different reactor environments. The neutron fluences were derived from in-reactor activation measurements corrected for the actual distribution of neutrons calculated to be present using reactor physics spectrum calculation codes.

From an applied engineering point of view, the damage functions derived are the best present descriptions of the elevated-temperature energy dependence of neutron embrittlement response of the two A350-series steels. Analyses of these steels should include the use of these damage functions with neutron spectra determined as accurately as possible.

One of the more important findings of this study is the continuing need for more accurate definition of the magnitude of the major components in a neutron-energy spectrum. Such accuracy can be obtained only through in-reactor exposure of a set of flux detector materials each having a different range of energies over which it is activated.[21,22] This study shows that an experimental determination of just the thermal and fast flux can be used to provide an acceptable adjustment of the spectrum magnitudes, where the spectrum is determined by reactor physics calculations. This can be attained by using just iron and cobalt in the bare and cadmium-covered mode. Despite the apparent simplicity of this minimum requirement, it is not commonly met. A strong effort should be made to provide for this minimum amount of neutron dosimetry in every radiation effects study and to publish at least these dosimetry results with the complete mechanical property results.

## ACKNOWLEDGMENTS

The authors are indebted to C. H. Hogg of the Idaho Nuclear Corporation for determination of the flux detector saturated activities, and to G. E. Shook of WADCO who assisted in the computer operations. This research was supported by the Army Nuclear Power Field Office, Fort Belvoir, Virginia, the Office of Naval Research, and the U.S. Atomic Energy Commission, Fuels and Materials Branch, Division of Reactor Development and Technology, Contract No. AT(49-5)-2110 at NRL and Contract No. AT(45-1)-1830 at WADCO Corporation, Richland, Washington.

## REFERENCES

1. U. POTAPOVS and J. R. HAWTHORNE, "The Effect of Residual Elements on the Response of Selected Pressure-Vessel Steels and Weldments to Irradiation at 550°F," *Nucl. Appl.*, **6**, 27 (1969).

2. J. R. HAWTHORNE and L. E. STEELE, "Initial Evaluations of Metallurgical Variables as Possible Factors Controlling the Radiation Sensitivity of Structural Steels," NRL-6420, Naval Research Laboratory (September 1966).

3. J. R. HAWTHORNE, "Demonstration of Improved Radiation Embrittlement Resistance of A533-B Steel Through Control of Selected Residual Elements," NRL-7121, Naval Research Laboratory (May 1970).

4. D. R. HARRIES, P. J. BARTON, and S. B. WRIGHT, "Effects of Neutron Spectrum and Dose Rate on Radiation Hardening and Embrittlement of Steels," ASTM-STP-341, p. 276, *Proc. Symp. Radiation Effects on Metals and Neutron Dosimetry*, American Society for Testing and Materials (1963).

5. N. E. HINKLE, S. M. OHR, and M. S. WECHSLER, "Dose Rate, Annealing, and Stress Relaxation Studies of Radiation Hardening in Iron, Effects of Radiation on Structural Metals," *ASTM Spec. Tech. Publ.*, **426**, 573 (1967).

6. C. Z. SERPAN, Jr. and H. E. WATSON, "Dose Rate Effect on Yield Strength of Neutron-Irradiated Steel," *Trans. Am. Nucl. Soc.*, **12**, 576 (1969).

7. R. E. DAHL and H. H. YOSHIKAWA, "Neutron Exposure Correlation for Radiation-Damage Studies," *Nucl. Sci. Eng.*, **21**, 312 (1965).

8. A. D. ROSSIN, "Comparison of Neutron Embrittlement of Steel in Different Reactor Spectra," *Nucl. Str. Eng.*, **1**, 76 (1965).

9. W. F. SHEELY, "Correlation of Radiation Damage to Steel with Neutron Spectrum," *Nucl. Sci. Eng.*, **29**, 165 (1967).

10. K. SHURE, "Radiation Damage Exposure and Embrittlement of Reactor Pressure Vessels," WAPD-TM-471, Westinghouse Atomic Power Department (November 1964).

11. W. N. McELROY, R. E. DAHL, Jr., and C. Z. SERPAN, Jr., "Damage Functions and Data Correlation," *Nucl. Appl. Technol.*, **7**, 561 (1969).

12. C. Z. SERPAN, Jr. and W. N. McELROY, "Damage-Function Analysis of Neutron-Energy and Spectrum

Effects Upon the Radiation Embrittlement of Steels," NRL-6925, Naval Research Laboratory (July 1969).

13. W. N. McELROY, R. E. DAHL, and E. R. GILBERT, "Neutron Energy Dependent Damage Function for Analysis of Austenitic Steel Creep Data," *Nucl. Eng. Design*, **14**, 319 (1970).

14. W. N. McELROY et al., "A Computer-Automated Iterative Method for Neutron Flux Spectra Determination by Foil Activation," AWFL-TR-67-41, Vols. I-IV, Air Force Weapons Laboratory (September 1967).

15. C. Z. SERPAN, Jr., "Notch Ductility and Tensile Property Evaluation of the PM-2A Reactor Pressure Vessel," NRL-6739, Naval Research Laboratory (June 1968).

16. U. POTAPOVS, J. R. HAWTHORNE, and C. Z. SERPAN, Jr., "Notch Ductility Properties of SM-1A Reactor Pressure Vessel Following the In-Place Annealing Operation," *Nucl. Appl.*, **5**, 389 (1968).

17. R. E. DAHL, Jr., J. A. ULSETH, and G. J. BUSSELMAN, Battelle-Northwest Laboratory, Private Communication to C. Z. SERPAN, Jr., Naval Research Laboratory (1965, 1967).

18. J. W. HELM, "High-Temperature Graphite Irradiations: 800 to 1200 Degrees C: Interim Report No. 1," BNWL-112, Battelle-Northwest Laboratory (September 1965).

19. L. E. STEELE, J. R. HAWTHORNE, C. Z. SERPAN, Jr., H. E. WATSON, and R. A. GRAY, Jr., "Irradiation Effects on Reactor Structural Materials," NRL Memorandum 2004, Naval Research Laboratory (May 1969).

20. W. N. McELROY, unpublished work, Battelle-Northwest Laboratory (1969).

21. R. L. SIMONS, L. S. KELLOGG, K. M. BARRY, and C. Z. SERPAN, Jr., "A Comparison of Measured and Calculated Integral Fluxes and Spectra in a Pressure Vessel Mockup," *Trans. Am. Nucl. Soc.*, **13**, 884 (1970).

22. W. N. McELROY and R. E. DAHL, Jr., Neutron Dosimetry for Fast Reactor Applications, *ASTM Spec. Tech. Publ.*, **484**, 375 (1971).

# A RADIOISOTOPE-FUELED STIRLING ENGINE ARTIFICIAL HEART SYSTEM

RADIOISOTOPES

**KEYWORDS:** *heart, Stirling cycle, power, design, operation, performance, plutonium-238, artificial heart*

W. R. MARTINI and P. RIGGLE
*Donald W. Douglas Laboratories, McDonnell Douglas Astronautics Company*
*2955 George Washington Way, Richland, Washington 99352*

L. T. HARMISON
*National Heart and Lung Institute, National Institutes of Health*
*Public Health Service, Department of Health, Education, and Welfare*
*Bethesda, Maryland 20014*

Received May 25, 1971
Revised September 20, 1971

*Steady improvements have been made through five systems for operating an artificial heart with a Stirling engine that will be heated by a radioisotope or by an electric heater which receives power from a transcutaneous transformer. A thermal storage reservoir assists in supplying peak power demands. The engine regenerator, a primary component, was substantially improved by changing from a porous to a hollow regenerator. Engine efficiency was doubled. The current engine, using a hot flexural support at the engine, a bellows-sealed lower support, a drive piston, and a flywheel for continuity of regenerator motion, has been quite successful. Potential reductions in size and isotope requirement are discussed. The computed dose rate for the system is also given. Development is continuing toward a reliable realistically sized artificial heart with reasonable power demands.*

## INTRODUCTION

The purpose of the radioisotope-fueled Stirling engine artificial heart power system under development at the Donald W. Douglas Laboratories is to assist the heart by pumping blood from the left ventricle of the heart into the aorta, the main artery of the body; power is obtained from the heat engine as pneumatic energy. In system 1, pneumatic energy was applied directly to a blood pump to produce pulses of pumped blood. In systems 2, 3, and 4, the engine produces a pneumatic output which is converted by a pump actuator to pulsatile hydraulic power to directly drive the blood pump. In all the systems, an attractive source of heat for the engine is $^{238}Pu$ because of its dose rate and long half-life. An alternate source of thermal energy is electric heat. With this arrangement, electric power is transmitted through the skin by a transformer and stored until used by melting a lithium salt such as LiF-NaF eutectic which melts at ~1200°F. This development effort for the National Heart and Lung Institute has progressed through four systems and work is beginning on the fifth system.

## SYSTEM 1

System 1 (Fig. 1) consists of a heat engine comprised of a cylinder heated on one end and cooled at the other. A porous plug regenerator pulsates back and forth inside the hollow cylinder. The average temperature of the gas in this cylinder increases and decreases as the oscillations occur because of heat transfer between the gas and the porous plug. In this way, gas temperature is rapidly increased and decreased without adding or rejecting heat from the system. These pressure pulses from the engine are transmitted through a short tube to the blood pump which consists of a flexible bladder containing blood and an

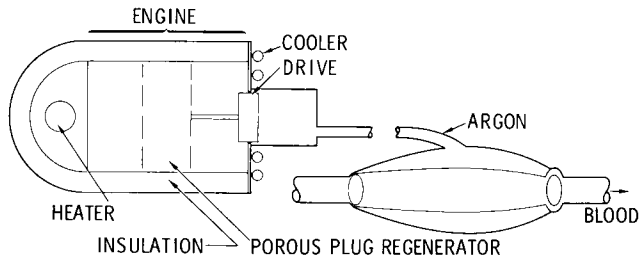


Fig. 1. System 1 concept.

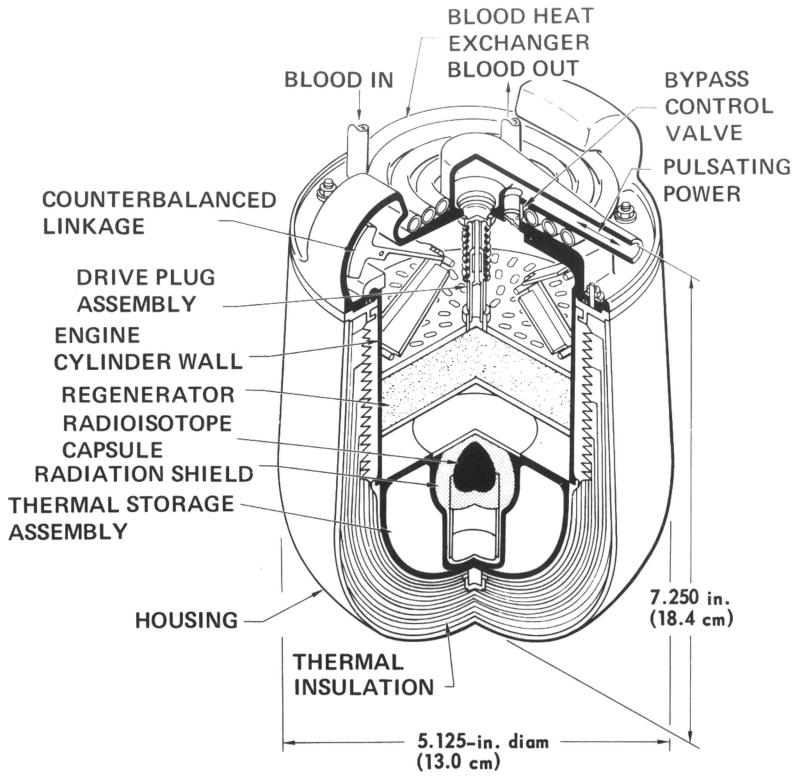


Fig. 2. Radioisotope-powered heat engine.

inlet and outlet valve on the two ends of the bladder. A rigid case surrounds the bladder, and gas pressure in this case draws blood into and expels blood from it. The drive system for the porous plug regenerator is a plug-in-orifice type discussed in previous papers. This drive has the advantages of simplicity and a self-starting capability. Other necessary components of this system are the heater (electric or radioisotope) and an efficient insulation around both the heater and the engine.

Figure 2 presents a design developed under joint NHLI-AEC sponsorship. The engine is basically the same as in Fig. 1. Radioisotopic heat is supplied from a spherical source centrally located inside the engine. A spherical radiation shield surrounds the primary fuel capsule; void volume is provided to accumulate helium produced by the decaying plutonium oxide fuel. A thermal storage assembly filled with LiF-NaF eutectic surrounds the radioisotope heater. This eutectic melts during periods of low heat demand (storing heat) and "freezes" to give up heat during short periods of high heat demand by the engine. The moving porous regenerator, designed to obtain the largest displacement in the smallest overall volume, uses a very porous gold-wire matrix with orifice plates on both ends of the regenerator to

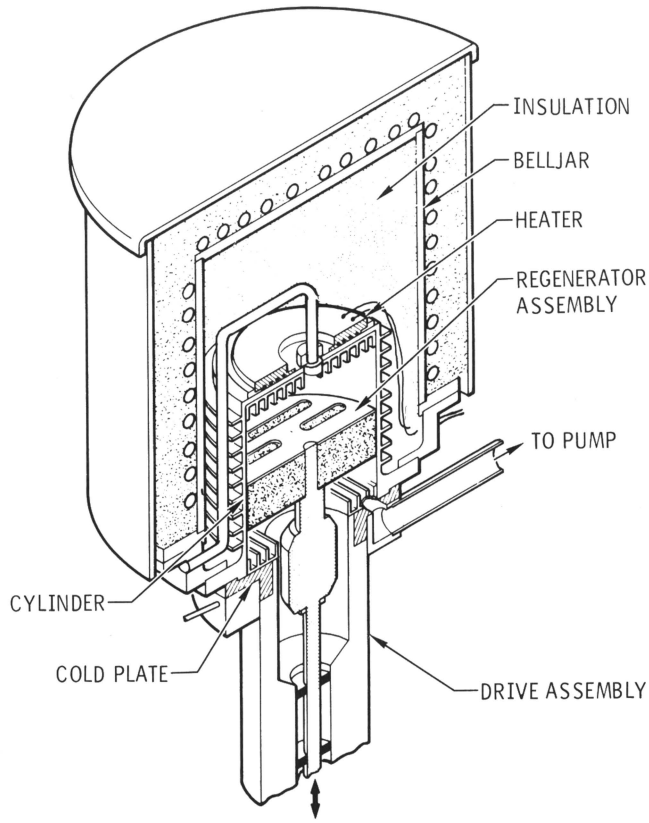


Fig. 3. Bench engine experiment.

jet gas against the isotope-heated hot plate or the blood-cooled cold plate. A Sarrut's linkage supports the regenerator and maintains proper clearance between the regenerator and cylinder wall. The primary advantage of this linkage is that it folds compactly into a small space in the cold plate. A plug-in-orifice drive is used which also has a telescoping arrangement to decrease overall volume of the engine. A bypass control valve spoils some of the drive energy when a lower power is needed by the blood pump. This design study was limited to the engine and did not consider in detail the blood pump or necessary control arrangements.

The second prototype engine for system 1 is shown in Fig. 3. The same porous-type regenerator as shown in Fig. 2 is used. An electric heater is the heat source and water cooling is provided as the heat sink. This regenerator has a more conventional bearing-and-spring support; data were taken with the device self-operating as well as externally driven. Figure 4 shows the lower portion of this early prototype after testing; the

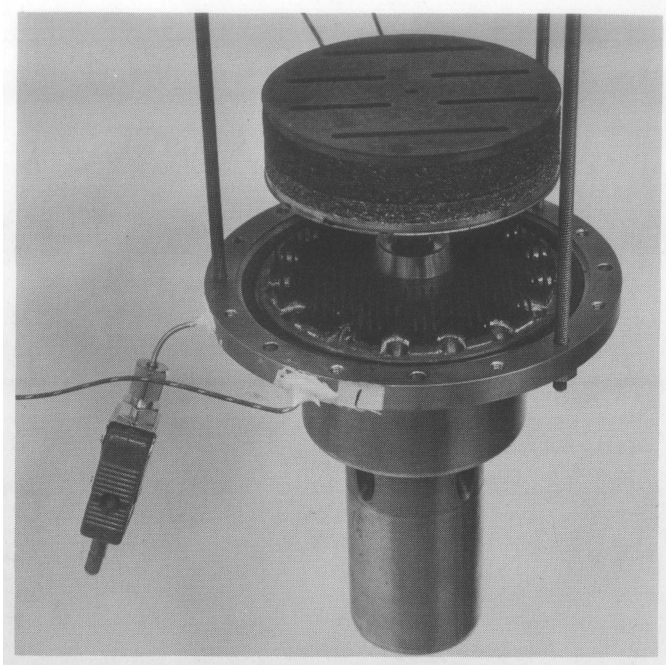

Fig. 4. Regenerator and cold plate of system 1 engine.

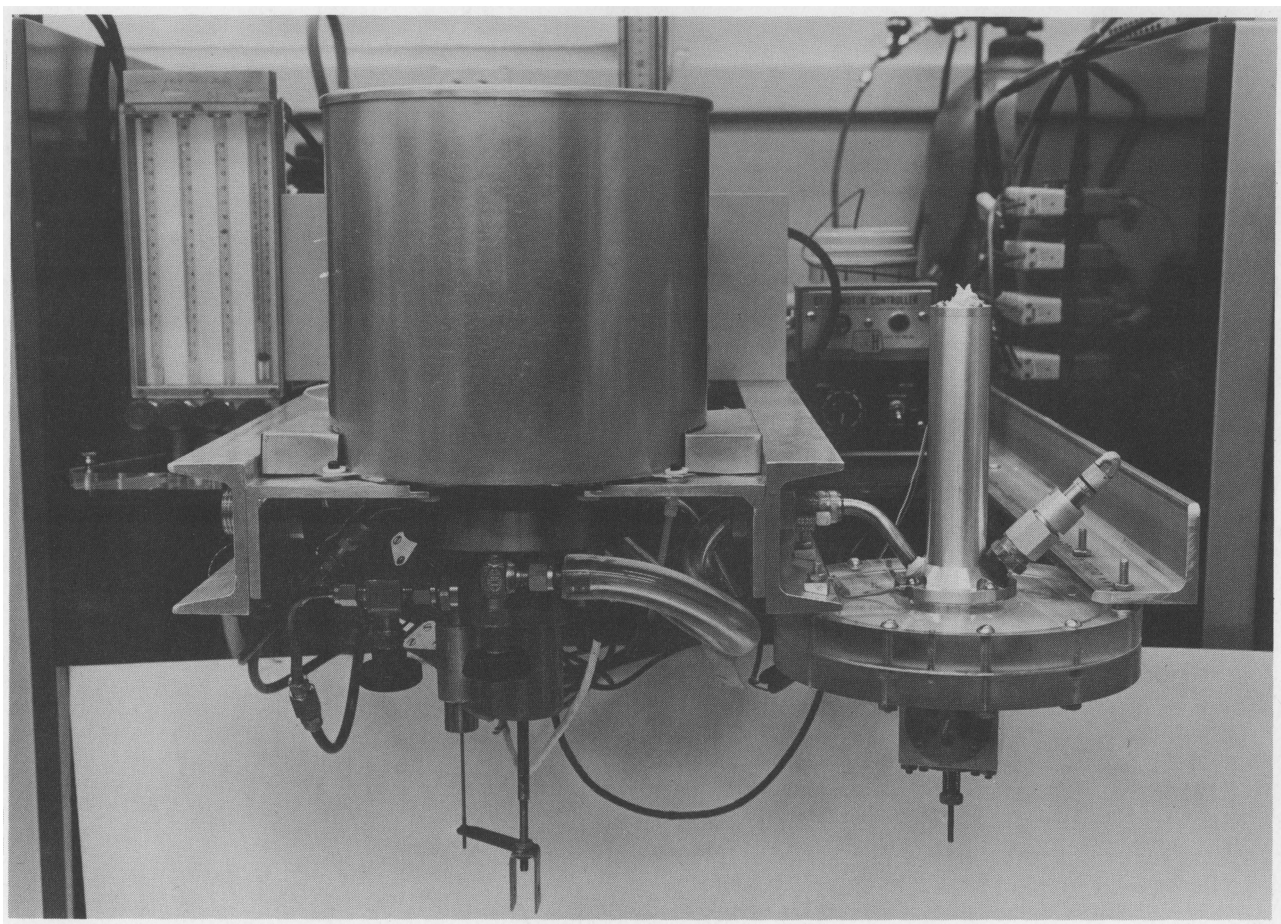

Fig. 5. Engine and load for system 1.

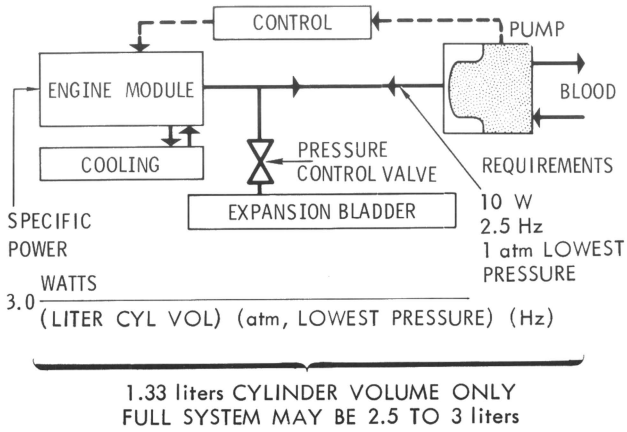


Fig. 6. Direct connection energy system.

porous regenerator is tarnished on top but still bright on the bottom. The fins used in this early model to enhance heat transfer to the cold plate were later found to have no net advantage and were removed. Figure 5 shows system 1 connected to a load which simulates the blood pump and measures volumetric displacement by sensing the position of a diaphragm. The low inlet and high outlet pressure of the blood pump are simulated by two adjustable pressure-relief valves.

Figure 6 summarizes DWDL experiences with system 1. The system requires an engine module directly connected to the blood pump. The blood pump required 10 W of pneumatic power at 2.5 Hz and a minimum pressure of 1 atm. Power in the engine was directly proportional to cylinder vol-

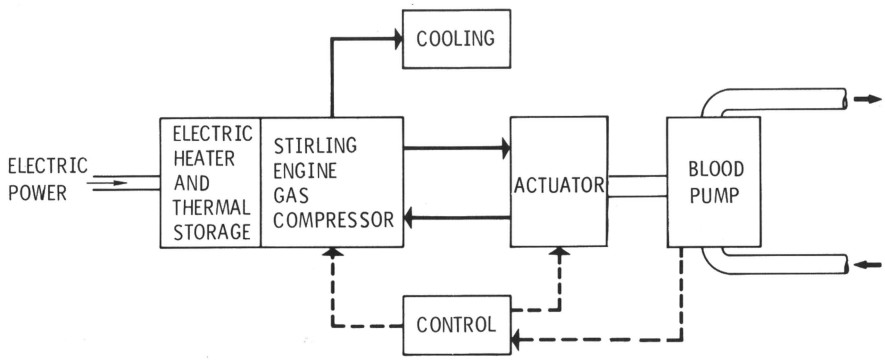


Fig. 7. Concept for systems 2, 3, and 4.

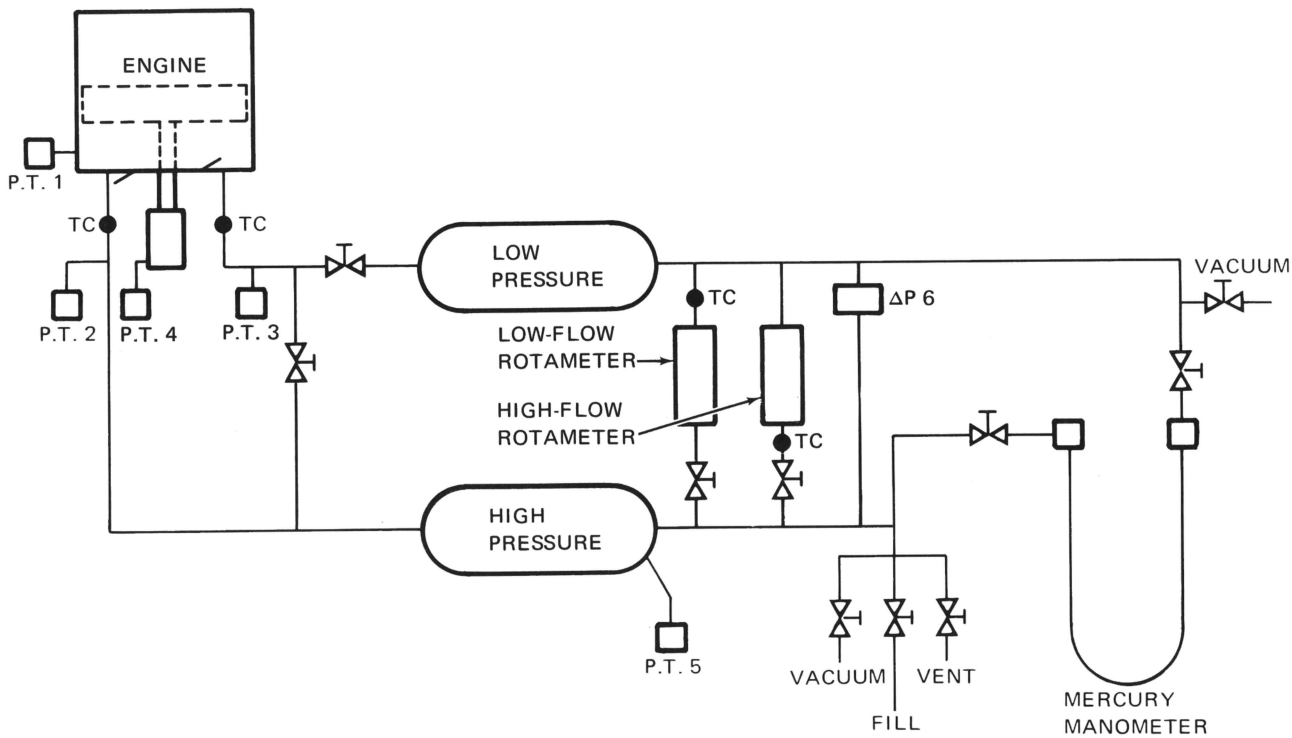


Fig. 8. System 2 cold plate.

ume, engine pressure, and operating frequency. Therefore, specific power for the engine can be expressed in watts per liter of cylinder volume per atmosphere at the lowest pressure per Hz. In these units, all engines tested to that time had a specific power of 3. When this specific power is combined with power requirements to the blood pump, $1\frac{1}{3}$ liters of cylinder volume is necessary. A full engine system, which includes controls, insulation, cooling, pressure control, and an expansion bladder to accommodate ambient pressure changes, has a volume of $2\frac{1}{2}$ to 3 liters. Because this volume is too large for practical implantation, system 1 was abandoned. The available options were:

1. a smaller engine running faster and pumping gas, and an automatically controlled valve system to operate the blood pump with this pumped gas
2. decreasing engine size by operating at a much higher pressure, then using a large and small piston coupled together to transform the high pressure low displacement from the engine to the low pressure high displacement hydraulic power needed by the blood pump
3. a combination of the two.

This third approach was used in systems 2, 3, and 4 because it allowed the greatest margin for design and required only minimal increases in pressure and operating frequency.

## SYSTEM 2

Principal components of systems 2, 3, and 4 are shown in Fig. 7. Electric or radioisotope heat, some of which is temporarily stored by melting salt in a thermal storage container, is applied to the Stirling engine gas compressor. The compressed gas is applied to a separate actuator which operates the blood pump. The engine requires cooling and both the engine and actuator require control signals from the blood pump. In system 2, the engine was tested separately to determine the increase in engine power density resulting from operation at higher gas pressures and higher engine speeds. The engine was fitted with an inlet and outlet valve (Fig. 8) in the cold plate, and gas was pumped from the low pressure tank into a high pressure tank, then through a flowmeter. Power output is expressed in watts by computing the energy available from the pumped gas if expanded isothermally at 40°C. Figure 9 shows the best results obtained with the

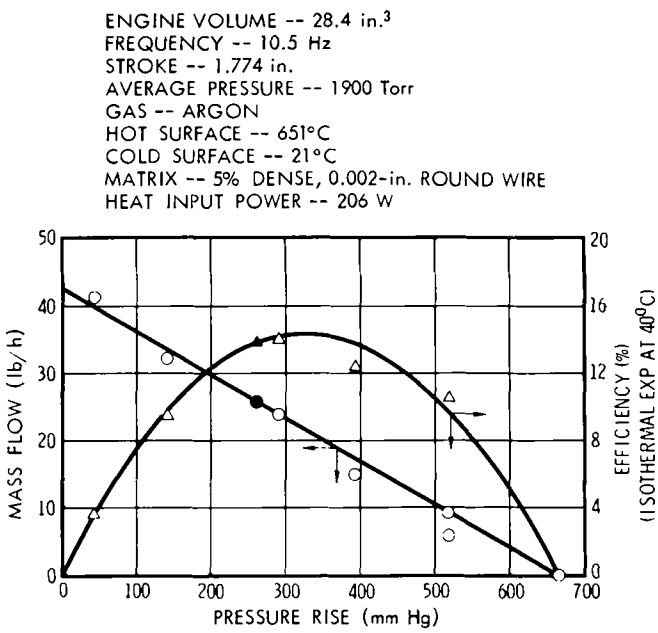


Fig. 9. System 2 engine test results.

system 2 engine. Engine efficiency (measured by determining electric heat input and pumped gas output, without insulation loss) was 14%. Specific power for this engine was 2.6 W per liter per atmosphere at lowest pressure per Hz. This was somewhat less than the system 1 engine which is probably attributable to lower effective gas temperature ratios inside the engine caused by the requirement to transfer more heat.

One problem with the plug-in-orifice type system was that power was obtained in spurts, and a considerable portion of this power was dissipated in the transmission line between the engine and the blood pump. A smoother drive system was developed for use in self-operating engines and was reduced to practice on system 2 (Fig. 10). The regenerator is supported by a piston connecting the gas space in the engine cylinder with the drive chamber. Inlet and outlet valves in the engine and drive chamber allow gas to be pumped from the low to the high pressure tank, then through a flowmeter; the pressure difference between the two tanks is measured. During the downstroke of the regenerator, cold gas from the bottom of the cylinder passes through or around the regenerator and is heated to the hot-gas temperature. The pressure difference between the cold and hot gas space is insignificant when compared to the pressure increase resulting from converting cold gas to hot gas inside a fixed volume (Fig. 10). Engine pressure, $P_E$, increases more rapidly than drive-chamber pressure, $P_P$. During part of the downstroke, engine pressure is

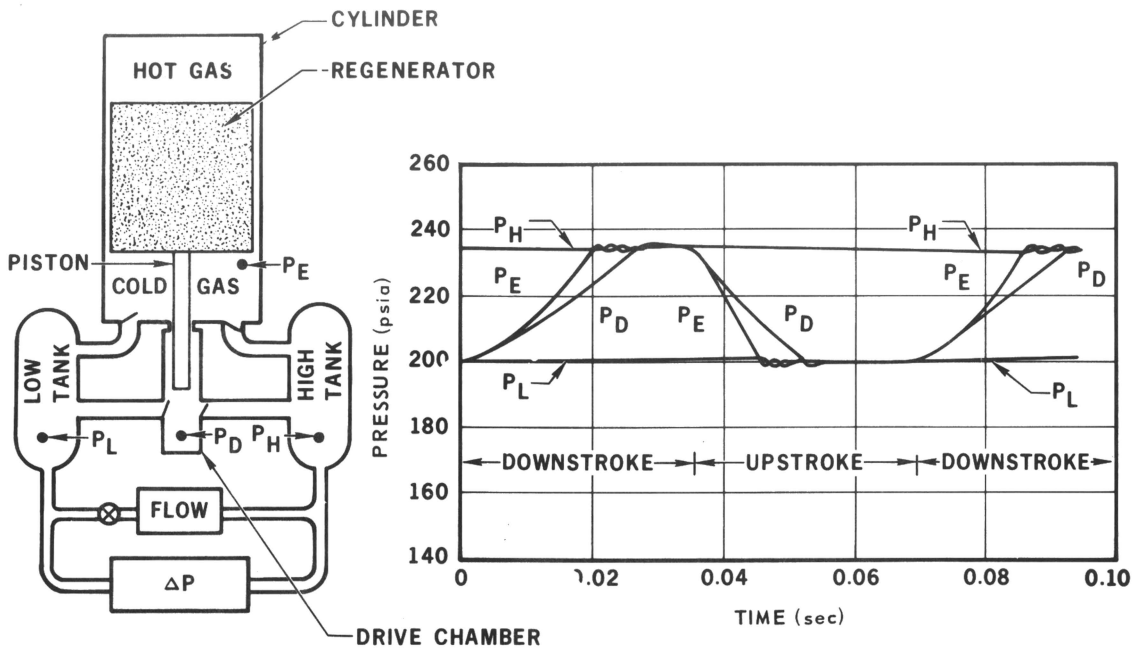


Fig. 10. Self-driven engine operation.

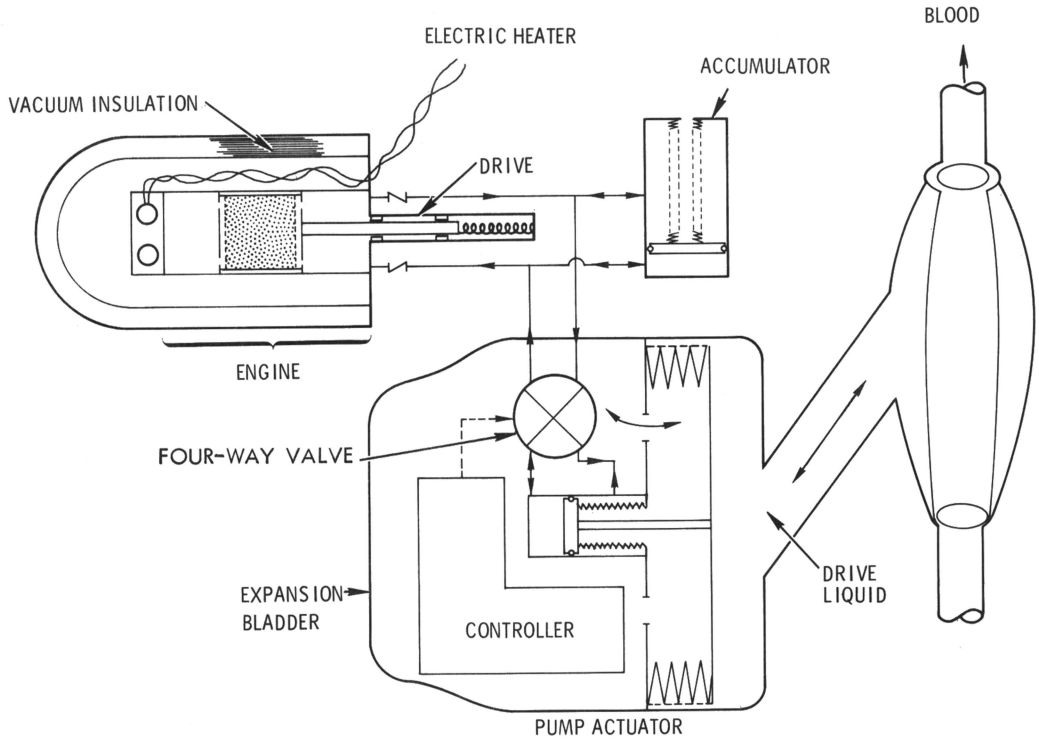


Fig. 11. System 3 concept.

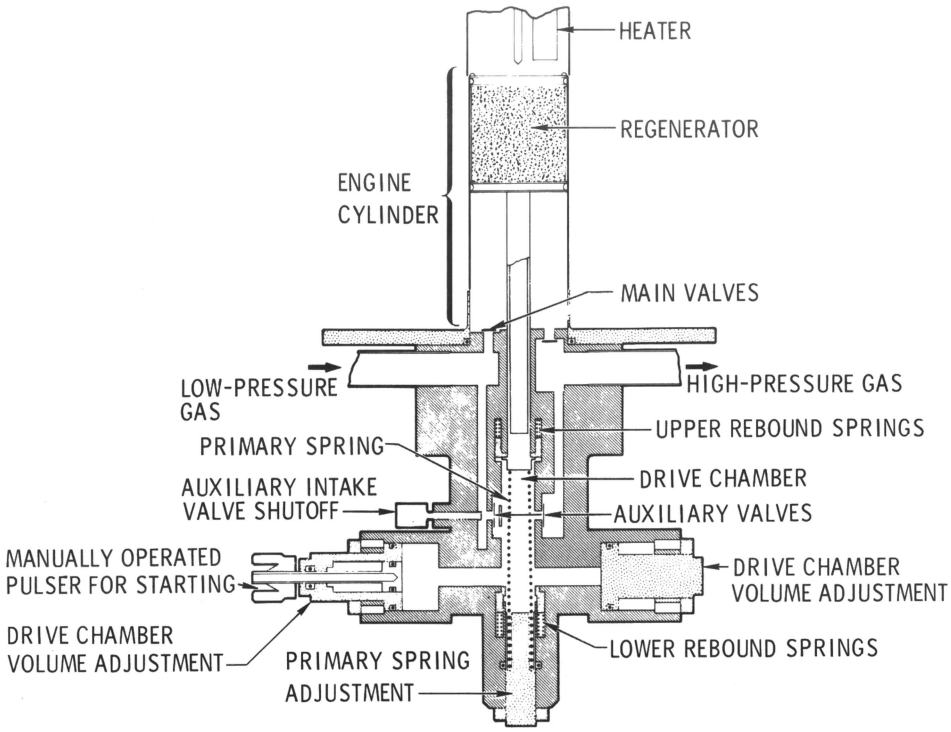


Fig. 12. System 3 engine.

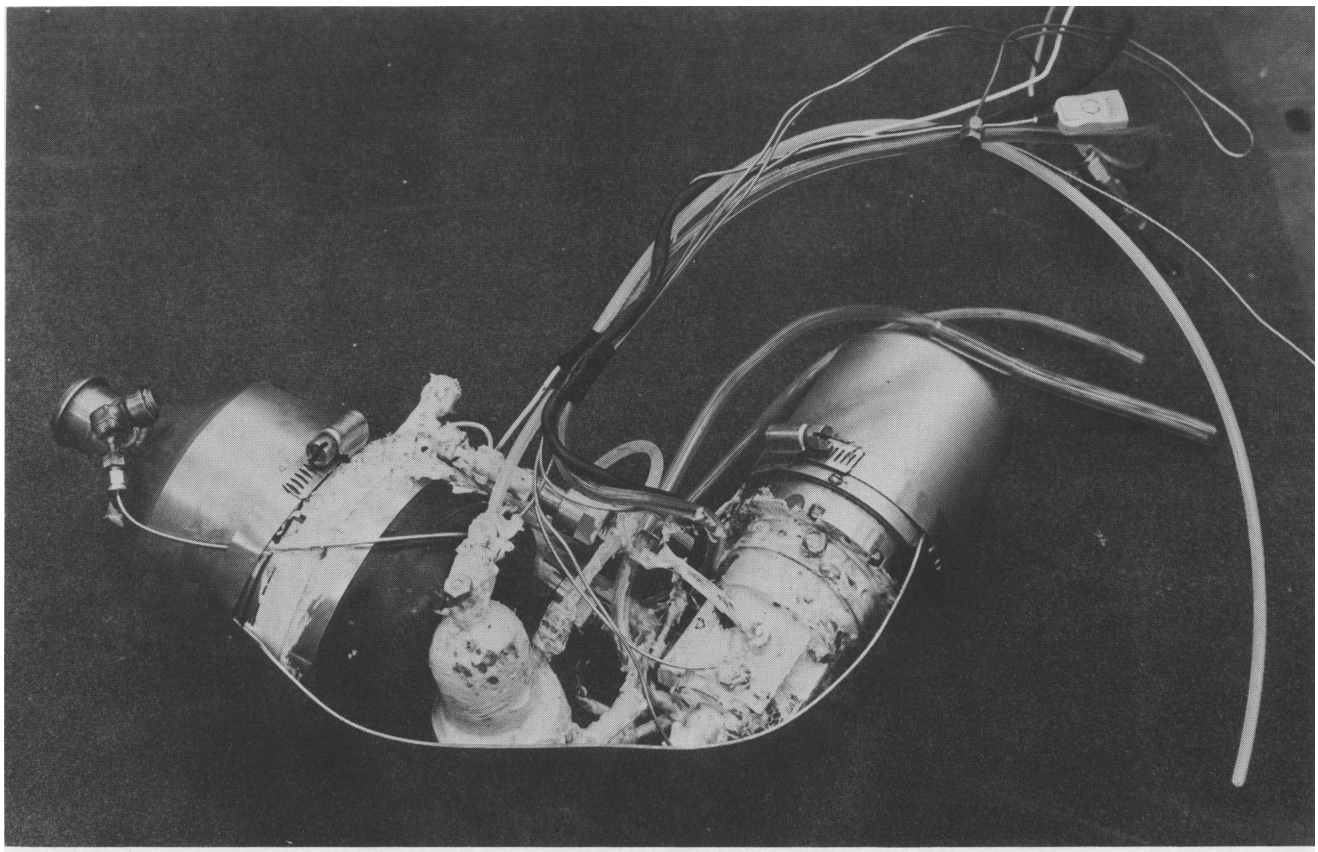

Fig. 13. System 3 ready for fourth *in vivo* test.

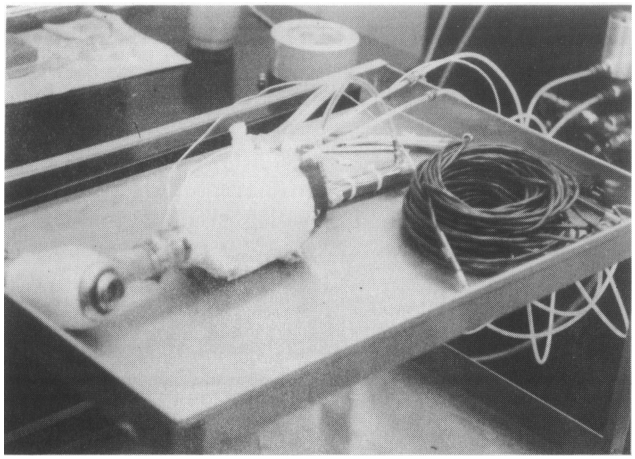

Fig. 14. Hardware for fifth *in vivo* test.

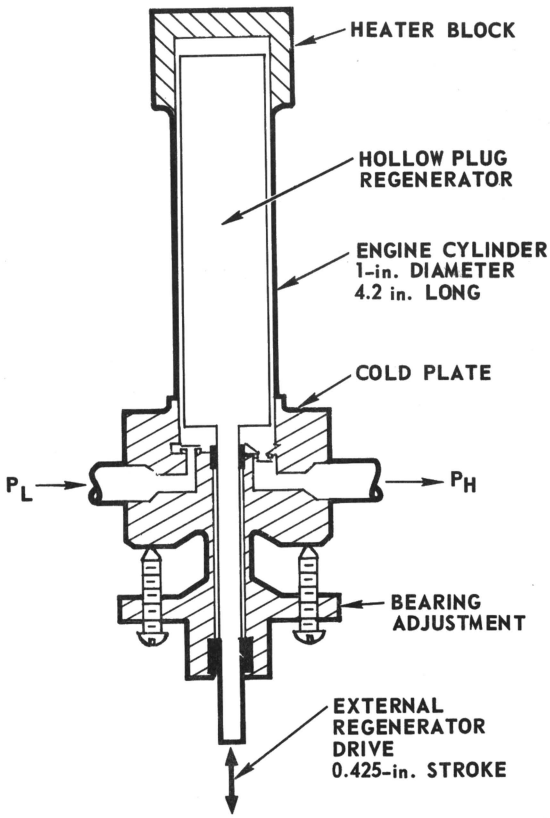


Fig. 15. IRAD engine.

substantially greater than drive chamber pressure, causing a downward force on the piston to reinforce motion. During the upstroke, the process reverses, and an upward force is applied to the piston. The regenerator is controlled to reverse at the end of each stroke; a bounce spring and a flywheel and crank mechanism have been used to reverse regenerator motion.

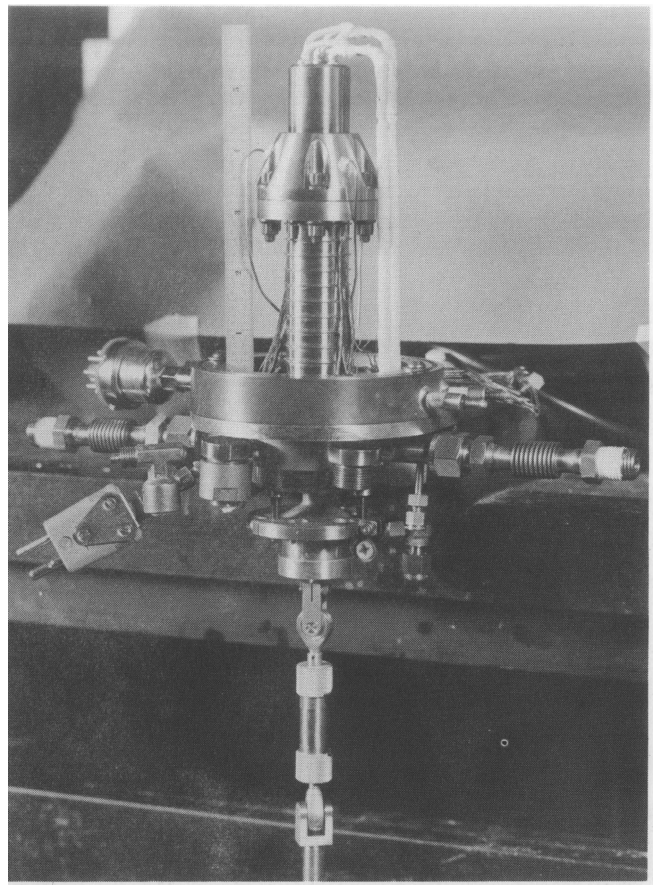

Fig. 16. IRAD engine ready for insulation.

## SYSTEM 3

System 2 efforts show that sufficient power can be obtained from an implantable size engine by increasing gas pressure and operating frequency. In system 3, engine cylinder volume was reduced from 28 to 2 $in.^3$. This small engine includes an electric resistance heater and vacuum insulation. Gas pumped by the engine is stored temporarily in an accumulator (Fig. 11) and applied through a four-way valve to the small piston of the pump actuator. The four-way valve is positioned by a controller which senses the end of stroke and velocity of blood being drawn into the pump. After more than half of the intake stroke is completed, this velocity sensor causes blood expulsion to start if intake flow falls below the set point. The small power piston is directly connected to the large bellows-sealed piston which displaces drive liquid into and out of the blood pump.

Figure 12 shows the system 3 engine. The support for the regenerator and drive system controls is larger and more massive than the engine itself. This engine was bench tested for 90 continuous hours and the test terminated without failure. It produced 10 W at 8% measured overall efficiency and had a specific power of 1.2 W/liter of cylinder volume per atmosphere per Hz.

Figure 13 shows the hardware used during the fourth *in vivo* test. This successfully implanted engine operated for $3\frac{1}{2}$ h during which the actuator synchronized with the heart beat; that is, the pump accepted blood from the heart during systole when the heart was expelling blood, then when the heart relaxed during diastole the pump expelled blood into the aorta. In this way, the mechanical blood pump works to relieve the load normally performed by the heart while still depending on the heart for control. During this test, the engine required 120 W of heat input. Engine stoppage

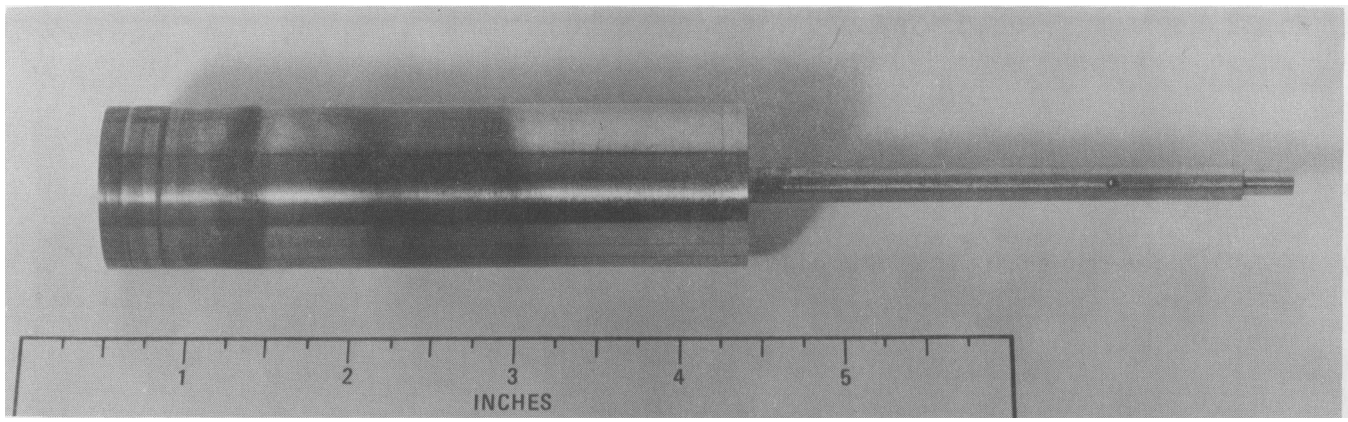


Fig. 17. IRAD engine displacer (engine 4).

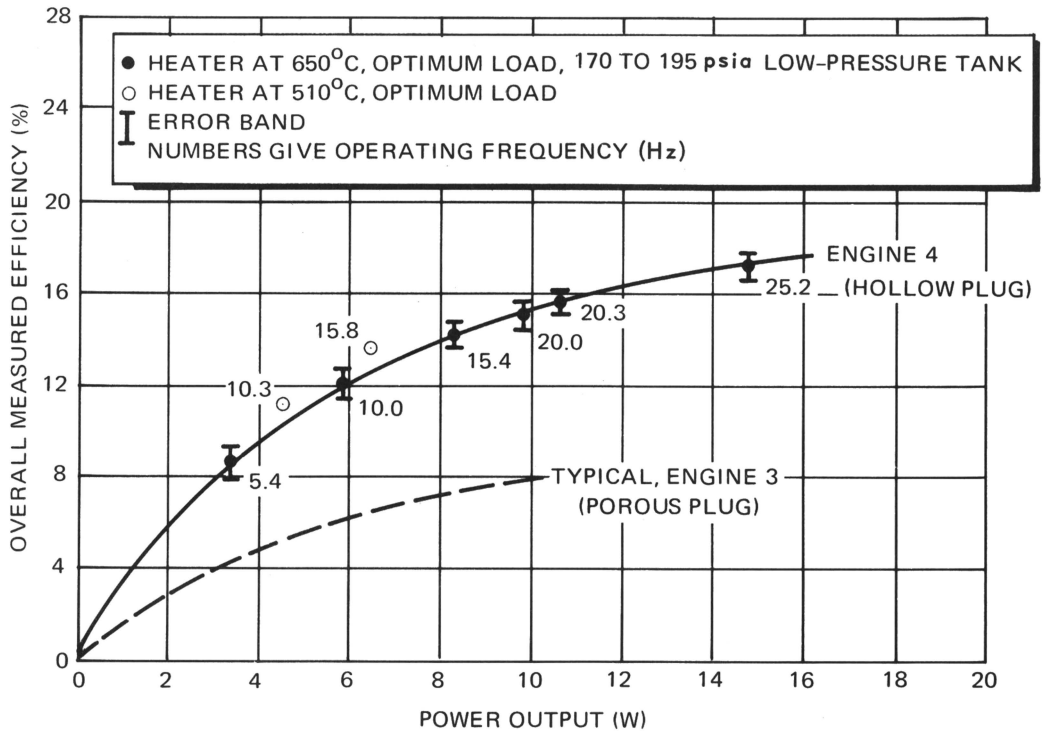


Fig. 18. Comparison of measured overall efficiencies for engines 3 and 4.

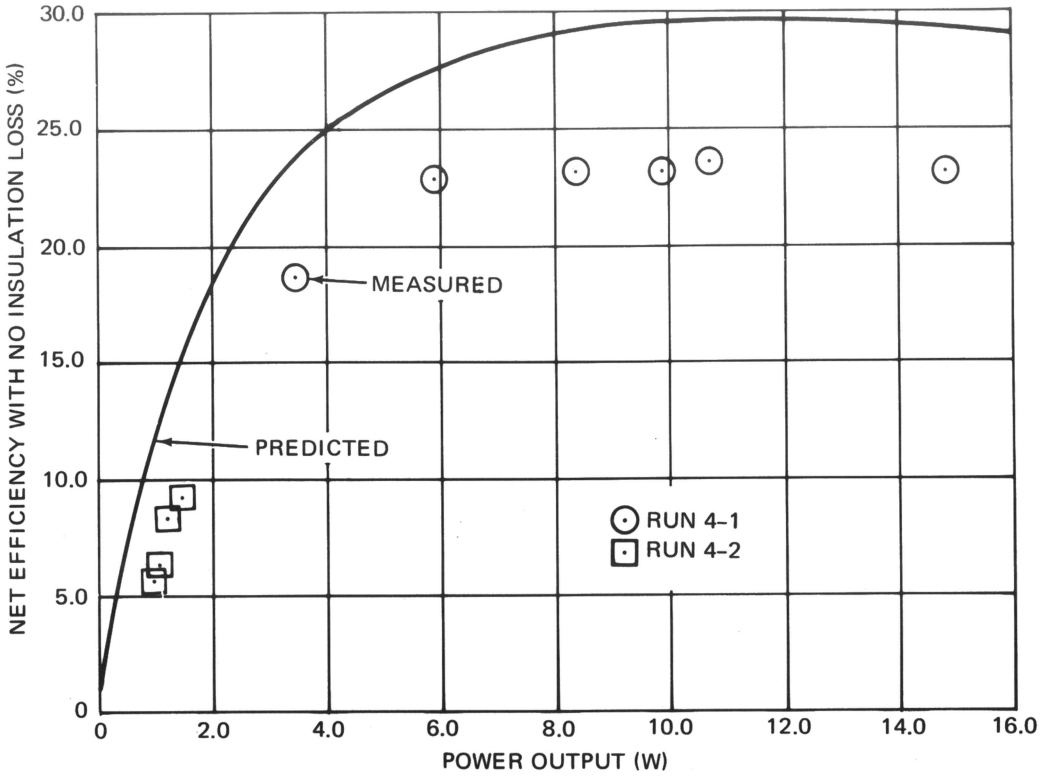


Fig. 19. IRAD engine measured and predicted efficiency (insulation loss-free basis).

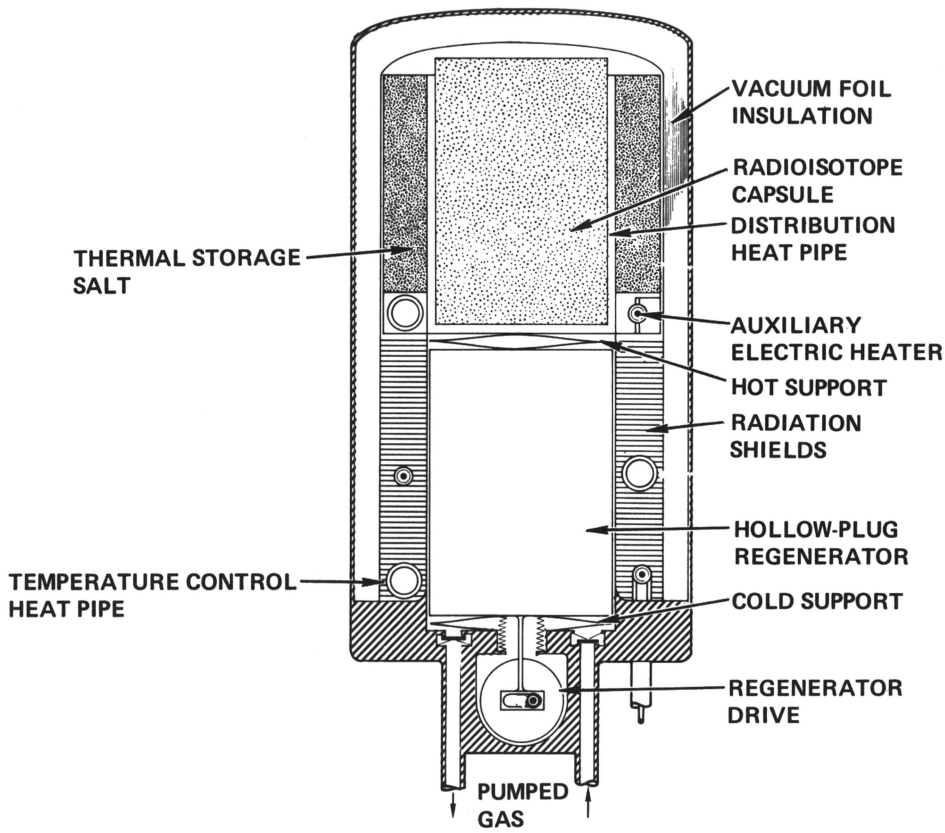


Fig. 20. System 4 engine concept.

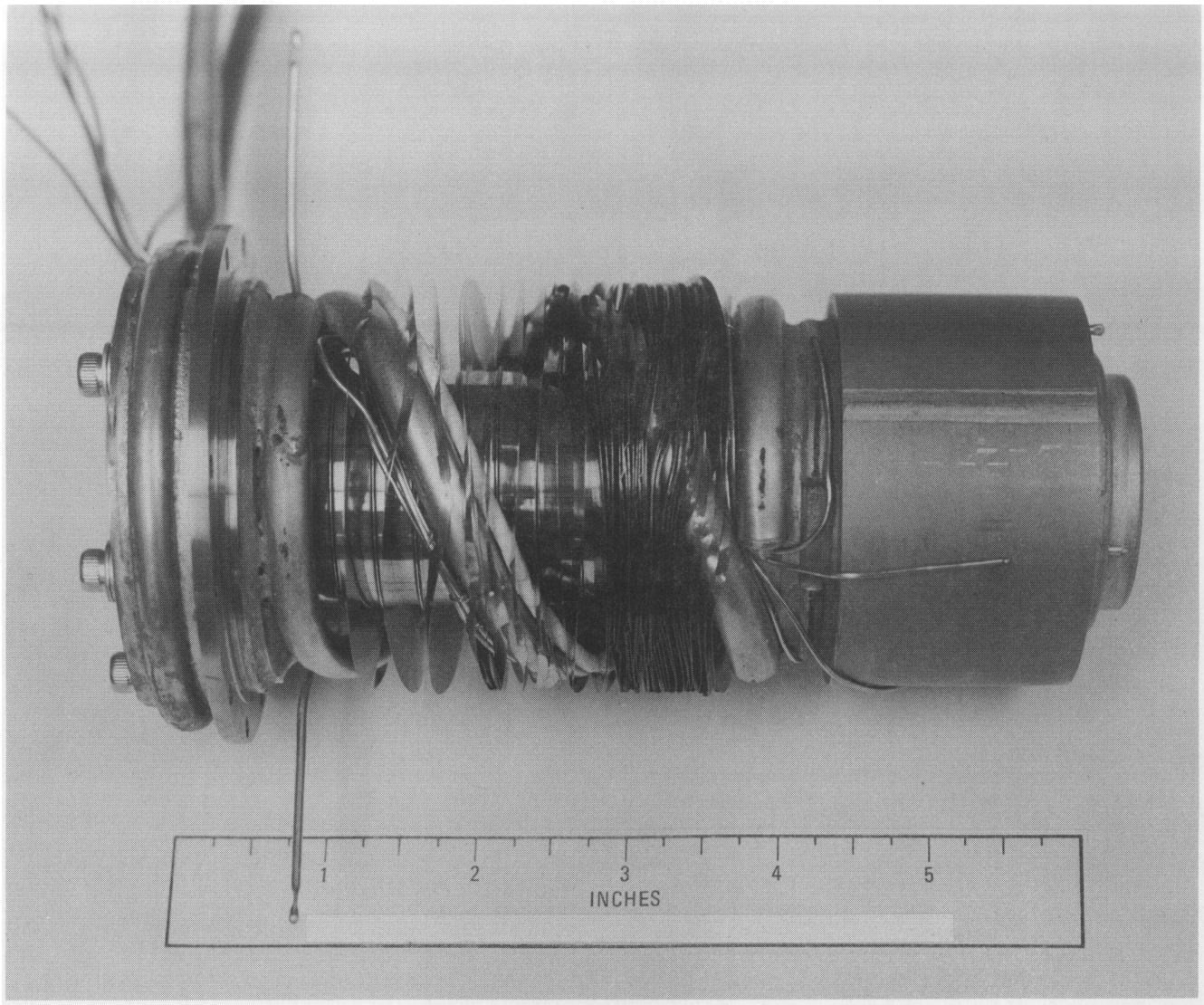


Fig. 21. Engine 5 cylinder assembly (system 4).

resulted from a stray wire wedging in the bearing.

The implant package for the fifth *in vivo* test is shown in Fig. 14. The purpose of this test was to determine if the actuator could synchronize with the heart and to determine heat rejection characteristics. The test established that the best synchronization and ventricle relief was obtained when drive line pressure between the blood pump and the actuator was maintained between 0 and -35 mm during blood intake. The actuator was covered with a $\frac{1}{8}$-in. layer of silicone rubber. Fifty watts from an electric heater standin for the engine was applied. With this heat, the drive liquid attained a temperature of 16.8°F above body temperature. The animal exhibited no discomfort from this source and, on autopsy, there was no tissue damage.

Because the miniature engine used in system 3 had not produced the power expected and had practical problems in containment of the moving porous regenerator packing, the decision was made to try an entirely different engine in a continuing independent research and development program (Fig. 15). This engine was designed for an externally driven regenerator supported from the cold end. These two features allowed rapid and confident engine fabrication and operation over a wide range of frequencies and pressure ratios so that maximum data could be independently developed on the engine.

A conventional Stirling engine has a hollow displacer sealed at the cold end by a gas seal. Movement of the displacer circulates gas from the hot gas space through heater tubes, a stationary

chamber filled with metallic packing acting as a regenerator, and through cooler tubes to the cold gas space. For miniature engines of the size needed for artificial hearts, the effect of these tubes and chambers filled with packing material can be accomplished by a small clearance space between a displacer and the cylinder wall. Consequently, engine construction is greatly simplified. Figure 16 shows this engine ready for installing the insulation package. Cylinder diameter of the engine is 1 in.; length is 3.2 in.

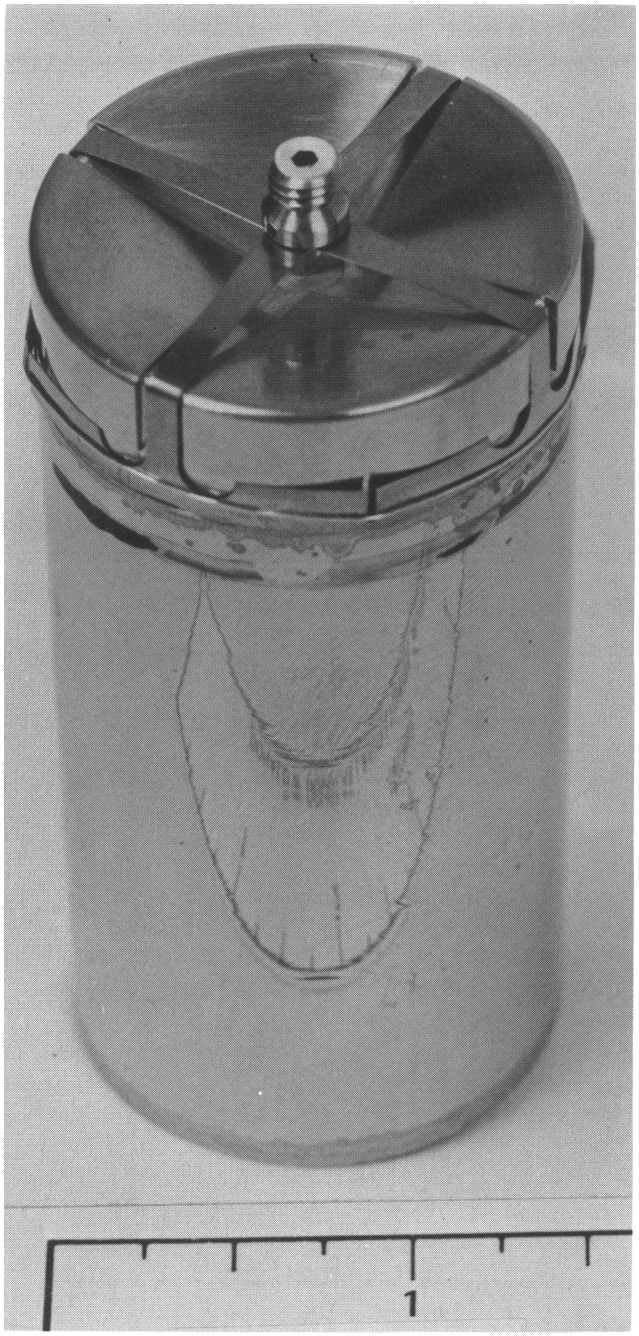

Fig. 22. Engine 5 displacer showing hot-end flexure support.

Figure 17 shows the displacer after operation in the engine. Although the engine operated on helium gas, enough oxygen was present to tarnish the displacer cylinder; the tarnish, however, shows the effectiveness of this cylinder in heating and cooling the gases during each cycle. Figure 18 shows the measured efficiency of this engine at power output levels normally needed for artificial heart applications. Overall measured power output divided by heat input doubled over that exhibited by previous engines. This engine used a makeshift insulation package, and engine performance on an insulation loss-free basis is 23% efficiency (Fig. 19).

## SYSTEM 4

In system 4, the objective was to build an engine which incorporated the clearance regenerator concept of the IRAD engine. This engine was designed to operate the pump actuator used in previous systems and to accommodate a 50-W plutonium radioisotope heat source (Fig. 20). The radioisotope is installed on top of the engine by removing the self-contained vacuum foil insulation. This insulation package has been tested and, at rated temperature, a 9-W heat loss has been established; 5 W is dissipated by conduction down the inside of the vacuum envelope, 4 W through the multifoil insulation. An electric heater is installed so that the engine can operate by supplementary heat or solely on electric heat. An annular container of thermal storage salt is also included so that the engine can operate solely on stored thermal energy for more than half an hour. The distribution heat pipe is included to transport heat isothermally among the radioisotope capsule, thermal storage reservoir, engine, and electric heater. Temperature control heat pipes spiral between the heat source and sink to remove heat under simulated engine failure conditions. At a heat source temperature of 1200°F, the temperature control heat pipes conduct 4 W; at 1400°F these heat pipes conduct 30 W of heat. The heat pipes use cesium as the working fluid with xenon gas to effect temperature control.

The regenerator drive is sealed from the engine space by a bellows. The regenerator drive consists of a crank-operated shuttle arrangement with a flywheel which stores energy between drive impulses from the bellows.

Figure 21 shows this engine cylinder complete with heat pipes, thermal storage reservoir, and radiation shields. The heat pipes are ready for trimming after which the insulation package is

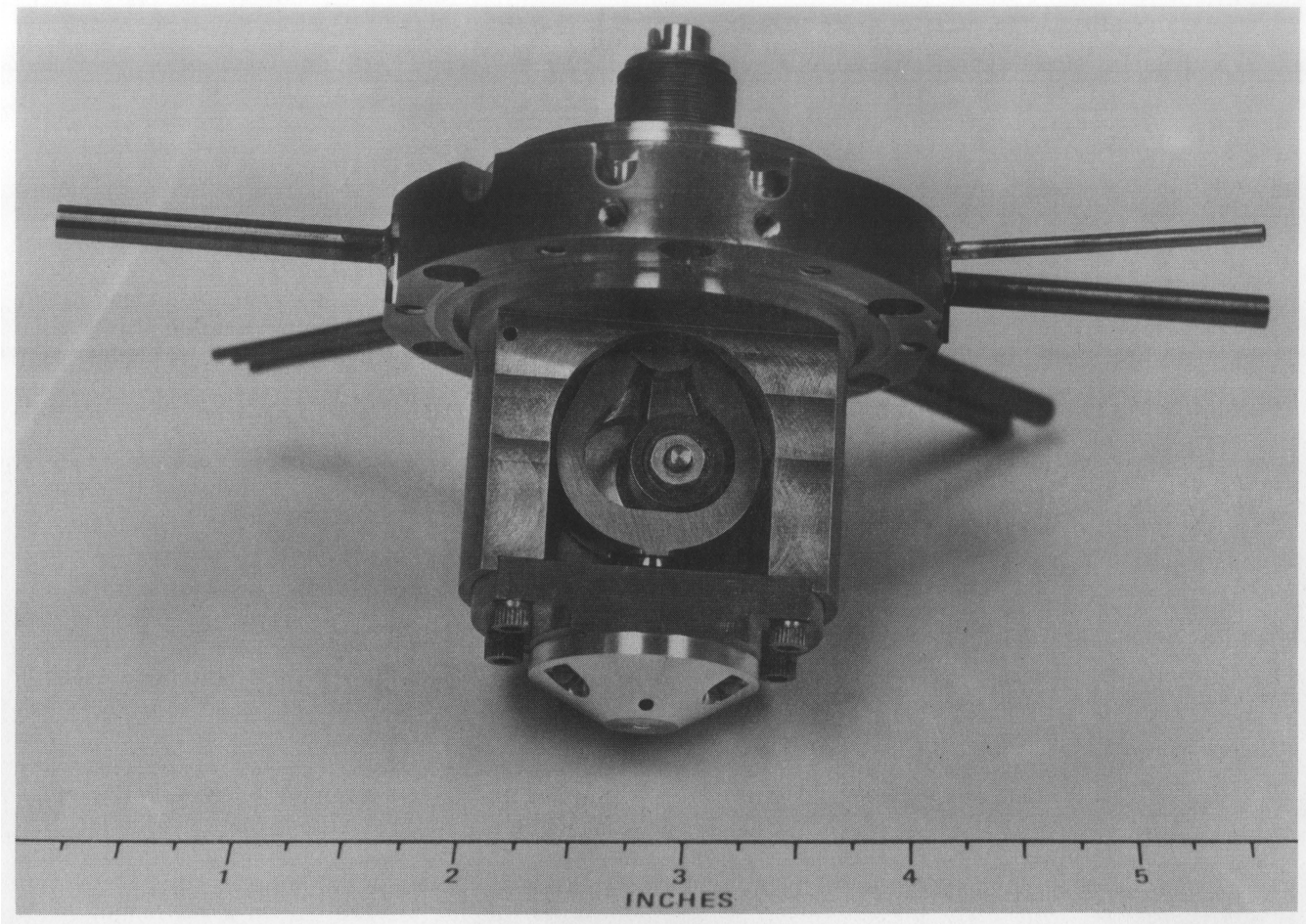


Fig. 23. Engine 5 regenerator drive.

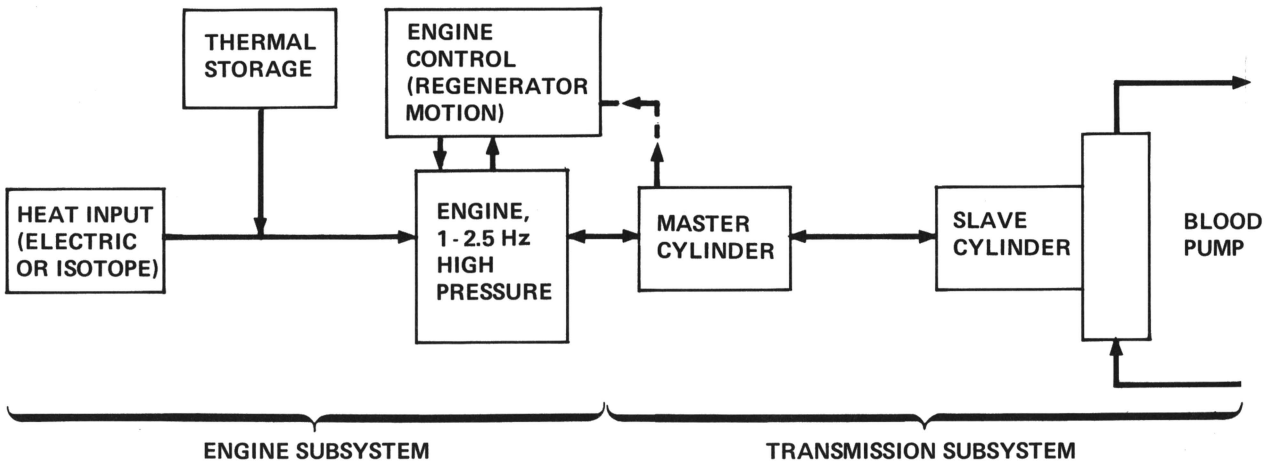


Fig. 24. System 5 concept (direct-drive engine to blood pump).

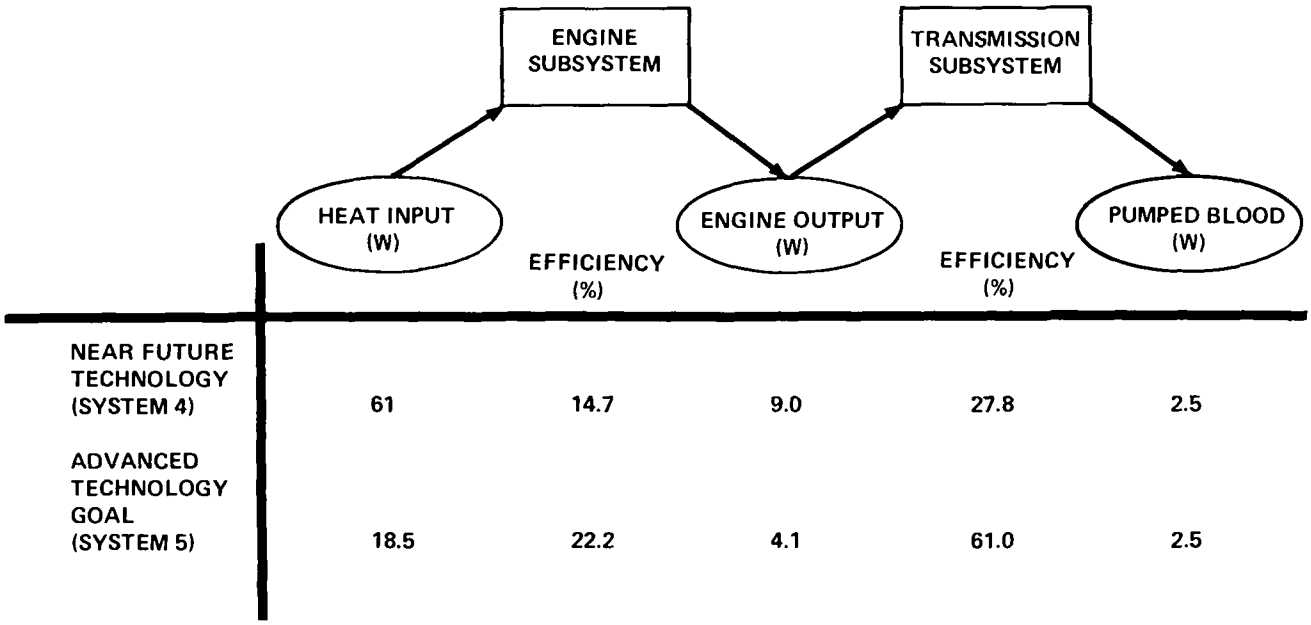


Fig. 25. Near-future and advanced artificial heart energy requirements at average activity.

| | NEAR FUTURE SYSTEM 4 | ADVANCED SYSTEM 5 |
|---|---|---|
| ENGINE SUBSYSTEM ($in.^3$) | 44 | 44 |
| TRANSMISSION SUBSYSTEM ($in.^3$ max) | 125 | 22 |
| TOTAL ($in.^3$) | 169 | 66 |
| (liters) | 2.77 | 1.08 |

Fig. 26. Near-future and advanced artificial heart volumes.

slipped over the entire assembly. Figure 22 shows the displacer with the flexural support at the hot end in place. This leaf spring operates at 1200°F and prevents appreciable lateral motion while allowing the displacer to stroke longitudinally. Figure 23 shows the flywheel regenerator drive. The flywheel is supported on ball bearings and operates freely.

## SYSTEM 5

System 5 (Fig. 24) is presented as an idealized future system to show what is possible in terms of reducing the radioisotope inventory by possible developments. The concept includes an engine and transmission subsystem. Unneeded heat from the isotope or electric heat is stored temporarily in the thermal reservoir. The engine operates at high pressure but at the speed required by the blood pump; regenerator motion is the point of control. A low-volume master/slave cylinder transmits motion of the power piston to the blood pump, as needed to pump the blood. Near-future and advanced energy requirements at average activity are presented in Fig. 25. The efficiency of both the engine and transmission subsystems can be substantially improved so that, with 2.5 W delivered to the blood, about one-third of the present 50 W of radioisotope heat will be required. Similarly (Fig. 26), the size of the artificial heart can be substantially reduced to a minimum of about 1 liter.

## EXPECTED DOSE RATE

Analysis has been made for a 50-W (thermal) $^{238}Pu$ heat source capsule installed in a Stirling engine designed for the artificial heart (Fig. 27). Assuming that the surgical implantation procedure requires $1\frac{1}{2}$ h with an average distance of 1 ft from the center of the engine, the surgeon receives a body dose of 5.3 mrems for the 3000 neutron fuel device and 12.6 mrems for the 12,000 neutron specification fuel. Limiting the surgeon to 5-rems body dose per year, the surgeon can perform 240 procedures per quarter for the 3000 and 100 for the 12,000 specification fuel. The

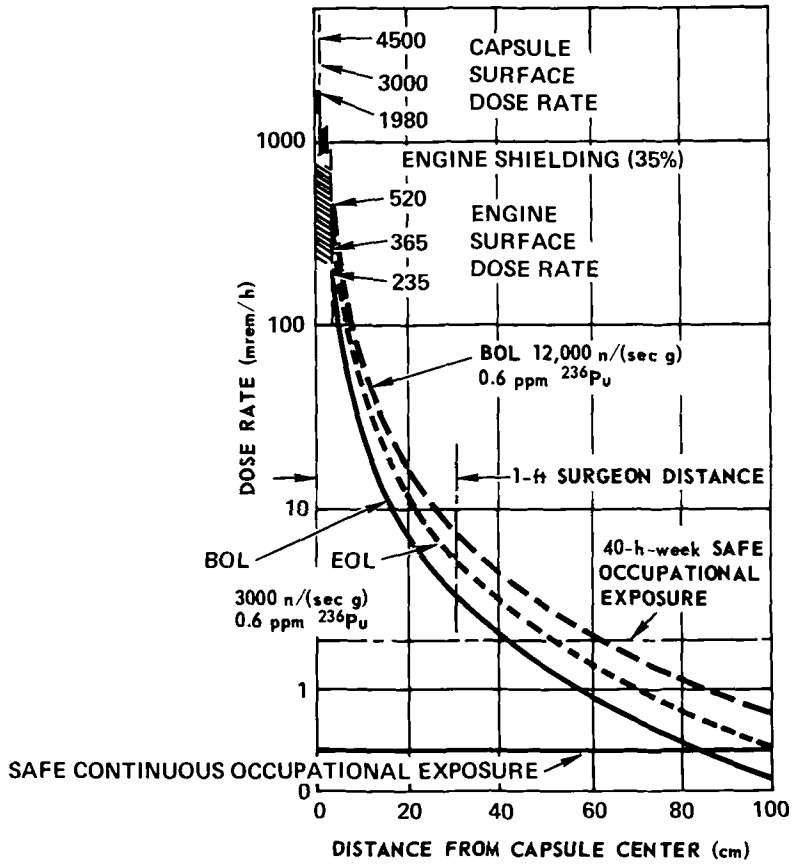


Fig. 27. 50-W capsule dose rate as a function of distance.

surgeon is somewhat more restricted if the limiting exposure is 75 rems to hands and forearms. In this case, assuming the device is held for $1\frac{1}{2}$ h during implant, the surgeon is limited to 50 and 25 procedures per quarter with the 3000 and 12,000 specification fuels, respectively.

Continuous exposure to the animal or human user of this heart assist device is of importance. The computed dose rate immediately outside the engine is 235 mrem/h and falls off rapidly with distance. At one foot it is 3.5 mrem/h. This dose rate is one-quarter that used by Thermo Electron Corporation for a dog which was still healthy after 26 months of exposure.

## CONCLUSIONS

Through a continuing program of design analysis and testing of the complete system, both on the bench and *in vivo*, an entirely workable artificial heart system designed to be fueled with a radioisotope capsule is now being constructed. Development has started on important improvements in the energy system which will make the use of radioisotopes more economical.

# BRACKETING THE PEAK PRIMARY GAMMA-RAY DOSE RATE FROM NUCLEAR DEVICES BY STEADY-STATE TRANSPORT CALCULATIONS

SHIELDING

**KEYWORDS:** *gamma radiation, dose rates, reactors, shielding, concretes, time dependence, computers, transport theory, programming, uranium-235*

H. C. CLAIBORNE and W. W. ENGLE, Jr.
*Oak Ridge National Laboratory, Oak Ridge, Tennessee 37830*

Received June 18, 1971
Revised October 6, 1971

*Electronic components can be affected by the dose rate from gamma rays delivered during the first few shakes ($10^{-8}$ sec/shake) of an exploding nuclear device. Determining such dose rates generally requires expensive time-dependent calculations. This paper demonstrates that relatively inexpensive steady-state transport calculations can be used to bracket time-dependent peak dose rates with meaningful upper and lower limits.*

*The model configuration consisted of a sphere of air surrounded by a spherical annulus of concrete with an isotropic source of gamma rays from fissioning $^{235}U$ located at the geometric center. Steady-state calculations were made with the discrete ordinates code ANISN and the time-dependent calculations with time-dependent ANISN (TDA). The upper limit dose rates were obtained by dividing the steady-state total dose by the pulse width of the device. This is equivalent to assuming that the uncollided and air-scattered fluxes arrive at the shield simultaneously. For a lower limit calculation, only the uncollided flux was considered incident on the shield.*

*Calculations were made for a 120-cm-thick concrete shield for ranges of 500, 1000, and 5000 m and for step-function burst pulse widths of 1 through 8 shakes. The results from the steady-state calculations generally bracketed the peak time-dependent dose rates within an acceptably narrow band except for the 500-m range at the back end of the shield where the peak time-dependent dose rates were highest for all pulse widths. This apparent anomaly is explained on the basis of using a moving boundary condition in the time-dependent solution and the effect is shown to be of no consequence.*

## INTRODUCTION

Electronic circuits and systems can fail permanently on receiving excessive doses of gamma rays and neutrons or have a temporary malfunction on being exposed to a momentary high dose rate of gamma rays or neutrons.[1] The transient radiation effects in electronic components are due to current and voltage changes caused by ionization of the component materials. Most of the ionization produced in the radiation environment at ranges removed from the fireball of a nuclear weapon is caused by gamma rays, both primary and secondary.

When considering nuclear weapon environments, primary gamma rays (regardless of origin) are defined as those that leak from the exploding device, and secondary gamma rays as those that result from neutron interactions with air and ground. The primary gamma rays will arrive first, followed almost immediately by secondaries which will quickly build to a peak. The degree of enhancement (if any) of the peak dose rate from the primaries by the secondary gamma rays depends on a number of variables. In this paper, only primary gamma rays are considered, which, for most conditions, will control the peak dose rate.

The primary purpose of this paper is to demonstrate that relatively inexpensive steady-state transport calculations can be used to bracket peak time-dependent dose rates with meaningful upper and lower limits.

The model configuration consisted of a sphere of air surrounded by a spherical annulus of concrete with an isotropic source at the geometric center. Steady-state calculations were made with the discrete ordinates code[2] ANISN and the time-dependent ones with time-dependent ANISN (TDA).[3] The upper limit on the dose rate was obtained by

dividing the steady-state total dose by the pulse width of the device. This is equivalent to assuming that the uncollided and scattered fluxes arrive simultaneously. For a lower limit calculation, only the uncollided flux was considered incident on the shield.

A more complete discussion of the model configuration and the calculations along with graphs and tables of the pertinent results are given in the following sections.

## CALCULATIONAL MODEL

Calculations for shielding against radiation from nuclear weapons are usually made in two steps: the air transport problem is first solved for a free-field flux which then becomes the source term for the separate shield transport calculation. The model used for these calculations, however, combines both air and shield transport of gamma radiation into a one-dimensional configuration which consists of an isotropic point source of gamma rays located at the center of a spherical mass of air and surrounded by a concrete shell with a thickness of 120 cm. Such a model is quite adequate since the radius of curvature is very large compared to the thickness of the concrete shell and distances are so large that backscattering from the concrete will have very little effect on the incident dose. In addition, the dose rate for smaller thicknesses obtained from the dose distribution curve for the 120-cm-thick shell represents a good approximation to the gamma-ray dose rate for slabs of corresponding smaller thicknesses since backscatter in the concrete is of little importance.

## UPPER AND LOWER LIMITS OF THE DOSE RATES

In an air-shield transport problem, the upper and lower limits of the dose rates from a step function source that is uniform over a specified time period can be established with steady-state calculations. For the model described previously, the lower limit can be obtained by assuming that the air-scattering cross section is zero and consequently the number of photons in each source energy group on striking the shield is reduced by $\exp(-\mu R)$, where $\mu$ is the total linear attenuation coefficient of the air and $R$ is the radius or distance between the source and the concrete wall. This is equivalent to assuming that the scattered flux arrives significantly later than the uncollided flux and, consequently, only the latter makes a significant contribution to the dose, which, when divided by the weapon pulse width, produces the lower limit for the peak dose rate. The upper limit of the peak dose rate is obtained with the air scattering included in the model, which for the steady-state calculation is equivalent to assuming that both the scattered and uncollided fluxes arrive at the same time.

These steady-state calculations that established the upper and lower limits were made with the discrete ordinates code ANISN using an $S_{16}P_3$ approximation and 14 energy groups (see Table I). The same total number of spatial increments (159) was used for the three ranges calculated. In all cases, the concrete spatial increments were 3-cm thick, but the thickness of the air increments varied with range. In about the first 10% of the distance from the source, the thickness of the air increments was gradually increased to its maximum value and in no instance was the total geometric attenuation across an increment greater than a factor of 2, a condition necessary for accurate calculations with the finite difference models used in ANISN. The maximum increment sizes in the air were 6.6, 15.6, and 50 m for the 500-, 1000-, and 5000-m ranges, respectively.

TABLE I

Gamma-Ray Energy Group Structure, Source Spectrum, and Silicon Response Functions

| Group | Energy Interval (MeV) | Silicon Response Functions [rads/($\gamma$/cm$^2$)] | Source Spectrum (fraction) |
|---|---|---|---|
| 1 | 9-10 | 2.84-9[a] | 1.34-4 |
| 2 | 8-9 | 2.52-9 | 1.34-4 |
| 3 | 7-8 | 2.22-9 | 1.34-4 |
| 4 | 6-7 | 1.94-9 | 1.46-3 |
| 5 | 5-6 | 1.68-9 | 3.14-3 |
| 6 | 4-5 | 1.41-9 | 7.47-3 |
| 7 | 3-4 | 1.15-9 | 2.14-2 |
| 8 | 2-3 | 8.83-10 | 6.22-2 |
| 9 | 1-2 | 5.86-10 | 2.47-1 |
| 10 | 0.6-1.0 | 3.50-10 | 2.48-1 |
| 11 | 0.4-0.6 | 2.34-10 | 1.87-1 |
| 12 | 0.2-0.4 | 1.25-10 | 1.68-1 |
| 13 | 0.1-0.2 | 7.04-10 | 5.42-2 |
| 14 | 0.01-0.1 | 1.58-9 | 0 |

[a] Read as $2.84 \times 10^{-9}$.

## TIME-DEPENDENT CALCULATIONS

All time-dependent calculations were made with the discrete ordinates code TDA,[3] which is an extension of the ANISN code to include the time dependence of the flux. In a series of calculations used to check TDA,[4] it was determined that an

analytic first-collision source was required in pulse propagation problems to reduce the severe restrictions on the space and time mesh intervals that would otherwise be required to describe the movement of the uncollided source particles through the system. Because of the finite difference techniques employed in TDA, it is also necessary to utilize a moving boundary condition which assures that the flux in the space intervals beyond the interval containing the uncollided pulse is identically zero while still maintaining particle balance. These techniques that were developed serve quite adequately for instantaneous point sources.

The source in the model described in this paper is not instantaneous but is defined as a square wave with a duration ranging from 1 to 8 shakes (1 shake = $10^{-8}$ sec). In the concrete the time intervals in the TDA calculation were 0.01 shake and the source description would be spread over 100 to 800 time intervals. Two problems were apparent. Proper description of the source would require an excessive number of time intervals and amount of computer time, and since the moving boundary condition can only be defined at the leading edge of the square wave, it would be possible for particles generated in the trailing portion of the square wave to propagate (due to the finite differencing) into the front of the uncollided pulse. The solution to both problems was to run one TDA calculation for each of the three ranges of interest using an instantaneous point source. Because of the finite size of the space and time intervals in the concrete, the instantaneous pulse was spread into the equivalent to a square pulse of 0.01-shake duration, which is the time required to traverse a 3-cm interval for a photon that does not interact with the concrete. The results of each calculation were then summed over the appropriate time intervals, depending on the source pulse width, for the space interval of interest. This is equivalent to dividing the 1-shake pulse, for example, into 100 identical parts, running a separate TDA calculation for each part, and summing the results to obtain the total response. The same technique could be used for other than a step function source, but each time interval in the summation would have to be weighted by the source intensity in that particular interval. It is also clear that for a square wave source, the peak dose rate occurs as the trailing edge of the uncollided pulse passes through the space interval of interest since both the uncollided flux and a maximum of collided flux are included in the response.

TABLE II

Calculated Peak Gamma-Ray Dose Rates for a 120-cm-Thick Concrete Shield for Ranges* of 1000 and 5000 m

| Range (m) | Pulse Width (shakes) | $4\pi R^2$ Dose Rate, [$cm^2$ rads (Si)/sec]/Source Gamma Photon | | | | | |
|---|---|---|---|---|---|---|---|
| | | Front End of Shield[a] | | | Back End of Shield[a] | | |
| | | | Steady-State | | | Steady-State | |
| | | Time Dependent | Uncollided + Scattered | Uncollided Only | Time Dependent | Uncollided + Scattered | Uncollided Only |
| 1000 | 1 | 6.22-4[b] | 2.50-3 | 5.32-4 | 4.47-7 | 4.93-7 | 3.70-7 |
| | 2 | 3.32-4 | 1.25-3 | 2.66-4 | 2.26-7 | 2.47-7 | 1.85-7 |
| | 3 | 2.35-4 | 8.32-4 | 1.77-4 | 1.53-7 | 1.64-7 | 1.23-7 |
| | 4 | 1.87-4 | 6.24-4 | 1.33-4 | 1.16-7 | 1.23-7 | 9.25-8 |
| | 5 | 1.58-4 | 4.99-4 | 1.06-4 | 9.38-8 | 9.87-8 | 7.40-8 |
| | 8 | 1.14-4 | 3.12-4 | 6.64-5 | 6.05-8 | 6.16-8 | 4.63-8 |
| 5000 | 1 | 1.79-8 | 7.13-8 | 1.21-8 | 4.19-11 | 6.86-11 | 3.13-11 |
| | 2 | 9.24-9 | 3.56-8 | 6.06-9 | 2.13-11 | 3.43-11 | 1.57-11 |
| | 3 | 6.35-9 | 2.38-8 | 4.04-9 | 1.44-11 | 2.29-11 | 1.04-11 |
| | 4 | 4.90-9 | 1.78-8 | 3.03-9 | 1.09-11 | 1.72-11 | 7.83-12 |
| | 5 | 4.04-9 | 1.43-8 | 2.42-9 | 8.59-12 | 1.37-11 | 6.26-12 |
| | 8 | 2.73-9 | 8.91-9 | 1.51-9 | 5.50-12 | 8.58-12 | 3.91-12 |

*Air density, 0.92 g/liter.

[a]Location is at the midpoint of the spatial increments at the shield edges, i.e., 1.5 cm from the edges.

[b]Read as $6.22 \times 10^{-4}$.

## INPUT DATA

The energy group structure, the source spectrum, and the gamma-ray response functions used in both the steady-state and time-dependent calculations are shown in Table I. All gamma-ray multigroup cross sections, including the response functions (which are simply the mean for each group of the product of the energy and the corresponding energy deposition cross section for silicon expressed in $cm^2$ rads/photon) were generated with the MUG code.[5] Other response functions could have been used to convert the calculated fluxes to dose rates of different types and still demonstrate the effectiveness of bracketing the time-dependent dose rates with steady-state calculations. The silicon response was chosen because some radiation damage specifications for electronic equipment are usually given in terms of the rate of energy deposition in silicon. The source spectrum was obtained using approximate exponential fits[6] to the data for prompt fission of $^{235}U$. For the higher energies, the spectrum is very uncertain so a conservative estimate of the number of photons above 7 MeV was simply divided equally among the highest energy groups. The actual spectrum is not too important since any reasonable one should suffice for the purpose of demonstrating the ability to bracket time-dependent calculations with steady-state ones. The absolute dose rates resulting from the assumed fission spectrum, which has no relation to a leakage spectrum from a nuclear device, are of little value for a real situation except to serve as rough guidelines. The air densities used (0.84 and 0.92 g/liter) were not selected for any particular reason except that they are typical of average air densities that could exist in the line of sight between a high air burst and a ground target. The concrete[7] was assumed to be 0-HW1 with a density of 2.33 $g/cm^3$.

## RESULTS AND DISCUSSION

Steady-state and time-dependent calculations were made for the previously described model for ranges of 500, 1000, and 5000 m and for step-function burst pulse widths of 1 through 8 shakes, a range of parameters that should be sufficient for testing the efficacy of using steady-state calculations to bracket the time-dependent case.

Table II gives the calculated peak dose rates at the front and back ends (actually 1.5 cm from the edges) of the shield for ranges of 1000 and 5000 m. Figures 1 and 2 show plots of these dose rates versus pulse width. Clearly, the time-dependent cases are bracketed by the steady-state results for these ranges. In the case of the 500-m range, however, the time-dependent results (labeled "standard" in Table III) for all pulse widths at the back end of the shield are slightly higher than the upper limit ANISN calculation. Aside from small effects caused by slight spatial mesh differences in the air region and the difference in treatment of the source (TDA uses a first-collision source routine and ANISN does not), the main reason for the apparent anomaly seems clear. In the time-dependent calculation, a boundary condition that moves with time is used to prevent particles from

TABLE III

Calculated Peak Gamma-Ray Dose Rates for a 120-cm-Thick Concrete Shield and a 500-m Range*

| Pulse Width (shakes) | $4\pi R^2$ Dose Rate [$cm^2$ rads (Si)/sec]/Source Gamma Photon | | | | | | |
|---|---|---|---|---|---|---|---|
| | Front End of Shield[a] | | | Back End of Shield[a] | | | |
| | | Steady State | | Time Dependent | | Steady State | |
| | Time Dependent | Uncollided + Scattered | Uncollided Only | Standard[b] | Special[b] | Uncollided + Scattered | Uncollided Only |
| 1 | 5.09-3[c] | 1.45-2 | 4.43-3 | 1.88-6 | 1.50-6 | 1.83-6 | 1.57-6 |
| 2 | 2.72-3 | 7.27-3 | 2.22-3 | 9.52-7 | 7.63-7 | 9.14-7 | 7.84-7 |
| 3 | 1.93-3 | 4.84-3 | 1.48-3 | 6.43-7 | 5.15-7 | 6.09-7 | 5.23-7 |
| 4 | 1.54-3 | 3.63-3 | 1.11-3 | 4.88-7 | 3.92-7 | 4.57-7 | 3.92-7 |
| 5 | 1.30-3 | 2.91-3 | 8.86-4 | 3.95-7 | 3.16-7 | 3.65-7 | 3.14-7 |
| 8 | 9.41-4 | 1.82-3 | 5.54-4 | 2.47-7 | 1.97-7 | 2.28-7 | 1.96-7 |

*Air density, 0.84 g/liter.
[a]Location is at midpoint of the spatial increments at the shield edges, i.e., 1.5 cm from edges.
[b]See text for explanation.
[c]Read as $5.09 \times 10^{-3}$.

appearing ahead of the uncollided wave front, which causes some accumulation of scattered particles in the space interval containing the moving boundary condition. The accumulation also occurs for greater ranges, but the larger spread between the limits on maximum dose rate prevents the effect from being noticed. To estimate the magnitude of this spurious accumulation, special calculations (labeled "special" in Table III) were made for the peak dose rate occurring when the moving boundary condition was applied to the last space interval in the concrete. These special calculations included the scattered radiation from previous time intervals but not that scattered within the last space interval by the last part of the uncollided wave front from the source as it passes through. This special case represents a lower limit for the time-dependent calculation

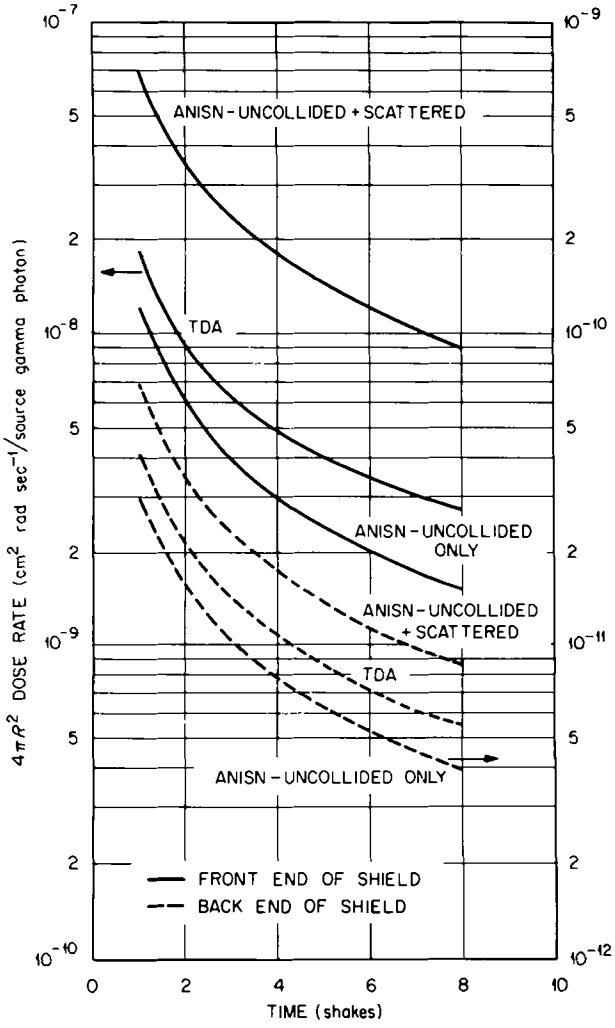


Fig. 1. $4\pi R^2$ peak dose rate as a function of pulse width for a 5000-m range. Air density, 0.92 g/liter.

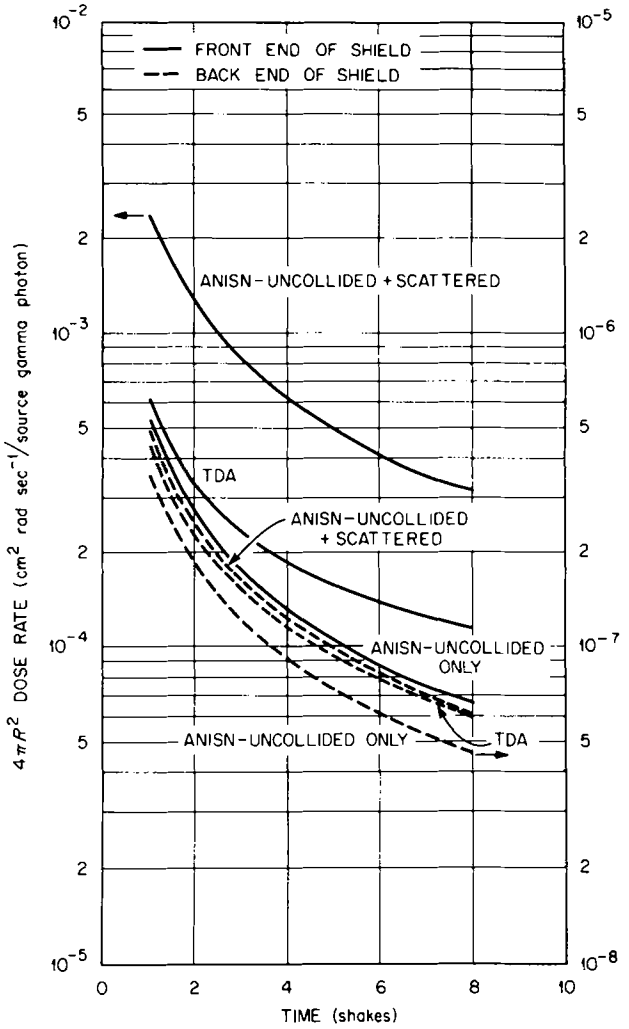


Fig. 2. $4\pi R^2$ peak dose rate as a function of pulse width for a 1000-m range. Air density, 0.92 g/liter.

since the peak dose rate contains no buildup due to scattering in the last interval by the last part of the uncollided wave and, consequently, no spurious accumulation is included. It is apparent that the true answer lies between the two time-dependent results, and the effect is not serious since the "special" dose rates are only about 20% lower than the "standard" ones. The peak dose rates as a function of pulse width for the 500-m case are shown plotted in Fig. 3. The special case results are not shown since they are too close to the lower values to be plotted separately.

The peak dose rates as a function of depth into the shield for both 1- and 8-shake pulse widths at ranges of 500, 1000, and 5000 m are shown in Figs. 4, 5, and 6, respectively. In general, the greater the range, the greater the spread between the upper and lower limits of the peak dose rate.

This results because the relative contribution to the dose rate by air-scattered photons increases with range due to the larger scattering volume. The spread decreases with shield penetration because the air-scattered photons, having been decreased in energy, are more easily absorbed in the concrete than the uncollided photons.

These results indicate that the peak dose rates resulting from gamma rays that leak from an exploding nuclear device can be bracketed within useful limits by steady-state calculations. For thick concrete shields (~4 ft or more) the ratios of the upper to the lower limit are only 1.2, 1.3, and 2.2 for 500, 1000, and 5000 m, respectively. As the shield thickness decreases to zero, the corresponding ratios increase to 3.3, 4.7, and 5.9, which are still not too large for most planning and estimation purposes.

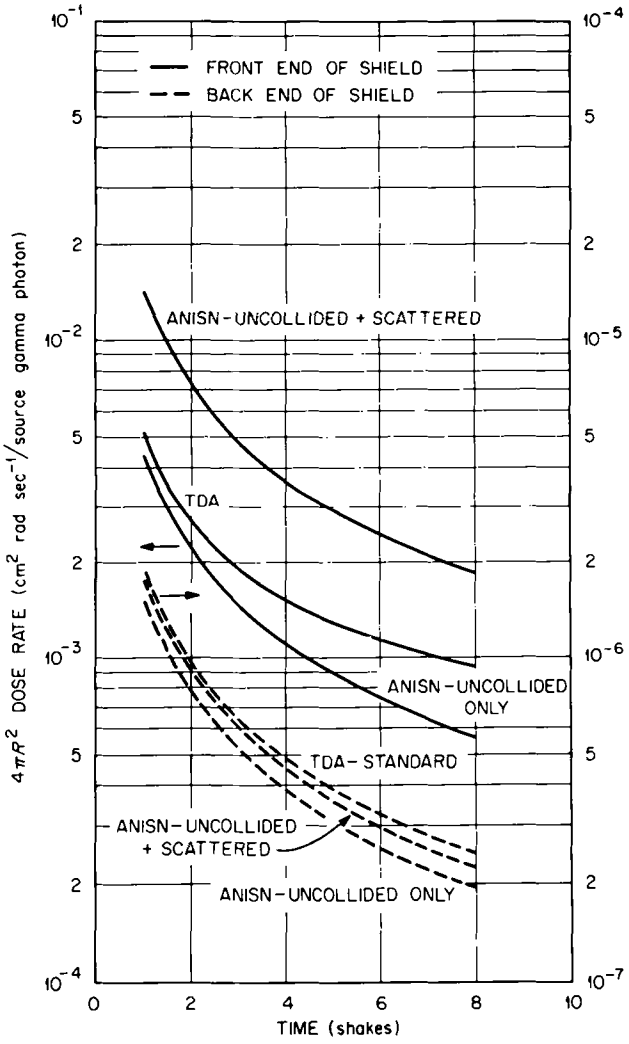


Fig. 3. $4\pi R^2$ peak dose rate as a function of pulse width for a 500-m range. Air density, 0.84 g/liter.

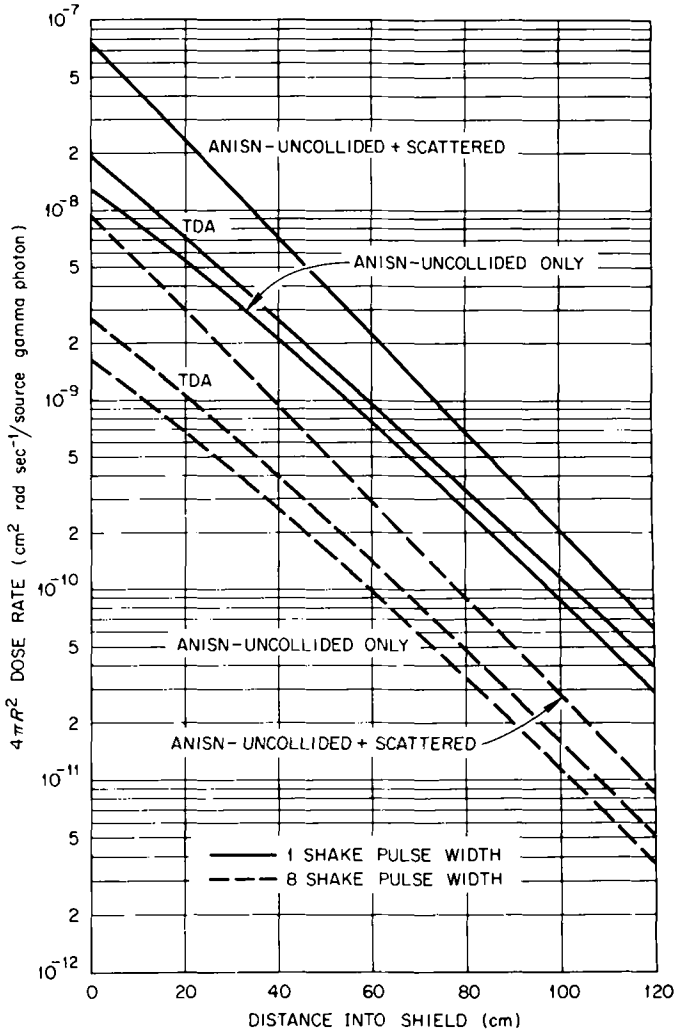


Fig. 4. $4\pi R^2$ peak dose rate as a function of shield thickness for a 5000-m range. Air density, 0.92 g/liter.

Although the results are basically for a hypothetical source spectrum and a step-function source, significant differences in the conclusions are not to be expected for other reasonable source spectra. For other than a step-function source, it can be anticipated that the ratios of the upper to the lower limit will decrease since the time interval containing the peak source will dominate and proportionately less air-scattered photons will strike the shield wall.

**ACKNOWLEDGMENTS**

This research was supported by the U.S. Corps of Engineers, Huntsville Division, Hunstville, Alabama, under Union Carbide Corporation contract with the U.S. Atomic Energy Commission.

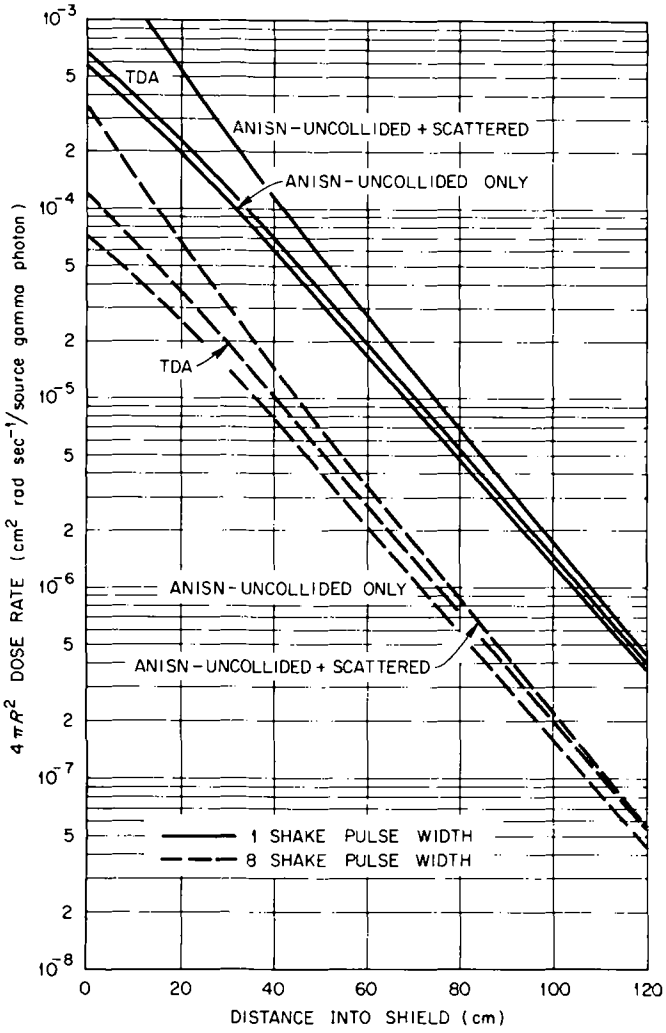


Fig. 5. $4\pi R^2$ peak dose rate as a function of shield thickness for a 1000-m range. Air density, 0.92 g/liter.

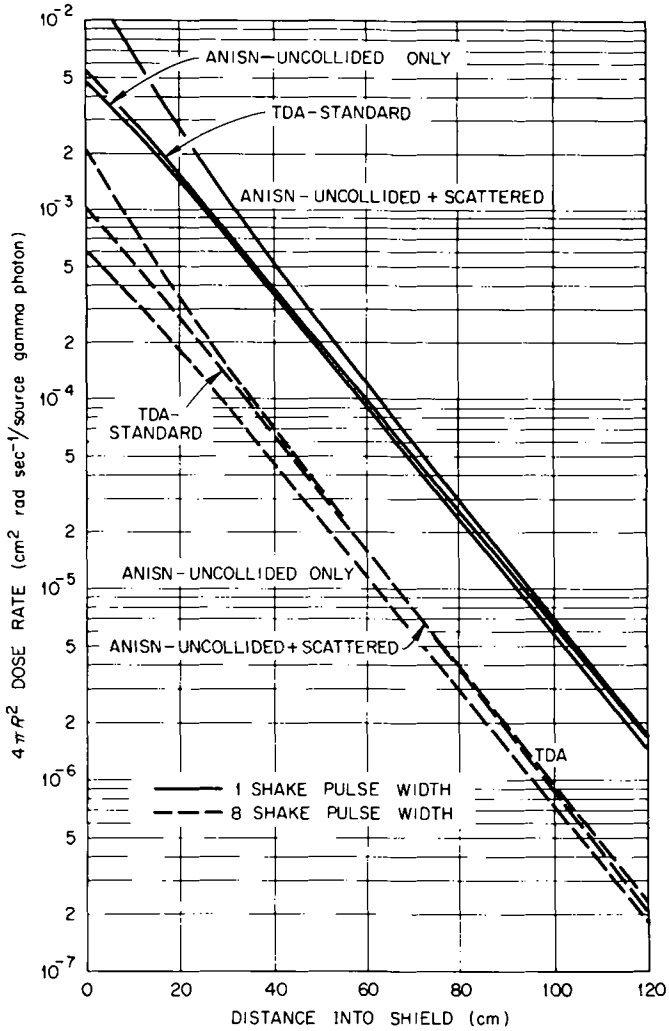


Fig. 6. $4\pi R^2$ peak dose rate as a function of shield thickness for a 500-m range. Air density, 0.84 g/liter.

## REFERENCES

1. D. C. JONES, Ed., *TREE Handbook*, DASA-1420, Defense Atomic Support Agency (1965).

2. W. W. ENGLE, Jr., "A User's Manual for ANISN," K-1693, Oak Ridge Gaseous Diffusion Plant (1967).

3. W. W. ENGLE, Jr., F. R. MYNATT, and R. S. BOOTH, "One-Dimensional Time-Dependent Discrete Ordinates," *Trans. Am. Nucl. Soc.*, **12**, 400 (1969).

4. E. A. STRAKER, W. W. ENGLE, Jr., and P. N. STEVENS, "Some Calculated Milestone Solutions to the Time-Dependent Radiation Transport Problems," ORNL-TM-2499, Oak Ridge National Laboratory (1969).

5. J. R. KNIGHT and F. R. MYNATT, "MUG—A Program for Generating Multigroup Photon Cross Sections," CTC-17, Computing Technology Center, Union Carbide Corporation (1970).

6. H. GOLDSTEIN, "Sources of Neutrons and Gamma Rays," *Reactor Handbook*, 2nd ed., Vol. III, Chap. 8, E. P. Blizard and L. S. Abbott, Eds., Interscience Publishers, New York (1962).

7. R. L. WALKER and M. GROTENHUIS, "A Summary of Shielding Constants for Concrete," ANL-6643, Argonne National Laboratory (1961).

# HEAVY ELEMENT ANALYSIS BY ISOTOPE-EXCITED X-RAY FLUORESCENCE

ANALYSIS

**KEYWORDS:** *x radiation, lead, fluorescence, atomic number, quantitative analysis, K absorption, zinc, tungsten, minerals*

J. KUUSI, M. VIRTANEN, and P. JAUHO
*The State Institute for Technical Research, Reactor Laboratory*
*Otaniemi, Finland*

Received June 15, 1971
Revised September 10, 1971

*One of the advantages of radioisotope x-ray techniques is the potential for using primary radiation, which has enough energy to excite K x rays of even the heaviest elements. In using these penetrating x rays in the analysis, the effects of some of the most severe sources of error in x-ray techniques are less significant than when using softer L x rays. This paper theoretically illustrates the advantages of isotope-excited K x-ray determinations of heavy elements and describes some feasibility studies and applications as determination of lead in zinc and tungsten in mineral samples.*

## INTRODUCTION

When analyzing elements with an atomic number greater than 50 (tin) with conventional x-ray techniques, the characteristic $L$ x rays of these elements have to be used in the determinations because the primary radiation from the x-ray generator does not have enough energy to excite the $K$ x rays of these heavy elements. If the x-ray generator is replaced by a certain radioisotope as the source of primary radiation, the $K$ x rays of even the heaviest elements can readily be excited. Using these penetrating x rays in the analysis, the effects of some of the major sources of error in x-ray fluorescence analysis—particle size, matrix absorption effects, and the effects of heterogeneous sample material—are in several cases considerably less significant than when using softer $L$ x rays. In addition, no very thin and fragile sample presentation or detector windows are needed, which is a significant advantage, especially in certain on-line applications.

Several successful applications in the determination of heavy elements such as lead in metallic compounds utilizing scintillation counters and differential filters to detect the $K$ x rays of these elements have been reported by Rhodes, Packer, and Boyce[1] and by Kuusi[2] and Virtanen.[3] High energy resolution Ge(Li) and Si(Li) semiconductor detectors widen the potential field of application significantly because they have the potential for carrying out these determinations with far greater sensitivity, even in ppm concentrations in favorable conditions.[3-5]

## METHOD

The principle of the measurements in the isotope-excited x-ray fluorescence analysis with a semiconductor detector can be seen in Fig. 1 where the measuring geometries used in this work are illustrated. In the arrangement shown in Fig. 1(a) the primary radiation emitted by a radioisotope disk source excites characteristic x rays of the elements present in the sample. Some of this radiation travels through the detector window to the detector, and pulses from the detector are fed through amplifiers to a multichannel pulse height analyzer.

When analyzing homogeneous sample material using a source emitting monoenergetic radiation, the counting rate $N$ $(1/s)$ of the characteristic $K$ x rays of the element to be analyzed may be estimated using the expression[3,6,7]

$$N = k A_0 \frac{w_k \tau r}{\mu_e + \frac{\sin \alpha}{\sin \beta} \mu_f} \times \left\{1 - \exp\left[-\left(\frac{\mu_e}{\sin \alpha} + \frac{\mu_f}{\sin \beta}\right) m\right]\right\} , \qquad (1)$$

where

$k$ = constant including counting efficiency, etc.

$A_0$ = activity of the source (1/s)

$w_k$ = fluorescent yield of the element to be analyzed for $K$ x rays

$\tau$ = photoelectric mass absorption coefficient of the element to be analyzed ($cm^2/g$)

$r$ = fraction by weight of the element to be analyzed in the sample material

$\mu_e$ = mass absorption coefficient of the sample material for the primary radiation ($cm^2/g$)

$\mu_f$ = mass absorption coefficient of the sample material for the excited characteristic x rays ($cm^2/g$)

$\alpha$ = angle between the sample surface and the primary radiation

$\beta$ = angle between the sample surface and the secondary radiation

$m$ = mass per unit area in the sample layer ($g/cm^2$).

As the thickness $m$ of the sample layer increases, the exponential term in expression (1) decreases rapidly and $m$ reaches its saturation value $m_s$, after which the counting rate is no more a function of $m$. In practice, the depth of the saturation layer is usually approximated by the expression

$$m_s = \frac{3}{\frac{\mu_e}{\sin \alpha} + \frac{\mu_f}{\sin \beta}} \qquad (2)$$

which corresponds to the layer giving 95% of the counting rate obtainable from the infinite sample layer.

Table I shows the magnitudes of saturation depths in some lead and cerium determinations using both $K$ and $L$ x-ray excitation. Lead represents the heavy end and cerium the light end of the elements, which in conventional x-ray analysis have to be determined using $L$ x rays. The energy of 16.5 keV of the primary radiation in $L$ x-ray excitation corresponds to the average effective energy of the radiation emitted by a $^{238}Pu$ source, while in $K$ x-ray excitation that of 122 keV is the dominant component of the radiation from a $^{57}Co$ source. Table I shows that using $K$ x rays the information-giving sample layer is approximately two orders of magnitude thicker than when using $L$ x rays. This is a very significant advantage in analyzing samples which may possess some degree of heterogeneity, as nearly all samples in practice do. To illustrate the decrease in the saturation depth when the angles between the sample surface and the primary and secondary radiation ($\alpha, \beta$) differ from a right angle, Table I also shows the saturation depths in $K$ x-ray excitation when these angles have a value of 60 deg.

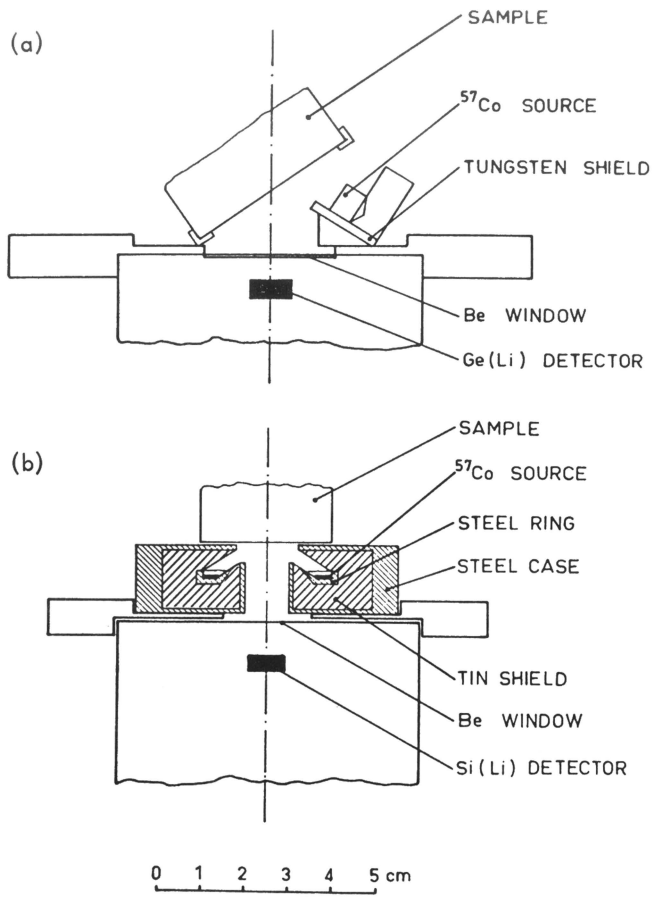


Fig. 1. Measuring geometries used in this work.

Using $K$ x-ray excitation of heavy elements the sample presentation and detector windows may be made less fragile than in conventional x-ray analysis. A steel layer 1.7 mm thick reduces the intensity of Pb $K_{\alpha 1}$ x rays (75 keV) to half its original value. This shows that heavy elements can be determined through resistant steel windows, which may even be made by thinning a small area of a process pipeline or tank wall. On the other hand, the analyzer may be installed in an air- and water-tight case with a resistant steel window covering a relatively small area at its most fragile point.

Due to the mass-absorption coefficients $\mu_e$ and $\mu_f$ in expression (1), the changes in the matrix composition affect the counting rate measured even if the content of the element to be determined

TABLE I

Magnitudes of Saturation Depths in Some Lead and Cerium Determinations Using Both $K$ and $L$ X-Ray Excitation

| Sample | | Radiation | | | Saturation Depth | |
|---|---|---|---|---|---|---|
| Matrix | Element to Be Analyzed | Exciting Radiation (keV) | X Rays to Be Measured | $\alpha,\beta$ (°) | $m_s$ (mg/cm$^2$) | $h_s$ ($\mu$m) |
| Zn, metallic | Pb | 16.5 | Pb $L$ | 90 | 11 | 15 |
| | 10 ppm Pb | 122 | Pb $K$ | 90 | 2230 | 3130 |
| | | 122 | Pb $K$ | 60 | 1930 | 2700 |
| Lead "ore" | Pb | 16.5 | Pb $L$ | 90 | 134 | 51 |
| 99% $SiO_2$ | 1% PbS | 122 | Pb $K$ | 90 | 7900 | 2980 |
| | | 122 | Pb $K$ | 60 | 6820 | 2570 |
| Water | Ce | 16.5 | Ce $L$ | 90 | 64 | 64 |
| | 0.1% $CeO_2$ | 122 | Ce $K$ | 90 | 5490 | 5460 |
| | | 122 | Ce $K$ | 60 | 3880 | 3860 |
| Apatite min. | Ce | 16.5 | Pb $L$ | 90 | 18 | 13 |
| 9% Apatite | 1% $CeO_2$ | 122 | Pb $K$ | 90 | 2760 | 1690 |
| 90% $SiO_2$ | | 122 | Pb $K$ | 60 | 1960 | 1190 |

remains constant. These effects are called matrix absorption effects and, together with the particle size effects discussed later, are the most significant sources of error in x-ray fluorescence analysis. Comparing the magnitude of the matrix absorption effects in $K$ x-ray excitation with that in $L$ x-ray excitation, we can see that in determining the concentration of a heavy element in a matrix of considerably lighter elements the matrix effects are much less significant using $K$ x-ray excitation. If the matrix also contains some other relatively heavy elements, the variations in the contents of these usually have greater effects when $K$ x rays are used. Both of these cases are illustrated in Table II which shows the calculated relative intensities of $K$ and $L$ x rays in some lead and cerium determinations as a function of the slight changes in the matrix composition.

When analyzing powder or slurry samples the particle size of the sample material also affects the counting rate measured even if the content of the element to be analyzed remains constant. These particle size effects are connected with the absorption of the primary and secondary radiation in the single sample particles. The highest counting rate is obtained when the particle size is very small. As this increases, the counting rate first remains nearly constant until the so-called transition region, where single particles begin to absorb the radiation to a significant degree, is reached. In this region the counting rate decreases rapidly with increasing particle size until the particle dimensions reach the value of the saturation depth, after which the particle size has only a very slight effect on the counting rate. Preferably as small a fraction as possible of the particles in the sample should be in the transition region.

TABLE II

Magnitudes of Matrix Absorption Effects in Some Lead and Cerium Determinations

| Sample | | | | Element to be Analyzed | Relative Intensity of X Rays to be Measured | |
|---|---|---|---|---|---|---|
| | | | | | $K$ X Rays | $L$ X Rays |
| Lead "ore" | | | | | | |
| Pb | Zn | $SiO_2$ | (%) | | | |
| 2 | 5 | 93 | | Pb | 1 | 1 |
| 2 | 10 | 88 | | Pb | 0.91 | 0.75 |
| 2 | 15 | 83 | | Pb | 0.82 | 0.60 |
| Lead "ore" | | | | | | |
| Pb | Sn | $SiO_2$ | (%) | | | |
| 2 | 5 | 93 | | Pb | 1 | 1 |
| 2 | 10 | 88 | | Pb | 0.78 | 0.90 |
| Gasoline | | | | | | |
| Pb | Br | Gasoline | (%) | | | |
| 0.1 | - | 99.9 | | Pb | 1 | 1 |
| 0.1 | 0.2 | 99.7 | | Pb | 0.99 | 0.93 |
| Apatite min. | | | | | | |
| $CeO_2$ | $La_2O_3$ | Apatite | $SiO_2$ (%) | | | |
| 3 | 2 | 10 | 85 | Ce | 1 | 1 |
| 3 | 2 | 40 | 55 | Ce | 0.86 | 0.76 |
| 3 | - | 10 | 87 | Ce | 1.18 | 1.02 |

Figures 2 and 3 show the calculated counting rates as a function of the average linear dimension $\bar{d}$ of the particles compared with those obtainable when $\bar{d}$ is 1 $\mu$m in determining lead and cerium in certain matrices using both $K$ and $L$ x-ray excitation; $\bar{d}$ is defined according to the relation

$$\bar{d} = \frac{v}{\bar{a}} \quad , \tag{3}$$

where

$v$ = particle volume
$\bar{a}$ = average particle area presented to the radiation.

For spherical particles, $\bar{d} = \frac{2}{3}$ of the particle diameter, and for cubical particles, $\bar{d} = \sim 0.7$ of the side of the cube.

The sample material corresponding to Fig. 2 consists of 3% PbS (fluorescent particles), 1% Ba, 6% Zn, and 90% $SiO_2$, and that corresponding to Fig. 3 consists of 0.3% $CeO_2$ (fluorescent particles), 0.2% $La_2O_3$, and 99.5% $CaSO_4$. The curves marked $a$ have been obtained using the theoretical model presented by Berry, Furuta, and Rhodes,[8] and those marked $b$ by Lubecki, Holýnska, and Wasilewska.[9] These two nearly equal models differ from each other slightly in summing the absorption effects of the single particles. In the former case the ratio of total solid volume to the volume of the sample $\eta$; i.e., the solids packing fraction has been used as a parameter. It has, however, a noticeable effect on the relative counting rate only in $L$ x-ray excitation.

In practice, the distribution of particle sizes ($\bar{d}$) of the material to be analyzed often covers the region 10 to 100 $\mu$m, although narrower distributions such as 10 to 20 $\mu$m often can be obtained through careful grinding.

Using $K$ x rays in the lead determinations corresponding to Fig. 2, the particle size range of 10 to 100 $\mu$m is practically out of the transition region, but when $L$ x rays are used this lies just inside the transition region. In the cerium determinations corresponding to those in Fig. 3 this particle size range lies in the transition region in both cases. Qualitatively, it may be said that when analyzing the heaviest elements, the particle size effects are considerably smaller if $K$ x rays are used but the superiority to $L$ x-ray excitation in this respect gradually decreases with the decreasing atomic number of the element to be analyzed.

To achieve as low detection limits as possible, the signal-to-background ratio must be made as great as possible. This means that the background due to the primary coherent and Compton

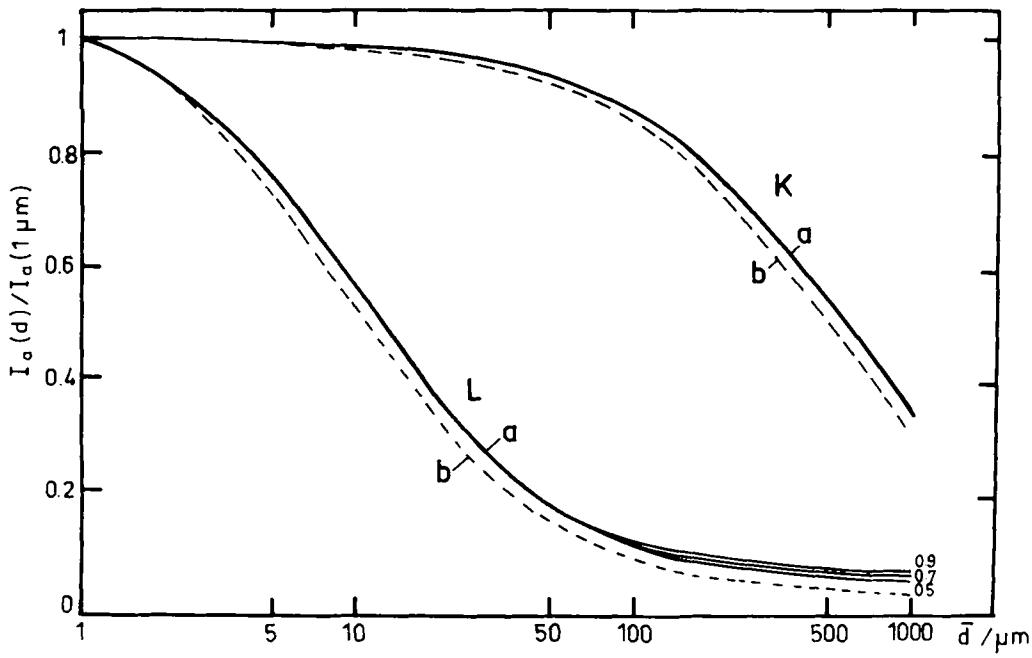


Fig. 2. Relative calculated counting rate as a function of the average linear dimension $\bar{d}$ of the particles using $K$ and $L$ x-ray excitation in determining lead in a sample consisting of 3% PbS (fluorescent particles), 1% Ba, 6% Zn, and 90% $SiO_2$. (a) and (b) refer to the theoretical models presented in Refs. 8 and 9. The effect of the solids packing fraction ($\eta$) is seen to become noticeable at the large values of $\bar{d}$ when $L$ x-ray excitation is used [curve (a)].

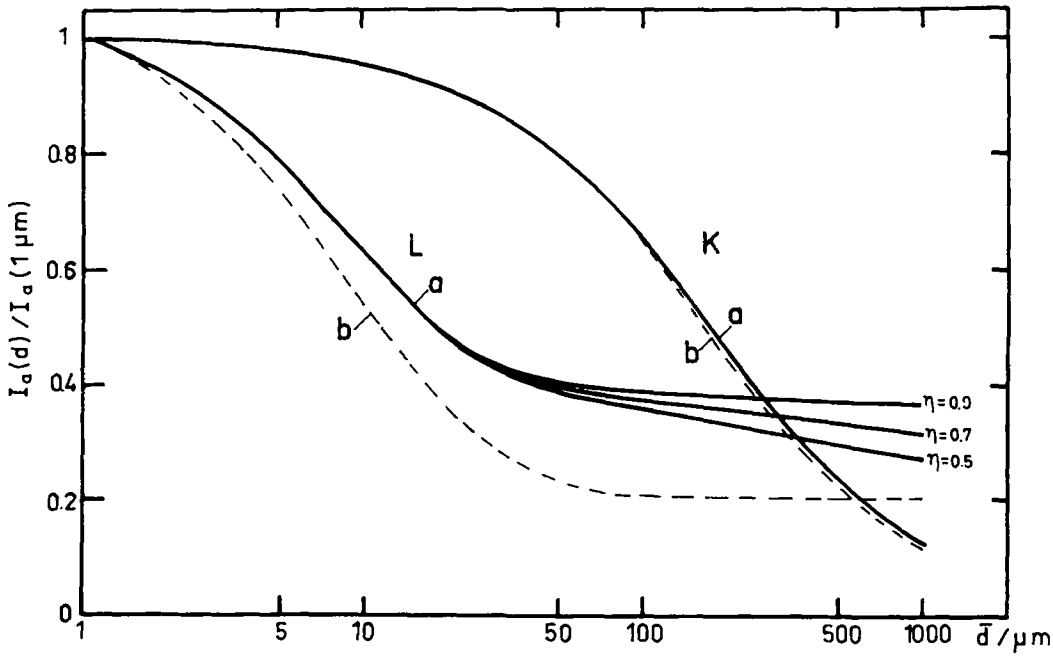


Fig. 3. Relative calculated counting rate as a function of the average linear dimension $\bar{d}$ of the particles using $K$ and $L$ x-ray excitation in determining cerium in a sample consisting of 0.3% $CeO_2$ (fluorescent particles), 0.2% $La_2O_3$, and 99.5% $CaSO_4$. (a) and (b) refer to the theoretical models presented in Refs. 8 and 9. The effect of the solids packing fraction ($\eta$) is seen to become noticeable at the large values of $\bar{d}$ when $L$ x-ray excitation is used [curve (a)].

scatter and multiple scatter under the $K$ x rays to be measured must be minimized and the energy resolution of the detector and its counting efficiency should be as high as possible. When analyzing the heaviest elements such as uranium and lead, these requirements are at present probably most completely met when thin Ge(Li) semiconductor detectors are used in a proper measuring geometry. As the atomic number of the element to be analyzed decreases, the Si(Li) detectors begin to compete. Even if the counting efficiency of Si(Li) detectors is approximately an order of magnitude lower than that of Ge(Li) detectors, their energy resolution is usually slightly higher, in addition to which they have such practical advantages as tolerance in warming up to room temperature.

A relatively wide energy range with a low background for determining bismuth and lighter elements can be established if a $^{57}Co$ source is used in a geometry where the angle between the primary radiation from the source and the radiation scattered from the sample to the detector is approximately 120 deg, as in both of the geometries shown in Fig. 1. The energy of the Compton scattered 122-keV gamma rays from the $^{57}Co$ source in this angle is 90 keV and thus is relatively far from the $K$ x rays of bismuth ($K_{\alpha 1}$ 77.1 keV, $K_{\alpha 2}$ 74.8 keV).

## EXPERIMENTAL

Figure 4 shows the energy spectra of the secondary radiation after background subtraction in some lead determinations measured using the geometry shown in Fig. 1(a). The activity of the $^{57}Co$ disk source was 0.5 mCi and the dimensions of the Ge(Li) detector were 5.6- × 10-mm diam. The Pb $K_\alpha$ peaks from the metallic zinc sample (80-ppm Pb) indicate potential for the determination of very low lead concentrations in metallic zinc, which is a common quality problem with electrolytically produced zinc, while the spectrum from a lead ore tailing (0.36% Pb, 1.0% Ba, 0.09% Ce) illustrates potential for simultaneous determination of several elements with an atomic number greater than 50 using $K$ x-ray excitation.

Figure 5 shows the calibration curve for the determination of lead in zinc, corresponding to a counting time of 20 min and obtained by plotting the counts under the $K_{\alpha 1}$ peak of lead against the lead content of the reference samples. The statistical error of counting corresponding to ± 11 ppm lead ($1\sigma$) is almost totally caused by the background under the $K_{\alpha 1}$ peak, which also determines the lower limit of the analysis. Table III shows the lead content of 12 unknown zinc samples determined using the calibration curve in Fig. 5 and the results of the chemical analyses carried out

after x-ray determinations. The standard deviation of the difference between these two determinations is 7.9 ppm Pb, which is of the same order of magnitude as the standard deviation due to statistical error of counting in the x-ray analysis.

Figure 6 shows the energy spectrum measured in the analysis of a mineral sample using a ring formed collimated $^{57}Co$ source (4 mCi) and a Si(Li) detector (3- × 8-mm diam) in the measuring geometry shown in Fig. 1(b). Contributions of a small amount of tungsten (0.135%), artificially added cerium (0.19%) and even as light an element as molybdenum (0.19%) can clearly be seen in the spectrum. Due to the collimated source and the scatter angle of 120 deg the Compton scatter peak is relatively narrow and lies outside the energy range of the $K$ x rays of bismuth ($K_{\alpha 1}$ 77.1 keV) and lighter elements.

Figure 7 shows the registered net counts under the characteristic $K_\alpha$ lines of tungsten and molybdenum plotted against the tungsten content determined using neutron activation analysis and the

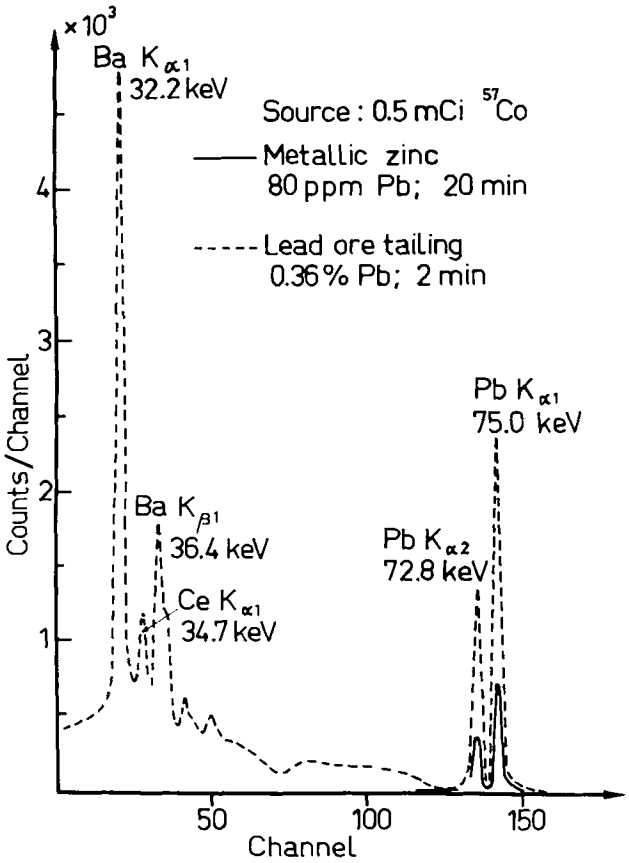


Fig. 4. Pb $K$ peaks from a metallic zinc sample (80-ppm Pb) and the fluorescent spectrum from a lead ore tailing sample consisting of 0.36% Pb, 1% Ba, and 0.09% Ce after background subtraction.

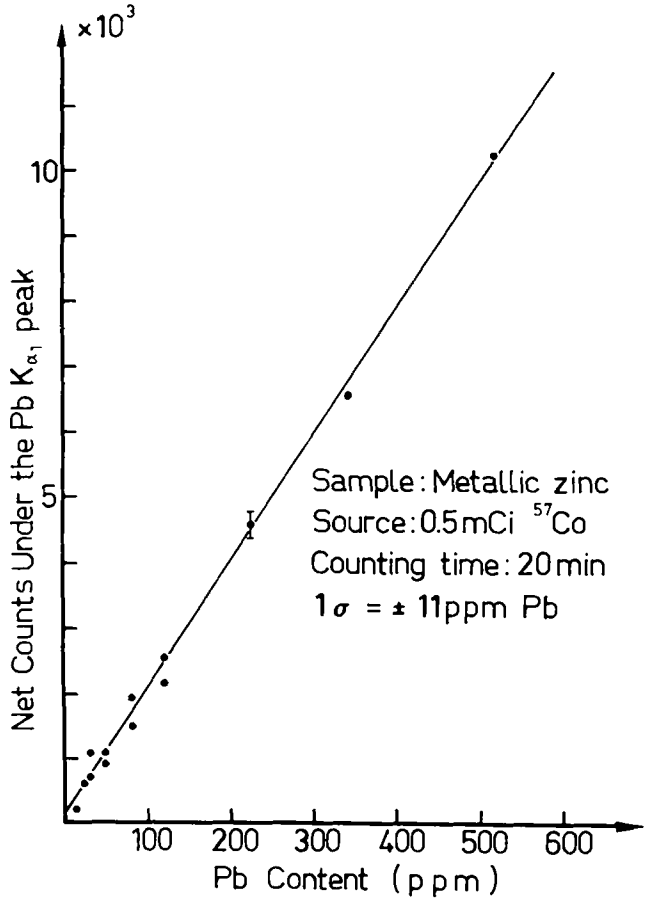


Fig. 5. Calibration curve obtained for lead in zinc.

TABLE III

Lead Content of 12 Zinc Samples Determined Independently Using Isotope-Excited $K$ X-Ray Fluorescence and Chemical Analysis

| Number of Metallic Zinc Sample | Pb Content (ppm) | | Difference |
|---|---|---|---|
| | Chemical Analysis | $K$ X-Ray Analysis | |
| 1 | 140 | 145 | -5 |
| 2 | 74 | 81 | -7 |
| 3 | 96 | 91 | +5 |
| 4 | 156 | 157 | -1 |
| 5 | 88 | 103 | -15 |
| 6 | 32 | 44 | -12 |
| 7 | 4 | 1 | +3 |
| 8 | 3 | 10 | -7 |
| 9 | 9 | 19 | -10 |
| 10 | 7 | 12 | -5 |
| 11 | 19 | 11 | +8 |
| 12 | 10 | 16 | -6 |
| | | Standard deviation 7.9 ppm | |

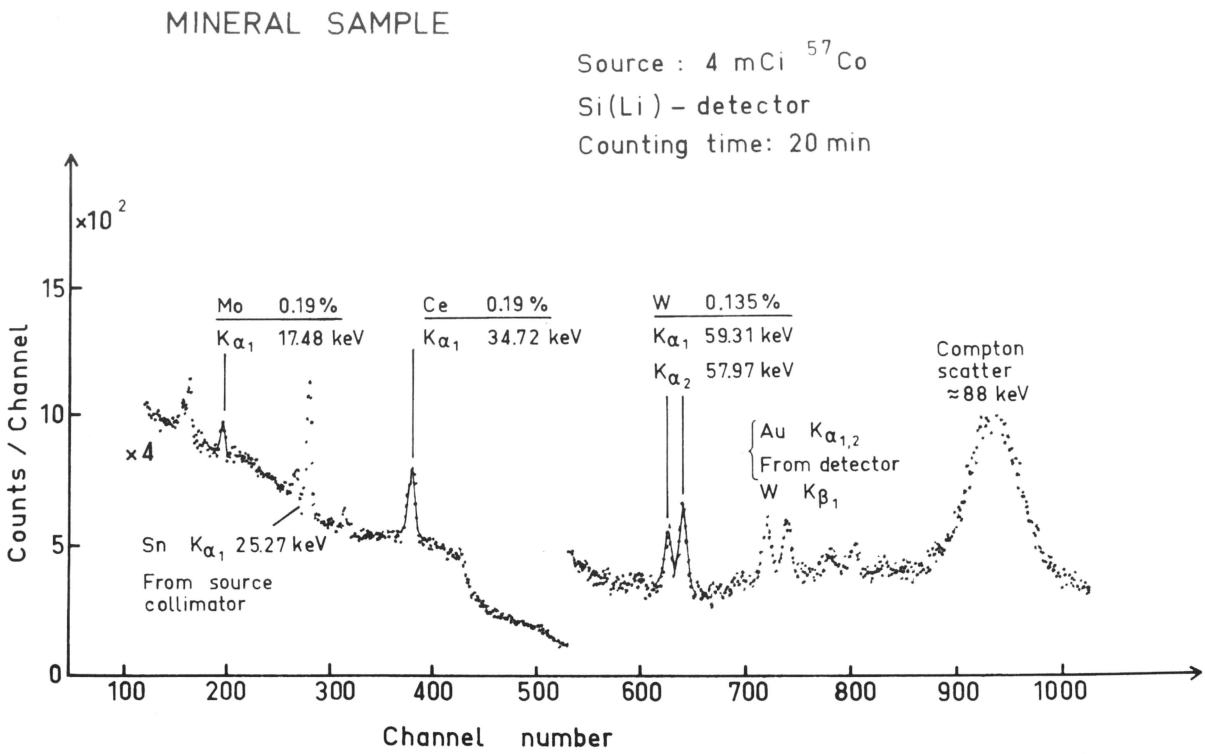


Fig. 6. Fluorescent spectrum from a mineral sample measured with an annular $^{57}Co$ source and Si(Li) detector.

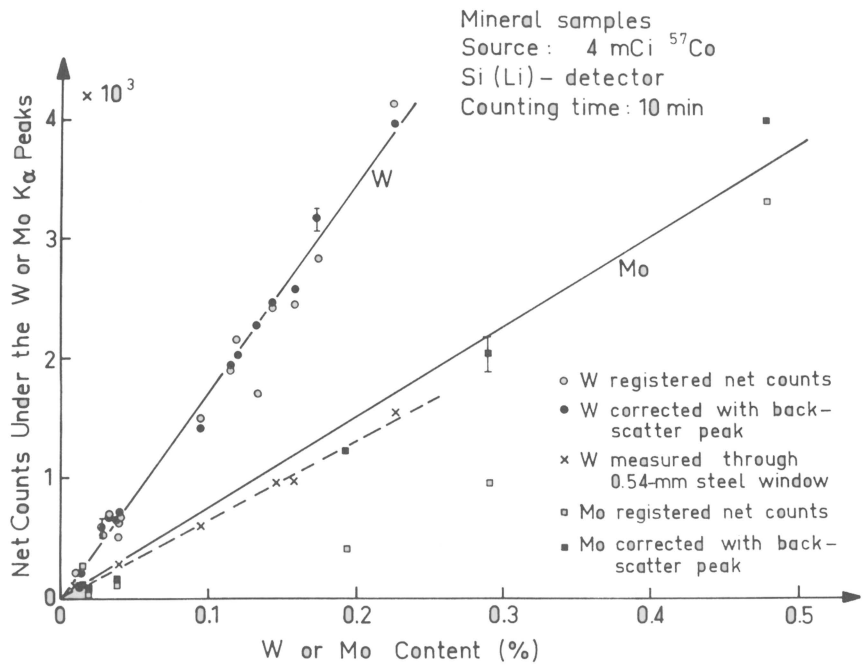


Fig. 7. Results from feasibility studies for simultaneous determination of tungsten and molybdenum using *K* x-ray excitation.

chemically determined molybdenum content of the mineral samples of the same type as that corresponding to Fig. 6. The black dots and squares in Fig. 7 correspond to the results obtained by dividing the counts under the $K_\alpha$ lines of tungsten and molybdenum by the relative normed intensity of the backscatter peak. This correction,[10] which reduces the effects of matrix scatter and absorption, is seen to reduce the deviation of the experimental points from the calibration curves obtained significantly. The statistical error of counting in determination of tungsten in this type of sample material would correspond to 0.004% W when the tungsten content is 0.1%. Figure 7 also shows the results obtained in the feasibility study of determining the tungsten content through a steel window 0.54 mm thick. The number of counts increases linearly in this case too, and with a reasonably high slope with increasing tungsten content, which shows the potential for determining heavy elements through very resistant sample presentation windows.

The results obtained in the determination of molybdenum are to be regarded only as a demonstration of the wide atomic number range of elements which may be determined simultaneously with reasonable accuracy using $K$ x-ray excitation. Better results would, of course, be achieved if a primary radiation of much lower energy were used. It should also be mentioned that in analyzing elements with an atomic number lower than or close to that of the lightest lanthanides, $^{57}$Co is no longer the most suitable long living isotopic source of primary radiation, even though it may often give sufficient accuracy. Figures 8 and 9 illustrate some cerium determinations carried out using $K$ x-ray excitation with an $^{241}$Am disk source (30 mCi), which is superior to $^{57}$Co in determinations of elements with an atomic number of approximately this magnitude. Figure 8 shows a calibration curve established for determining the cerium content of a large amount of drill core material samples and Fig. 9 shows a calibration curve for determining cerium in several process water samples.

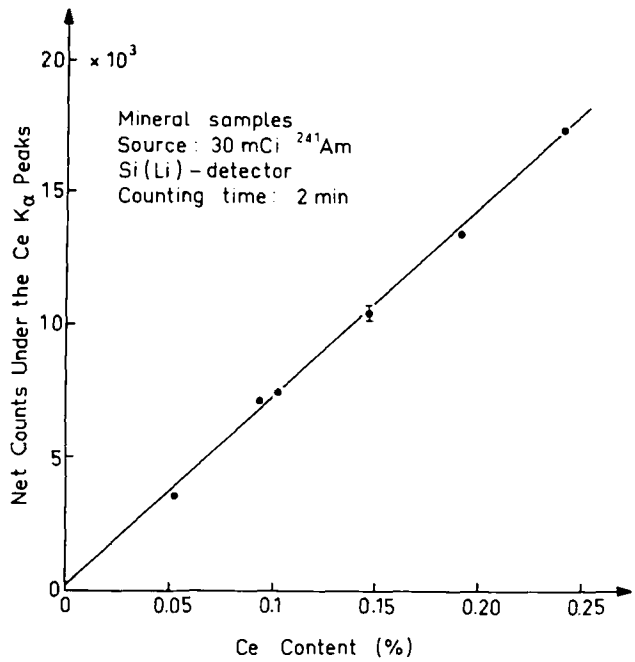


Fig. 8. Calibration curve established for determining the cerium content of drill core material samples.

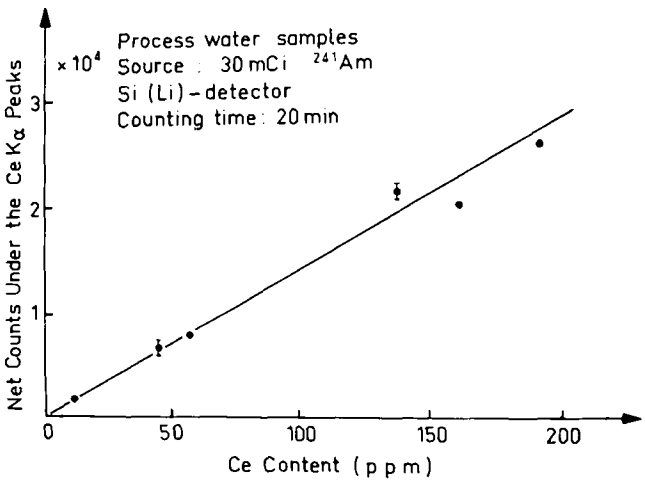


Fig. 9. Calibration curve established for determining the cerium content of process water samples.

## DISCUSSION

The theoretical considerations stated, the feasibility studies on and applications in radioisotope excited $K$ x-ray determinations of heavy elements described show that this method of analysis has an extensive field of potential applications where its special characteristics offer significant advantages in one respect or another. The constant development of semiconductor x-ray detectors and the gradual adoption of these instruments in various types of industrial measurements will also increase the use of this method of analysis. To a certain extent this will probably take place together with the development of nondispersive x-ray fluorescence analyzer systems utilizing a low-power x-ray tube and a semiconductor detector.

#### ACKNOWLEDGMENTS

The authors wish to express their sincere appreciation to the Finnish Atomic Energy Commission for the support and sponsorship of the radioisotope x-ray analysis project with which this work was connected. The reference samples and chemical analyses for this work were provided by Jorma Kinnunen, chief chemist, and Pentti Rautavalta at the Outokumpu Oy, Pori Works, and is gratefully appreciated.

#### REFERENCES

1. J. R. RHODES, T. W. PACKER, and I. S. BOYCE, in *Radioisotope Instruments in Industry and Geophysics*, Vol. I, p. 127, International Atomic Energy Agency, Vienna (1966).

2. J. KUUSI, *Kem. Teollisuus*, **25**, 478 (1968).

3. M. VIRTANEN, Diploma Thesis, Helsinki University of Technology, Finland (unpublished).

4. P. L. GANT and B. G. MOTES, *Trans. Am. Nucl. Soc.*, **12**, 518 (1969).

5. P. G. BURKHALTER and H. E. MARR III, *Int. J. Appl. Radiat. Isotop.*, **21**, 395 (1970).

6. J. F. CAMERON, J. R. RHODES, and P. F. BERRY, AERE-R-3086, Atomic Energy Research Establishment, Harwell (1959).

7. C. G. CLAYTON and J. F. CAMERON, in *Radioisotope Instruments in Industry and Geophysics*, Vol. I. p. 15, International Atomic Energy Agency, Vienna (1966).

8. P. F. BERRY, T. FURUTA, and J. R. RHODES, in *Advances in X-Ray Analysis*, Vol. 12, Plenum Publishing Corporation, New York (1969).

9. A. LUBECKI, B. HOLYNSKA, and M. WASILEWSKA, *Spectrochim. Acta*, **23B**, 465 (1967).

10. P. G. BURKHALTER, *Anal. Chem.*, **43**, 10 (1971).

# IMPURITY EFFECTS ON THE SWELLING OF IRRADIATED ALUMINUM OXIDE

MATERIALS

TECHNICAL NOTE

R. A. SKARUPA and C. E. BACKUS
*Arizona State University, Tempe, Arizona 85281*

Received June 21, 1971
Revised September 27, 1971

**KEYWORDS:** *aluminum oxides, swelling, neutrons, radiation effects, irradiation, impurities, production, helium, nuclear reactions*

*The role of impurity content in the irradiation of alumina has been investigated. The extra helium production from the impurities contributes only 2% or less of the helium production from pure alumina. It is concluded that the lower swelling indicative of higher purity alumina is probably due to its smaller grain size rather than a mechanism associated with the impurities per se.*

In an earlier article in *Nuclear Technology*, Keilholtz and Moore[1] suggested that the impurity content in alumina may be a factor that contributes to the swelling of alumina under irradiation by fast neutrons. A more recent report by Keilholtz, Moore, and Robertson[2] contains the observation that gross damage correlated better with the impurity content than with any other variable. Although analysis[3] of the data from both ORNL and LASL indicates that the major damage in alumina is caused by fast neutron scattering, there is a slight difference in swelling from one type of alumina sample to another. A study to determine if the extra helium production due to the impurities could account for this difference in swelling[4] was recently completed at Arizona State University.

The effective $(n, \alpha)$ cross sections were determined from a collection of the latest data for all the impurities listed in the spectrographic analysis of each of the irradiated alumina samples. These effective cross sections were calculated for a light-water-type neutron spectra (ETR or OWR) since that is where most of the irradiations have been performed. A check was made on the calculational procedure by calculating the effective aluminum cross section for the Watt fission spectrum. The value obtained was 0.63 mb which compares well with the value of 0.65 mb obtained by Roy and Hawton[5] in 1960 for aluminum in a Watt spectrum. The amount of helium production due to impurities for each of the types of alumina was calculated as a percent of helium production from pure alumina. The values obtained are given in Table I. The exact error bands for these values cannot be determined because the precision of the cross-section energy curves in most cases is unknown.

Not only do the results show that the extra helium production in the alumina is essentially negligible, but there is an inverse relationship between extra helium production and total impurity content. This is, of course, due to the fact that just a few of the impurities dominate the helium production. The major impurities in the three different types of alumina are given in Table II.

This investigation has shown that the swelling mechanism in alumina cannot be attributed to the excess helium production that the impurities contribute. Thus, if the swelling is indeed related to the impurities, it must be by a mechanism such as their role in acting as nucleation sites for vacancies. The more likely explanation is that, in general, the higher purity samples have smaller grain sizes, and thus have a more probable resistance to swelling.

TABLE I

Helium Production from Impurities in Various Types of Alumina as a Percent of Helium from Pure Alumina

| Type | % |
|---|---|
| AD 999 | 2.0 |
| Al 995 | 1.5 |
| Lucalox | 1.4 |

TABLE II

Major Impurities in the Different Types of Alumina (ppm)

| Impurity | AD 999 | Al 995 | Lucalox |
|---|---|---|---|
| Mg | 200 | >1000 | >1000 |
| Si | 100 | >1000 | 300 |
| K | 300 | <100 | <100 |
| Ca | 10 | 300 | 3 |
| Fe | 100 | 300 | 15 |
| Zn | 100 | <100 | <100 |

REFERENCES

1. G. W. KEILHOLTZ and R. E. MOORE, "Irradiation Damage to Aluminum Oxide Exposed to 5 x $10^{21}$ Fast Neutrons per $cm^2$," *Nucl. Appl.*, **3**, 686 (1967).

2. G. W. KEILHOLTZ, R. E. MOORE, and H. E. ROBERTSON, "Effects of Fast Neutrons on Polycrystalline Alumina and

Other Electrical Insulators at Temperatures from 60° to 1230°C," ORNL-4678, Oak Ridge National Laboratory (May 1971).

3. E. W. SALMI, C. E. BACKUS, T. G. FRANK, and C. D. SUTHERLAND, "Effect of Neutron Spectra on the Swelling of Alumina Under Irradiation," IEEE Thermionic Conversion Specialist Conference, Miami, Florida (October 1970).

4. R. A. SKARUPA, "Irradiation Damage Due to Impurities in Metal Oxide Insulators," Master's Thesis, Arizona State University (1971).

5. J. C. ROY and J. J. HAWTON, "Table of Estimated Cross-Sections for $(n,p)$, $(n,\alpha)$ and $(n,2n)$ Reactions in a Fission Neutron Spectrum," CRC-1003, Canadian Chalk River Report (1960).

# BOOK REVIEWS

Selection of books for review is based on the editors' opinions regarding possible reader interest and on the availability of the book to the editors. Occasional selections may include books on topics somewhat peripheral to the subject matter ordinarily considered acceptable.


**Physical Problems in Biological Systems**

*Editors* Cecile DeWitt and Jean Matricon

*Publishers* Gordon and Breach Science Publishers, Inc. (1969)

*Pages* 430

*Price* $19.50

*Reviewer* Donald J. Hanahan

This book contains lectures delivered at the Summer School of Theoretical Physics of the University of Grenoble at Les Houches during an eight-week session in the summer of 1969. Originally intended at its beginning in 1951 as a theoretical physics study program, this conference has now developed toward an understanding of the roles that physics can play in biology and vice versa. There are 14 chapters in this book, 5 of which are in French and 9 of which are in English. If a person is fluent in French scientific language then they would encounter no difficulty with this book. Basically, there are seven major contributions with several short papers included. In an introductory chapter, Chantrenne outlines the fundamental concepts of molecular biology and biochemistry covering such topics as conservation of energy, respiration, photosynthesis, genetic information, the genetic code, etc. all in quite a workman-like manner and in a very readable style. Even though presented in French, this contribution by Chantrenne is easily followed and well constructed. Changeux presents an excellent chapter entitled "Allosteric Interactions in Proteins and Membranes," which spans two major areas: (a) the Control of Biochemical Reactions and (b) Remarks on the Symmetry and Cooperative Properties of Biological Membranes. In his usual able manner, Luzzati describes in a contribution entitled "Lipids and Membranes" the current status of this difficult area of study. In particular, he is concerned with the physical state of lipid-water systems, as revealed by x-ray diffraction patterns, and how these observations may interrelate with what one sees in membranes. A brief discussion centers on the interactions of proteins and lipids. Feher presents a lengthy and detailed description of the application of electron paramagnetic resonance (EBR) to selected problems in biology. He first discusses the basic principles of EPR and then outlines in some detail EPR in heme-proteins and photosynthesis and lastly the use of spin labeled biomolecules. This material should have provided the conferees a sound basis for appreciation of the use of EPR in biological systems. In another chapter, Weill discusses the optical properties of biopolymers. His contribution, in French, outlines in considerable mathematical detail the optical behavior of polypeptides and nucleic acids. Other chapters of short length and which obviously cover only a lecture or two of this conference are: Bimolecular Phospholipid Membranes by Lia, NMR Studies on Lipids, by Rigny and Charvolin, Regulation of Gene Expression by Hoffnung, Genetics of Lambda Bacteriophage by Pereira De Silva and by Eisen, and a short essay by Lifson on Intramolecular Forces in Protein Structure, essentially a statistical mechanical treatment.

If this book were meant as an introduction for the initiated to the complex topics under discussion, this goal was not achieved. Perhaps given in the setting of individual lectures at Les Houches where intimate and detailed discussion could be fostered, then it could be of obvious value. Certainly, the chapters of Changeus, Feher, Weill, and Chantrenne are of high quality and merit. Nonetheless, the book is poorly edited with little or no inter-tie between presentations, and for some odd reason the table of contents is placed at the end of the book and is terse to a fault. As a final injustice, there is no subject index. In general, one can conclude that this would have been an interesting conference to have attended but to consider this book as important to one's own library is at the present time questionable.

*Donald J. Hanahan, professor and head, Department of Biochemistry at the University of Arizona, has been involved in research on biochemistry of simple and complex lipids, lipolytic enzymes, and lipid-protein interactions. Prior to coming to the University of Arizona, he was located in the Department of Biochemistry at the University of Washington School of Medicine, Seattle. He has a doctorate in chemistry from the University of Illinois at Urbana and did post-doctoral work at the University of California in Berkeley.*

**Preservation of Fish by Irradiation**
(Proceedings of a Joint FAO/IAEA Panel, Vienna, 1969)

*Editors* IAEA

*Publisher* Unipub, Inc.

*Pages* 163

*Price* $5.00

*Reviewer* M. A. Robkin

*Preservation of Fish by Irradiation* is the report of the proceedings of a panel held in Vienna, December 15-19, 1969. For someone with even a general knowledge of radiation and biology, it is a very good survey of what one might expect to accomplish with radiation pasturization of seafoods. There are ten papers presented, and they overlap sufficiently to provide a unified collection, with enough variation of methods and species to make each paper relatively distinct.

Paper 1 by Ronsivalli et al., describes an interesting experiment in long distance shipping but does not discuss the results sufficiently. In particular, it would have been illuminating to discuss why the shipments to Jacksonville, Florida resulted in a lower plate count of the final bacterial titer (Table I) than did the shipments to Seattle, Washington. Presumably, the shorter distance is more important a factor than the effect on the packing ice of the higher average ambient temperature, but it would have been nice to have the authors discuss the difference. The authors do not identify the components of the bacterial titer, although it has been shown that the sensory evaluation of seafood depends strongly on which microorganisms are suppressed and which are growing. They also make a big point of the evaluation of the botulism hazard, but never actually present any real data. It would have also been interesting to learn why the organoleptic scores of the 200-krad samples never were superior to the scores from the 100-krad samples, even after a storage time longer than what might be expected for the disappearance of the fugitive irradiation odor. Since dosimetry is not discussed, the reader is left in the dark as to how reliable the irradiation dose can be considered.

Paper 2 by Laycock and Regier is a generally excellent review of the growth of aerobic organisms on irradiated fish, although again the authors do not discuss their dosimetry.

Paper 3 by dela Sierra Serrano reports on a very complete study under many varying conditions of storage of irradiated fish. He, also, does not report on the dosimetry and does not explain the entry "eliminated" in his tables. The author claims that irradiation of 100 krad resulted in no appreciable variation in the organoleptic source which is in distinct disagreement with most of the other authors (for example, paper 2, Fig. 1). This point certainly should have been discussed.

Paper 4 by Hannesson and Dagbjartsson is generally very good. The discussion of the dosimetry is complete and convincing. It is unfortunate that there is not an internationally agreed upon hedonic scale for the organoleptic evaluation of radiation processed seafoods. These authors use a five point scale, the basis of which is not disclosed, while most others use a five or ten point scale, the characteristics of which are told to the reader.

Paper 5 by Ehlermann and Munzer discusses the results of irradiating some fresh water species which makes a welcome addition to the remainder of the papers which all deal with seafoods. Their results with carp point up a fact known to fishermen: the coarser the fish the more abuse it will tolerate. They report a 30 to 1 ratio of the dose which can be applied to carp as compared to trout before a radiation induced loss of sensory quality is noticed.

Paper 6 by Kumta and Sreenivasan discusses some Asian species. Their paper is a long and comprehensive report on the chemistry and bacteriology of irradiated seafoods processed in a large variety of ways. There are only two points where they might be faulted. The first is the use of a storage temperature of 10 to 12°C for so much of their work. This seems like an unrealistically high temperature for serious preservation of fish and must have an effect on the distribution of the spoilage organisms as a function of storage time. The second is the evaluation of fish for freshness indices at 10°C. Certainly the detection of odors at a given state of spoilage will be considerably reduced by low temperature, and it seems to this reviewer that 20°C would be a fairer temperature to evaluate the organoleptic score in particular. Dosimetry is also not discussed.

Paper 7 by Matutano Aranda and Alonso Rodriguez discusses irradiation treatment of fillets of hake. They also use a five point hedonic scale but completely define it so that it is not too difficult to relate to a ten point scale. Their paper, however, suffers from some procedural and reporting defects. In particular, the sensory evaluation of the irradiated samples would be more convincing if they were mixed with the unirradiated samples in a blind test. Since the test panel knew that the fish were irradiated, one cannot help but suspect that the test scores were affected. (Appendix 3, paper 7). The cooking procedure was not the same for the irradiated and unirradiated fish, and without proof to the contrary one must assume that the relative subjective scores will be affected. There is no explanation of why the sensory scores of fish irradiated at 200 krad are higher at one week's storage than are the fish irradiated at 150 krad and lower after two weeks. One might suppose that if irradiation produces a fugitive "foreign odor" that it would be stronger for the higher dose level and that the higher dose would suppress microorganisms more strongly. Table IV is labeled to imply a dependence on packaging temperature, but no temperature data are given. Dosimetry is not discussed.

Paper 8 by Shewan and Hobbs is a very good exposition of the botulism hazard. The authors point out that *Clostridium botulinum* can grow, even at low temperatures, during an extended storage life. Although normal cooking destroys the toxin, the fanciers of raw smoked fish are advised to watch their step. Dosimetry again is not mentioned.

Paper 9 by Eklund and Poysky continues the story of the botulism hazard in rather greater detail. Their results show that the degree of risk depends not only on the storage temperature but on the species of fish. They raise the fascinating idea of the use of bacteriophages to control the growth of *Clostridium* and, like the Saturday matinee serial, leave the reader impatiently waiting

for the next installment. One hardly notices that once again dosimetry is an act of faith.

Paper 10 by Leone finally gets down to cases and considers the pitfalls of dosimetry which can trap the unwary. He shows that for a fairly standard irradiation geometry, the exposure can be nonuniform by as much as a factor of 2. Since very different results in fish quality and biological load are seen within dosage variations smaller than a factor of 2, his warning seems very timely.

The summary statement at the end of the book is, in the opinion of this reviewer, excellent. It would, if one were tempted to plagiarize, serve as an admirable review in its own right.

The number of misprints, missteps, and mistakes are minimal and, for the price ($5.00), packs a lot of information in its 160 pages. If you have irradiated fish to fry, its a good book to have.

*Maurice Robkin received his PhD at Massachusetts Institute of Technology in nuclear engineering. Since 1967, after a six-year stint at the Vallecitos Atomic Laboratory with the plutonium recycle program, he has been an associate professor in the Department of Nuclear Engineering at the University of Washington. His primary interest and research efforts at the U of W have been in bio-nuclear engineering. He is a member of, among others, the American Nuclear Society, the Radiation Research Society, and the Northwest Steelheaders Council of Trout Unlimited (which may explain his interest in fish).*